

University of Warwick institutional repository: <http://go.warwick.ac.uk/wrap>

A Thesis Submitted for the Degree of PhD at the University of Warwick

<http://go.warwick.ac.uk/wrap/34682>

This thesis is made available online and is protected by original copyright.

Please scroll down to view the document itself.

Please refer to the repository record for this item for information to help you to cite it. Our policy information is available from the repository home page.

High Resolution Characterisation of
Microcapsule Structure, Adhesion and
Release Properties

by

Isabel R. Lee

A thesis submitted for the degree of

Doctor of Philosophy

Department of Chemistry, University of Warwick

March 2005

*For my parents, without whose support I
would not have got this far*

Table of Contents

List of Figures.....	v
List of tables.....	xiii
Acknowledgements.....	xiv
Declaration.....	xvi
Abstract.....	xvii
Abbreviations.....	xviii

Chapter 1 - Introduction

1.1 Controlled release systems.....	1
1.1.1 Microencapsulation.....	2
1.1.1.1 Physical methods.....	2
1.1.1.2 Phase separation methods.....	3
1.1.1.3 Polyelectrolyte multilayer methods	4
1.1.1.4 Interfacial polymerisation reaction methods.....	5
1.1.2 Preparation of Microcapsules used in this project	6
1.1.3 Microcapsules – Current knowledge and reasons for study.....	9
1.2 Self-Assembled Monolayers	12
1.3 High resolution force microscopy.....	15
1.3.1 Atomic force microscopy (AFM).....	15
1.3.2 Chemical force microscopy (CFM).....	22
1.3.3 AFM studies of polymeric microcapsules.....	26
1.4 Fluorescence microscopy	27
1.5 Confocal laser scanning microscopy (CLSM).....	30
1.5.1 CLSM in the study of microcapsules.....	33
1.6 Aims of thesis.....	35
1.7 References.....	37

Chapter 2 – Experimental Section

2.1 Force measurements.....	45
2.1.1 Instrumentation.....	45
2.1.2 Micromanipulation.....	46
2.1.3 Spring constants.....	49

2.2 Substrate preparation for force measurements.....	49
2.2.1 Self-assembled monolayers of alkylthiols on gold.....	49
2.2.2 Cuticle substrate formation.....	51
2.3 Confocal microscopy.....	51
2.3.1 Instrumentation.....	51
2.3.2 Experimental procedures.....	52
2.3.2.1 Microcapsule release into solution.....	52
2.3.2.2 Microcapsule release in the dry state.....	53
2.3.2.3 Combined CLSM and electrochemical studies.....	54
2.4 Electrochemical techniques.....	55
2.4.1 Ultramicroelectrode fabrication.....	55
2.4.2 Electrochemical Measurements.....	57
2.5 Chemicals and solutions.....	58
2.5.1 Preparation of buffer solutions.....	59
2.5.2 Preparation of solutions used in electrochemical measurements.....	59
2.6 References.....	60

Chapter 3 - Investigation into the adhesion properties of functionalised microcapsules to different substrates

3.1 Introduction.....	61
3.2 Experimental.....	63
3.2.1 Formation of functionalised microcapsules.....	63
3.2.2 Experimental procedure for force measurements.....	64
3.3 Results and discussion.....	65
3.3.1 Characterisation of SAMs.....	65
3.3.2 Characterisation of spring constants.....	68
3.3.3 SEMs of microcapsules attached to AFM cantilevers.....	71
3.3.4 Force measurements between functionalised microcapsules and an –OH terminated SAM.....	72
3.3.5 Force measurements between functionalised microcapsules and SAMs of differing functionality.....	81
3.3.6 Force measurements between functionalised microcapsules and a leaf cuticle.....	84

3.4 Conclusions.....	87
3.5 References.....	88
 Chapter 4 - Investigations into the release of pesticide from microcapsules under solution	
4.1 Introduction.....	91
4.2 Theory.....	93
4.3 Experimental.....	95
4.4 Results and discussion.....	97
4.4.1 Preliminary studies.....	97
4.4.2 Release studies into ethanolic solution.....	100
4.4.2.1 Concentration of ethanolic solution used.....	101
4.4.2.2 Investigation of the effect of wall thickness and cross linking density on the permeability of microcapsules.....	103
4.4.2.3 Calculation of the product of the mass transfer coefficients of lambda cyhalothrin across the microcapsule wall and the solubility coefficients of the pesticide in the polymer wall	108
4.5 Conclusions.....	111
4.6 References.....	111
 Chapter 5 – Studies into the release of pesticide in the dry state	
5.1 Introduction.....	113
5.2 Experimental.....	115
5.2.1 Leaf, caterpillar and microcapsule selection.....	115
5.2.2 Confocal measurements.....	116
5.3 Results and discussion.....	118
5.3.1 High resolution imaging of <i>Prunus laurocerasus</i>	118
5.3.2 Release studies of emamectin benzoate and lambda cyhalothrin capsules..	122
5.3.3 High resolution imaging of caterpillars.....	130
5.4 Conclusions.....	134
5.6 References.....	135

Chapter 6 - Preliminary studies into the use of confocal microscopy for the trace detection of heavy metal ions	
6.1 Introduction	137
6.1.1 Stripping Voltammetry.....	137
6.1.2 Fluorescence detection of metal ions.....	140
6.2 Experimental	143
6.3 Results and discussion	145
6.3.1 Mercury hemisphere ultramicroelectrode growth.....	145
6.3.2 Hg UME Stripping Voltammetry of Cd(II).....	146
6.3.3 Current-time studies of Cd ²⁺ release from Hg.....	148
6.3.4 Combined ASV and CLSM studies for the detection of Cd ²⁺	150
6.4 Conclusions	160
6.5 References	160
 Chapter 7 – Conclusions	 163

List of Figures

Chapter 1 – Introduction

- Figure 1.1** Schematic illustrations of the polyelectrolyte deposition process and of subsequent core decomposition. Initial steps **(a-d)** involve stepwise film formation by repeated exposure of the colloids to polyelectrolytes of alternating charge with excess polyelectrolyte removed by washing and centrifugation. The coated particles are then exposed to 100 mM HCl whereupon the core immediately decomposes **(e-f)**.
- Figure 1.2** Interfacial condensation polymerisation processes.
- Figure 1.3** Process steps in interfacial condensation polymerization.
- Figure 1.4** Monomers used in the polyfunctional isocyanate microcapsule system.
- Figure 1.5** Wall forming reaction for the polyfunctional isocyanate microcapsule system.
- Figure 1.6** Butylated urea-formaldehyde pre-polymer used in the aminoplast pre-polymer microcapsule.
- Figure 1.7** Wall-forming reaction for the aminoplast pre-polymer microcapsule system.
- Figure 1.8** Cross linking mechanism used in the formation of the microcapsule wall in the aminoplast prepolymer system, showing the structure of the crosslinker pentaerythritol tetrakis(3-mercaptopropionate) (HSR).
- Figure 1.9** Artificially broken microcapsule made using the polyfunctional isocyanate microcapsule system – Magnification: 5200
- Figure 1.10** Schematic representation of microcapsule demonstrating parameters included in the release rate equation 1.1.
- Figure 1.11** Schematic representation of some of the supramolecular structures possible with SAMs of thiols on gold.
- Figure 1.12** Graph showing the comparison between mole fraction of thiol in an original solution with a methyl terminated thiol (χ^p_{solution}) and the corresponding mole fraction of the thiol in the monolayer (χ^p_{surface}).
- Figure 1.13** A schematic of a typical AFM experimental apparatus showing a V-shaped silicon nitride cantilever with a close up of the pyramidal tip.
- Figure 1.14** Schematic representation of an AFM force-distance (approach) curve.
- Figure 1.15** Scheme for the chemical modification of tips and sample substrates. In this case the tip and substrate have been modified with thiols which have end groups which are capable of hydrogen bonding with one another leading to enhanced interaction.
- Figure 1.16** **(a)** Representative force distance curves in ethanol recorded for COOH/COOH, CH₃/CH₃ and CH₃/COOH tip-sample functionalisation (tip radius ~ 60 nm). **(b)** Image of patterned CH₃ / COOH SAM determined from friction measurements using CFM with a methyl-terminated tip.

- Figure 1.17** Schematic of an avidin functionalised AFM tip and a biotinylated agarose bead, shown here partially blocked with avidin.
- Figure 1.18** (a) schematic demonstrating the sequential unfolding of individual titin immunoglobulin domains with the associated force distance curve. (b) an example of the characteristic sawtooth pattern of unfolding observed in these measurements.
- Figure 1.19** Jablonski diagram illustrating the processes involved in the creation of an excited electronic singlet state by optical absorption and subsequent emission of fluorescence.
- Figure 1.20** The excitation and emission spectra of a fluorescent molecule showing the change in wavelength between absorption and emission.
- Figure 1.21** The optical path in a typical epi-illumination fluorescence microscope.
- Figure 1.22** A comparison of the illumination experienced by the specimen during (a) full field illumination in a conventional fluorescence microscope and (b) Single point illumination in a CLSM.
- Figure 1.23** The principles of confocal laser scanning microscopy. Solid red lines indicate light from the focal plane, black dashed lines indicate light above and below the focal plane that is prevented from being detected by the confocal aperture.
- Figure 1.24** (a) Schematic for the FRAP experiment. CLSM images of capsules: (b) before bleaching; (c) after bleaching inside the capsule; (d) fluorescence recovery; (e) fluorescence intensity from a fixed area within the capsule as a function of time.

Chapter 2 – Experimental Section

- Figure 2.1** Photograph of the micromanipulation set up used in this project.
- Figure 2.2** Optical micrographs from the optical microscope (magnification x 200) of etched 250 μm diameter tungsten wires.
- Figure 2.3** Schematic representation of micromanipulation rig used in this project.
- Figure 2.4** Schematic representation of the procedure for the formation of SAMs of alkyl thiols on a gold surface.
- Figure 2.5** Molecular structure of the pyrethroid insecticide Lambda Cyhalothrin.
- Figure 2.6** Molecular structure of the pesticide Emamectin Benzoate
- Figure 2.7** Images from the optical microscope of the finished UME (a) Side view of the UME (b) Top view of the UME defining the terms for calculating RG.

Chapter 3 - Investigation into the adhesion properties of functionalised microcapsules to different substrates

- Figure 3.1** Structures of modifier molecules which react into the polymer wall via the NH_2 group to control the surface functionality of the microcapsule.

- Figure 3.2** Schematic representation of the experimental set-up for force measurements between microcapsule and substrate.
- Figure 3.3** AFM images of (a) non-annealed gold surface and (b) a gold substrate annealed at 350 °C for 6 hours. Scan size 1 μ m x 1 μ m.
- Figure 3.4** Images captured during enlargement of water droplet on (a) 100% -COOH terminated SAM, (b) 50% -COOH and 50% -CH₃ terminated SAM, (c) 100% -CH₃ terminated SAM. (θ = contact angle of droplet to surface)
- Figure 3.5** (a) The sequential frequency response of a silicon nitride cantilever with the addition of 4 borosilicate spheres. (b) The added mass of the spheres is plotted as a function of the resonance frequency to allow the determination of the spring constant and cantilever mass.
- Figure 3.6** Graph showing the fit of equation 3.1 to the experimental thermal resonance peak obtained from a long thick silicon nitride cantilever.
- Figure 3.7** SEMs of microcapsule attached to silicon nitride AFM cantilevers using 5-minute epoxy.
- Figure 3.8** Schematic of the functional groups investigated in force measurements: (a) sulfonate modified microcapsule; (b) alkyl modified microcapsule; (c) anionic modified microcapsule; (d) cationic modified microcapsule.
- Figure 3.9** (a) Examples of force-distance curves for an alkyl modified microcapsule to an OH-terminated SAM at different pHs. (b) Examples of force-distance curves for a sulfonate-modified microcapsule to an OH-terminated SAM at different pHs.
- Figure 3.10** Schematic representation of hydrogen bonding between ethylene oxide and propylene oxide groups present in modifier molecules on the surface of sulfonate and alkyl modified microcapsules with an OH-terminated SAM.
- Figure 3.11** Force titration showing adhesion forces normalised with respect to the radius of microcapsule to an OH-terminated SAM for an alkyl (•), sulfonate (●) and an unmodified (●) microcapsule.
- Figure 3.12** (a) Monomers used in the polyfunctional isocyanate system (b) Representative portion of microcapsule wall structure.
- Figure 3.13** Force titration showing 'jump to contact' forces observed in adhesion measurements normalised with respect to the radius of microcapsule to an OH-terminated SAM for an alkyl (•) and a sulfonate (●).
- Figure 3.14** Force titration showing adhesion forces normalised with respect to the radius of microcapsule to an OH-terminated SAM for a cationic (●), anionic (■) and an unmodified (◆) microcapsule.
- Figure 3.15** (a) Force titration showing adhesion forces normalised with respect to the radius of a sulfonate modified microcapsule to an OH-terminated SAM (■) and a CH₃ terminated SAM (●). (b) Force titration showing adhesion forces normalised with respect to the radius of an alkyl modified microcapsule to an OH-terminated SAM (■) and a CH₃ terminated SAM (●).

- Figure 3.16** (a) Force titration showing adhesion forces for a sulfonate modified microcapsule to an CH₃-terminated SAM (■) and a mixed 70:30 CH₃:COOH terminated SAM (●). (b) Force titration showing adhesion forces for an alkyl modified microcapsule to an CH₃-terminated SAM (■) and a mixed 70:30 CH₃:COOH terminated SAM (●).
- Figure 3.17** Examples of force distance curves for (a) a sulfonate modified microcapsule and (b) an alkyl modified microcapsule to a 70:30 CH₃:COOH mixed SAM at 3 different sites on the surface of the SAM.
- Figure 3.18** Force titration showing adhesion forces normalised with respect to the radius of microcapsule to a cuticle of the prunus laurocerasus leaf for an alkyl (●), sulfonate (■) cationic(♦) and an unmodified (▲)microcapsule.
- Figure 3.19** Examples of force distance curves of an alkyl modified microcapsule to a leaf cuticle all measured at the same pH at 4 different locations on the cuticle surface.
- Figure 3.20** (a) Force titration showing adhesion forces normalised with respect to the radius of a sulfonate modified microcapsule to a leaf cuticle (■) and a mixed 70:30 CH₃:COOH terminated SAM (●). (b) Force titration showing adhesion forces normalised with respect to the radius of an alkyl modified microcapsule to a leaf cuticle (■) and a mixed 70:30 CH₃:COOH terminated SAM (●).

Chapter 4 - Investigations into the release of pesticide from microcapsules under solution

- Figure 4.1** Schematic representation of the parameters described in equation 4.1
- Figure 4.2** Experimental set up for studying the release of active ingredient from microcapsule into solution.
- Figure 4.3** 3D projection images of polyurea microcapsules filled with the dye Nile Red.
- Figure 4.4** Slice through the centre of a group of microcapsules containing the dye Nile Red at (a) 0 min, (b) 30 min, (c) 60 min, (d) 90 min (e) 120 min (f) 180 min.
- Figure 4.5** Slices through the centre of polyurea microcapsules containing (a) the pesticide lambda cyhalothrin and the solvent Solvesso and (b) the solvent Solvesso alone.
- Figure 4.6** Series of images taken through the centre of a lambda cyhalothrin filled microcapsule showing the release of the pesticide over time. The time scale between each image was 2 minutes with the first being taken at 0 minutes.
- Figure 4.7** Plots of $(I_0 - I_t)/I_t$ vs time showing the release of lambda cyhalothrin from capsules with 10% wall, 1:10 crosslinking density. Measurements were taken in solutions of differing ethanol:water concentrations; ● 100% water, ● 25:75 EtOH:Water, ● 75:25 EtOH:Water.
- Figure 4.8** Plots of $(I_0 - I_t)/I_t$ vs time showing the release of lambda cyhalothrin from

capsules with 10% wall, 1:10 crosslinking density. Measurements were taken in solutions of differing ethanol:water concentrations; • 100% water, • 25:75 EtOH:Water, • 75:25 EtOH:Water.

Figure 4.9 Graphs detailing the release of lambda cyhalothrin from capsules measured as the average light intensity within the capsules normalised with respect to the initial intensity against time. Measurements were taken in 75:25 EtOH:Water and the capsules used were 15% wall with (a) • 1:20 crosslinking, (b) • 1:10 crosslinking, (c) • 1:1 crosslinking.

Figure 4.10 Graphs detailing the release of lambda cyhalothrin from capsules measured as the average light intensity within the capsules normalised with respect to the initial intensity against time. (a) 10% wall with • 1:20 cross linking, • 1:10 cross linking, • 1:1 cross linking; (b) 15% wall with • 1:20 cross linking, • 1:10 cross linking, • 1:1 cross linking.

Figure 4.11 Graphs detailing the release of lambda cyhalothrin from capsules investigating the effect of changing the wall thickness on the release profile. (a) 1:20 cross linking with • 10% wall, • 15% wall; (b) 1:10 cross linking with • 10% wall, • 15% wall and (c) 1:1 cross linking with • 10% wall, • 15% wall.

Figure 4.12 Cropped release profile for microcapsule with 10% wall and 1:1 crosslinking density ratio.

Chapter 5 – The release of pesticides from microcapsules in the dry state

Figure 5.1 Schematic representation of the structure of a leaf showing the different components present within the leaf.

Figure 5.2 (a) High resolution imaging of the *Prunus laurocerasus* in different focal planes using CLSM. Serial optical sections were acquired from the top (top left image) to the bottom (bottom right image) of the sample in defined steps of 2 μm . (b) 3D projection of *Prunus laurocerasus* reconstructed from 82 serial optical sections through the cuticle of the caterpillar. (c) Single optical slice on surface of *Prunus laurocerasus* and reconstructions of 82 serial optical sections (step size 1 μm) to produce orthogonal cross-sections in the x - z and y - z planes, along directions defined by the green and red line. The position of the single slice image in the z -stack is shown by the blue line in the x - z and y - z orthogonal projections.

Figure 5.3 Series of single optical slices taken just below cuticle of *Prunus laurocerasus* and reconstructions of 82 serial optical sections (step size 1 μm) to produce orthogonal cross-sections in the x - z and y - z planes, along directions defined by the green and red line. The position of the single slice image in the z -stack is shown by the blue line in the x - z and y - z orthogonal projections. Each slice in the series is taken in the same position of the leaf at half hour time intervals. Samples used were (a) a 1 cm diameter disc cut out of a leaf and (b) an intact leaf attached to water soaked cotton wool.

Figure 5.4 (a) Series of single optical slices taken in the centre of a single

microcapsule on the surface of a leaf of the *Prunus laurocerasus* and reconstructions of 55 serial optical sections (step size 1 μm) to produce orthogonal cross-sections in the x - z and y - z planes, along directions defined by the green and red line. The position of the single slice image in the z -stack is shown by the blue line in the x - z and y - z orthogonal projections. Each slice in the series is taken in the same position of the leaf at hour time intervals. **(b)** Slices taken through the centre of a single capsule showing the decrease in fluorescence relating to the release of pesticide with time.

- Figure 5.5** Graph detailing the release of the pesticide lambda cyhalothrin from microcapsules onto a leaf of *Prunus Laurocerasus*.
- Figure 5.6** Schematic representation of parameters involved in the release of lambda cyhalothrin from a polymeric microcapsule onto a surface.
- Figure 5.7** Plot of $V\ln(I_t/I_0)$ against time for lambda release onto *Prunus laurocerasus*.
- Figure 5.8** **(a)** 3D projections of an emamectin benzoate capsule on the surface of a leaf of *Prunus laurocerasus* reconstructed from a z -stack consisting of 125 slices taken 1 μm apart. The images were taken at different times after application of microcapsule to leaf. **(b)** Slice through the centre of the emamectin benzoate capsule taken at half hour time intervals.
- Figure 5.9** Graph detailing the release of the pesticides • lambda cyhalothrin and • emamectin benzoate from microcapsules onto a leaf of the *Prunus laurocerasus*.
- Figure 5.10** Graph detailing the average release from microcapsules containing the pesticide emamectin benzoate when applied to • a glass slide and • a glass slide covered in Parafilm.
- Figure 5.11** **(a)** High resolution image series z -stacking through the cuticle of *Plutella xylostella*. Images shown are taken at 5 μm intervals from above to below the cuticle. **(b)** 3D projection reconstructed from 150 serial optical sections through the cuticle of the caterpillar.
- Figure 5.12** **(a)** High resolution image series z -stacking through the cuticle of *Heliothis virescens*. Images shown are taken at 5 μm intervals from above to below the cuticle. **(b)** 3D projection reconstructed from 150 serial optical sections through the cuticle of the caterpillar.
- Figure 5.13** **(a)** z -stack through Nile red microcapsules on the surface of the *Heliothis virescens*. Images were taken every 5 μm . **(b)** Single optical slice on surface of *Heliothis virescens* and reconstructions of 150 serial optical sections (step size 1 μm) to produce orthogonal cross-sections in the x - z and y - z planes, along directions defined by the green and red line. The position of the single slice image in the z -stack is shown by the blue line in the x - z and y - z orthogonal projections.

Chapter 6 - Preliminary studies on the combined use of CLSM and electrochemistry for the trace detection of heavy metal ions

- Figure 6.1** Principles of anodic stripping. Values shown are typical ones used; potentials and E_p are typical of Cu^{2+} analysis. **(a)** Preelectrolysis at E_d ; stirred solution. **(b)** Rest period; stirrer off. **(c)** Anodic scan ($v = 10\text{-}100$ mV/s).
- Figure 6.2** Visual screening of fluorescent indicator responses to metal ions. The image shows a 96-well microplate containing various combinations of ions and indicators in 50 mM MOPS pH 7.0. Each row of wells represents a different indicator; each column of wells represents a different ion. The indicators (top to bottom) are: Calcium Green-5N (0.5 μM), Calcium Green-2 (0.2 μM), fluo-4 (2 μM), fluo-5N (2 μM), FluoZin-1 (2 μM), Newport Green DCF (2 μM), Phen Green FL (2 μM) and calcein (0.5 μM). The left-hand column of wells contains 10 mM EGTA + 10 μM TPEN (ion-free reference solution). Subsequent columns (left to right) represent 1 μM concentrations of Ca^{2+} , Ba^{2+} , Mn^{2+} , Fe^{2+} , Co^{2+} , Ni^{2+} , Cu^{2+} , Zn^{2+} , Cd^{2+} , Hg^{2+} , and Pb^{2+} , respectively. The microplate was scanned using a FLA3000G laser scanner (Fuji Photo Film Co.) with excitation at 473 nm and fluorescence emission detected at 520 nm. The image is pseudocolored according to fluorescence intensity (high = red > orange > yellow > green > blue = low).
- Figure 6.3** **(a)** Metal-ion response screening for Calcium Green-5N. The maximum relative fluorescence intensity was measured for indicator concentrations in solutions containing 10 mM EGTA + 10 μM TPEN, 1 μM ion (100 μM for Mg^{2+}) and 100 μM ion (10 mM for Mg^{2+}). Results are plotted as fluorescence changes relative to the ion-free (10 mM EGTA + 10 μM TPEN) reference solution expressed as $(F-F_0)/F_0$, where F is the fluorescence intensity of ion-containing solutions and F_0 is the fluorescence intensity of the reference solution. Blue bars indicate the response to 1 μM ion (100 μM for Mg^{2+}), and red bars indicate the response to 100 μM ion (10 mM for Mg^{2+}). **(b)** Structure of the fluorescence indicator Calcium Green-5N.
- Figure 6.4** **(a)** Photograph of the experimental set-up showing the trough and electrode on the stage of the confocal microscope. **(b)** Schematic of experimental arrangements for studies of Cd^{2+} stripping experiments.
- Figure 6.5** A typical current-time growth transient for the electrodeposition of mercury onto a 25 μm diameter Pt UME, from a solution containing 10 mM mercurous nitrate, 0.1 M HNO_3 and 0.5 M KNO_3 with the electrode held at 0.225 V.
- Figure 6.6** Typical stripping voltammogram of cadmium from a Hg/Pt UME. Preconcentration time 240 seconds.
- Figure 6.7** Current time plots for the stripping of cadmium from a mercury UME. The electrode was preconcentrated for 10 seconds then held at the potentials shown in the legend.
- Figure 6.8** Plot showing the dependence of charge passed during stripping with the potential applied.

- Figure 6.9** Current time plots for the stripping of cadmium from a mercury UME. The electrode was held at -0.8 V and was preconcentrated with cadmium for the times shown in the legend.
- Figure 6.10** Plot showing the dependence of charge passed during stripping with deposition time.
- Figure 6.11** Normalised light intensity as a function of Cd^{2+} concentration for a solution of Calcium green 5N and cadmium nitrate with CLSM images at marked concentration values.
- Figure 6.12** Time series of frames taken over surface of electrode in $1 \times 10^{-5} \text{ mol dm}^{-3}$ CdNO_3 and $0.5 \text{ } \mu\text{mol dm}^{-3}$ Calcium Green 5N. Frames were taken every 7 seconds. Series recorded concurrently with ASV with preconcentration time of 60 seconds. Preconcentration time started at 14 seconds. Preconcentration was followed by a potential sweep from -1.1 to -0.5 V.
- Figure 6.13** Schematic representation showing how spatiotemporal data collected relates to the system studied.
- Figure 6.14** Stripping voltammograms of Cd^{2+} from a Hg UME recorded after specified preconcentration times. Associated spatiotemporal images are shown in Figure 6.12.
- Figure 6.15** Plot showing the dependence of charge passed during stripping on the deposition time of cadmium into the mercury hemisphere UME.
- Figure 6.16** Line scans taken across the centre of the electrode over time for deposition times of (a) 10 seconds, (b) 20 seconds, (c) 30 seconds, (d) 40 seconds, (e) 50 seconds (f) 60 seconds (g) 70 seconds (h) 80 seconds.

List of Tables

Table 2.1	Details of microcapsules used in release into solution experiments
Table 2.2	Grades and suppliers of chemicals used in these studies
Table 3.1	Experimentally determined contact angle measurements
Table 4.1	Details of properties of microcapsules used in release into solution measurements
Table 4.2	Product of mass transfer and solubility coefficients of microcapsules with differing wall properties

Acknowledgements

Firstly I would like to thank Prof. Patrick Unwin and Dr. Julie Macpherson for all their enthusiasm, encouragement and friendship through the three years of this project. Their advice and support have been invaluable in the completion of these studies. I must also express my gratitude to my industrial supervisors at Syngenta, especially Ian Shirley, Colin Brennan and Anne Waller who have helped me understand how the fundamental science I was carrying out was applicable to real life.

Huge thanks must go to all the members, past and present, of the Electrochemistry and Interfaces group at Warwick. Naf, Cat and Doug, I blame you entirely for persuading me to stay and do a PhD, that first year with you three was perhaps my best. I would like to thank Dr. Anna Barker for all of her advice over the years, explaining things to me in simple terms. I would also like to thank Dr. Neil Wilson for his help with spring constant work and explaining physics to me.

Lucy and Sophie, thanks for listening to me when things weren't going right and helping me to realise I wasn't the only one who couldn't do it. Mark and Dave, we have come through this together and we will all come out the other side, thank you both for entertaining me over the years. Nikki thanks for all your help being my contact on campus when writing up at home. Everyone else in the group, thank you so much for your friendship and advice over the years, you have really made my time at Warwick enjoyable.

I could not have got through these studies if it hadn't been for the lunch time crew. I have looked forward to lunch every day though I don't know why – the ridicule, the shoe throwing, the tango incident – all a sign of how much you care I guess! I must also thank members of the women's rugby club who have kept me feeling young and provided me with a much needed distraction from work.

Special thanks must go to Cat who has been far more than just a housemate, lab mate and best mate. Her insanity matches mine completely and together over the past three years we have triumphed over adversity to complete our studies and finally leave the bubble.

Finally, I must thank my parents and Euan. They have been there for me throughout and have born the brunt of my frustrations during the write up. Thank you so much for all of your support, without it I would never have got this far.

Declaration

The work contained within this thesis is entirely original and my own work, except where acknowledged in the text. I confirm that this thesis has not been submitted for a degree at another university.

Abstract

This thesis aims to characterise the structural, adhesion and release properties of polymeric microcapsules which are used in agriculture for the controlled delivery of pesticides to crops.

An adaptation of atomic force microscopy (AFM) known as chemical force microscopy (CFM) has been used to investigate the adhesion characteristics of functionalised polyurea microcapsules to surfaces. The adhesion properties of microcapsules (attached to AFM cantilevers) to self-assembled monolayers (SAMs) of alkyl thiols on gold have been investigated at the single capsule level, and as a function of polymer wall surface functionality. Measurements have been made to OH-terminated, CH₃-terminated and mixed CH₃: COOH-terminated SAMs. The importance of microcapsule topography and elasticity on adhesion measurements has been discussed. The surface pK_{1/2} of a capsule with a surface modified with a sulfonate-terminated molecule has been estimated using force titration methodology. The adhesion properties of functionalised microcapsules to the leaf cuticle of *Prunus laurocerasus* have been examined, highlighting areas of hydrophilicity on the surface of the leaf.

The release properties of active ingredients from polyurea microcapsules into solution using confocal laser scanning microscopy (CLSM) have been investigated. Preliminary studies obtained the optimum species to use inside the microcapsule and the solution into which the species should be released. The release characteristics of six varieties of microcapsule, differing in the wall thickness and cross linking density were examined and from the release profiles obtained, the product of the mass transfer coefficient and solubility coefficient could be calculated.

The high resolution imaging capabilities of the confocal microscope have been demonstrated, providing detail on the structure of the leaf of the *Prunus Laurocerasus* plant and the caterpillars *Heliothis virescens* and *Plutella xylostella*, two of the most common pests, which the microcapsules of interest are aimed at controlling. The release properties to leaf surfaces of two types of polyurea microcapsules, which have different release mechanisms, were investigated using CLSM. Detailed release studies to model surfaces showed that one type of capsule (lambda cyhalothrin) released in the dry state and the other (emamectin benzoate) did not. A release rate was determined in the former case.

A technique has been developed which is capable of visualising the release and diffusion of a species (Cd²⁺) from a hemisphere. Voltammetry has been used in conjunction with CLSM to monitor quantitatively and visually the preconcentration and release of Cd²⁺ into and away from a mercury hemisphere UME. The fluorescent indicator used was Calcium Green-5N, which is a cadmium-sensitive fluorophore that fluoresces upon binding Cd²⁺ and can thus be detected by CLSM. A delay was observed between the release of Cd²⁺ from the hemisphere (determined voltammetrically) and binding to the fluorophore (visualised using CLSM).

Abbreviations

AFM	atomic force microscopy
CFM	chemical force microscopy
CLSM	confocal laser scanning microscopy
PMPPI	polymethylene-polyphenylisocyanate
TDI	toluene diisocyanate
SEM	scanning electron microscopy
SAM	self-assembled monolayer
XPS	x-ray photoelectron spectroscopy
PSD	photosensitive diode detector
DNA	deoxyribosenucleic acid
FOCG	Fowkes, van Oss, Chaudhury and Goog
FRAP	fluorescence recovery after photobleaching
DI	Digital Instruments
VCR	video cassette recorder
LSM	laser scanning microscope
UME	ultramicroelectrode
AgQRE	silver quasi-reference electrode
WE	working electrode
RICM	reflection interference contrast microscopy
HPLC	high performance liquid chromatography
UV	ultraviolet
vis	visible
FEM	finite element method
3D	three dimensional
NAA	naphyl acetic acid
HMDE	hanging mercury drop electrode
MFE	mercury film electrode
LSV	linear sweep voltammetry
o.d.	outer diameter
i.d.	inner diameter

Chapter 1

Introduction

This thesis is concerned with investigating the structural, release and adhesion properties of polymeric microcapsules.

This chapter outlines briefly the concept of controlled release systems and microencapsulation, detailing the procedure by which the microcapsules studied in this thesis are synthesised and the principles of their action. The chapter goes on to discuss the principles of self assembled monolayers and how they are applicable as a model system in these studies. A review of the technique atomic force microscopy (AFM) in particular an adaptation of AFM known as chemical force microscopy (CFM) is presented along with an introduction to confocal laser scanning microscopy (CLSM). Details of how these techniques have been used previously to study microcapsules are included.

1.1 Controlled release systems

Nature uses controlled release processes to deliver chemical species. Examples include the oxygenation of blood in mammals by the diffusion of oxygen through the alveolar walls and the delivery and control of the flow of food and waste across the exterior membrane of a prokaryote. By mimicking nature's controlled release mechanisms, it may be possible to develop more efficient and effective means of delivering chemicals to intended targets synthetically. The pharmaceutical industry has provided a major scientific impetus for this type of technology. There is often concern over the administration of single, high doses of conventional drugs. This has led to the development of controlled release oral drugs and more recently implantable devices¹⁰⁻¹².

In its broadest sense, the concept of sustained or prolonged release of biologically active agents has existed for decades^{13,14}. The majority of early products

were sustained release systems, meaning that the release of the active agent, although slower than in conventional formulations was still substantially affected by the external environment into which it is released. By comparison, controlled release systems provide a release profile predominantly controlled by the design of the system itself. In this case, the release of active agents is largely independent of external factors.

Using these principles, scientists in the pesticide field have developed new technologies and formulations for the delivery of pesticides to required locations, which have a number of associated advantages¹⁵⁻¹⁷. These advantages include: a reduction in the hazard associated with the use of highly toxic chemicals; extension of the duration of effectiveness of the pesticides without increasing the rates of application; improving pest control efficiency; prolonging the effective life of unstable, volatile or hydrolysable pesticides; and minimising pollution of the environment.

1.1.1 Microencapsulation

In this project the controlled release mechanism to be studied is the release of an active ingredient (pesticide) from a microcapsule. A microcapsule is a spherical object with an outer polymeric shell which encloses the active ingredient. The process by which the microcapsule with the pesticide oil inside is formed is called microencapsulation. Microencapsulation fabrication processes can be divided into four main categories: the physical methods category; the phase separation category¹; the multilayer polyelectrolyte film category⁹; and the interfacial reaction category^{1,3}.

1.1.1.1 Physical methods

In this category, wall material (monomers) and core particles (active ingredient, AI) are physically brought together and the wall flows around the core particles to form

the microcapsule. This is done by one of two methods, either the use of biliquid extrusion nozzles or biliquid multiorifice centrifugal devices^{18,19}. After forming the microcapsule, the polymer wall is hardened by chemical reaction, evaporation of solvent or cooling. These processes have limited use in the microencapsulation of pesticides as throughput is low and it is difficult to produce particle sizes less than 100 μm .

Other physical methods such as spray drying²⁰, spray chilling²¹ and fluidised bed spray coating²² bring wall and core together via an atomisation process. Problems with these methods include volatility losses and the fact that under most conditions not all of the pesticide is encapsulated and not all of the polymer particles actually contain pesticide.

1.1.1.2 Phase separation methods

In this category, microcapsules are formed by emulsifying or dispersing the core material in an immiscible continuous phase in which the wall material is dissolved, separated physically from the continuous phase and deposited around the core particles. A variety of techniques such as a change in pH, addition of a non-solvent or addition of a salt, force the dissolved polymers out of solution^{1,23}.

There are process control and pesticide loading limitations associated with these phase separation techniques. Reproducible phase separation conditions are difficult to achieve and it is difficult to ensure that the phase-separated polymer will preferentially wet the core droplets. As the polymer phase separates from the continuous phase in these processes, causing flow resistance between forming microcapsules, it is not possible to produce pesticide microcapsule formulations with pesticide loading much greater than 240 g active ingredient per litre.

1.1.1.3 Polyelectrolyte multilayer methods

A more recently introduced technique for the encapsulation of species is the fabrication of supramolecular shell structures (micro- and nanocapsules) consisting of ultra-thin multilayer polyelectrolyte films⁹. The capsules are produced by the stepwise adsorption of polyelectrolytes of opposite electric charge from their aqueous solutions onto the surface of colloidal particles. This is followed by the dissolution of the templating core, resulting in the polyelectrolyte capsules being replicas of the templating core. See Figure 1.1 for details of formation.

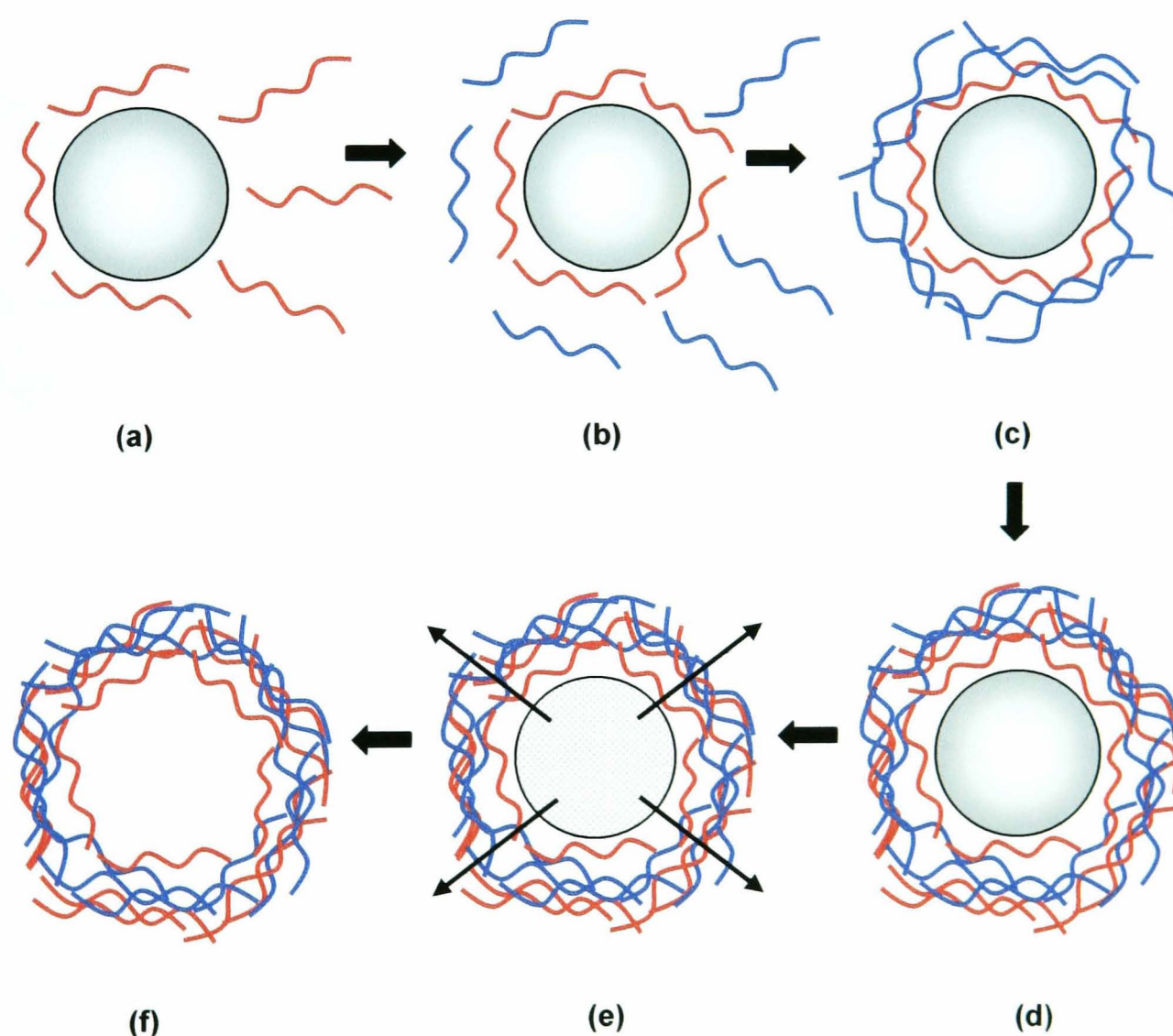


Figure 1.1 Schematic illustrations of the polyelectrolyte deposition process and of subsequent core decomposition. Initial steps **(a-d)** involve stepwise film formation by repeated exposure of the colloids to polyelectrolytes of alternating charge with excess polyelectrolyte removed by washing and centrifugation. The coated particles are then exposed to 100 mM HCl whereupon the core immediately decomposes **(e-f)**. Reproduced from reference 9.

1.1.1.4 Interfacial polymerisation reaction methods

The interfacial reaction category can be divided into two subcategories:

1. Interfacial addition. These processes use unsaturated monomers and have limited use in pesticide microencapsulation due to the presence of impurities in technical pesticides which interfere with the action of free radical producing catalysts.

2. Interfacial condensation. In this process two different monomers are brought together at the oil/water interface where they react by condensation polymerisation to form the microcapsule wall. The two different interfacial condensation polymerisation types are demonstrated schematically in Figure 1.2.

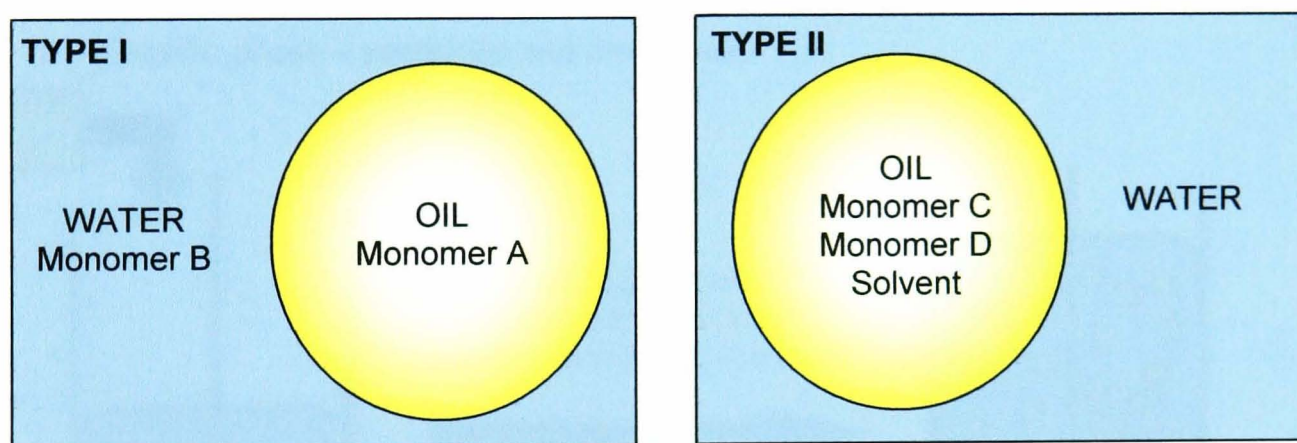


Figure 1.2 Interfacial condensation polymerisation processes. Reproduced from reference 1.

Type I – One reactive monomer is incorporated in the organic phase (monomer A) and a second in the aqueous phase (monomer B). Typically the organic phase monomer is a polyfunctional isocyanate and the water phase is a polyfunctional amine²⁴⁻²⁶. Interfacial polymerisation occurs rapidly at ambient temperatures.

Type II – Monomers are incorporated in the oil phase only and are polymerised interfacially by increasing temperature.

Interfacial condensation microencapsulation processes are very suitable for the microencapsulation of pesticides as they are characterised by high pesticide loading and uncomplicated processing steps.

1.1.2 Preparation of Microcapsules used in this project

The interfacial condensation microencapsulation process (Type II) is used to make the microcapsules used in this project. The process involves first dissolving the monomers in the pesticide oil to be encapsulated to form the organic phase. The aqueous phase is then prepared by addition of emulsifiers and protective colloids to water. The next step is to add the organic phase to the aqueous phase with appropriate agitation to form an oil-in-water emulsion with an average particle size in the range of 2-15 μm . Finally the microcapsule wall formation is initiated by heating the batch. Figure 1.3 demonstrates schematically the process involved.

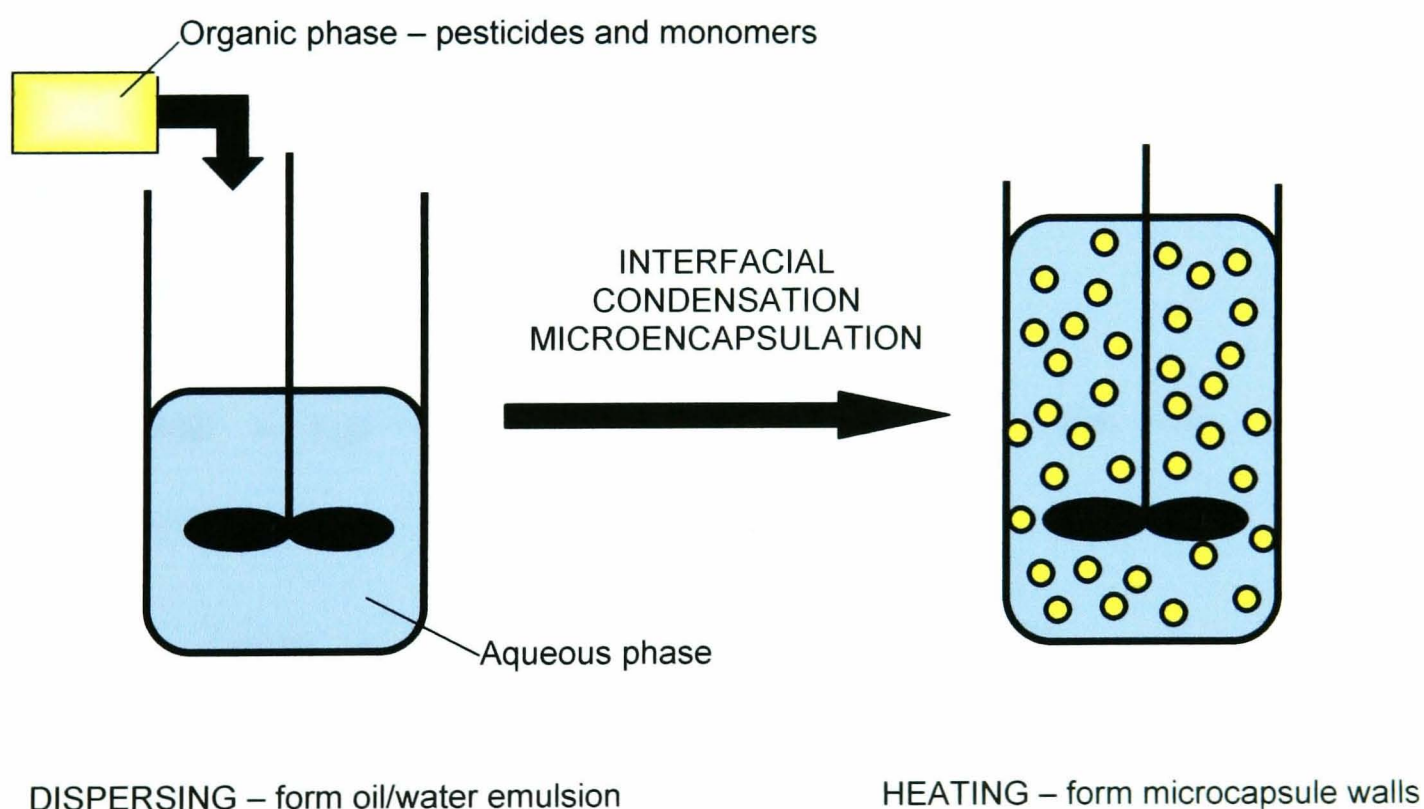


Figure 1.3 – Process steps in interfacial condensation polymerisation. Reproduced from reference 3.

Two interfacial condensation microencapsulation systems were involved in the synthesis of microcapsules used in these studies. These are known as the polyfunctional isocyanate system, which produces the microcapsules predominantly studied, and the aminoplast pre-polymer system³.

In the polyfunctional isocyanate system, the monomers that are incorporated in the organic phase to form the wall of the microcapsules are polymethylene-polyphenylisocyanate (PMPPI) and toluene diisocyanate (TDI) (Figure 1.4).

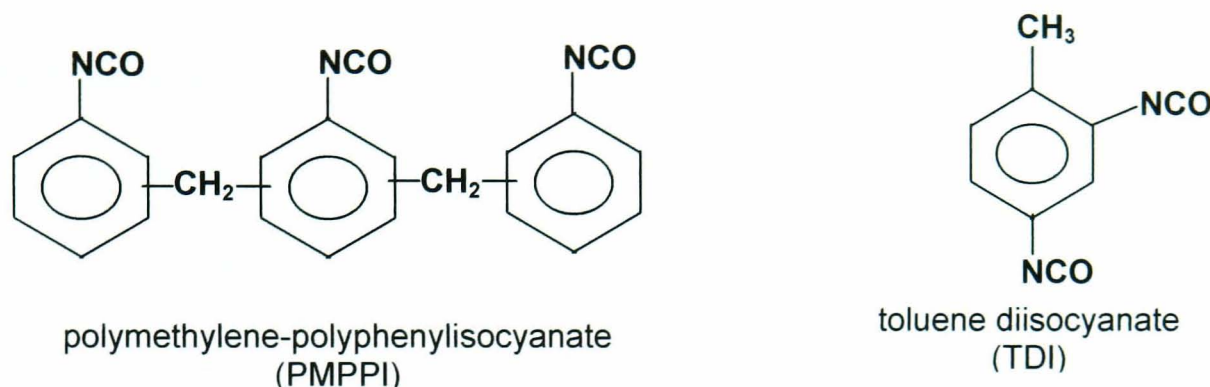


Figure 1.4 Monomers used in the polyfunctional isocyanate microcapsule system

The wall forming reaction is initiated when the oil-in-water emulsion is heated to 50 °C, at which point the isocyanate monomers are hydrolysed at the interface (slow step) to form amines which in turn react with unhydrolysed monomers to form the microcapsule wall. The mechanism is shown in Figure 1.5.

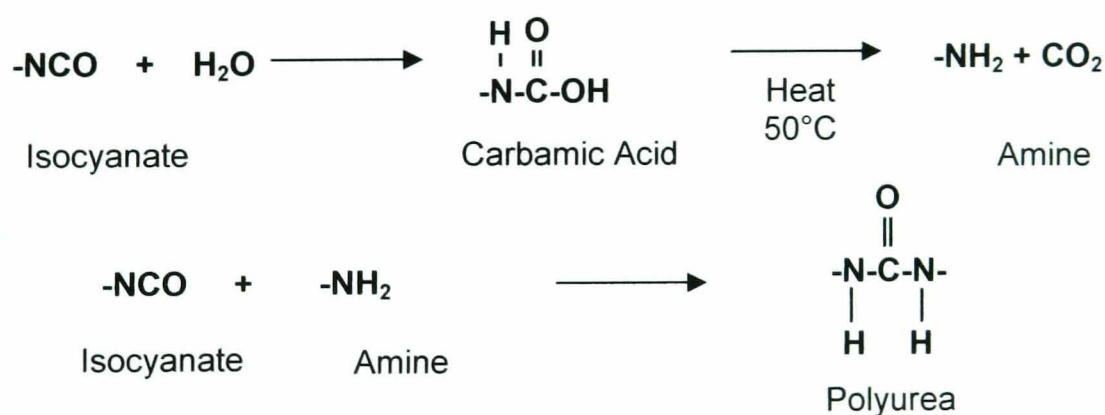


Figure 1.5 Wall forming reaction for the polyfunctional isocyanate microcapsule system.

The interfacial reaction occurs on the oil side of the interface and is limited to the interface because of the unavailability of water in the core of the oil particle. Water diffuses into the oil droplet, across the interface and reacts with isocyanate monomers diffusing from the core of the particle to the interface. As interfacial polymerisation is initiated by water which is at its highest concentration at the interface, decreasing as the distance increases from the interface, the wall formed is asymmetric in construction.

The structure of the wall of the microcapsule can be altered by dissolving a modifier molecule in the aqueous phase prior to making the emulsion. Some of the modifiers will react into the capsule wall (via reaction between amine group(s) and isocyanate). The modifiers enable the wall of the microcapsule to become charged (for further details see section 3.2)

In the second system used for microcapsule formation, the aminoplast prepolymer system, the wall forming agent used is a butylated urea-formaldehyde prepolymer, the structure of which is shown in Figure 1.6.

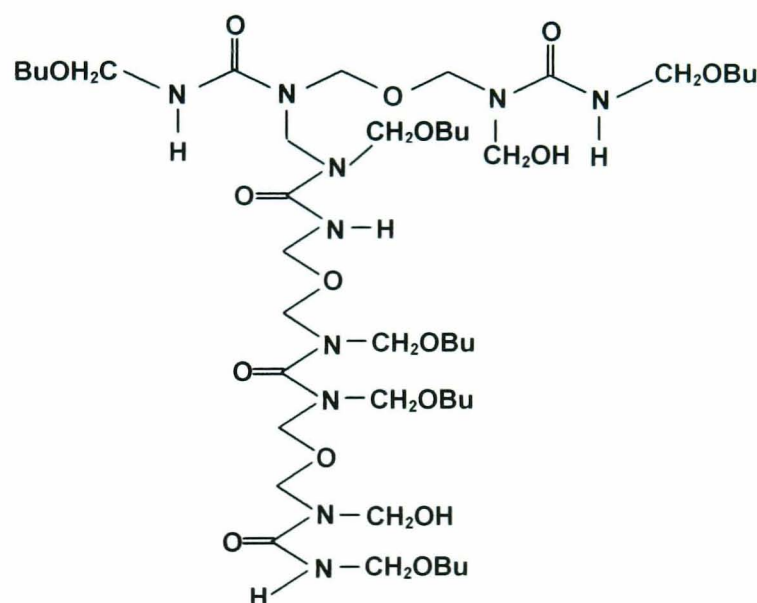


Figure 1.6 Butylated urea-formaldehyde pre-polymer used in the aminoplast pre-polymer microcapsule.

The wall forming reaction is initiated by adjusting the pH of the oil-in-water emulsion to pH 2 and heating the emulsion to 55 °C. At this point a butylated methylol group on the prepolymer, located on the oil side of the droplet interface, is activated by the addition of a proton from the surface active sulfonic acid catalyst, and this activated prepolymer then reacts with a methylol group from another pre-polymer located on the oil side of the interface to form a methylene linkage (mechanism shown in Figure 1.7). The membrane produced is also asymmetric because the concentration of the activated pre-polymer decreases rapidly as the distance from the interface increases.

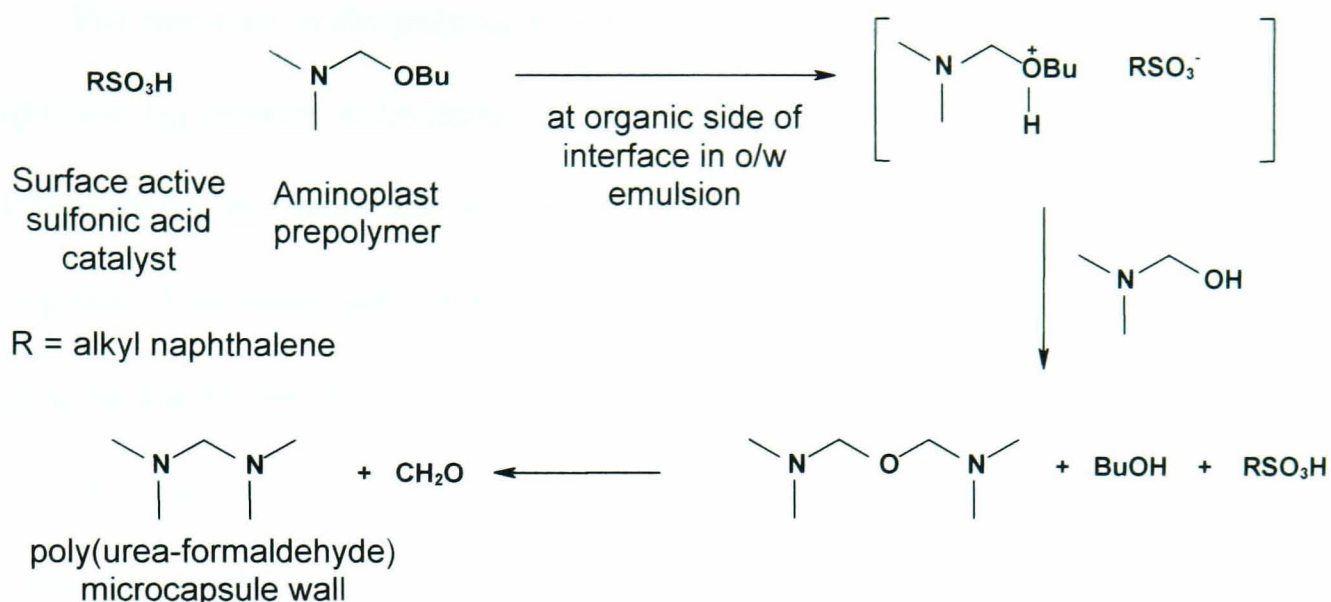


Figure 1.7 Wall-forming reaction for the aminoplast pre-polymer microcapsule system.

The polymer formed is then cross-linked with a tetrafunctional thiol (pentaerythritol tetrakis(3-mercaptopropionate) – for structure see Figure 1.8) to complete the microcapsule wall. The crosslinking mechanism is shown in Figure 1.8.

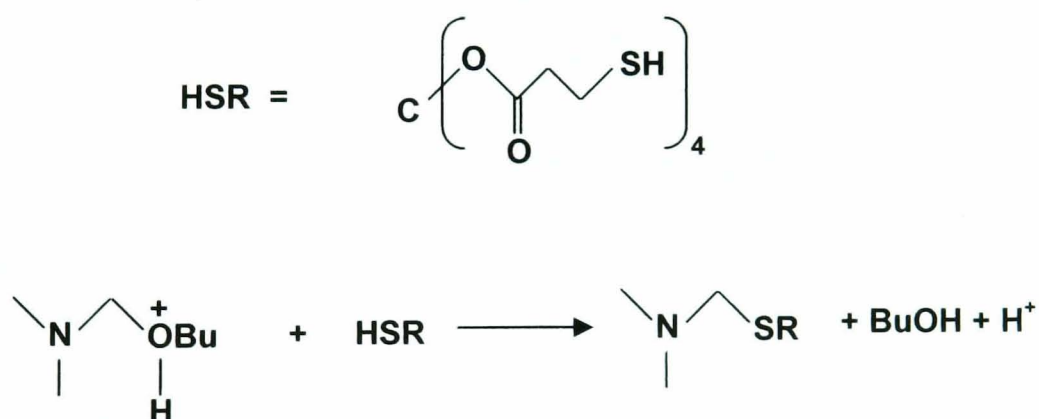


Figure 1.8 Cross linking mechanism used in the formation of the microcapsule wall in the aminoplast prepolymer system, showing the structure of the crosslinker pentaerythritol tetrakis(3-mercaptopropionate) (HSR).

1.1.3 Microcapsules – Current knowledge and reasons for study

The microcapsules discussed in this thesis are used to deliver pesticides to leaf and soil samples. The microcapsule, after release from a source site such as a spray, adheres to the surface of a leaf or soil particulate. Release of the active ingredient occurs by diffusion from the microcapsule, through the polymer wall and away. The nature of the adhesion process and local permeability of microcapsules are still little understood.

The structure of the polymeric wall of these microcapsules has been investigated using scanning electron microscopy (SEM) and the membrane shown to be asymmetric in construction as predicted in section 1.1.2³. In Figure 1.9 a scanning electron micrograph of an artificially broken microcapsule is shown and a thin (0.05 μm) outer dense layer can be observed in addition to a much thicker (0.5 μm) spongy underlayer.

The thin outer dense layer is the working end of the membrane offering resistance to the flow of pesticide. The thick inner spongy layer provides mechanical support.

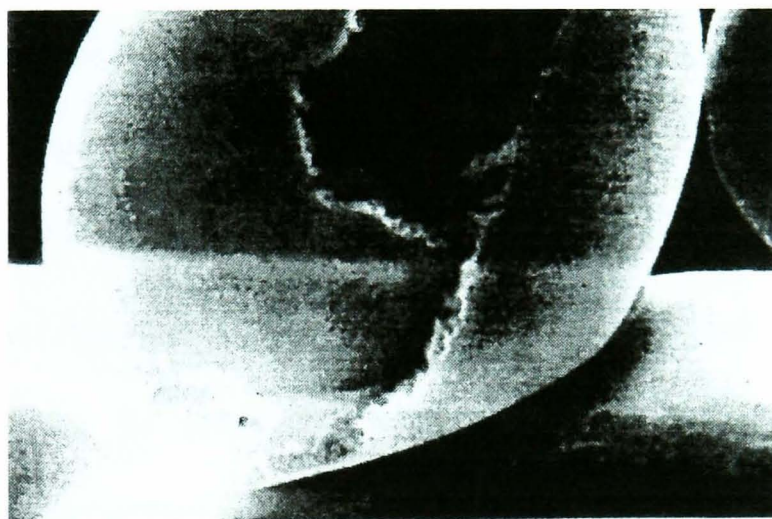


Figure 1.9 Artificially broken microcapsule made using the polyfunctional isocyanate microcapsule system – Magnification: 5200. Reproduced from reference 3.

The release rate of pesticide from the microcapsule has also been studied. The microcapsule release rate (diffusion mechanism) is described in equation 1.1.

$$\frac{dM}{dt} = \text{release rate} = \frac{(4\pi ab)P(C_1 - C_2)}{b - a} \quad 1.1$$

where $4\pi ab$ is the surface area of the sphere, $C_1 - C_2$ is the concentration difference across the polymer wall, $b - a$ is the thickness of the microcapsule wall. P is the permeability of the microcapsule. Figure 1.10 gives a schematic representation of the microcapsule demonstrating these terms.

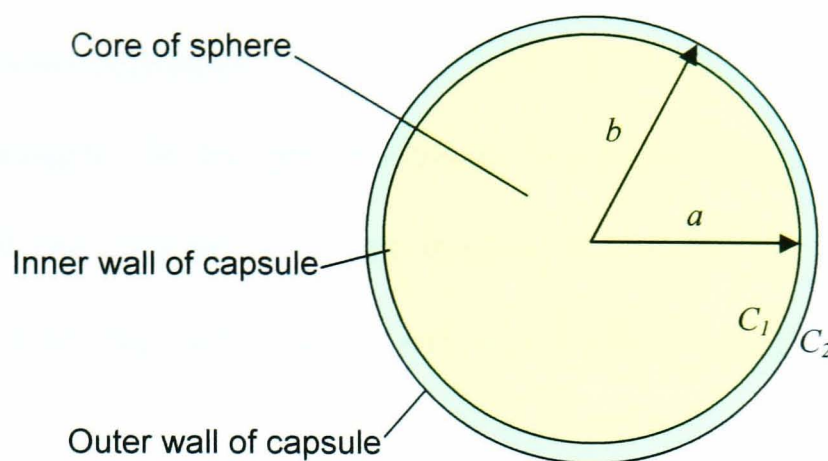


Figure 1.10 Schematic representation of microcapsule demonstrating parameters included in the release rate equation 1.1.

Equation 1.1 shows that the release rate of the microcapsule is directly proportional to the surface area, permeability and concentration difference across the wall and is inversely proportional to wall thickness.

The concentration difference across the wall is generally considered to be a constant when the microcapsule is exposed to foliar or a soil environment. The foliage or soil acts as a 'sink' for pesticide and hence pesticide exists at a very low concentration at the outer surface of the microcapsule. The average particle radius and wall thickness are generally fixed within narrow limits to satisfy process and physical stability conditions.

This means that the release rate from the microcapsule can only be varied by varying the permeability of the wall. For a given pesticide, the permeability is defined as the product of the solubility coefficient and the diffusion coefficient as described in equation 1.2.

$$P = DK \quad 1.2$$

where P is the permeability of the microcapsule wall, D is the diffusion coefficient of the active ingredient across the wall and K is the solubility coefficient of the active ingredient into the polymer wall. Varying the chemical composition of the

wall can vary the solubility coefficient and varying the cross-link density of the wall can vary the diffusion coefficient.

For example, in the polyfunctional isocyanate system, varying the ratio of PMPPI to TDI can vary the cross-link density. The higher the ratio of PMPPI to TDI, the more cross-linking and hence lower the diffusion coefficient and the lower the permeability.

The solubility coefficient of the wall is related to the ease with which a given pesticide can partition from the core into the wall. The closer the chemical composition of pesticide is to the chemical composition of the wall, the greater the solubility coefficient and greater the permeability.

1.2 Self-Assembled Monolayers

One of the ultimate aims of the studies herein was to investigate the adhesive properties of individual functionalised microcapsules to first, a surface of known functionality, second, a representation of a leaf surface and finally, the leaf itself. The self assembly of alkyl thiols on gold provide an ideal surface whose functionality can be altered, simply by altering the tail group of the alkyl thiol from which the self assembled monolayer (SAM) is formed.

SAMs involve the spontaneous formation of monolayers of long chain organic molecules on solid surfaces, resulting in an ultra thin film with a high degree of structural order. They are characterised by a strong chemisorption bond that ties the molecules to the surface and by lateral interactions between molecules that favour a densely packed and locally crystalline environment².

The surfaces used are most commonly metals such as gold, silver, mercury, platinum or copper²⁷⁻³¹, although surfaces such as mica or silicon³²⁻³⁴ have also been

employed. Gold surfaces have been studied predominantly, particularly with organic molecules containing a thiol group, where linkage proceeds via a Au-S bond³⁵⁻⁴⁰.

The properties of the gold upon which the SAM is formed have been investigated and it was found that a better coverage of monolayer was obtained after the gold had been annealed at high temperatures for period of time⁴¹⁻⁴³.

Studies of SAM formation from a dilute solution indicate that for moderate concentrations (1 mM) a well ordered full coverage is achieved within an hour⁴⁴. Monolayer formation proceeds by the initial adsorption of molecules in a configuration parallel to the gold surface. As the surface concentration becomes greater, a transition occurs and clusters of molecules form which rearrange, through surface diffusion, to the most stable packing structure⁴⁵.

SAMs have many advantages in that they are robust and extremely versatile. An infinite variety of structures can be created by, for example, changing the length of the alkyl chain or the functional group at its end or by co-adsorbing two or more different molecules at the same time. A schematic representation of SAMs of alkanethiols gold is shown in Figure 1.11.

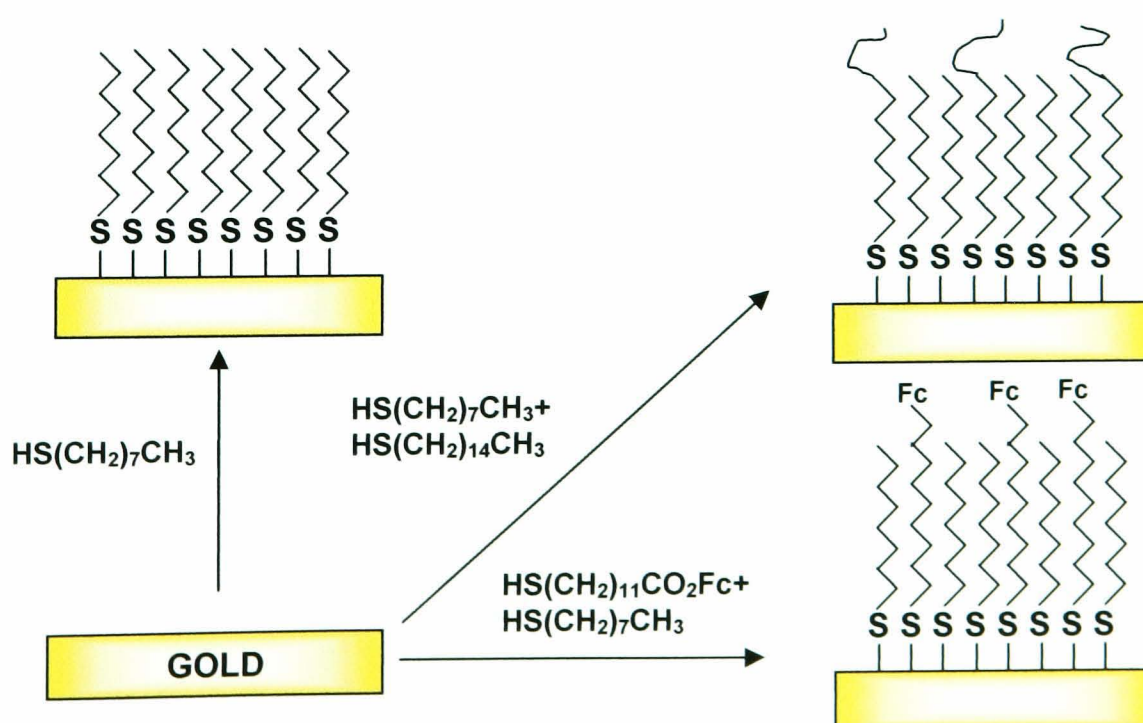


Figure 1.11 Schematic representation of some of the supramolecular structures possible with SAMs of thiols on gold. Reproduced from reference 2.

In order to simulate the waxy surface of a leaf, mixed SAMs must be formed as the surface of a leaf consists of approximately 5-20% hydrophilic sites and 80-95% hydrophobic sites⁴⁶. Mixed SAMs have been studied extensively⁴⁷ notably by Bain and Whitesides who carried out detailed investigations of the variation of head group, tail group, and alkyl chain length of thiols coadsorbed onto gold^{6,48}.

Characterisation of the properties of these mixed monolayers was carried out by contact angle measurements and x-ray photoelectron spectroscopy (XPS). It was found that the relationship for the coadsorption of methyl (CH_3) terminated thiols and carboxylic acid (COOH) terminated thiols was not linear with the concentration ratio in solution. Rather, there was a strong preferential adsorption of the apolar methyl terminated thiol. Thus, using XPS, it was found that the ratio of the concentrations of the two components on the surface of the mixed monolayer differed from that in solution⁶.

Figure 1.12 is a reproduction of these results showing a graph of the mole fraction of an alcohol, bromide, nitrile or carboxylic acid terminated thiol in a solution containing this thiol and a methyl terminated thiol (χ^p_{solution}), plotted against the mole fraction of thiol of interest that was present in the SAM (χ^p_{surface}) determined by XPS.

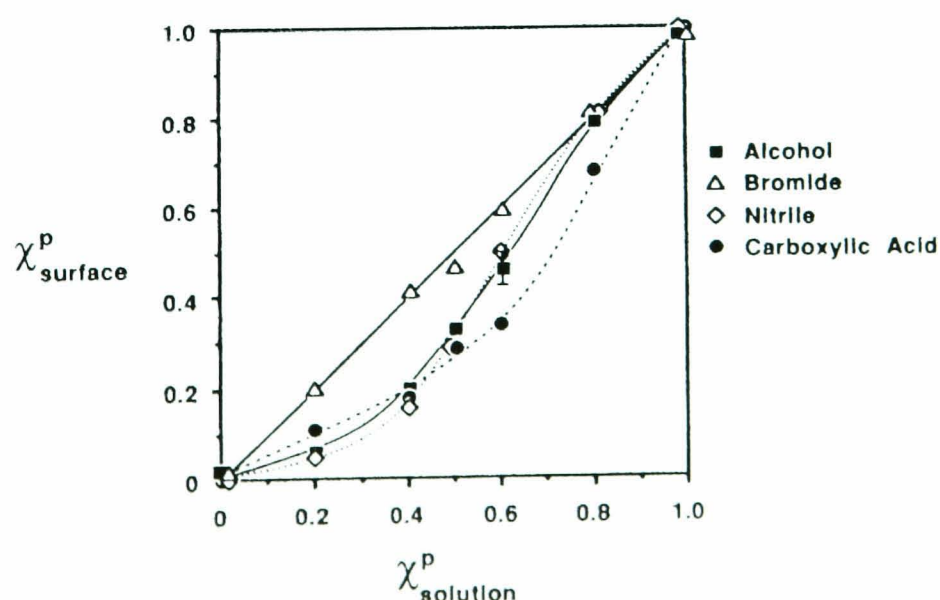


Figure 1.12 Graph showing the comparison between mole fraction of thiol in an original solution with a methyl terminated thiol (χ^p_{solution}) and the corresponding mole fraction of the thiol in the monolayer (χ^p_{surface}). Reproduced from reference 6.

1.3 High resolution microscopy

1.3.1 Atomic Force Microscopy (AFM)

One type of high-resolution microscopy employed in this project is AFM. AFM belongs to a group of techniques known as scanned probe microscopies. The AFM was introduced by Binnig, Gerber and Quate in the mid-80's⁴⁹. They developed the idea of using a force sensing cantilever, with an attached very sharp tip, which was capable of measuring the force between the apex of the tip and substrate at the nm level.

The AFM is complementary to other force measuring techniques such as surface force apparatus⁵⁰, optical tweezers^{51,52} and interfacial force microscopy⁵³, among others. However, these techniques lack the ability to provide high spatial resolution mapping of forces. The key interactions which control the adhesive properties of microcapsules to surfaces are electrostatic⁵⁴, hydrophobic^{55,56}, steric⁵⁷, capillary⁵⁸ and Van der Waals⁵⁹ all of which are measurable by AFM.

In AFM, the cantilever stiffness reflected in the spring constant, k , is usually such that the cantilever deflects, rather than the substrate deforming upon tip contact with the surface.

The spring constant of a rectangular cantilever loaded with a negligible mass can be estimated using equation 1.3:

$$k = \frac{Ew}{4} \left(\frac{t}{l} \right)^3 \quad 1.3$$

where w , t , and l are the width, thickness and length of the cantilever and E is the Young's modulus, a measure of the elasticity of the material employed.

The integrated cantilever-tip assemblies can have single or V-shaped beams⁶⁰ and normal spring constants in the range 0.01-100 N m⁻¹. The k value can be varied by changing the physical characteristics, t , l and w of the lever. Albrecht et al. were the first

to fabricate silicon nitride microcantilevers⁶¹. Today they are mass-produced from either silicon or silicon nitride based materials.

To monitor and maintain a constant deflection of the cantilever a feedback system is employed. A laser is shone onto the back surface of the cantilever and reflected back onto a split photosensitive diode detector (PSD). As the cantilever bends the movement of the reflected beam is detected by the PSD. The tip-substrate separation is adjusted to maintain a constant cantilever deflection, in a closed feedback loop, and for contact mode imaging, a topographical image is obtained in this way. A sharp tip attached to the cantilever spring follows the contour of the surface.

The sharper the radius of curvature of the tip apex, the higher the resolution of the image (\sim nm level). A schematic representation of an experimental AFM set-up is shown in Figure 1.13.

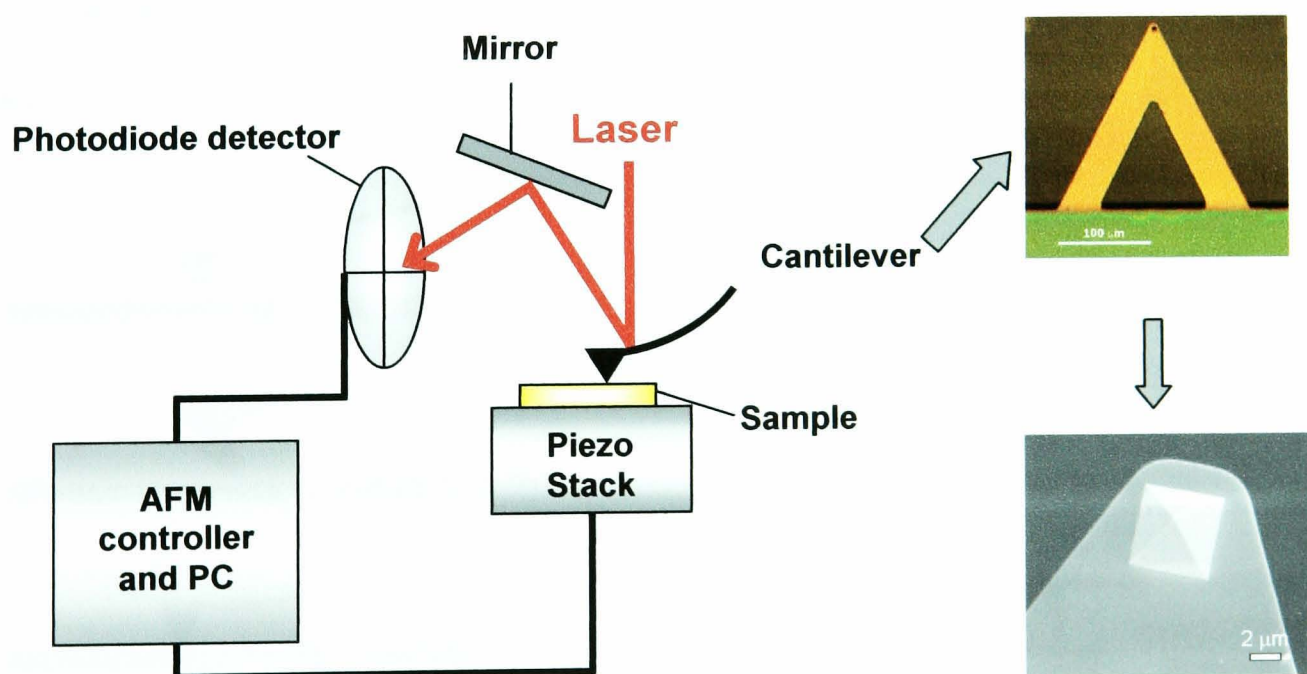


Figure 1.13 A schematic of a typical AFM experimental apparatus showing a V-shaped silicon nitride cantilever with a close up of the pyramidal tip.

In addition to topographical imaging, however, the AFM can also probe nanomechanical and other properties relating to the force experienced between the tip

and the substrate such as local adhesive forces. It is this latter property of AFM that will be exploited in this project.

Force values are determined from the normal displacement, Δz , of the cantilever from its resting position. With an instrumental sensitivity on the order of 0.1 \AA , minimal forces in the range of 10^{-13} - 10^{-8} N (depending on cantilever thickness) can be measured⁴. This means that in principle, the AFM can measure molecular interactions ranging from weak Van der Waals ($<10^{-12} \text{ N}$) to strong covalent (10^{-7} N) bonds⁶².

The AFM can record the amount of force felt by the cantilever as the probe tip is brought close to a sample surface and then pulled away. The deflection of the cantilever is recorded during approach and retract and a force-distance curve is produced, an example of which is shown in Figure 1.14. Experimentally this is done by applying a triangular wave voltage pattern to the z-axis scanner causing it to expand and then contract in the vertical direction generating relative motion between the probe and sample.

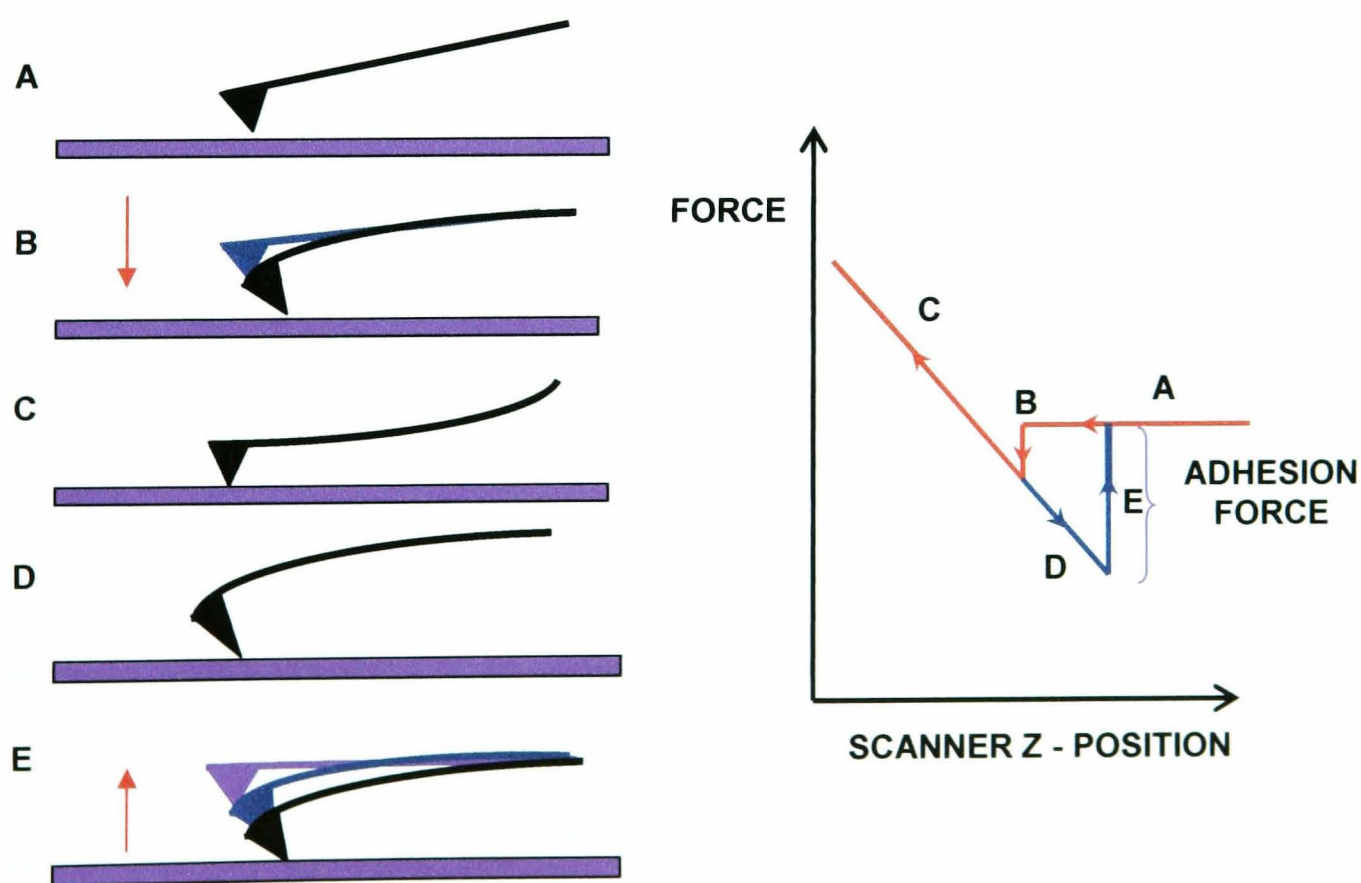


Figure 1.14 Schematic representation of an AFM force-distance (approach) curve.

The cantilever position at several points along the force curve in Figure 1.12 is shown to the left of the curve. At position A, the beginning of the measurement, the cantilever is not in contact with the surface. If the cantilever feels a long-range attractive (or repulsive) force then it will deflect downwards (or upwards) before making contact with the surface. In the case shown, there is minimal long-range force so the force curve shows no deflection response from the cantilever.

At position B the probe tip is brought very close to the substrate and if there is sufficient attractive force (often a Van der Waals attractive force), it ‘jumps into contact’. At position C, the tip is in contact with the substrate and as the tip pushes against the surface, the cantilever deflects upwards. This region is known as ‘constant compliance’. For hard substrates, the distance the cantilever deflects is equal to the distance moved by the tip (or substrate) as they are pushed against each other.

After loading the cantilever to a desired force value, the process is reversed (position D). As the cantilever is withdrawn, adhesion or bonds formed during contact with the surface may cause the cantilever to adhere to the sample past the initial contact point B.

The key measurement of the AFM force curve is the point at which these adhesion forces are broken and the cantilever comes free from the surface (position E). The observed cantilever deflection is converted to a force using the cantilever spring constant.

To obtain quantitative force values requires knowledge of the cantilever spring constants, and in some cases, tip contact radii. Several methods have been reported for measuring the spring constant of an AFM cantilever. These include the use of finite element analysis by Sader and White⁶³ and formulas provided by Neumeister and Ducker⁶⁴ to calculate the spring constant from geometric and material data. However,

the thickness and modulus of elasticity of cantilevers are not very easy to determine and if the back of cantilevers are coated with aluminium or gold, to increase the reflectivity, the influence on the mechanical properties is difficult to assess. A method to determine the spring constant of a cantilever experimentally is therefore extremely desirable and a number of experimental methods have been developed.

A non-destructive technique was used by Cleveland et al⁶⁵, which involved measuring the change in resonance frequency of the cantilever, ν_0 , as a range of end masses were added to the cantilever, secured to the beam by capillary action.

The dependence of ν_0 as a function of the end mass, M , can be described by equation 1.4:

$$\nu_0 = \frac{1}{2\pi} \left(\frac{k}{M + m_0} \right)^{1/2} \quad 1.4$$

where m_0 is the effective mass of the cantilever. Rearranged, this equation gives:

$$M = \frac{k}{(2\pi\nu_0)^2} - m_0 \quad 1.5$$

A linear plot of added mass versus $1/(2\pi\nu_0)^2$ gives a straight line of gradient k , and intercept m_0 .

Hutter et al⁶⁶ found a value for the spring constant of a cantilever by measuring the deflection of the cantilever in response to thermal noise. A vibrating cantilever can be described as a simple harmonic oscillator. Thus, in the absence of external forces and other noise sources, the root mean square amplitude of the tip, A_{rms} , can be related to the temperature of the system, T :

$$A_{rms} = \left(\frac{k_B T}{k} \right)^{1/2} \quad 1.6$$

where k_B is the Boltzmann constant ($k_B = 1.382 \times 10^{-23} \text{ J K}^{-1}$). If A_{rms} is measured at a fixed temperature, it is possible to estimate k .

A method employing hydrodynamics has been demonstrated by Maeda and Senden⁶⁷. A macroscopic model of a cantilever was used to obtain a semi-empirical relationship between the response to the distributed load on the cantilever due to viscous drag and the response on known point loads at the end of the cantilever. From this the spring constant of the cantilever was determined by measuring the hydrodynamic deflection due to the linear movement in liquid.

Several groups⁶⁸⁻⁷¹ have reported methods that use a reference cantilever with a known spring constant for calibration. When pressing the cantilever to be calibrated against the reference cantilever, the spring constant can be calculated from the measured deflection. A fast and simple method for measurement of spring constants was presented by Holbery et al⁷², measuring the constant using a nanoindenter. The instrumentation required for these measurements is expensive and so other techniques are preferred.

The other parameter which needs to be characterised is tip radius. This affects the contact area between the tip and sample, i.e. the number of molecular contacts. Estimates of tip radii are obtained by inspection of electron microscope images^{73,74}, or by profiling sharp features⁷⁵⁻⁷⁹, uniform latex spheres^{80,81} or colloidal gold clusters on the surface^{82,83}. One method by which the actual tip radii is known is to use spheres of defined diameter, attaching them to the end of the AFM cantilever to act as the tip⁵⁴. This method, known as colloidal force microscopy, is relevant for the studies in this project, as spherical microcapsules of known diameter are attached to the tip of an AFM cantilever. This method is discussed later in this introduction.

One of the first uses of force measurements was to improve the quality of AFM images by monitoring and minimising the attractive capillary forces between tip and sample. Capillary forces arise during in air imaging from the attractive pull of a thin

layer of water on the surface of the substrate, on the tip. These forces cause the tip to be pulled onto the surface with greater force potentially causing damage to soft samples.

Capillary forces can be minimised by immersing the sample in solution, notably water. Weisenhorn and co-workers⁸⁴ noted that the typical adhesive force of 100 nN between a silicon nitride tip and a mica surface in ambient air could be reduced by a factor of 100 by immersion in water.

Capillary forces were used advantageously by Mate and others⁸⁵ who recorded the distance between the onset of the capillary force and the point at which the AFM tip contacts the surface. From this they could measure the thickness of the adsorbed molecular layers (ca. 2 nm).

For AFM probing of the adhesion forces between the tip and substrate it is extremely important to work under solution so that the dominating capillary forces are minimised. Moreover by adjusting the properties of the solution it is possible to make measurements such as the effect of electrostatic double layer tip-sample force as a function of pH and ionic strength^{59,86,87}.

The ill-defined geometry of the AFM tip becomes a problem when comparing measured force-distance profiles between an AFM tip and a surface to theoretical models. Hutter et al⁸⁸ have demonstrated an approach to get a better defined geometry by etching silicon AFM tips in an oven in the presence of oxygen to obtain tips with a spherical end of defined radius.

The colloidal probe technique was first developed by Ducker et al^{54,89} and Butt⁵⁹, providing a more universal solution to the problem by replacing the tip with a colloidal particle of well defined spherical shape. Since then, it has become a well established and powerful technique for the study of surface forces. The measuring

principle involved predestines it for the investigation of particle-surface interactions, making single particle experiments feasible.

This technique has been used to study the dependence of force between a particle and a surface on applied load and contact time⁹⁰⁻⁹⁵. Other factors investigated include the influence of humidity^{96,97} and surface roughness⁹⁸⁻¹⁰², and also the effect of surface coverage with polymers¹⁰³⁻¹⁰⁷.

The technique has also been used to probe adhesion forces in technical applications such as mineral flotation¹⁰⁸⁻¹¹¹, conductive surface coatings¹¹², powder inhalation systems for drugs¹¹³⁻¹¹⁶, printing¹¹⁷⁻¹¹⁹ and stainless steel polishing¹²⁰.

1.3.2 Chemical Force Microscopy (CFM)

Although force microscopy can provide nanoscale information about friction, adhesion and compliance, conventional force measurements lack chemical specificity. To overcome this apparent limitation of AFM, it is possible to chemically modify the probes to make them sensitive to specific molecular interactions. The ability of the chemically modified tips to distinguish between chemically distinct functional groups has led to this variation of AFM being called chemical force microscopy (CFM).

To be able to probe interactions between functional groups, the tip must be modified with well-defined molecular layers. One successful method which has been reported^{74,121,122} is the use of self assembled monolayers (see Section 1.2) of functionalised organic thiols on gold-coated silicon or silicon nitride tips (Figure 1.15).

Covalent modification of AFM probes with thiols and silanes has been well reported, including studies of adhesion^{73,123-128}, contact potential⁷³ and surface topography¹²⁹.

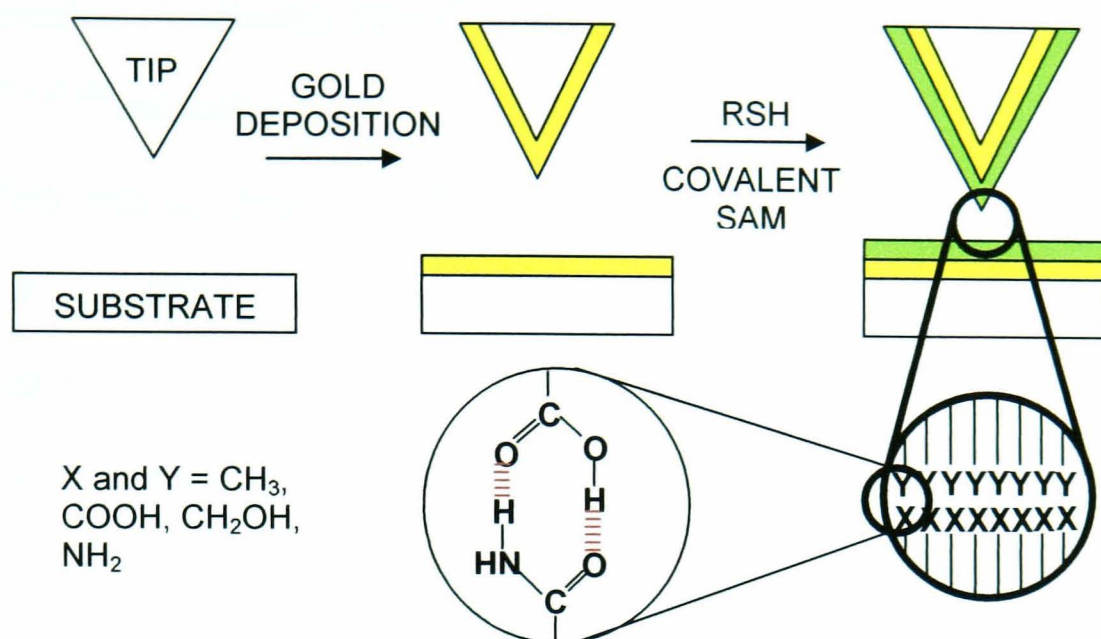


Figure 1.15 Scheme for the chemical modification of tips and sample substrates. In this case the tip and substrate have been modified with thiols which have end groups which are capable of hydrogen bonding with one another leading to enhanced interaction.

As discussed earlier, the experimental environment in which the surfaces of the tip and substrate interact plays a crucial role in determining the measured forces. To probe bare interactions (i.e. interactions resulting from solid-surface free energies), adhesion forces must be measured in ultra-high vacuum. If force measurements are carried out in ambient air, capillary forces^{62,130} dominate, which are usually 1-2 orders of magnitude larger than the specific chemical interactions, making interpretation extremely difficult.

Measurements carried out in dry, inert gas atmospheres are a better representation of the chemical sensitivity of bare interactions^{73,125} but it is difficult to exclude or account for the presence of adsorbed vapour on high energy surfaces when interpreting measurements. The capillary effect can be eliminated if measurements are carried out in liquid instead of air^{84,131}. Adhesion force measurements in liquid will reflect the interplay between surface free energies of solvated groups.

The benefits of AFM studies in liquid have been reported, especially in reference to biological systems^{132,133}. It has been found that images of biomolecules are

highly dependent on adhesive forces¹³⁴, which can be sensitive to solution pH and ionic strength^{59,135,136} and surface composition¹³⁷.

Work with covalently modified tips and substrates includes a study by Charles Lieber and co workers at Harvard¹²² who bound functionalised thiol monolayers to gold-coated AFM probes and samples. By varying the functional groups terminating the monolayers on the tip and sample, they studied the adhesion and friction between combinations of methyl (-CH₃) and acid (-COOH) functional groups. Force curves and images obtained from these studies are shown in Figure 1.16.

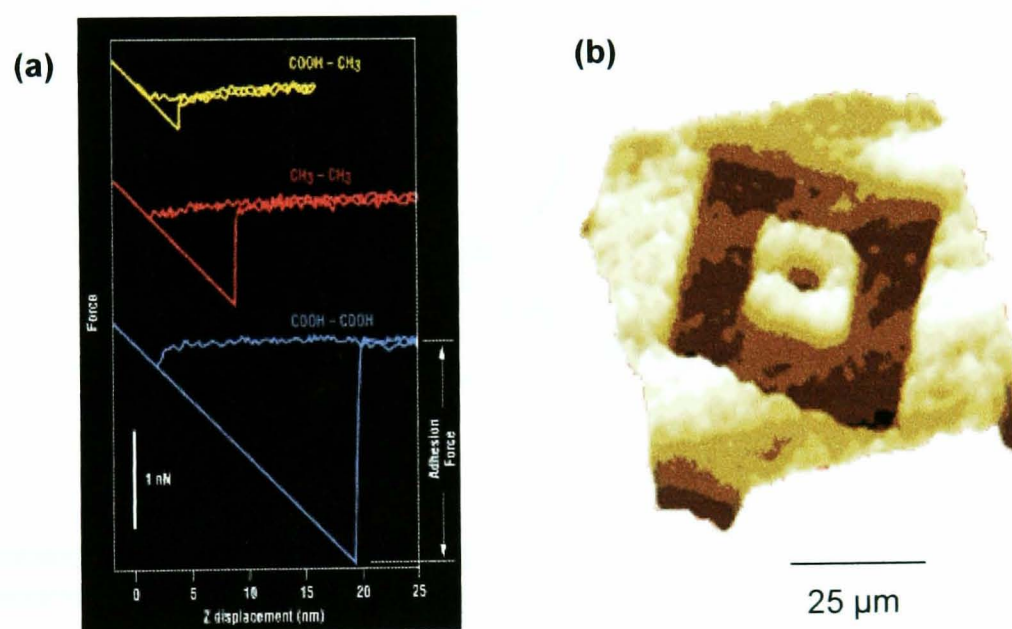


Figure 1.16 (a) Representative force distance curves in ethanol recorded for COOH/COOH, CH₃/CH₃ and CH₃/COOH tip-sample functionalisation (tip radius ~ 60 nm). (b) Image of patterned CH₃ / COOH SAM determined from friction measurements using CFM with a methyl-terminated tip. Reproduced from reference 4.

The observed trend in the magnitudes of the adhesive interactions between tip/sample functional groups - COOH/COOH > CH₃/CH₃ > CH₃/COOH - agrees with the qualitative explanation that interactions between hydrogen-bonding groups (i.e. COOH) will be greater than between non-hydrogen-bonding groups (i.e. CH₃).

CFM has many biological applications as well. It has been used to measure forces between complementary strands of DNA¹³⁸. DNA oligonucleotides were covalently attached to a spherical probe and surface. The adhesive forces measured between 20 base complementary strands fell into 3 distinct distributions which

corresponded to the rupture of the interchain interaction between a single pair of molecules involving 20, 16 and 12 base pairs.

The binding force between individual ligand-receptor pairs has also been studied using CFM. Florin et al. examined the adhesion force between the protein avidin (a receptor) and a ligand, biotin⁵. The AFM tip was modified so that its outer surface was coated with avidin receptor molecules and an agarose bead coated with biotin molecules served as the substrate, as shown schematically in Figure 1.17.

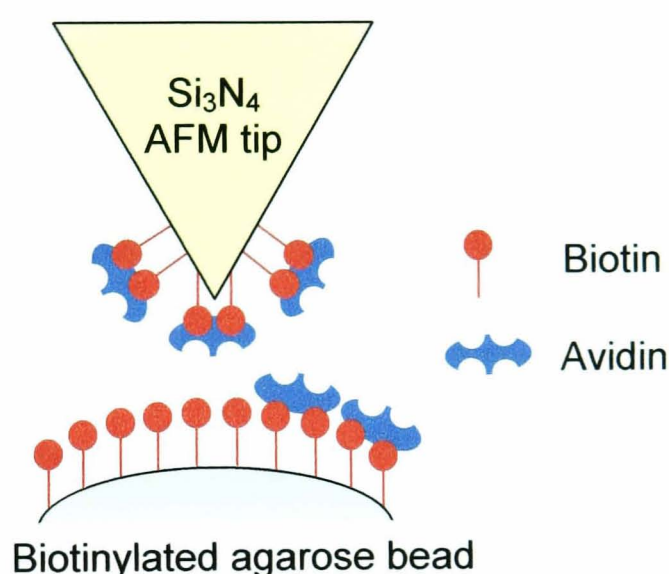


Figure 1.17 Schematic of an avidin functionalised AFM tip and a biotinylated agarose bead, shown here partially blocked with avidin. Reproduced from reference 5.

Under conditions that allowed only a limited number of molecular pairs to interact, the force required to separate tip and bead was measured and this was interpreted as the unbinding forces of individual molecular pairs.

Rief et al used AFM to investigate the reversible unfolding of individual titin immunoglobulin domains⁸. The AFM tip was brought down onto a gold surface onto which native titin molecules had been adsorbed from solution. The tip was brought into and kept in contact with the surface for several seconds whereupon a fraction of the protein adsorbed onto the tip. When the tip was retracted, force-distance curves typified by the one shown in Figure 1.18 were observed. This sawtooth pattern observed while

stretching the titin corresponded to the sequential unfolding of individual titin immunoglobulin domains as demonstrated in the schematic drawing in Figure 1.18(a).

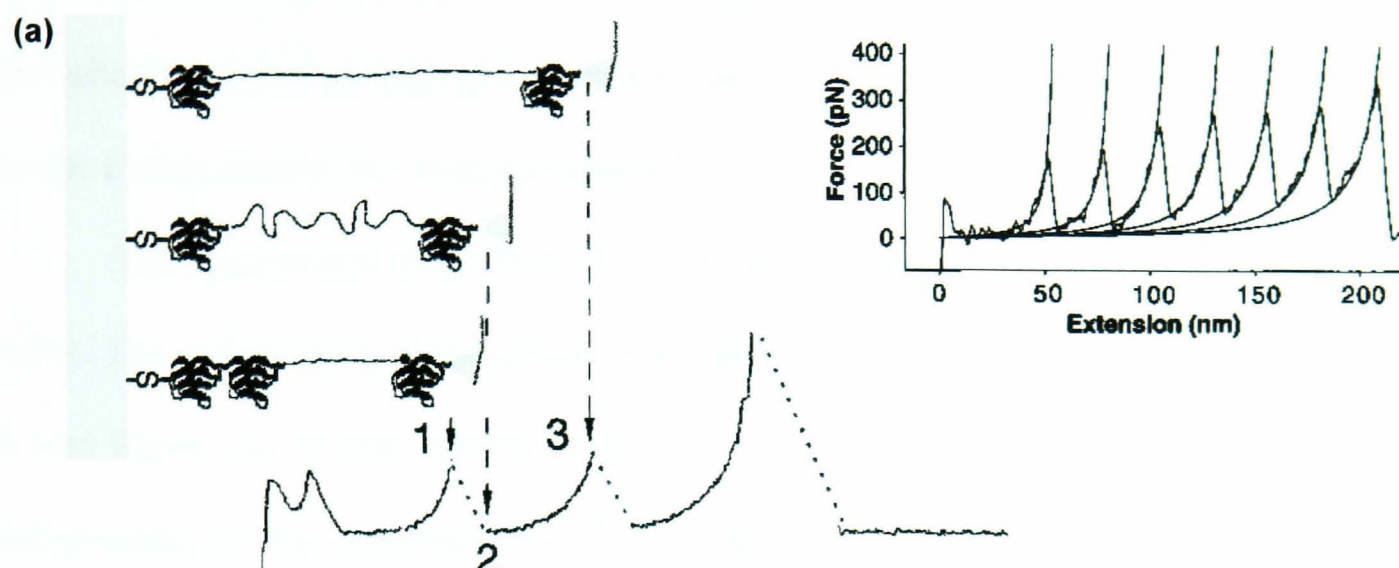


Figure 1.18 (a) schematic demonstrating the sequential unfolding of individual titin immunoglobulin domains with the associated force distance curve. **(b)** an example of the characteristic sawtooth pattern of unfolding observed in these measurements. Reproduced from reference 8.

Of particular relevance to the studies herein, CFM has been used to characterise the surface properties of polymers¹³⁹⁻¹⁴². Charles Lieber et al¹³⁹ used chemical force microscopy to study adhesive forces between surfaces of epoxy resin and self assembled monolayers capable of hydrogen bonding to different extents. They also investigated the influence of the liquid medium on adhesive properties. The trends in the magnitude of adhesion forces for chemically heterogeneous systems measured with CFM were shown to be quantitatively rationalised using the surface tension components approach by Fowkes, van Oss, Chaudhury and Goog (FOCG)¹⁴³⁻¹⁴⁶. It was also shown that for other epoxy polymers, inelastic deformations also contributed heavily to measured adhesion forces¹³⁹.

1.3.3 AFM studies of polymeric microcapsules

AFM has been used to investigate both topographical and deformation properties of microcapsules. Imaging of the surface of intact capsules, i.e. spherical capsules which

have not collapsed, has been carried out on individual cross-linked alginate capsules¹⁴⁷ and nanocapsules made from biodegradable polymers¹⁴⁸. Topographical images of dried polyelectrolyte capsules have also been obtained, enhancing the idea that upon drying, the spherical films making up the capsule, collapse exhibiting creases and folds caused by the evaporation of the aqueous content^{7,149,150}.

The mechanical properties of microcapsules have also been investigated with AFM. The deformation of individual polyelectrolyte microcapsules has been studied¹⁵¹. It was found that at low applied load, capsule deformation was elastic, reversible and independent of the concentration of the inner polymer. Deformation was controlled completely by the properties of the shell. Above a certain load, however, capsules deformed substantially and, partly, irreversibly. The effect of pH and salt on the stiffness of polyelectrolyte capsules has also been investigated, with moderate softening being observed upon addition of electrolyte, but there was dramatic softening at both low and high pH¹⁵².

1.4 Fluorescence Microscopy

Fluorescence is a type of luminescence resulting from a 3 stage process that occurs in certain molecules, called fluorophores or fluorescent dyes. This process is demonstrated by the simple electronic state diagram in Figure 1.19.

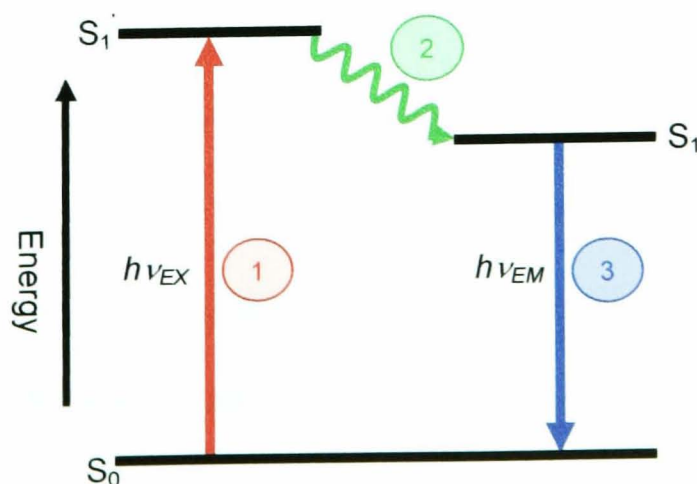


Figure 1.19 Jablonski diagram illustrating the processes involved in the creation of an excited electronic singlet state by optical absorption and subsequent emission of fluorescence.

A photon of energy $h\nu_{EX}$ is supplied by an external source such as a laser, adsorbed by the fluorophore to create an excited singlet state S_1^* (1). This excited state typically has a lifetime of 1-10 nanoseconds, and during this period the fluorophore may undergo conformational changes or be subject to possible interactions with its molecular environment. During these processes the energy of S_1^* is partially dissipated to yield a relaxed singlet excited state, S_1 (2). Finally, a photon of energy $h\nu_{EM}$ is emitted returning the fluorophore to its ground state, S_0 (3).

The wavelength of the emitted light is characteristically longer than the wavelength of the absorbed light, as the energy of the emitted photon is lower due to the energy dissipation during the excited state lifetime. This shift in wavelength is called the Stoke's shift (Figure 1.20).

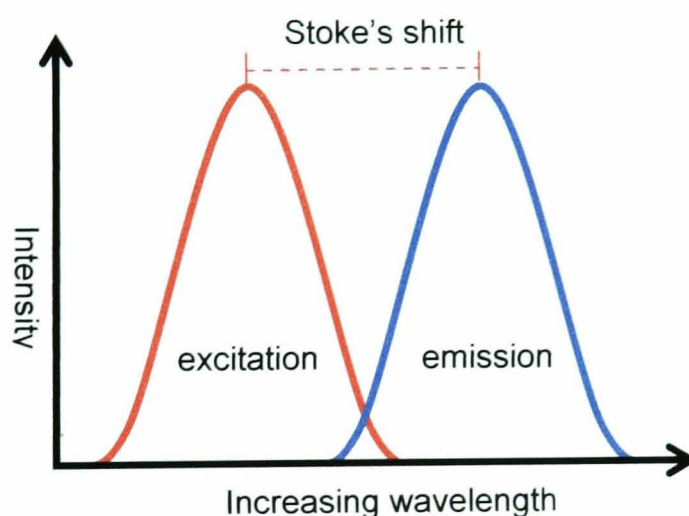


Figure 1.20 The excitation and emission spectra of a fluorescent molecule showing the change in wavelength between absorption and emission.

Compounds containing an aromatic ring tend to produce the most intense fluorescent emissions¹⁵³ and fluorescence is particularly favoured as a means of de-excitation, by rigid molecules¹⁵⁴. Many naturally occurring molecules autofluoresce e.g., proteins containing the aromatic groups tryptophan, tyrosine and phenylalanine when excited at 250-280 nm¹⁵⁵, but for most biological applications, fluorescent probes are used.

A fluorescent probe is a fluorophore that is incorporated into the substrate under investigation to cause it to fluoresce. A fluorophore can be made to meet many criteria. It can be added to increase fluorescent intensity, to emit or absorb at a specific wavelength, or to chemically react at a selected site. Fluorescein and its derivatives are examples of common fluorescent probes.

Fluorescence microscopy is a widely used method in biophysical studies¹⁵⁵ and the main advantage of this technique is that the signal to noise ratio is high since under ideal conditions, the background should not fluoresce. It is also specific as fluorescent molecules adsorb and emit at characteristic wavelengths with the signal being sensitive to small numbers of fluorescing molecules and to changes in the chemical environment. A schematic diagram of a typical epi-illumination fluorescence microscope is shown in Figure 1.21.

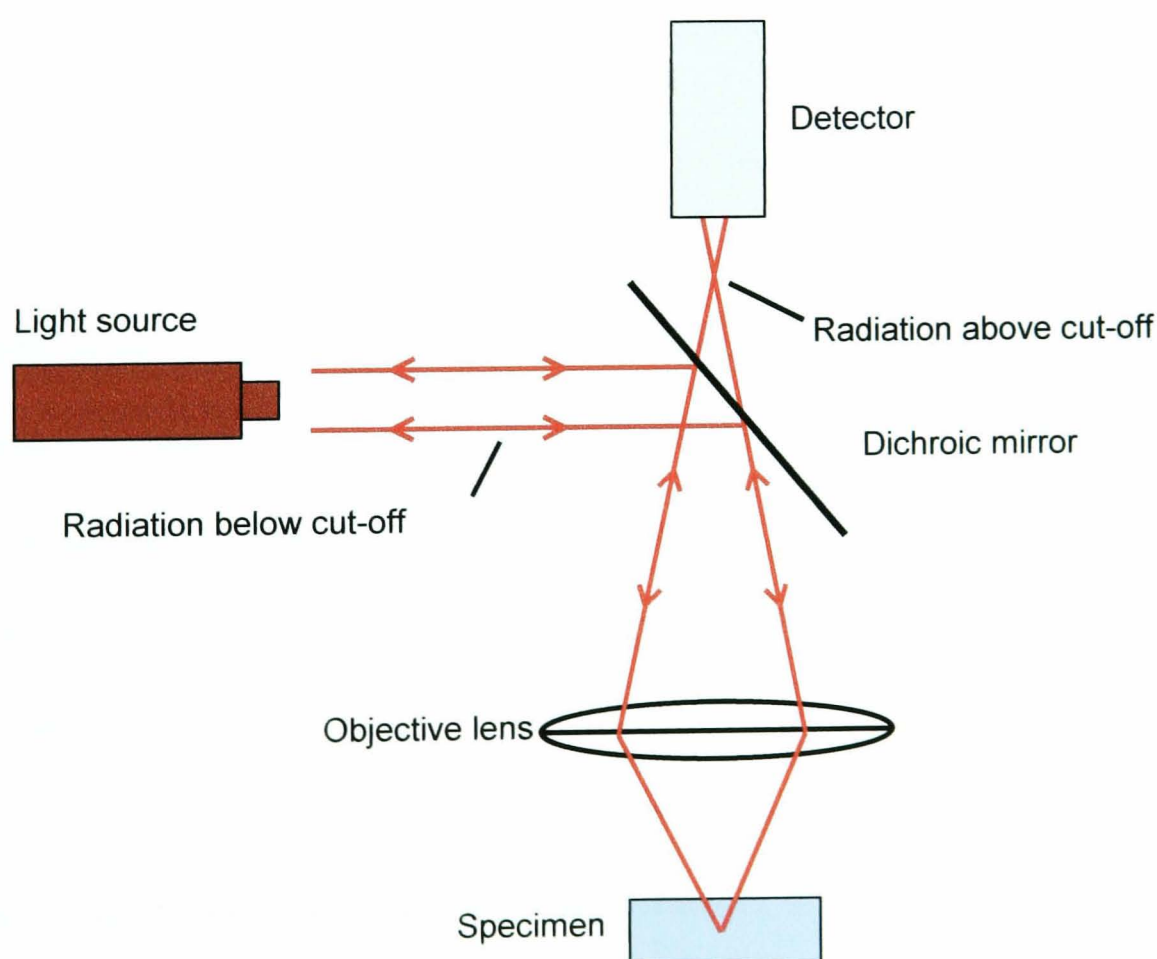


Figure 1.21 The optical path in a typical epi-illumination fluorescence microscope.

One of the main features of the fluorescence microscope is the dichroic mirror. This has the ability to split the exciting light from the emission radiation. There is a coating on the mirror which reflects light below a certain wavelength at an angle of 45° but permits light above that certain wavelength to pass through it to the waiting detector. Light emitted by the specimen will have a longer wavelength, due to Stoke's shift, and will therefore pass through to the detector whilst the excitation emissions will be deflected back to the light source.

1.5 Confocal laser scanning microscopy (CLSM)

The idea of a confocal microscope was first introduced by Minsky in 1957¹⁵⁶, but it was not until a decade later that Eggar and Pentran¹⁵⁷ designed and produced the first purely analogue mechanical confocal microscope. In the late seventies the advent of affordable computers and lasers and the development of digital image processing, led to the first single-beam CLSM.

In epi-illumination fluorescence microscopy, the entire field of view of a specimen is illuminated causing excitation and fluorescence emissions throughout the whole depth of the specimen rather than just the focal plane (full-field illumination, see Figure 1.22a). The image formed will therefore be out of focus due to the high proportion of light reaching the detector, causing a loss in contrast and sharpness. This factor reduces the value of the technique as it restricts the thickness of sample that can be viewed.

In contrast, in confocal laser scanning microscopy (CLSM), the out of focus blur is significantly reduced, since illumination of the specimen is restricted to a single point (or an array of points) which is scanned to produce a complete image (point scanning illumination – see Figure 1.22b). The insertion of a confocal imaging pinhole

or aperture into the epi-illumination fluorescence microscope (see Figure 1.23) reduces the out of focus blur further. These two features ensure that almost all of the emissions emanating from regions above and below the focal plane are prevented from reaching the detector resulting in the image formed containing only in-focus information.

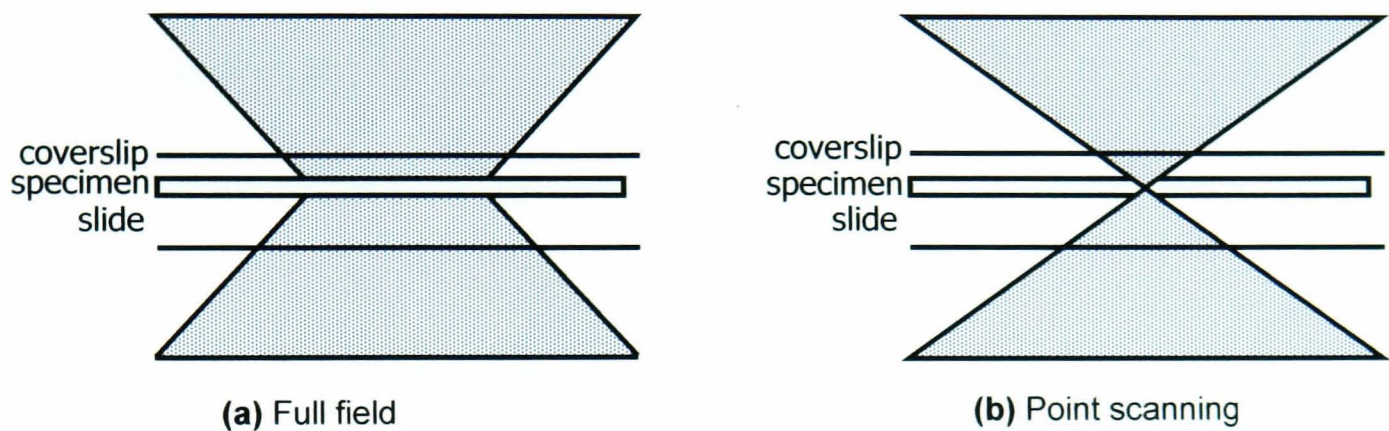


Figure 1.22 A comparison of the illumination experienced by the specimen during **(a)** full field illumination in a conventional fluorescence microscope and **(b)** Single point illumination in a CLSM.

The benefits of these features of the CLSM are that the microscope can carry out direct, non-invasive serial optical sectioning of intact or even living specimens, leading to the possibility of generating 3D images of thick transparent objects. The surfaces of multilayer structures can also be studied by this non-contacting, non-destructive method.

In CLSM, a beam of excitatory laser light from the illuminating aperture passes through an excitation filter and is reflected by a dichroic mirror to be focused by the microscope objective lens to a diffraction limited spot at the focal plane within a 3D specimen. Fluorescence emissions excited both within the illuminated in-focus region, and within the illuminated cones above and below it, are collected by the objective and pass through the dichroic mirror and emission filter. However, only emissions from the in-focus region are able to pass through the confocal detector aperture, or pinhole, to be detected by the photomultiplier. This process is demonstrated schematically in Figure 1.23.

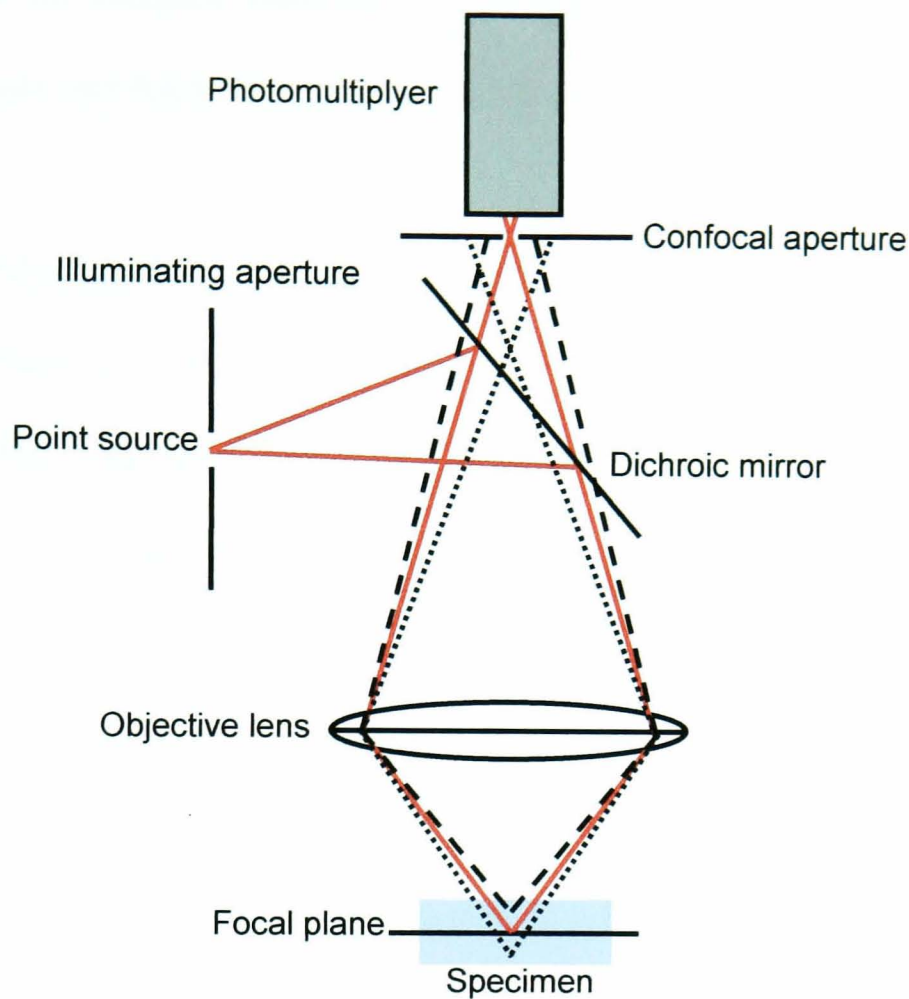


Figure 1.23 The principles of confocal laser scanning microscopy. Solid red lines indicate light from the focal plane (—) black dashed lines indicate light above and below the focal plane that is prevented from being detected by the confocal aperture (---, - -).

There are many advantages of the confocal microscope over the standard light microscope including the fact that it is superior in areas of image contrast, signal to noise ratio and axial and lateral resolution¹⁵⁸. However, the achievement of high resolution images requires the confocal aperture to be very small. This greatly restricts the amount of light detected, producing a poor signal level, especially from weakly fluorescing specimens. The optical sectioning performance of the microscope depends upon the axial resolution which, in turn, depends upon a variety of experimental parameters, such as the wavelength of the illuminating light, the Stoke's shift of the fluorophore, the numerical aperture of the objective and the size of the confocal aperture. The resolution is given by equation 1.7.

$$d = 0.61 \frac{\lambda}{NA} \quad 1.7$$

where d is the distance between two resolved points (nm), λ is the wavelength of emitted light and NA is the numerical aperture of the objective.

1.5.1 CLSM in the study of microcapsules

CLSM has been used as a technique to investigate various properties of microcapsules. The structure and composition of the capsule wall has been studied extensively by Lamprecht et al amongst others^{159,160}. In these studies the confocal microscope was used to visualise and quantify the distribution of polymers within the wall of microcapsules prepared by complex coacervation.

The technique has also been used to investigate the innards of microcapsules. Used in conjunction with transmitted light detection, the difference between air-containing and oil-containing microcapsules has been demonstrated, the oil phase being stained with Nile red¹⁶⁰. Cross sections through microcapsules prepared by the double emulsion technique have also been recorded using CLSM to visualise the matrix structure. The data obtained has been shown to compare favourably with cross sections through the microcapsules obtained by SEM^{161,162}.

Another interesting way in which CLSM has been used to study microcapsules is the use of FRAP (fluorescence recovery after photobleaching) to investigate the permeability of the microcapsule wall⁷. In these studies, hollow polyelectrolyte capsules were placed in a solution containing 1×10^{-6} M 6-carboxyfluorescein dye. The dye transferred into the centre of the capsule, whereupon the dye inside the capsule was bleached photochemically and the fluorescence intensity due to the penetration of dye molecules from outside into the capsule was recorded. A summary of these studies is shown in Figure 1.22.

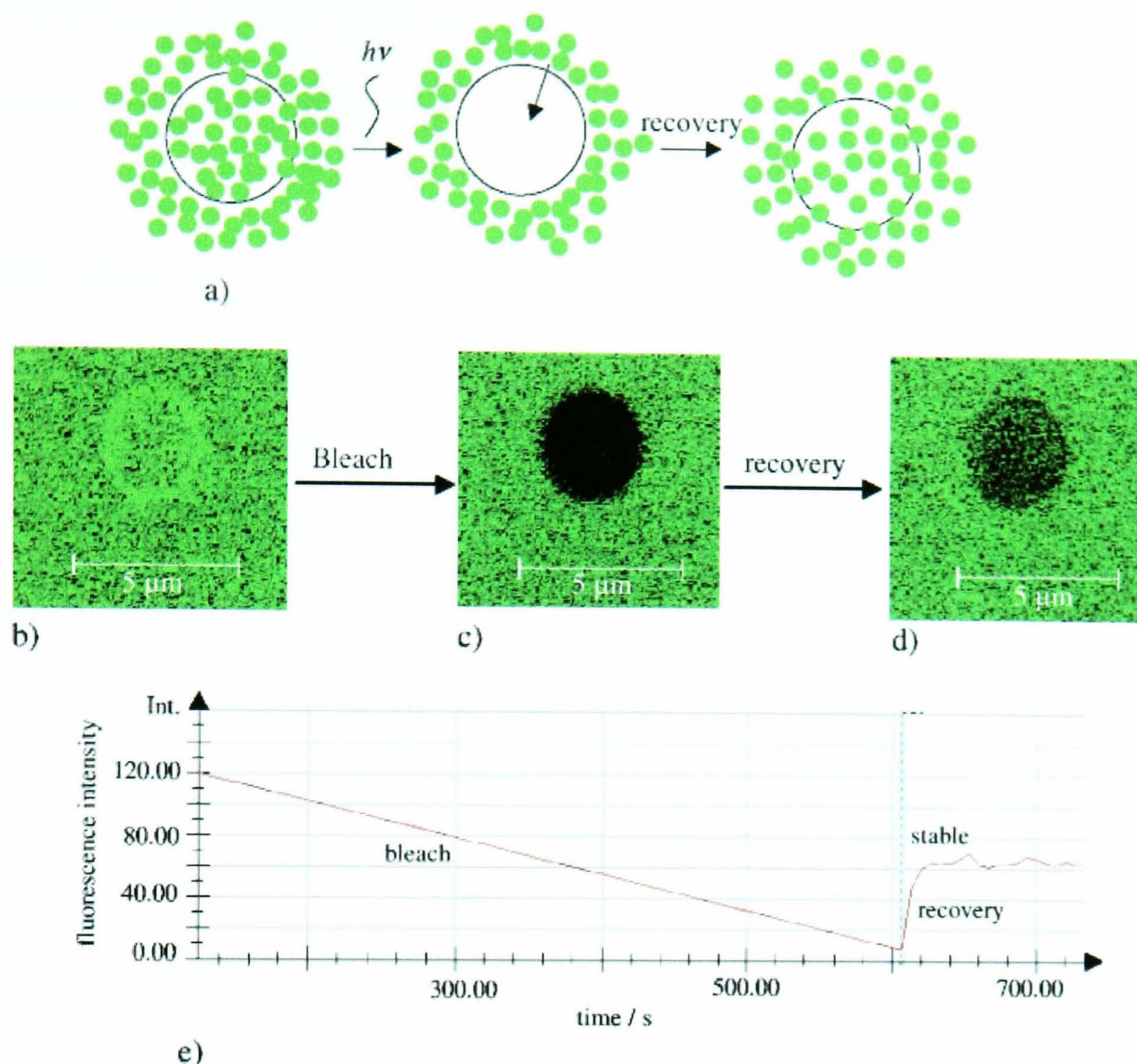


Figure 1.24 (a) Schematic for the FRAP experiment. CLSM images of capsules: (b) before bleaching; (c) after bleaching inside the capsule; (d) fluorescence recovery; (e) fluorescence intensity from a fixed area within the capsule as a function of time. Reproduced from reference 7.

CLSM has been used to investigate the shrinking properties of ultrathin polyelectrolyte capsules upon annealing¹⁵⁰. The images recorded before and after annealing clearly showed that the capsules shrank, with a reduction in the diameter of ca. 1 μm . In a further study, the diameter of capsules made from different polyelectrolytes increased upon annealing but shrank back to their original size upon cooling¹⁴⁹. When annealed a second time, the capsules grew once again but not to the extent of the first annealing. This suggested that there was a permanent microstructure rearrangement of the microcapsule wall upon cooling of the annealed capsules.

The mechanical properties of microcapsules have also been investigated using CLSM. For example CLSM has been used in conjunction with AFM to investigate the

deformation properties of microcapsules¹⁵², examining the effect of pH and salt on the stiffness of polyelectrolyte multilayer microcapsules.

1.6 Aims of Thesis

The overall goal of this thesis is to explore some of the properties of polymeric microcapsules, specifically the adhesion capabilities and the release characteristics of microcapsules in both solution and in the dry state. This chapter describes some of the techniques and applications that are developed later in this thesis. In Chapter 2, these techniques are described further by providing the experimental details for investigations into the use of AFM in adhesion measurements, the use of confocal microscopy in release measurements and for high resolution imaging of biological samples. Experimental details are also given relating to combined electrochemical and confocal microscopy studies into the trace detection of cadmium.

The following four results and discussion chapters have been written so that specific background relating to each chapter is considered in an introductory section, followed by any significant additional experiment details relevant to that chapter. Experiment results are then described, discussed and concluded.

In Chapter 3, the adhesion properties of microcapsules are investigated using AFM. The aim is to explore how changing the surface functionality of the microcapsule wall affects its adhesion characteristics. This is achieved by performing adhesion measurements between a single microcapsule and a surface of known functionality using AFM. The ultimate aim of these investigations is to characterise the adhesion of functionalised microcapsules to the surface of leaves. This chapter details how a substrate was developed to mimic the surface of a leaf and the results of adhesion measurements to this surface and to an actual leaf cuticle.

The development of confocal microscopy as a technique for measuring the release of an active ingredient from microcapsules into solution is discussed in Chapter 4. The aim in this case is to be able to study the release of active from inside an individual microcapsule in real time. The effect of wall thickness and crosslinking density of the microcapsule wall on the release rate into an ethanol/water solution is investigated and mass transfer coefficients of the pesticide across the microcapsule wall are estimated.

The microcapsules studied in this thesis are used in agriculture to release pesticide once dried down out of aqueous solution onto the crop of interest. It would therefore be beneficial to carry out release studies on microcapsules in the dry state. In Chapter 5, the high resolution imaging capabilities of the confocal microscope are demonstrated using biological samples such as leaves and caterpillars. They are also used to investigate the release to leaf surfaces from two types of polyurea microcapsules, which have different release mechanisms.

This thesis is concerned with characterising the release properties of microcapsules. Chapter 4 uses confocal microscopy to monitor the release from microcapsules into solution. It would be beneficial to extend the use of CLSM to monitor the diffusion characteristics of species away from surfaces in solution. Chapter 6 details preliminary studies using CLSM to monitor the diffusion of species released from a hemispherical mercury drop ultramicroelectrode. Anodic stripping voltammetry is used to preconcentrate the mercury drop with cadmium which is then released from the electrode by oxidation to Cd^{2+} into solution whereupon they bind to a cadmium-selective fluorophore which fluoresces and can be detected by CLSM.

1.7 References

1. Scher, H. B.; Maars, G. J. *Controlled delivery of crop protection agents*; Taylor & Francis: London, 1990.
2. Bain, C. D.; Evans, S. D. *Chem. Br.* **1995**, *31*, 46.
3. Scher, H. B.; Rodson, M.; Lee, K. S. *Pestic. Sci.* **1998**, *54*, 394.
4. Noy, A.; Vezenov, D. V.; Lieber, C. M. *Annu. Rev. Mater. Sci.* **1997**, *27*, 381.
5. Florin, E. L.; Moy, V. T.; Gaub, H. E. *Science* **1994**, *264*, 415.
6. Bain, C. D.; Evall, J.; Whitesides, G. M. *J. Am. Chem. Soc.* **1989**, *111*, 7155.
7. Ge, L. Q.; Mohwald, H.; Li, J. B. *ChemPhysChem* **2003**, *4*, 1351.
8. Rief, M.; Gautel, M.; Oesterhelt, F.; Fernandez, J. M.; Gaub, H. E. *Science* **1997**, *276*, 1109.
9. Donath, E.; Sukhorukov, G. B.; Caruso, F.; Davis, S. A.; Mohwald, H. *Angew. Chem.-Int. Edit.* **1998**, *37*, 2202.
10. Otsuka, M.; Matsuda, Y.; Baig, A. A.; Chhettry, A.; Higuchi, W. I. *Adv. Drug Deliv. Rev.* **2000**, *42*, 249.
11. Miyamoto, H.; Ogura, Y.; Hashizoe, M.; Kunou, N.; Honda, Y.; Ikada, Y. *Curr. Eye Res.* **1997**, *16*, 930.
12. Kuzma, P.; MooYoung, A. J.; Moro, D.; Quandt, H.; Bardin, C. W.; Schlegel, P. H. *Macromol. Symp.* **1996**, *109*, 15.
13. Nasim, K.; Meyer, C.; Autian, J. J. *J. Pharm. Sci.* **1972**, *61*, 1775.
14. Hansch, C.; Anderson, S. M. *J. Org. Chem* **1967**, *32*, 2583.
15. Hirech, K.; Payan, S.; Carnelle, G.; Brujes, L.; Legrand, J. *Powder Technol.* **2003**, *130*, 324.
16. Tsuji, K. *J. Microencapsul.* **2001**, *18*, 137.
17. Shirley, I. M.; Scher, H. B.; Perrin, R. M.; Wege, P. J.; Rodson, M.; Chen, J. L.; Rehmke, A. W. *Pest Manag. Sci.* **2001**, *57*, 129.
18. Goodwin, J. T.; Somerville, G. R. *Microencapsulation processes and applications*; Plenum Press: NY, 1974.
19. Somerville, G. R. British Patent 1142708, 1966.
20. Macaulay, N. Microencapsulation processes and applications US Patent 3016308, 1962.
21. Sparks, R. E.; Mason, N. S. Method for coating particles or liquid droplets, US Patent 4675140, 1987.

22. Hall, H. S.; Hinkes, T. M. *Microencapsulation processes and applications*; Plenum Press: NY, 1974.
23. Bakan, J. A. *Controlled release techniques: methods, theory and applications*; CRC Press: Boca Raton, FL, USA, 1980.
24. Beestman, G. B.; Deming, J. M. Encapsulation by interfacial polymerisation and aqueous herbicidal composition containing microcapsules produced thereby. US Patent 4280833, 1981.
25. Beestman, G. B.; Deming, J. M. Encapsulation by interfacial polycondensation. US Patent 4417916, 1983.
26. Vandegaer, J. E. Encapsulation by interfacial polymerisation, US Patent 3577515, 1971.
27. Haag, R.; Rampi, M. A.; Holmlin, R. E.; Whitesides, G. M. *J. Am. Chem. Soc.* **1999**, *121*, 7895.
28. Han, S. W.; Ha, T. H.; Kim, C. H.; Kim, K. *Langmuir* **1998**, *14*, 6113.
29. Hu, K.; Bard, A. J. *Langmuir* **1997**, *13*, 5418.
30. Tsuduki, T.; Imanishi, A.; Isawa, K.; Terada, S.; Matsui, F.; Kiguchi, M.; Yokoyama, T.; Ohta, T. *J. Synchrotr. Radiat.* **1999**, *6*, 787.
31. Xu, L. S.; Allee, D. R. *J. Vac. Sci. Technol. B* **1995**, *13*, 2837.
32. Hozumi, A.; Sugimura, H.; Yokogawa, Y.; Kameyama, T.; Takai, O. *Colloid Surf. A-Physicochem. Eng. Asp.* **2001**, *182*, 257.
33. Jourdan, J. S.; Cruchon-Dupeyrat, S. J.; Huan, Y.; Kuo, P. K.; Liu, G. Y. *Langmuir* **1999**, *15*, 6495.
34. Kim, Y.; Kim, K. S.; Park, M.; Jeong, J. *Thin Solid Films* **1999**, *341*, 91.
35. Hayes, W. A.; Shannon, C. *Langmuir* **1996**, *12*, 3688.
36. Hobara, D.; Miyake, O.; Imabayashi, S.; Niki, K.; Kakiuchi, T. *Langmuir* **1998**, *14*, 3590.
37. Lukkari, J.; Kleemola, K.; Meretoja, M.; Ollonqvist, T.; Kankare, J. *Langmuir* **1998**, *14*, 1705.
38. Schonherr, H.; Vancso, G. J. *Langmuir* **1997**, *13*, 3769.
39. Wells, M.; Dermody, D. L.; Yang, H. C.; Kim, T.; Crooks, R. M.; Ricco, A. J. *Langmuir* **1996**, *12*, 1989.
40. Yang, H. C.; Dermody, D. L.; Xu, C. J.; Ricco, A. J.; Crooks, R. M. *Langmuir* **1996**, *12*, 726.
41. Chen, S. F.; Li, L. Y.; Boozer, C. L.; Jiang, S. Y. *Langmuir* **2000**, *16*, 9287.

42. Zhong, C. J.; Brush, R. C.; Anderegg, J.; Porter, M. D. *Langmuir* **1999**, *15*, 518.
43. Tamada, K.; Nagasawa, J.; Nakanishi, F.; Abe, K.; Ishida, T.; Hara, M.; Knoll, W. *Langmuir* **1998**, *14*, 3264.
44. Wagner, P.; Hegner, M.; Guntherodt, H. J.; Semenza, G. *Langmuir* **1995**, *11*, 3867.
45. Hong, S. H.; Zhu, J.; Mirkin, C. A. *Langmuir* **1999**, *15*, 7897.
46. Perkins, M. C.; Roberts, C. J.; Briggs, D.; Davies, M. C.; Friedmann, A.; Hart, C. A.; Bell, G. A. *Planta* **2005**, *221*, 123.
47. Bain, C. D.; Troughton, E. B.; Tao, Y. T.; Evall, J.; Whitesides, G. M.; Nuzzo, R. G. *J. Am. Chem. Soc.* **1989**, *111*, 321.
48. Bain, C. D.; Whitesides, G. M. *J. Am. Chem. Soc.* **1989**, *111*, 7164.
49. Binnig, G.; Quate, C. F.; Gerber, C. *Phys. Rev. Lett.* **1986**, *56*, 930.
50. Israelachvili, J. *Accounts Chem. Res.* **1987**, *20*, 415.
51. Kuo, S. C.; Sheetz, M. P. *Science* **1993**, *260*, 232.
52. Block, S. M. *Nature* **1992**, *360*, 493.
53. Joyce, S. A.; Houston, J. E. *Rev. Sci. Instrum.* **1991**, *62*, 710.
54. Ducker, W. A.; Senden, T. J.; Pashley, R. M. *Nature* **1991**, *353*, 239.
55. Yakubov, G. E.; Butt, H. J.; Vinogradova, O. I. *J. Phys. Chem. B* **2000**, *104*, 3407.
56. Craig, V. S. J.; Ninham, B. W.; Pashley, R. M. *Langmuir* **1999**, *15*, 1562.
57. Butt, H. J.; Kappl, M.; Mueller, H.; Raiteri, R.; Meyer, W.; Ruhe, J. *Langmuir* **1999**, *15*, 2559.
58. Vinogradova, O. I.; Yakubov, G. E.; Butt, H. J. *J. Chem. Phys.* **2001**, *114*, 8124.
59. Butt, H. J. *Biophys. J.* **1991**, *60*, 1438.
60. Albrecht, T. R.; Akamine, S.; Carver, T. E.; Quate, C. F. *J. Vac. Sci. Technol. A-Vac. Surf. Films* **1990**, *8*, 3386.
61. Albrecht, T. R.; Quate, C. F. *J. Appl. Phys.* **1987**, *62*, 2599.
62. Israelachvili, J. *Intermolecular and surface forces*; Academic: New York, 1992.
63. Sader, J. E.; White, L. *J. Appl. Phys.* **1993**, *74*, 1.
64. Neumeister, J. M.; Ducker, W. A. *Rev. Sci. Instrum.* **1994**, *65*, 2527.
65. Cleveland, J. P.; Manne, S.; Bocek, D.; Hansma, P. K. *Rev. Sci. Instrum.* **1993**, *64*, 403.
66. Hutter, J. L.; Bechhoefer, J. *Rev. Sci. Instrum.* **1993**, *64*, 1868.
67. Maeda, N.; Senden, T. J. *Langmuir* **2000**, *16*, 9282.

68. Gibson, C. T.; Watson, G. S.; Myhra, S. *Nanotechnology* **1996**, 7, 259.
69. Torii, A.; Sasaki, M.; Hane, K.; Okuma, S. *Meas. Sci. Technol.* **1996**, 7, 179.
70. Scholl, D.; Everson, M. P.; Jaklevic, R. C. *Rev. Sci. Instrum.* **1994**, 65, 2255.
71. Rabinovich, Y. I.; Yoon, R. H. *Langmuir* **1994**, 10, 1903.
72. Holbery, J. D.; Eden, V. L.; Sarikaya, M.; Fisher, R. M. *Rev. Sci. Instrum.* **2000**, 71, 3769.
73. Thomas, R. C.; Houston, J. E.; Crooks, R. M.; Kim, T.; Michalske, T. A. *J. Am. Chem. Soc.* **1995**, 117, 3830.
74. Noy, A.; Frisbie, C. D.; Rozsnyai, L. F.; Wrighton, M. S.; Lieber, C. M. *J. Am. Chem. Soc.* **1995**, 117, 7943.
75. Atamny, F.; Baiker, A. *Surf. Sci.* **1995**, 323, L314.
76. Griffith, J. E.; Grigg, D. A.; Vasile, M. J.; Russell, P. E.; Fitzgerald, E. A. *J. Vac. Sci. Technol. A-Vac. Surf. Films* **1992**, 10, 674.
77. Markiewicz, P.; Goh, M. C. *Rev. Sci. Instrum.* **1995**, 66, 3186.
78. Sheiko, S. S.; Moller, M.; Reuvekamp, E.; Zandbergen, H. W. *Phys. Rev. B* **1993**, 48, 5675.
79. Westra, K. L.; Thomson, D. J. *J. Vac. Sci. Technol. B* **1994**, 12, 3176.
80. Li, Y.; Lindsay, S. M. *Rev. Sci. Instrum.* **1991**, 62, 2630.
81. Odin, C.; Aime, J. P.; Elkaakour, Z.; Bouhacina, T. *Surf. Sci.* **1994**, 317, 321.
82. Vesenka, J.; Manne, S.; Giberson, R.; Marsh, T.; Henderson, E. *Biophys. J.* **1993**, 65, 992.
83. Vesenka, J.; Miller, R.; Henderson, E. *Rev. Sci. Instrum.* **1994**, 65, 2249.
84. Weisenhorn, A. L.; Hansma, P. K.; Albrecht, T. R.; Quate, C. F. *Appl. Phys. Lett.* **1989**, 54, 2651.
85. Mate, C. M.; Lorenz, M. R.; Novotny, V. J. *J. Chem. Phys.* **1989**, 90, 7550.
86. Butt, H. J. *Biophys. J.* **1991**, 60, 777.
87. Kekicheff, P.; Marcelja, S.; Senden, T. J.; Shubin, V. E. *J. Chem. Phys.* **1993**, 99, 6098.
88. Huttl, G.; Beyer, D.; Muller, E. *Surf. Interface Anal.* **1997**, 25, 543.
89. Ducker, W. A.; Senden, T. J.; Pashley, R. M. *Langmuir* **1992**, 8, 1831.
90. Vakarelski, I. U.; Higashitani, K. *J. Colloid Interface Sci.* **2001**, 242, 110.
91. Vakarelski, I. U.; Toritani, A.; Nakayama, M.; Higashitani, K. *Langmuir* **2001**, 17, 4739.

92. Vakarelski, I. U.; Ishimura, K.; Higashitani, K. *J. Colloid Interface Sci.* **2000**, 227, 111.
93. Gady, B.; Reifengerger, R.; Schaefer, D. M.; Bowen, R. C.; Rimai, D. S.; Demejo, L. P.; Vreeland, W. *Journal Of Adhesion* **1998**, 67, 19.
94. Biggs, S.; Spinks, G. *J. Adhes. Sci. Technol.* **1998**, 12, 461.
95. Schaefer, D. M.; Carpenter, M.; Reifengerger, R.; Demejo, L. P.; Rimai, D. S. *J. Adhes. Sci. Technol.* **1994**, 8, 197.
96. Fuji, M.; Machida, K.; Takei, T.; Watanabe, T.; Chikazawa, M. *Langmuir* **1999**, 15, 4584.
97. Fuji, M.; Machida, K.; Takei, T.; Watanabe, T.; Chikazawa, M. *J. Phys. Chem. B* **1998**, 102, 8782.
98. Cooper, K.; Gupta, A.; Beaudoin, S. *J. Colloid Interface Sci.* **2001**, 234, 284.
99. Rabinovich, Y. I.; Adler, J. J.; Ata, A.; Singh, R. K.; Moudgil, B. M. *J. Colloid Interface Sci.* **2000**, 232, 10.
100. Rabinovich, Y. I.; Adler, J. J.; Ata, A.; Singh, R. K.; Moudgil, B. M. *J. Colloid Interface Sci.* **2000**, 232, 17.
101. Cooper, K.; Gupta, A.; Beaudoin, S. *J. Colloid Interface Sci.* **2000**, 228, 213.
102. Cooper, K.; Ohler, N.; Gupta, A.; Beaudoin, S. *J. Colloid Interface Sci.* **2000**, 222, 63.
103. Braithwaite, G. J. C.; Luckham, P. F.; Howe, A. M. *J. Colloid Interface Sci.* **1999**, 213, 525.
104. Giesbers, M.; Kleijn, J. M.; Fleer, G. J.; Stuart, M. A. C. *Colloid Surf. A-Physicochem. Eng. Asp.* **1998**, 142, 343.
105. Braithwaite, G. J. C.; Luckham, P. F. *J. Chem. Soc.-Faraday Trans.* **1997**, 93, 1409.
106. Braithwaite, G. J. C.; Howe, A.; Luckham, P. F. *Langmuir* **1996**, 12, 4224.
107. Ducker, W. A.; Xu, Z. G.; Israelachvili, J. N. *Langmuir* **1994**, 10, 3279.
108. Wangsa-Wirawan, N. D.; Ikai, A.; O'Neill, B. K.; Middelberg, A. P. J. *Biotechnol. Prog.* **2001**, 17, 963.
109. Xu, Z. H.; Chi, R.; Difeo, T.; Finch, J. A. *J. Adhes. Sci. Technol.* **2000**, 14, 1813.
110. Preuss, M.; Butt, H. J. *Langmuir* **1998**, 14, 3164.
111. Muster, T. H.; Toikka, G.; Hayes, R. A.; Prestidge, C. A.; Ralston, J. *Colloid Surf. A-Physicochem. Eng. Asp.* **1996**, 106, 203.

112. Bele, M.; Kocevar, K.; Pejovnik, S.; Besenhard, J. O.; Musevic, I. *Langmuir* **2000**, *16*, 8334.
113. Willing, G. A.; Burk, T. R.; Etzler, F. M.; Neuman, R. D. *Colloid Surf. A-Physicochem. Eng. Asp.* **2001**, *193*, 117.
114. Sindel, U.; Zimmermann, I. *Powder Technol.* **2001**, *117*, 247.
115. Ibrahim, T. H.; Burk, T. R.; Etzler, F. M.; Neuman, R. D. *J. Adhes. Sci. Technol.* **2000**, *14*, 1225.
116. Willing, G. A.; Ibrahim, T. H.; Etzler, F. M.; Neuman, R. D. *J. Colloid Interface Sci.* **2000**, *226*, 185.
117. Mizes, H.; Ott, M.; Eklund, E.; Hays, D. *Colloid Surf. A-Physicochem. Eng. Asp.* **2000**, *165*, 11.
118. Mizes, H. A. *Journal Of Adhesion* **1995**, *51*, 155.
119. Mizes, H. A. *J. Adhes. Sci. Technol.* **1994**, *8*, 937.
120. Bowen, W. R.; Lovitt, R. W.; Wright, C. J. *J. Mater. Sci.* **2001**, *36*, 623.
121. Frisbie, C. D.; Rozsnyai, L. F.; Noy, A.; Wrighton, M. S.; Lieber, C. M. *Science* **1994**, *265*, 2071.
122. Vezenov, D. V.; Noy, A.; Rozsnyai, L. F.; Lieber, C. M. *J. Am. Chem. Soc.* **1997**, *119*, 2006.
123. Nakagawa, T.; Ogawa, K.; Kurumizawa, T. *J. Vac. Sci. Technol. B* **1994**, *12*, 2215.
124. Nakagawa, T.; Ogawa, K.; Kurumizawa, T.; Ozaki, S. *Jpn. J. Appl. Phys. Part 2 - Lett.* **1993**, *32*, L294.
125. Green, J. B. D.; McDermott, M. T.; Porter, M. D.; Siperko, L. M. *Journal Of Physical Chemistry* **1995**, *99*, 10960.
126. Pierce, M.; Stuart, J.; Pungor, A.; Dryden, P.; Hlady, V. *Langmuir* **1994**, *10*, 3217.
127. Sinniah, S. K.; Steel, A. B.; Miller, C. J.; ReuttRobey, J. E. *J. Am. Chem. Soc.* **1996**, *118*, 8925.
128. Wood, J.; Sharma, R. *Langmuir* **1995**, *11*, 4797.
129. Alley, R. L.; Komvopoulos, K.; Howe, R. T. *J. Appl. Phys.* **1994**, *76*, 5731.
130. Grigg, D. A.; Russell, P. E.; Griffith, J. E. *J. Vac. Sci. Technol. A-Vac. Surf. Films* **1992**, *10*, 680.
131. Drake, B.; Prater, C. B.; Weisenhorn, A. L.; Gould, S. A. C.; Albrecht, T. R.; Quate, C. F.; Cannell, D. S.; Hansma, H. G.; Hansma, P. K. *Science* **1989**, *243*, 1586.

132. Shao, Z. F.; Yang, J. Q. *Rev. Biophys.* **1995**, 28, 195.
133. Vesenska, J.; Mosher, C.; Schaus, S.; Ambrosio, L.; Henderson, E. *Biotechniques* **1995**, 19, 240.
134. Lyubchenko, Y. L.; Oden, P. I.; Lampner, D.; Lindsay, S. M.; Dunker, K. A. *Nucleic Acids Res.* **1993**, 21, 1117.
135. Vanderwerf, K. O.; Putman, C. A. J.; Degrooth, B. G.; Greve, J. *Appl. Phys. Lett.* **1994**, 65, 1195.
136. Weisenhorn, A. L.; Maivald, P.; Butt, H. J.; Hansma, P. K. *Phys. Rev. B* **1992**, 45, 11226.
137. Ishino, T.; Hieda, H.; Tanaka, K.; Gemma, N. *Jpn. J. Appl. Phys. Part 1 - Regul. Pap. Short Notes Rev. Pap.* **1994**, 33, 4718.
138. Lee, G. U.; Chrisey, L. A.; Colton, R. J. *Science* **1994**, 266, 771.
139. Vezenov, D. V.; Zhuk, A. V.; Whitesides, G. M.; Lieber, C. M. *J. Am. Chem. Soc.* **2002**, 124, 10578.
140. Garoff, N.; Zauscher, S. *Langmuir* **2002**, 18, 6921.
141. Schonherr, H.; Hruska, Z.; Vancso, G. J. *Macromolecules* **2000**, 33, 4532.
142. Feldman, K.; Tervoort, T.; Smith, P.; Spencer, N. D. *Langmuir* **1998**, 14, 372.
143. Fowkes, M. F. *Ind. Eng. Chem.* **1964**, 56, 40.
144. Fowkes, M. F. *Surfaces and Interfaces I. Chemical and Physical Characteristics*; Syracuse University Press: Syracuse, NY, 1967.
145. Vanoss, C. J.; Chaudhury, M. K.; Good, R. J. *Chem. Rev.* **1988**, 88, 927.
146. Vanoss, C. J.; Good, R. J.; Chaudhury, M. K. *Langmuir* **1988**, 4, 884.
147. Zimmermann, H.; Hillgartner, M.; Manz, B.; Feilen, P.; Brunnenmeier, F.; Leinfelder, U.; Weber, M.; Cramer, H.; Schneider, S.; Hendrich, C.; Volke, F.; Zimmermann, U. *Biomaterials* **2003**, 24, 2083.
148. Mu, L.; Feng, S. S. *J. Control. Release* **2003**, 86, 33.
149. Gao, C. Y.; Leporatti, S.; Moya, S.; Donath, E.; Mohwald, H. *Chem.-Eur. J.* **2003**, 9, 915.
150. Leporatti, S.; Gao, C.; Voigt, A.; Donath, E.; Mohwald, H. *Eur. Phys. J. E* **2001**, 5, 13.
151. Lulevich, V. V.; Radtchenko, I. L.; Sukhorukov, G. B.; Vinogradova, O. I. *Macromolecules* **2003**, 36, 2832.
152. Lulevich, V. V.; Vinogradova, O. I. *Langmuir* **2004**, 20, 2874.

-
153. Skoog, D. A.; West, D. M.; Holler, F. J. *Analytical chemistry: An introduction*, 6th ed.; Saunders College Publishing: USA, 1994.
 154. Davidson, R. S. *Chem. Soc. Rev.* **1996**, 25, 241.
 155. Taylor, D. L.; Wang, Y. *Fluorescence microscopy of living cells in culture. Parts A and B*; Academic Press Inc., 1989.
 156. Minsky, M. *Scanning* **1988**, 10, 128.
 157. Egger, M. D.; Petran, M. *Science* **1967**, 157, 305.
 158. Sheppard, C. J. R.; Shotton, D. M. *Confocal laser scanning microscopy*; BIOS Scientific Publishers Ltd: Oxford, UK, 1997.
 159. Lamprecht, A.; Schafer, U. F.; Lehr, C. M. *Int. J. Pharm.* **2000**, 196, 223.
 160. Lamprecht, A.; Schafer, U. F.; Lehr, C. M. *Eur. J. Pharm. Biopharm.* **2000**, 49, 1.
 161. Lamprecht, A.; Schafer, U.; Lehr, C. M. *J. Control. Release* **2001**, 72, 278.
 162. Yang, Y. Y.; Chung, T. S.; Ng, N. P. *Biomaterials* **2001**, 22, 231.

Chapter 2

Experimental

This chapter describes the experimental techniques employed in these studies. Details are given for:

- i) AFM instrumentation
- ii) Micromanipulation apparatus
- iii) Calibration of AFM cantilever spring constants
- iv) Substrate preparation
- v) Confocal experiments
- vi) Electrochemical experiments
- vii) Reagents and preparation of solutions

More specific information on particular experimental procedures is included in the relevant chapters that follow.

2.1 Force measurements

2.1.1 Instrumentation

Two models of AFM were used in these studies. For determination of the spring constant of the AFM cantilever, a Multimode atomic force microscope with a Nanoscope IIIA controller (Digital Instruments, California) was used. For force measurements, the model used was a PicoSPM microscope running Picoscan 5.1 software (Molecular Imaging Corp., Phoenix, Arizona).

In all AFM experiments the probes used were standard silicon nitride contact mode imaging cantilevers of beam width 21 μm and length either 100 or 200 μm (Digital Instruments). Each cantilever had an integrated pyramidal tip, with a height of 2.86 μm , base width of 4.0 μm and radius of tip curvature of between 20 and 60 nm. Once the microcapsule had been attached to the tip, much higher adhesion forces

resulted than with a normal tip and due to the limited range of piezo-movement and dynamic range of the split photodiode detector, a stiff cantilever had to be used to ensure detachment of the particle from the target surface after contact.

2.1.2 Micromanipulation

A micromanipulation rig was designed and constructed in house. It consisted of two x , y , z positioning stages (New Focus Inc. CA, USA) mounted on aluminium blocks. Each stage had attached a long metal arm, onto the end of which was attached a sharp probe which could be positioned directly under the lens of an optical microscope (Olympus BH2-UMA light microscope with Nomarski differential-contrast objectives, range $\times 50$ to $\times 1000$ magnification). The whole set up was placed on an isolated vibrational support to minimise vibration of the probes during micromanipulation. The stages were placed either side of the microscope as shown in the photograph in Figure 2.1.

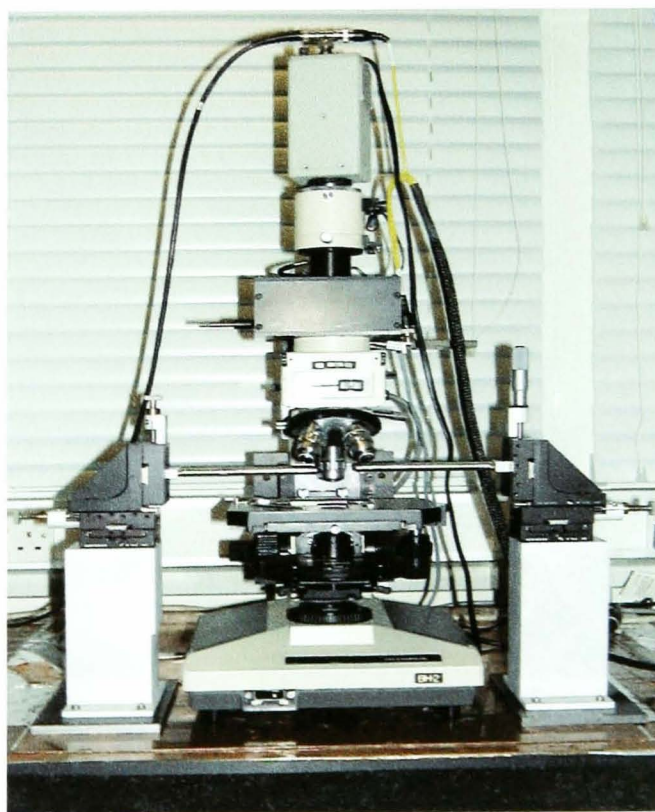


Figure 2.1 Photograph of the micromanipulation set up used in this project.

To manipulate the microcapsules, probes were needed that had a tip diameter smaller than that of the microcapsule *i.e.* smaller than 10 μm . This was achieved by etching 250 μm tungsten wires (Goodfellow, Cambridge) to a fine point (~ 500 nm). Tungsten wire is rigid and thus was the optimum choice for micromanipulation work.

The tungsten wire was etched to a fine point by heating in the hottest point of a Bunsen burner flame until the wire glowed white. It was then immediately dipped into a saturated solution of sodium nitride (NaNO_3) for ca. 30 seconds¹. This process was repeated until it was possible to observe, by optical microscopy, that the wire had been etched. At this stage, the probe was removed and an optical microscope connected to a PC with image analysis software was used to measure the tip diameter. The etching process was repeated until the tip diameter was approximately 10 μm . Typical optical micrographs of etched tungsten wires are shown in Figure 2.2.

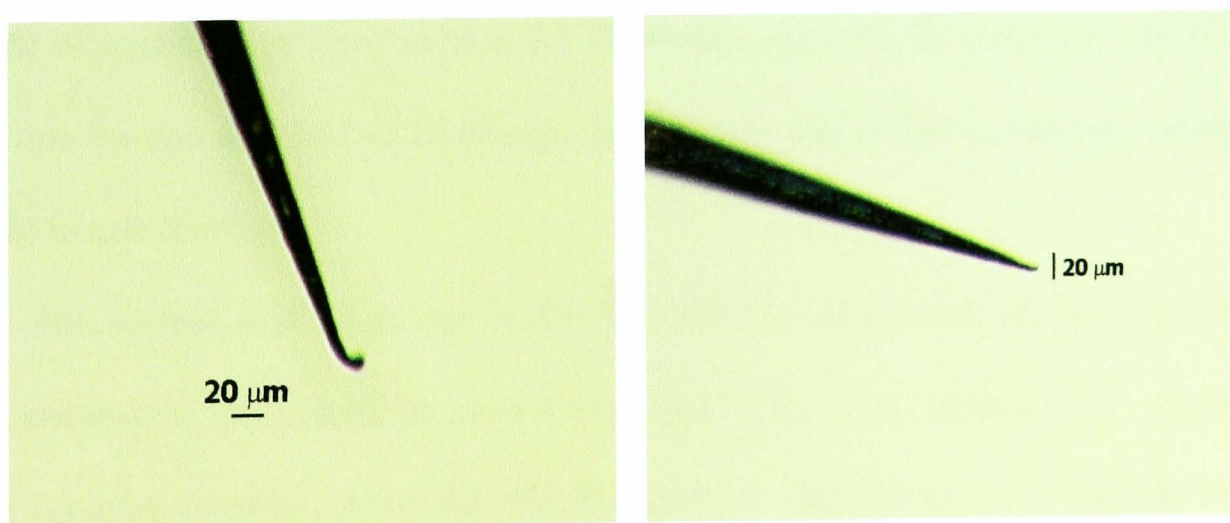


Figure 2.2 Optical micrographs from the optical microscope (magnification $\times 200$) of etched 250 μm diameter tungsten wires.

The etched tungsten wire was then attached to a length of copper wire with araldite (Bostik Ltd, Leicester). The copper wire was used as it could easily be attached to the metal arms of the micromanipulation set-up and bent into the shape so that the tip of the etched tungsten wire could be positioned directly beneath the lens of the microscope. A schematic of the micromanipulation set up is shown in Figure 2.3.

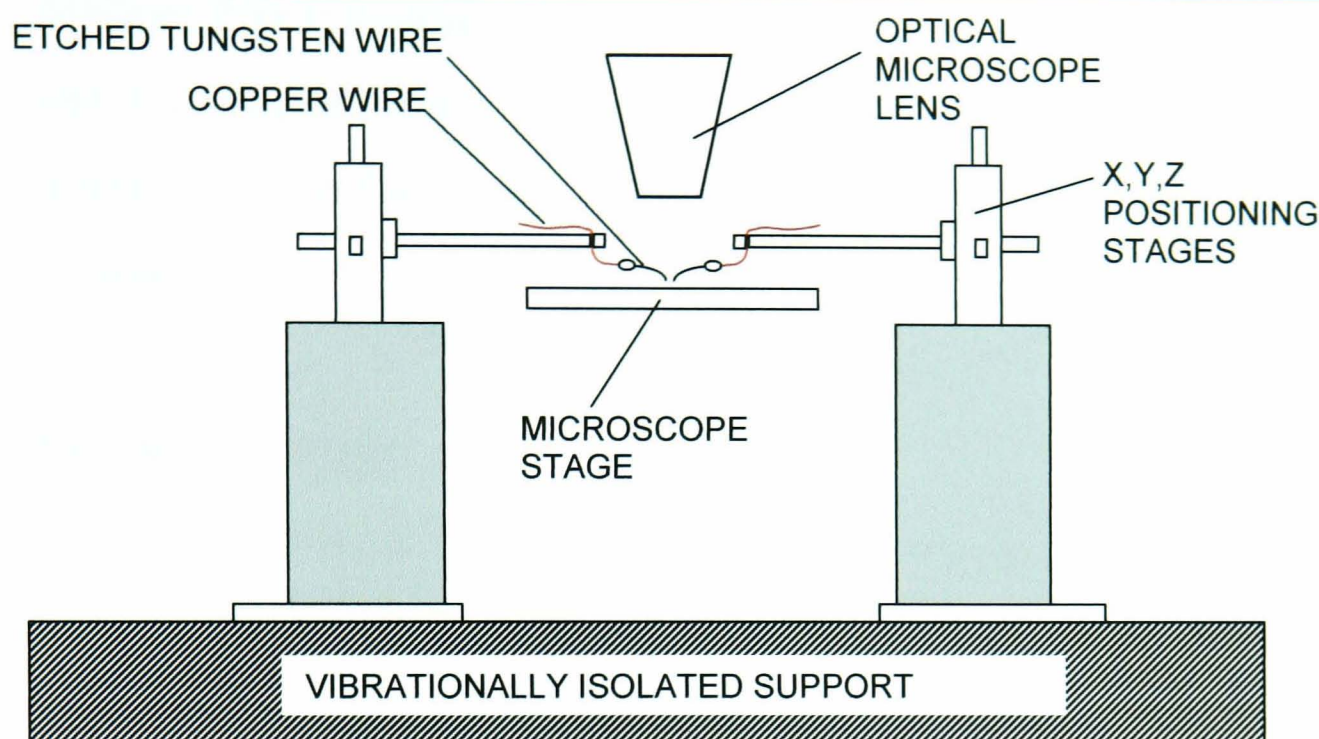


Figure 2.3 Schematic representation of micromanipulation rig used in this project.

This micromanipulation rig had two main uses in this project. First, it was used to place borosilicate spheres ($14.5\ \mu\text{m}$, Duke Scientific) onto the tip of a silicon nitride AFM cantilever to carry out the ‘added mass’ method for determining the spring constant of a cantilever² (see section 2.1.3). In this case, the borosilicate spheres were added one by one and had to be placed on the very end of the cantilever, as close as possible to one another.

The second and main use of the rig was the attachment of microcapsules to AFM cantilevers. The procedure used was adapted from a DI support note³. An amount of glue (general purpose epoxy, fast set, Permabond, Hampshire, UK), smaller than the diameter of the microcapsule, was placed on the tip end of a commercial V-shaped Si_3N_4 tip cantilever assembly using a tungsten probe. The other tungsten probe was used to transfer a single microcapsule (adhered to the probe using capillary forces alone) onto the drop of glue, thus securing it to the end of the cantilever. Cantilever/microcapsule assemblies were then left to dry overnight.

A scanning electron microscope (SEM, Jeol, JSM 6100, equipped with Oxford ISIS Analytical System) was used to obtain SEMs of each microcapsule attached to the

cantilever. Prior to imaging, the cantilever-microcapsule assemblies were coated with a thin layer of gold. These were acquired in order to obtain the true microcapsule diameter, of importance when comparing adhesion data from different sized microcapsules.

2.1.3 Spring constants

Two methods of spring constant determination were carried out on the silicon nitride AFM cantilevers used in the force measurements. The first was the ‘added mass’ method, which involved placing borosilicate spheres as close to the tip of a silicon nitride cantilever as possible². The cantilever was placed in the AFM and its resonance frequency was measured using a Spectrum Analyser (Stanford Research Systems Ltd.). The measurement was repeated with up to five spheres.

The second method was the ‘thermal noise’ method⁴. The cantilever was brought into contact with a hard substrate in the AFM and a force curve was measured from which the tip deflection sensitivity of the cantilever was determined. The tip was then retracted from the surface and its resonance frequency spectrum recorded on the spectrum analyser. In the latter case, the resonant frequency was due purely to thermal effects.

2.2 Substrate preparation for force measurements

2.2.1 Self-assembled monolayers of alkylthiols on gold

Si (100) wafers were coated in a Plassys MEB 4 50 electron beam evaporator with a 20 nm adhesion layer of Ti deposited at 0.1 nm per second, followed by 120 nm of Au deposited at 0.3 nm per second, with a background pressure of 10^{-6} mbar. The substrates were annealed in a ‘muffle furnace’ for 6 hours at 350 °C.

The annealed substrates were then cleaned thoroughly by submerging them in ‘piranha’ solution for 30 minutes. This solution is made up of a 3:1 ratio of concentrated sulphuric acid: hydrogen peroxide (30%) **CAUTION:** this solution reacts aggressively with any organic material. Upon careful mixing, this solution came to the boil spontaneously, at which point the substrates to be cleaned were added. After removal from the cleaning solution, the substrates were thoroughly rinsed with deionised water and blown dry in a stream of nitrogen. The gold surface was characterised with topographical AFM imaging (Molecular Imaging PicoSPM) before and after annealing.

The substrates were then placed into solutions containing the thiols of interest. The solutions from which the SAMs were formed consisted of 1 mM of either 11-mercapto-1-undecanol, 16-mercaptohexadecanoic acid ($\text{HS}(\text{CH}_2)_{15}\text{COOH}$) or 1-hexadecanethiol ($\text{HS}(\text{CH}_2)_{15}\text{CH}_3$) or a 1 mM mixture of the latter two thiols in ethanol. SAMs were formed by placing the gold-coated substrates in these solutions for 48 hours. Substrates were then removed, rinsed with fresh ethanol and dried using nitrogen. A schematic representation of this procedure is shown in Figure 2.4.

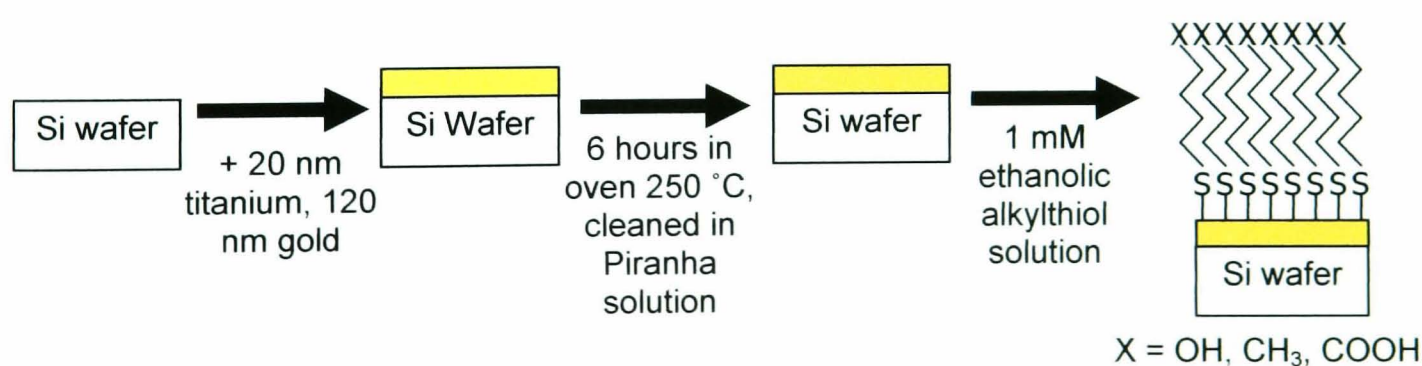


Figure 2.4 Schematic representation of the procedure for the formation of SAMs of alkyl thiols on a gold surface.

The SAMs on gold were characterised using contact angle measurements. The substrate was placed in front of a video microscope and a drop of distilled water was placed upon the surface. Adding more solution enlarged the drop; the enlargement was

captured using a VCR and then transferred to a computer. The angle that the drop made with the substrate during enlargement was then measured using image analysis software (PaintShopPro, Jacs software).

2.2.2 Cuticle substrate formation

A 10 mm hole cork borer was used to punch discs out of a leaf of the plant *Prunus laurocerasus* avoiding the main veins. The lower surface of the leaf was marked with a water indelible marker pen. The discs were then placed in an enzyme solution consisting of 500 mg cellulase from *Aspergillus niger*, 5 g pectinase from *Aspergillus niger* and 1 g sodium azide added to 1 litre of 0.2 M citrate buffer (sodium citrate and citric acid). The solution was then evacuated until all the leaf discs sank.

The discs in solution were incubated at 37 °C and the enzyme solution was changed every 3-4 days until the cuticles became completely transparent. All unwanted tissue such as marked cuticles and leaf tissue was removed during this time. The remaining cuticles were rinsed in Milli-Q reagent water for 24 hours before they were dried flat on a Teflon sheet. The upper side of the cuticle was shiny and the underside was dull so the substrates were used shiny side up.

2.3 Confocal microscopy

2.3.1 Instrumentation

The microscope used in all of these measurements was a Zeiss LSM 510, Axioplan 2, upright confocal microscope. It was equipped with Helium/Neon and Argon lasers enabling wavelengths of 543 nm, 517 nm, 488 nm, 453 nm, 438 nm to be used for excitation of samples.

2.3.2 Experimental procedures

2.3.2.1 Microcapsule release into solution

The microcapsules used in these experiments were formed by interfacial condensation polymerisation (see section 1.1.2). They all contained the pesticide lambda cyhalothrin, the structure of which is shown in Figure 2.5. Six sets of microcapsules were synthesised with the properties outlined in Table 2.1.

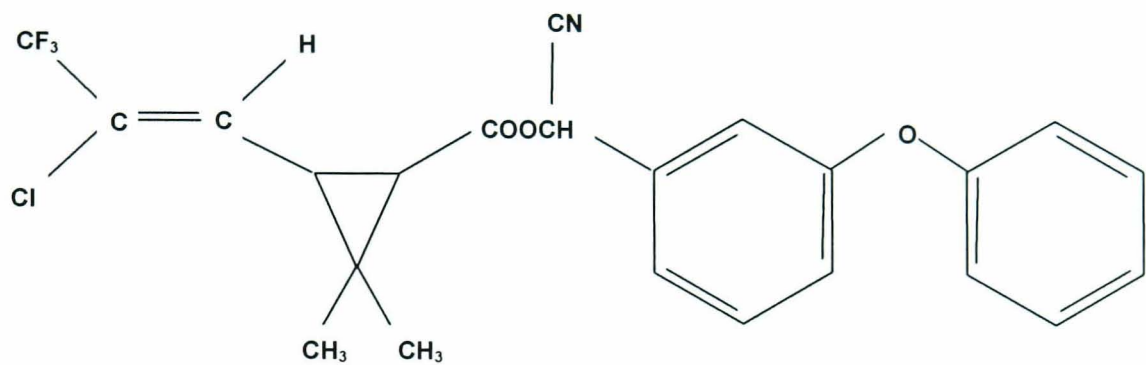


Figure 2.5 Molecular structure of the pyrethroid insecticide lambda cyhalothrin.

Table 2.1 Details of microcapsules used in release into solution experiments

Microcapsule	% Monomers in original organic phase	Ratio of monomers PMPPI:TDI
1	10%	1:1
2	10%	1:10
3	10%	1:20
4	15%	1:1
5	15%	1:10
6	15%	1:20

The percentage wall thickness relates to the percentage of monomers used in the original reaction mixture. 10% yielded a thinner wall than 15%. The ratio of monomers used in the original reaction mixture relates to the crosslinking density within the polymer wall. The greater the proportion of TDI in the original reaction mixture, the weaker the crosslinking density within the microcapsule wall.

All CLSM images (512 x 512, 8 bit pixel) in solution were acquired with a water immersion objective lens (Zeiss, Achroplan 20x/0.50 W) with a 10x tube lens. To observe the auto-fluorescence of the lambda cyhalothrin within the microcapsules both an argon laser ($\lambda = 488$ nm) and a helium/neon laser ($\lambda = 543$ nm) were used for excitation and any emitted light was collected through one long pass filter (560nm) and one band pass filter (505 - 530 nm). .

Images were processed using the LSM Image Browser software (Zeiss). Average pixel intensities were calculated over the area corresponding to single microcapsules using Paint Shop Pro. All confocal microscopy analyses were carried out in an air conditioned room at $23 \pm 0.5^\circ\text{C}$.

For further details of experimental procedures see section 4.3.

2.3.2.2 Microcapsule release in the dry state

Two types of microcapsules were studied for these measurements. One was the lambda cyhalothrin capsule used in the studies described in the previous section and the second type were microcapsules formed by the crosslinking of a butylated urea-formaldehyde prepolymer with a tetrafunctional thiol (see section 1.1.2). These capsules contained the pesticide emamectin benzoate, the structure of which is shown in Figure 2.6.

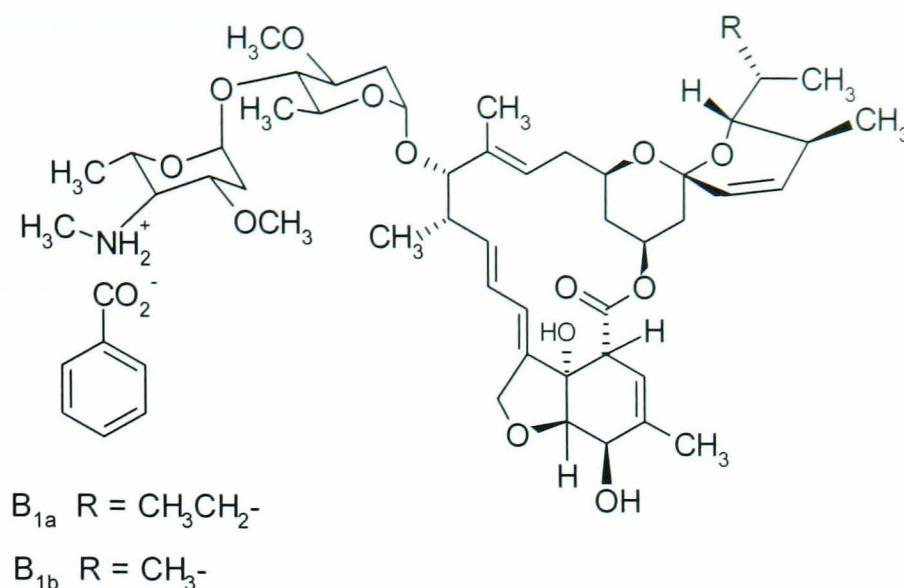


Figure 2.6 Molecular structure of the pesticide emamectin benzoate

For the detailed study of the cuticle of the caterpillars *Heliothis virescens* and *Plutella xylostella*, an argon laser (488nm) was used in conjunction with a long pass filter (505nm). Release from microcapsules was studied onto the surface of *Prunus laurocerasus* and onto glass and parafilm. For release studies a z-stack through the microcapsule and substrate was taken every hour using an objective lens (Zeiss, epiplan-neofluar 50x / 0.80 W). The slices taken in the z-stack were 1 μm apart. The helium/neon (543 nm) and the argon (488 nm) lasers were used in conjunction with long pass 560 nm and band pass 505 - 530 nm filters, respectively.

For further details of experimental procedures used see section 5.2.2.

2.3.2.3 Combined CLSM and electrochemistry studies

An argon laser (488nm) used in conjunction with a 505 nm long pass filter, was employed when recording the fluorescence of the Calcium Green-5N solution. To achieve the optimum compromise between resolution and image intensity, the confocal aperture was set to give an optical slice of 1.1 μm . All CLSM images were recorded using a water immersion lens (Zeiss, Achroplan 20x/0.50 W). For further details see section 6.2.

2.4 Electrochemical techniques

2.4.1 Ultramicroelectrode fabrication

A borosilicate glass capillary (2.0 mm o.d., 1.16 mm i.d., Harvard Apparatus, Kent) was pulled to a fine point using a micropipette puller (Narishige PB7, Japan) and the tip was closed by melting in a Bunsen burner flame. An optical microscope (Meiji Techno, Model BM 29821) was used to ensure that the tip of the pulled capillary was completely sealed. Approximately 1 cm length of the required diameter platinum microwire (either 50 μm or 25 μm diameter, Goodfellow, Cambridge U.K.) was inserted into the glass capillary, as close to the sealed end as possible.

The capillary was then placed under vacuum for ca. 20 minutes, after which the microwire was sealed into the glass capillary by melting the glass around ca. $\frac{3}{4}$ of the length of the microwire, using a home-built heating element. A higher power optical microscope (Olympus BH2-UMA light microscope with Nomarski differential-contrast interference objectives, range x50 to x1000 magnification) was used to ensure that the glass had formed a complete seal around the wire.

The surface of the wire was exposed by polishing the tip of the glass capillary on a course carbimet paper disc (240 grit, Buehler, Coventry). A 600 grit disc (Buehler, Coventry) was then used to polish the surface gently, ensuring that the capillary was held vertical at all times, until the surface was free of any major imperfections and relatively smooth. The electrode was then polished with an impregnated diamond polishing pad (9 μm grade, Buehler, Coventry) on a custom built polishing wheel, followed by a 0.1 μm grade impregnated diamond polishing pad (Buehler, Coventry) to produce a mirror-finish surface with no imperfections. Throughout the preparations of the electrode surface, the flatness and dimensions were monitored periodically with the BH2 optical microscope.

After the electrode surface had been polished back to a sufficient smoothness, the sides of the electrode were coned on a fine grit carbimet paper disc, until the RG value of the electrode was approximately 10.

$$RG = \frac{r_{glass}}{a} = 10$$

where r_{glass} is the radius of the whole glass tip and a is the radius of the electrode microwire (see Figure 2.7b)

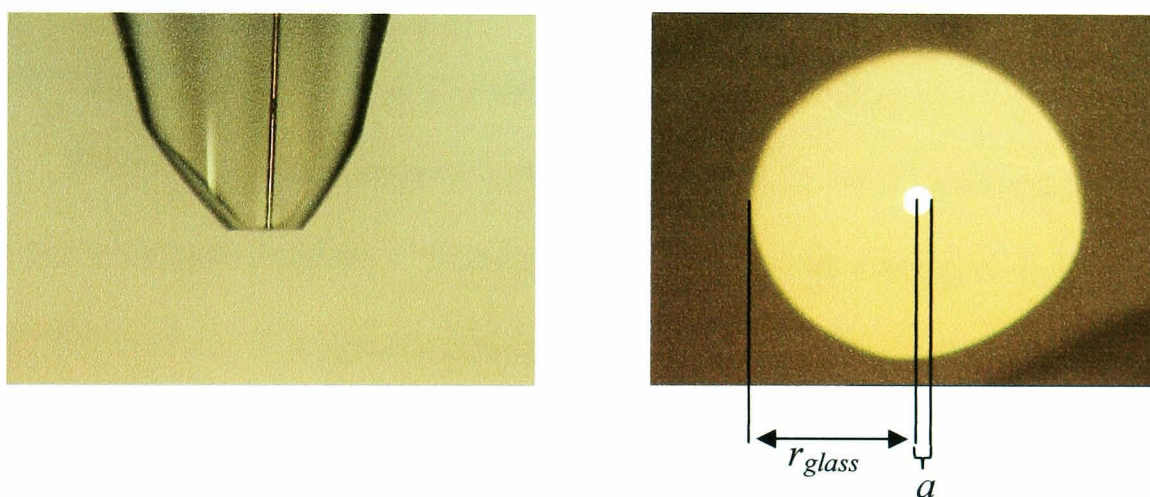


Figure 2.7 Images from the optical microscope of the finished UME **(a)** Side view of the UME **(b)** Top view of the UME defining the terms for calculating RG .

The next stage of the fabrication process was to make electrical contact to the microwire. A piece of solder (ca. 1 cm length, 60:40 tin:lead alloy, R.S. Components, Corby) was placed into the capillary ensuring that it was in contact with the microwire. A length of stripped, tinned copper wire (R.S. Components, Corby) which made contact with the solder and was long enough to protrude from the end of the capillary was added next. The capillary was then held in a horizontal position and the solder was melted with a soldering iron (450°C, Antex TCSU D2) to form the connection between the two wires.

The voltammetric response of the UME was then tested (using linear sweep voltammetry (LSV) see section 2.4.2) to ensure that a good electrical connection had been made. Finally the open end of the capillary was sealed using Araldite (Bostik Ltd,

Leicester) which was carefully placed around the exposed metal wire and left to dry overnight.

Before each use, the UME was polished on a polishing pad with 0.5 μm γ -alumina polish to ensure a clean, smooth surface.

2.4.2 Electrochemical Measurements.

All electrochemical measurements were made using a two electrode setup, with a UME fabricated as described in Section 2.4.1 as the working electrode (WE), and a silver wire (Goodfellow) as a quasi reference electrode (AgQRE).

Electrochemical measurements to test the UMEs were performed using an Eco-Chemie (Holland) Autolab Electrochemical Workstation, equipped with a low current detection module. A known concentration of a well behaved electroactive mediator – ferrocyanide $\text{Fe}(\text{CN})_6^{4-}$ - was used. Voltammetric potential scans were carried out from 0 – 1.2 V versus AgQRE to effect the one-electron oxidation to ferricyanide. The potential scan rate was typically 20 mV/s and the scans were carried out with the UME placed in bulk solution, i.e. at a distance greater than $10a$ from the interface.

For the combined electrochemical/confocal experiments, a 25 μm diameter platinum UME was used and potentials were applied using a potentiostat (Model CHI400, CH Instruments Inc, USA). For mercury deposition, a solution of mercurous nitrate was held at -0.225V until the steady-state current response increased by $2\pi/4$ times. The hemispherical mercury drop electrode produced was then held at -1.1 V for specified times in a solution containing cadmium nitrate and the dye Calcium Green 5N to deposit cadmium into the mercury hemisphere. Cadmium ions were then released during scan from -1.1 to -0.3 V at a potential sweep rate of 10 mV/s. For further details of experimental procedures see section 6.2.

2.5 Chemicals and solutions

All aqueous solutions were prepared using Milli-Q-reagent water (Millipore Corp., resistivity $\geq 18\text{ M}\Omega\text{cm}$). Table 2.2 details grades and suppliers for all other chemicals used.

Table 2.2 Grades and suppliers of chemicals used in this project

Chemical	Grade	Supplier
Sodium hydroxide	A.R.	B.D.H.
Ethanol	A.R.	B.D.H.
16-Mercaptohexadecanoic acid	90%	Aldrich
1-Hexadecanethiol	92%	Aldrich
11-mercapto-1-undecanol	95%	Aldrich
Sodium nitride	>99.5%	Sigma
Potassium dihydrogen phosphate	ACS	Sigma Aldich
Disodium hydrogen phosphate	>99.5%	Fluka BioChemika
Sodium carbonate	A.R.	BDH
Sodium hydrogen carbonate	A.R.	BDH
Sodium citrate	99%	Sigma Aldrich
Citric acid	99.5%	Aldrich
Potassium hydroxide	A.R.	Fisher
Cellulase from Aspergillus's Niger	N/A	Sigma
Pectinase from Aspergillus's Niger	N/A	Sigma
Sodium azide	A.R.	Sigma
Acetone	> 99%	Fisher
Hydrochloric acid	0.1M std solution	Sigma-Aldrich
Nitrogen	pureshield	BOC
Nile red	N/A	Molecular Probes, USA
Mercurous nitrate	98%	Sigma Aldrich
Nitric acid	69%	BDH
Sulphuric acid	98%	BDH
Hydrogen peroxide	30%	Sigma Aldrich
Potassium nitrate	99%	Sigma Aldrich
Cadmium nitrate	95%	Sigma Aldrich
Calcium Green – 5N	N/A	Molecular Probes

2.5.1 Preparation of buffer solutions

Buffer solutions used in the force measurement experiments, with ionic strength of 0.01 mol dm^{-3} , were made up using quantities of potassium dihydrogen phosphate and disodium hydrogen phosphate for low pH buffers (up to 7.8) and sodium hydrogen carbonate and sodium carbonate for high pH buffers, as described in reference 5. The pH of the buffer solution was measured using a pH meter (PHM201 Portable pH meter, Radiometer, Copenhagen) calibrated over an appropriate pH range with standard solutions (Philip Harris, Ashby de la Zouch, UK).

2.5.2 Preparation of solutions used in electrochemical experiments

To test the UMEs, solutions prepared were 0.5 M in KNO_3 , added to act as a supporting electrolyte, and 10 mM potassium hexacyanoferrate (II).

The solution from which the mercury drop electrode was formed was 0.1 M in HNO_3 , 0.5 M in KNO_3 , and 10 mM in $\text{Hg}_2(\text{NO}_3)_2 \cdot 2\text{H}_2\text{O}$. The solution used for cadmium deposition and stripping contained 0.5 μmol Calcium Green-5N and $1 \times 10^{-5} \text{ mol}$ $\text{Cd}(\text{NO}_3)_2$. Due to the very small amounts of Calcium Green-5N used, it was necessary to weigh it out on a seven figure analytical balance (Mettler).

Unless otherwise stated all reagents were weighed out on a four-figure analytical balance (Sartorius A2008).

2.6 References

1. Kerfriden, S.; Nahle, A. H.; Campbell, S. A.; Walsh, F. C.; Smith, J. R. *Electrochim. Acta* **1998**, *43*, 1939.
2. Cleveland, J. P.; Manne, S.; Bocek, D.; Hansma, P. K. *Rev. Sci. Instrum.* **1993**, *64*, 403.

3. Digital Instruments support note No.226, Rev A.
4. Hutter, J. L.; Bechhoefer, J. *Rev. Sci. Instrum.* **1993**, *64*, 1868.
5. Harrison, R. D. *Book of Data*; Nuffield Advanced Science, Longman Group Ltd.

Chapter 3

Investigation into the adhesion properties of functionalised microcapsules to different substrates

The adhesive properties of microcapsules are of essential importance in agriculture applications of microcapsules^{1,2}. The ability of a microcapsule to adhere to a specimen of interest such as foliage, crops or an insect affects the targeted delivery of the pesticide within the capsule to the relevant surface.

This chapter details how AFM has been used, for the first time, to investigate the adhesion properties of functionalised polyurea microcapsules. The adhesion properties of polyurea microcapsules (attached to AFM cantilevers) to SAMs of alkyl thiols on gold are investigated at the single capsule level, and as a function of polymer wall surface functionality. The properties of alkyl thiol SAMs are well defined³⁻⁶ and provide an appropriate substrate against which the complex adhesion properties of the microcapsules can be characterised.

3.1 Introduction

Past AFM studies investigated the deformation properties⁷ and surface topography⁸ of a variety of capsules, but AFM has never been used to specifically quantify the adhesive characteristics of microcapsules to surfaces. The development of the colloidal probe technique⁹⁻¹¹ (detailed in section 1.3.1), inspired the idea of attaching a single microcapsule to an AFM cantilever to investigate its adhesion characteristics.

A variety of different techniques have been used to study microcapsule adhesion. Microcontact printing of polyelectrolytes on a flat substrate has been used to create alternating regions of positive and negative charge. It has been shown that polyelectrolyte microcapsules of a certain charge preferentially adsorb to the surface in

regions of opposite charge, as evident from using fluorescent microscopy techniques^{12,13}. The adhesion area of these charged polyelectrolyte capsules to a glass substrate have also been investigated using reflection interference contrast microscopy (RICM) but no studies have recorded the actual adhesion force between an individual microcapsule and a substrate.

In order to characterise the surface adhesive properties of the polymeric microcapsules employed herein, a technique known as a force titration has been used¹⁴. This technique is an extension of chemical force microscopy (CFM), in which the solution pH is systematically varied and the change in adhesion between the tip and sample is measured as a function of pH.

This technique has been used previously to determine the $pK_{1/2}$, the pH at which half the surface groups are ionised, of surface bound groups such as hydroxy, amine¹⁵, carboxylic acid^{16,17} and phosphonic acid¹⁸ groups and it has also been used to investigate the distribution of functional groups within surface treated polymers such as oxyfluorinated films of isotactic polypropylene¹⁹. The high resolution capability of the chemical force titration has been demonstrated by the study of the acid /base properties of a patterned SAM²⁰.

Another use of CFM has been to examine the effect of electrolyte concentration on the force titration behaviour of carboxylic and phosphonic acid terminated SAMs²¹. These studies showed evidence for the formation of strong hydrogen bonds between neutral and ionised species at low electrolyte concentrations which was prevented at high electrolyte concentrations by the formation of an electrical double layer.

Details on how this technique has been applied to probe the surface characteristics of functionalised microcapsules to SAMs of alkyl thiols on gold appear

in this chapter. The technique has also been used to investigate the adhesion properties of the functionalised microcapsules to the cuticle of a leaf, specifically *Prunus laurocerasus*. This leaf was chosen as it has a very thick waxy cuticle, with well defined properties^{22,23}, which can be easily extracted from the leaf to provide a flat substrate, which is required for the force measurements.

3.2 Experimental

3.2.1 Formation of functionalised microcapsules

All polyurea microcapsules used in these force studies were prepared (Syngenta, Jealotts Hill, Bracknell) using interfacial condensation microencapsulation. For details on the reaction mechanism of polymer wall formation see section 1.1.2. The structure of the wall of the microcapsule can be altered by the addition of modifier molecules (Figure 3.1) which react via their amine group into the microcapsule wall giving the surface of the microcapsule defined functionality. In this thesis, the modified microcapsules will be referred to by the functional groups which terminate their modifier molecule molecular structure.

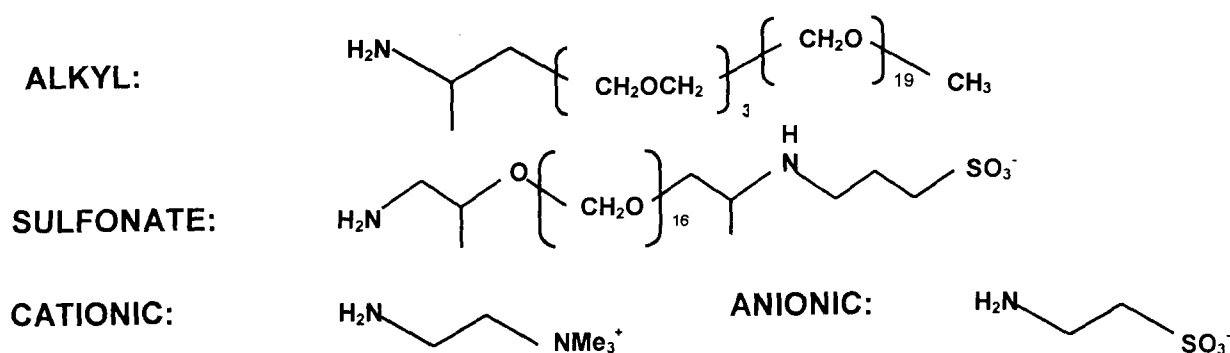


Figure 3.1 Structures of modifier molecules which react into the polymer wall via the NH₂ group to control the surface functionality of the microcapsule.

The microcapsules were then separated from solvent by centrifugation with Milli-Q reagent water (Millipore Corp., resistivity $\geq 18 \text{ M}\Omega \text{ cm}$). A diluted sample was spread on a glass slide and the water was allowed to evaporate in air.

3.2.2 Experimental procedure for force measurements

Adhesion force measurements were obtained using a Molecular Imaging PicoSPM (Molecular Imaging Ann Arbor, USA) equipped with a Teflon fluid cell. The adhesive interaction between the microcapsule and substrate was determined by recording the deflection versus displacement curves at varying pH against an Au-SAM surface. The fluid cell was rinsed thoroughly 5 times with each buffer solution prior to measurement to ensure the pH of the solution inside the cell at the time of measurement was correct. The experimental set-up is shown in Figure 3.2.

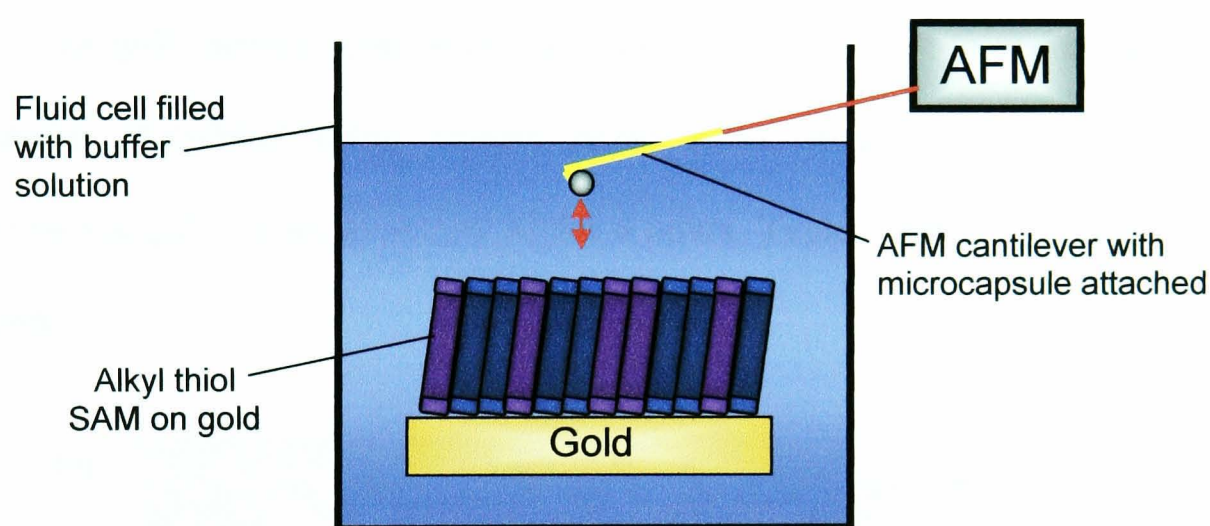


Figure 3.2 Schematic representation of the experimental set-up for force measurements between microcapsule and substrate.

At each pH, adhesion measurements were made at three or four different positions on the monolayer approximately 300 times in total. The average deflection at each pH was obtained from the mean value of the pull off force recorded. This deflection was then converted into a force via the tip deflection sensitivity and normal spring constant of the cantilever which had been determined prior to tip modification. All forces observed were normalised with respect to the radius of the microcapsule.

This procedure was repeated for microcapsules with different surface functionality to SAMs of either hydroxyl-terminated (11-mercapto-1-undecanol), methyl-terminated (1-hexadecanethiol) or carboxylic acid-terminated (16-mercaptohexadecanoic acid) thiols on gold.

Chapter 2 gives details of experimental procedures for the formation and characterisation of SAMs (section 2.2.1), measurement of AFM cantilever spring constant and tip deflection (section 2.1.3), micromanipulation and attachment of microcapsule to AFM cantilever (section 2.1.2), extraction of leaf cuticles (section 2.2.2), preparation of buffer solutions (2.4) and apparatus used (section 2.1.1).

3.3 Results and discussion

3.3.1 Characterisation of SAMs

The gold surface upon which the thiols were adsorbed to make the SAMs was structurally elucidated using contact mode AFM imaging both before and after annealing the gold substrate at 350 °C for 6 hours. Typical images obtained are shown in Figure 3.3.

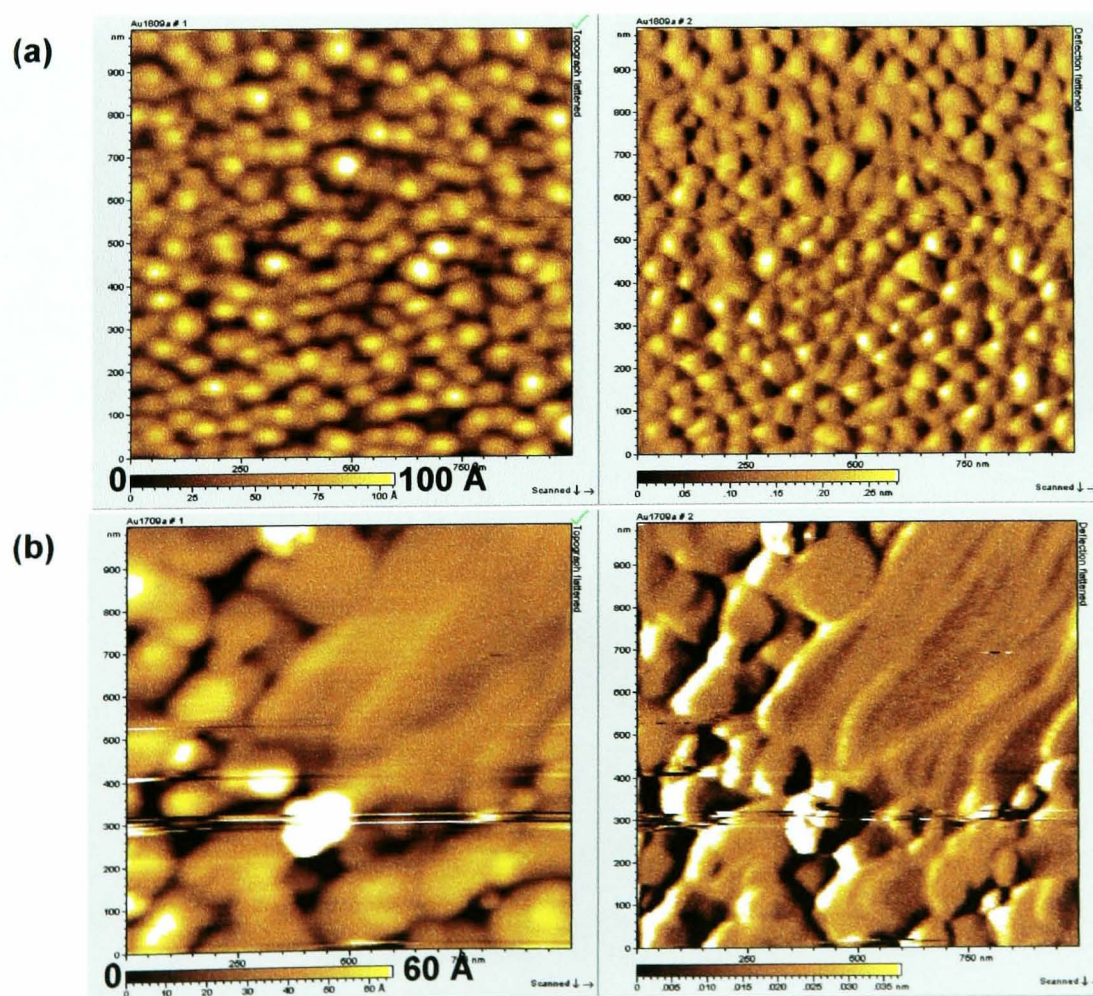


Figure 3.3 AFM images of (a) non-annealed gold surface and (b) a gold substrate annealed at 350 °C for 6 hours. Scan size 1 μm x 1 μm .

The gold islands increase in size significantly upon annealing. On the top surface of the islands the gold is atomically smooth. The overall height change of the surface is ca. 60 Å. Annealed surfaces are thus significantly better for producing SAMs with longer range order than non-annealed surfaces.

The SAMs were characterised using contact angle measurements. A drop of water was placed onto the surface of each SAM and the advancing contact angle was measured as the droplet spread over the surface of the SAM. Figure 3.4 shows how the wettability of the different SAMs changed as the functional end group of the monolayer was varied. Images shown are for SAMs formed from: (a) an ethanolic solution of 16-mercaptohexadecanoic acid ($\text{HS}(\text{CH}_2)_{15}\text{COOH}$); (b) an ethanolic solution made up of 50% COOH terminated and 50% CH_3 terminated (hexadecanethiol, $\text{HS}(\text{CH}_2)_{15}\text{CH}_3$) thiols; (c) an ethanolic solution of hexadecanethiol.

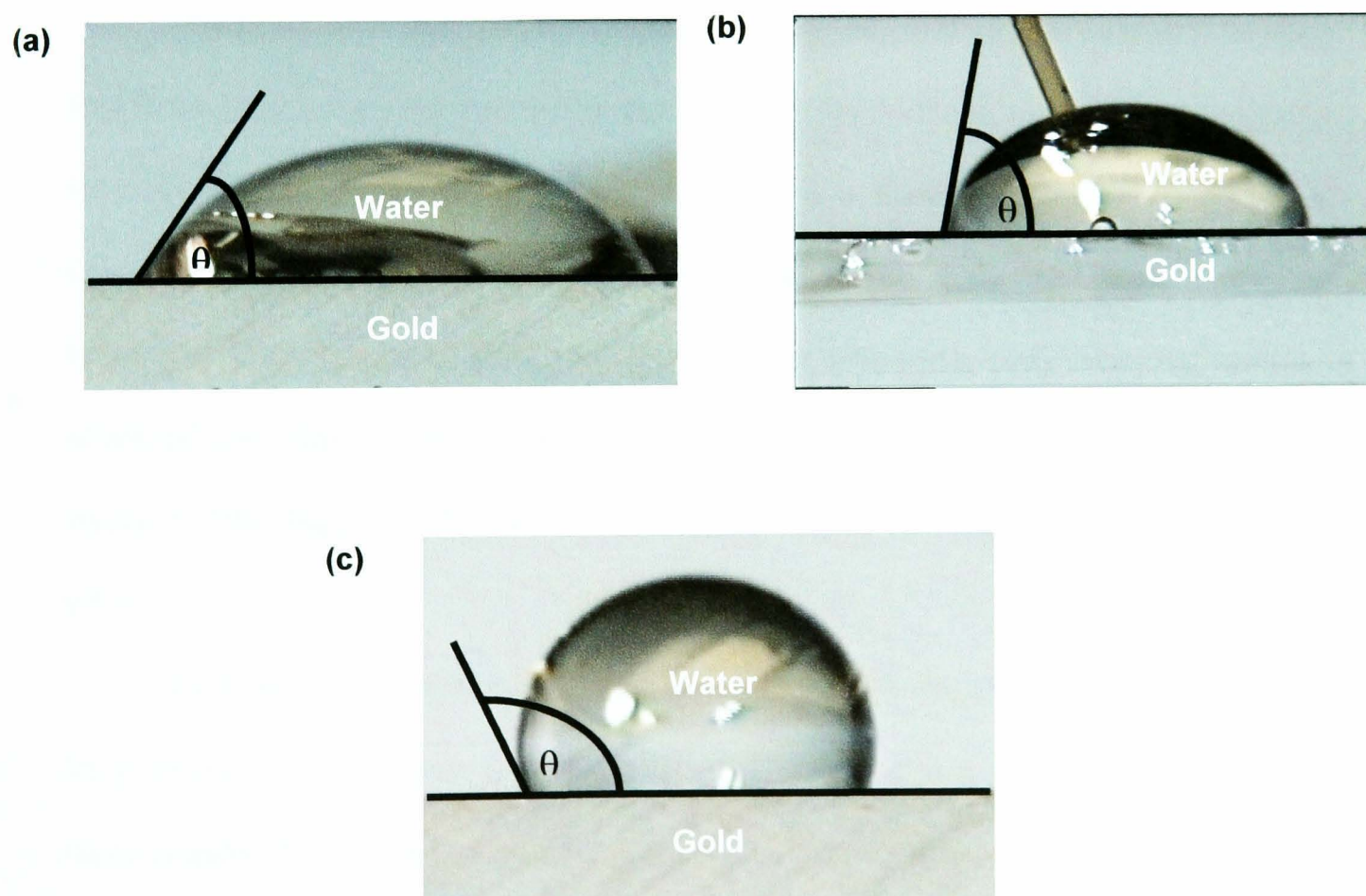


Figure 3.4 Images captured during enlargement of water droplet on (a) 100% -COOH terminated SAM, (b) 50% -COOH and 50% - CH_3 terminated SAM, (c) 100% - CH_3 terminated SAM. (θ = contact angle of droplet to surface).

From the above optical images it is apparent that as the concentration of $-\text{CH}_3$ terminated thiols on the surface of the monolayer increases, the contact angle increases, as the surface becomes increasingly hydrophobic. The actual contact angles measured are quoted in Table 3.1.

Table 3.1 Experimentally determined contact angle measurements.

% -COOH terminated thiols in original SAM solution	% -CH₃ terminated thiols in original SAM solution	Experimental contact angle measurement (°). Theoretical value in brackets.
100	0	56 (60-65) ²⁴
70	30	74
50	50	81
40	60	86
30	70	102
20	80	107
0	100	110 (109-112) ²⁴

There is good agreement between the experimental values obtained in these experiments and the values stated in the literature for 100% $-\text{CH}_3$, and 100% $-\text{COOH}$ terminated SAMs²⁴. Table 3.1 shows that there is a marked difference in the value measured for the contact angle when the concentration of $-\text{CH}_3$ terminated thiol in the bathing solution increased from 0 to 70%. Smaller differences were observed between solutions with high concentrations of $-\text{CH}_3$ terminated thiols (70-100%) in the bathing solution. This suggests competitive adsorption effects between the different types of SAM.

Bain and Whitesides carried out XPS studies³ on mixed monolayers of similar Au-thiol systems, *i.e.* thiols which had the same functional end groups but shorter alkyl chain lengths (C_{10}). They found that there was a marked difference between the mole fraction of each thiol in the bathing solution (from which the monolayer was formed)

and the mole fraction of thiol on the gold surface. This was attributed to preferential adsorption of the $-\text{CH}_3$ terminated molecules. The contact angle measurements reported here are consistent with this prior work: with a high mole fraction of $-\text{CH}_3$ terminated thiols in the bathing solution, there is little difference in the measured value of θ , which tends towards that of a pure $-\text{CH}_3$ terminated monolayer suggesting that this does, indeed, adsorb preferentially.

3.3.2 Characterisation of spring constants

In order to quantify the adhesion force between the microcapsule of interest attached to an AFM tip and a target surface (CFM) it is necessary to characterise the spring constant of the cantilever accurately. To establish the most effective method for spring constant determination, the added mass method (Cleveland *et al*²⁵) was compared to the thermal noise method (Hutter *et al*²⁶) for the same cantilevers.

For the added mass method, borosilicate spheres (diameter $14.5 \mu\text{m} \pm 1.0 \mu\text{m}$, density 2.52 g cm^{-3} , mass 4.0226 ng) were added, one at a time, to the cantilever and the resonance frequency, ν_0 , recorded as shown in Figure 3.5(a). A linear plot of added mass versus $1/(2\pi\nu_0)^2$ (see equation 1.3) shown in Figure 3.5(b), gave a straight line of gradient $7.15 (\pm 0.005)$ equating to $k = 0.072 (\pm 0.005) \text{ Nm}^{-1}$, and an intercept, $m_0 = 3.8 (\pm 0.1) \text{ ng}$.

The spring constant quoted by the manufacturer for this particular long, thick, silicon nitride cantilever was 0.12 Nm^{-1} . However the value should serve only as a guide. In particular, it assumes a uniform cantilever thickness across the wafer, which is often not the case during the microfabrication process of AFM probes. As k depends on t^3 (see equation 1.3), small variations in t can lead to a large change in k . The values

within which the spring constant should fall for a long, thick silicon nitride cantilever are 0.191 Nm^{-1} and 0.036 Nm^{-1} ²⁷.

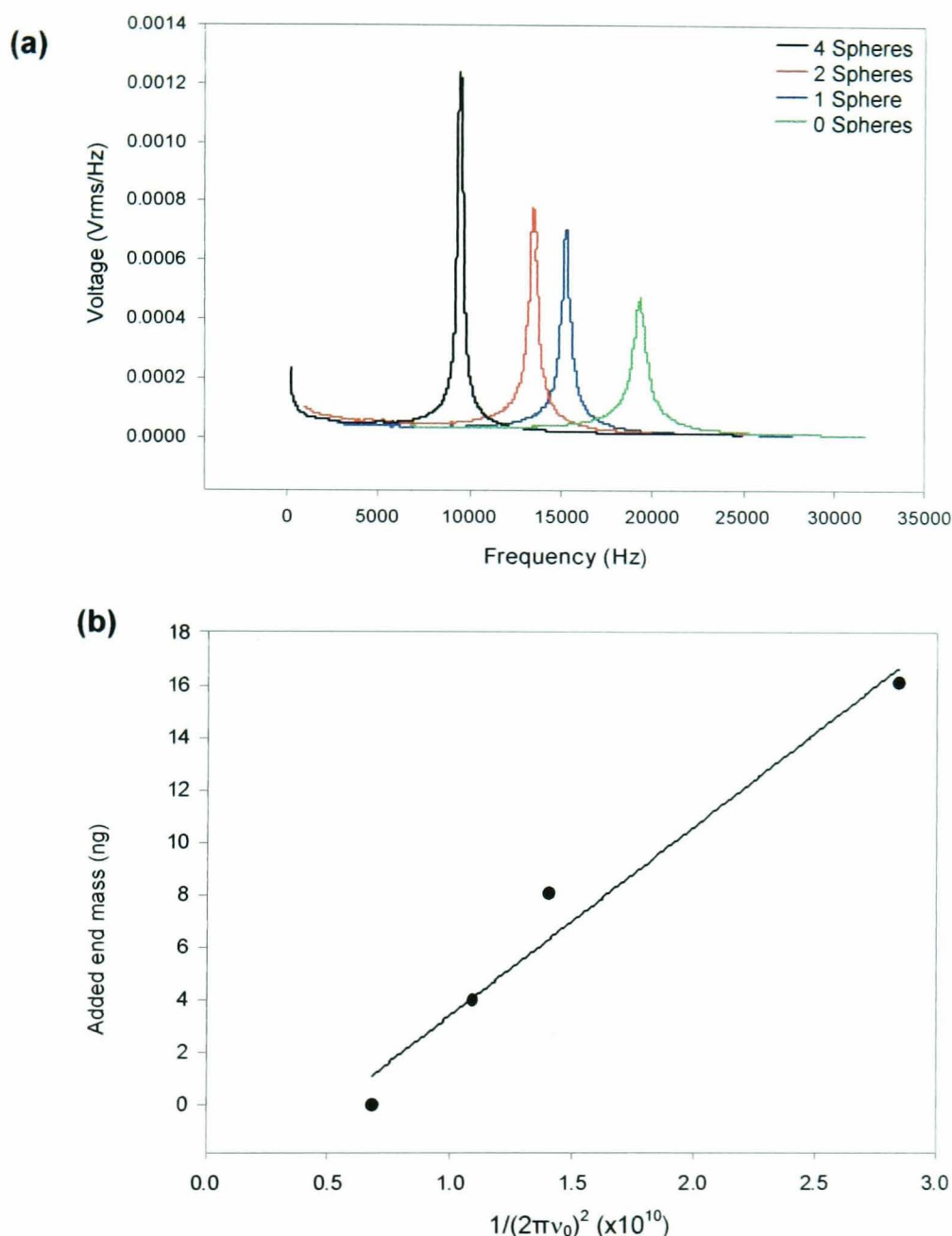


Figure 3.5 (a) The sequential frequency response of a silicon nitride cantilever with the addition of 4 borosilicate spheres. **(b)** The added mass of the spheres is plotted as a function of the resonance frequency to allow the determination of the spring constant and cantilever mass.

To assess the accuracy of the added mass method, it was compared to the thermal noise method. The latter methodology is far less time consuming, involving just one measurement parameter and without the need for micromanipulation.

For the thermal noise method, the thermal resonance frequency peak was identified for the same cantilever with no added spheres. The amplitude of the peak was converted to a length scale (nm). This was calculated using the tip deflection sensitivity

of the cantilever, which can be obtained from the gradient of the approach curve of AFM tip to a hard surface.

The resonance peak was then fitted to equation 3.1²⁸ using Origin lab:

$$A(\nu) = A_{dc} \frac{\nu_0^2}{\sqrt{(\nu_0^2 - \nu^2)^2 + \frac{\nu_0^2 \nu^2}{Q^2}}} \quad 3.1$$

where A_{dc} is the dc amplitude, Q is the quality factor and $A(\nu)$ is the amplitude response function.

The fit of equation 3.1 to the resonance peak was excellent as shown in Figure 3.6.

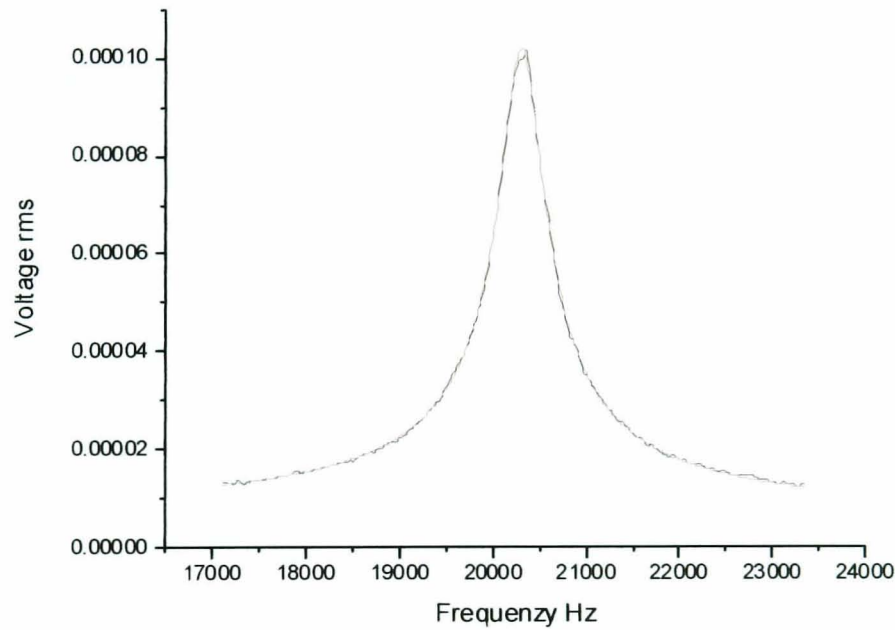


Figure 3.6 Graph showing the fit of equation 3.1 to the experimental thermal resonance peak obtained from a long thick silicon nitride cantilever.

From this fit, the parameters A_{dc} , Q and ν_0 were obtained which were then substituted into equation (3.2) to find the mean square cantilever displacement $\langle x^2 \rangle$:

$$\langle x^2 \rangle = \left(\frac{\pi}{2} \right) \nu_0 Q A_{dc}^2 \quad 3.2$$

The mean square cantilever displacement was then used to calculate the spring constant of the cantilever via equation 3.3:

$$k = \frac{k_B T}{\langle x^2 \rangle} \quad 3.3$$

where k_B is Boltzmann's constant, T is the absolute temperature and x^2 is the mean square displacement of the cantilever in any one mode.

Using this method, for the same short thick cantilever, a value of 0.107 (± 0.0005) Nm^{-1} was obtained which, again, falls within the manufacturer's guidelines for the long thick silicon nitride cantilever. As the results of these methods are relatively consistent, it was decided that the thermal noise method would be used in these studies for spring constant determination due to the ease of measurement.

3.3.3 SEMs of microcapsules attached to AFM cantilevers.

Figure 3.7 shows examples of scanning electron micrographs of microcapsule/cantilever assemblies taken after they have been used for force measurements and coated in a thin layer of gold. It is clear that the surface topography of the microcapsules varies considerably and this is taken into account when analysing the force data obtained. The diameters of the microcapsules used in these experiments ranged from 15-30 μm . All forces recorded in force measurements were normalised with respect to the radius of the microcapsule used in the experiments.

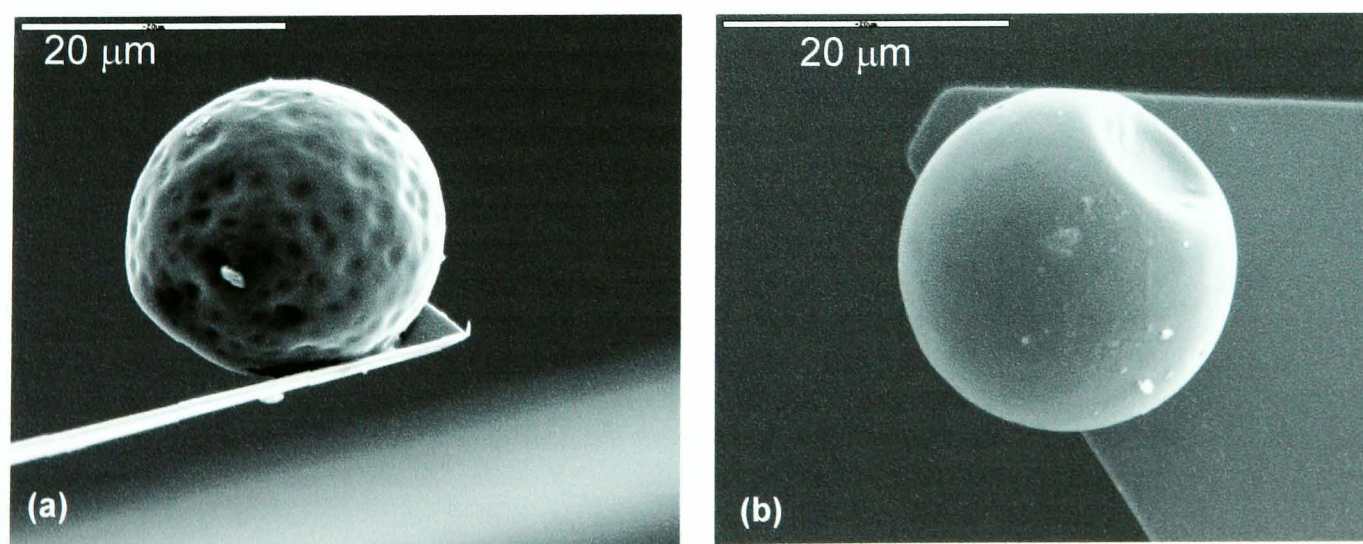


Figure 3.7 SEMs of microcapsules attached to silicon nitride AFM cantilevers using 5-minute epoxy. **(a)** sulfonate modified microcapsule used in force measurements. **(b)** alkyl modified microcapsule used in force measurements.

3.3.4 Force measurements between functionalised microcapsules and an -OH terminated SAM

In order to characterise the adhesion properties of functionalised microcapsules fully, over a range of pH, a SAM was used whose surface functionality would not vary over the pH range investigated. An -OH terminated SAM was chosen. Four sets of microcapsules, each with a different surface functionality were investigated. Figure 3.8 provides a schematic of the surface functionalities investigated.

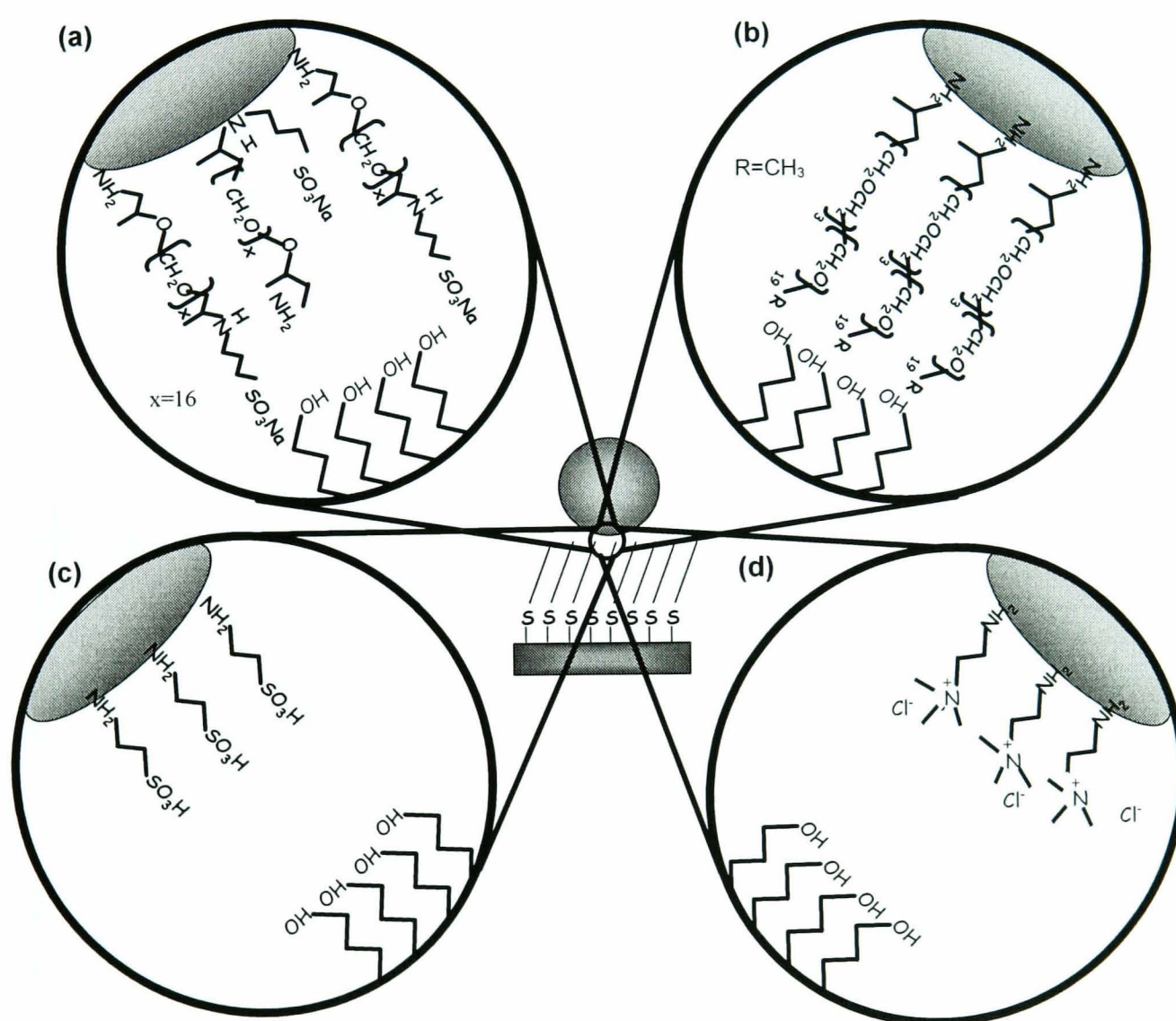


Figure 3.8 Schematic of the functional groups investigated in force measurements: (a) sulfonate modified microcapsule; (b) alkyl modified microcapsule; (c) anionic modified microcapsule; (d) cationic modified microcapsule.

Figure 3.9 shows a small selection of some of the force-distance curves recorded during these measurements. Figure 3.9(a) shows the adhesive behaviour of an alkyl-modified microcapsule (Figure 3.8b, Figure 3.7b) to an OH-terminated SAM over the pH range 4.7 - 9.94; Figure 3.9(b) shows the adhesive behaviour of a sulfonate (Figure 3.8a, Figure 3.7a) modified microcapsule to an OH-terminated SAM over the pH range 3.24 - 7.84. The structures of both modifier molecules are shown in Figure 3.1.

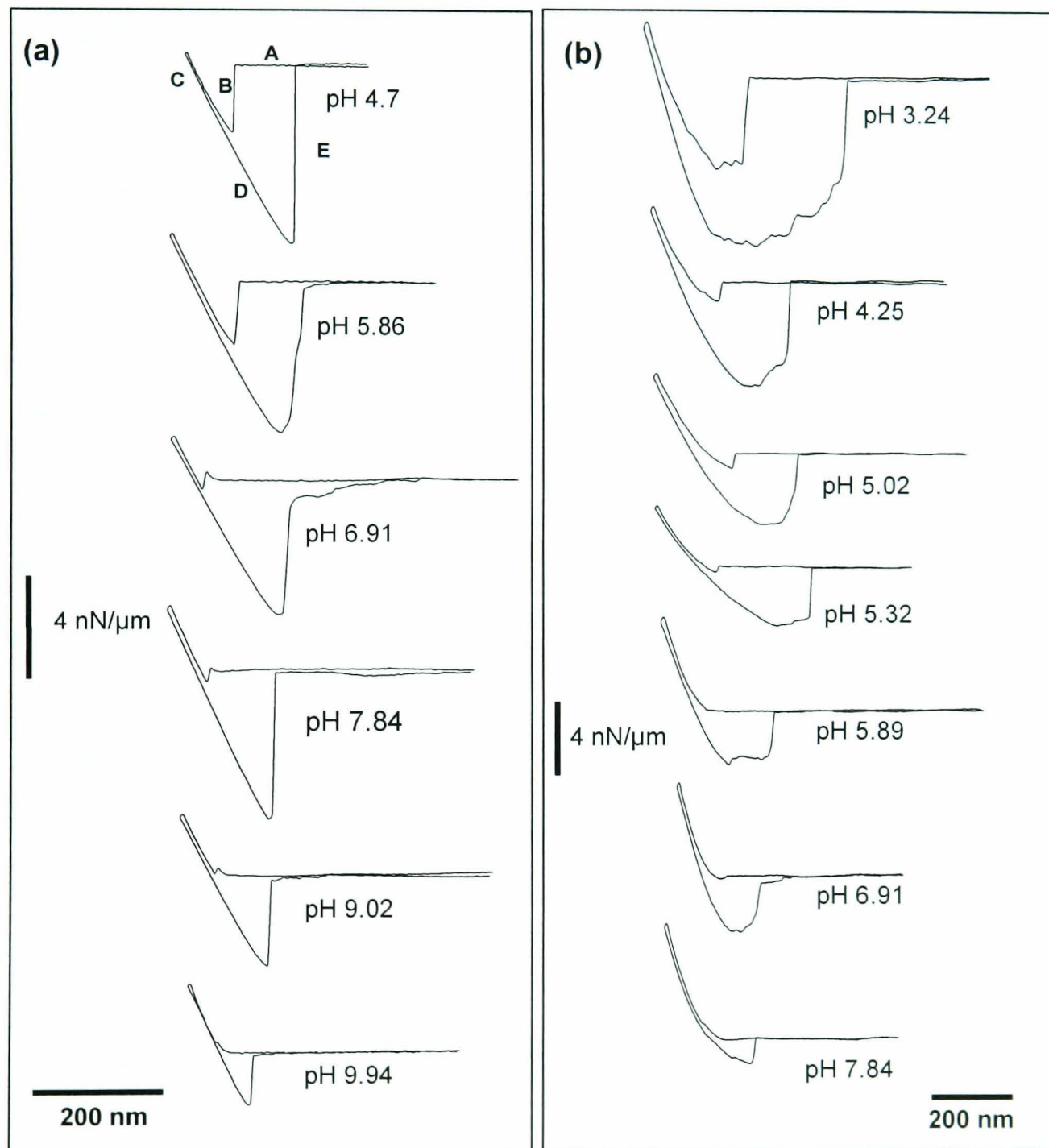


Figure 3.9 (a) Examples of force-distance curves for an alkyl modified microcapsule to an OH-terminated SAM at different pHs. (b) Examples of force-distance curves for a sulfonate-modified microcapsule to an OH-terminated SAM at different pHs. Forces are all normalised with respect to the radius of the microcapsule studied.

Considering the first force-distance curve in Figure 3.9(a), recorded at pH 4.7, the cantilever/microcapsule assembly is brought towards the SAM (A) and when the attractive force exceeds the spring constant of the cantilever, the microcapsule will 'jump into contact' with the substrate (B). The cantilever is then pressed into the surface (C) before being drawn back away from the SAM substrate. The microcapsule adheres to the substrate past the initial point of contact (D) before breaking free from the surface (E). The deflection of the cantilever over the distance travelled is recorded and converted into a force which is normalised by the particle radius, r , and the normalised force vs distance curve shown is produced.

The force-distance curves in Figure 3.9 show that there is strong adhesion of the microcapsule to the surface of the SAM. We believe that the strong adhesion observed in the case of these two types of microcapsules is due to ethylene and propylene oxide groups present in the modifier molecules reacted into the walls of the microcapsule, hydrogen bonding with the OH groups terminating the SAM as demonstrated in the schematic in Figure 3.10.

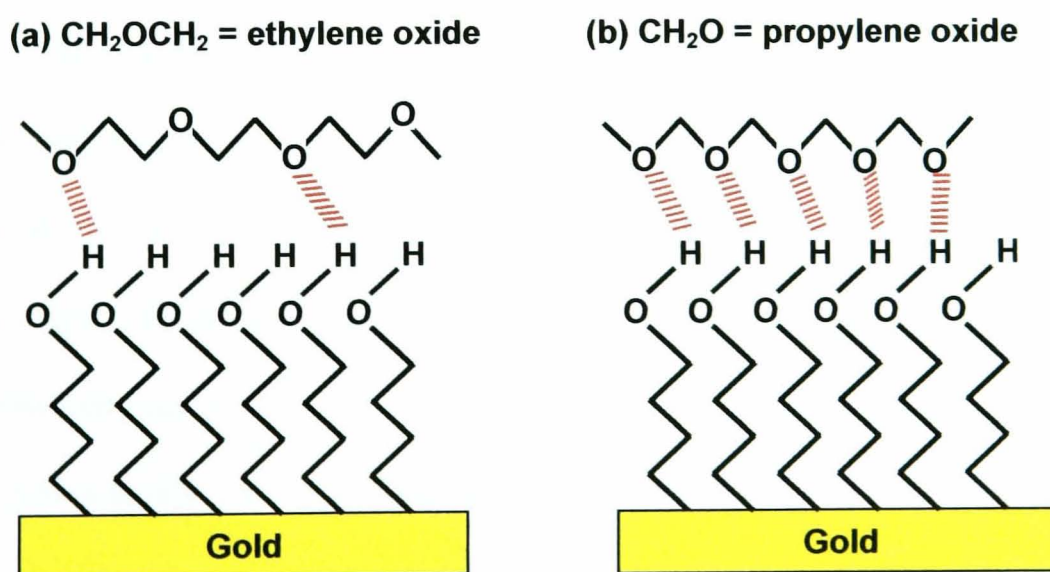


Figure 3.10 Schematic representation of hydrogen bonding between ethylene oxide and propylene oxide groups present in modifier molecules on the surface of the sulfonate and alkyl modified microcapsules with OH-terminated SAM.

The adhesion observed for the alkyl modified microcapsule over the pH range studied is ca. $2\text{ nN}\mu\text{m}^{-1}$ greater than the sulfonate modified capsule. This is probably due to the greater number of ethylene and propylene oxide groups present in the modifier molecule which are capable of hydrogen bonding with the SAM.

The large area of microcapsule in contact with the SAM means that there are multiple interactions between the surface groups on the wall of the microcapsule and the SAM, as many interacting groups are in contact. Multiple interactions are evident for the sulfonate modified microcapsule (Figure 3.9(b)) with a long, drawn out pull-off force observed. However, a much sharper pull off force is observed for the alkyl modified microcapsule.

The drawn out pull off force observed in the force-distance curves in Figure 3.9(b) for the sulfonate microcapsule could be explained in relation to the capsules outer surface topography, elasticity and the modifier molecules located on the surface of the capsule. The most dominant factor of these is most likely to be the topography of the surface of the microcapsule. Figure 3.7 shows SEMs of the (a) sulfonate modified and (b) alkyl modified capsules taken after measurement has been made. It is apparent from these images that the surfaces of the capsules studied vary considerably.

The sulfonate modified capsule has an extremely pitted or dimpled surface which would cause bonds made with the OH-terminated SAM to break at different points upon withdrawal of the cantilever-capsule assembly from the surface leading to the multiple interactions observed in the pull off force. The alkyl modified capsule however has a much smoother surface meaning any area in contact with the SAM will not be pitted leading to a much sharper pull off force observed during withdrawal.

Another factor which may have a significant effect on the normalised force-distance curves measured is the elasticity of the wall of the capsule studied. The

elasticity of the wall of the capsule will affect the contact area of the capsule with the surface. If the wall is very elastic, as the cantilever-capsule assembly is brought down onto the surface and pressed against it, the capsule will exhibit increased deformation leading to different contact areas of the capsule with the substrate. The elasticity of the capsule can be estimated from the original deflection-distance data obtained. The closer the gradient of the force curve is to 1, the less deformation is occurring upon compression. The gradient of deflection-distance curves for both the alkyl-modified and the sulfonate-modified microcapsules studied are similar to each other but they are considerably less than one indicating deformation upon compression. This will cause the contact area of capsule with substrate to increase significantly for both capsules leading to multiple interactions.

A minor factor which may also affect the shape of the pull off force is the structure of the modifier molecules located on the surface of the capsules. The sulfonate modifier molecule has the ability to bind into the microcapsule wall via two points in its structure during the microencapsulation process (see Figure 3.1). The modifiers bind into the wall of the microcapsule via the NH_x group in the structure, so in the case of the sulfonate modifier, either the NH_2 group at the end of its chain or the NH group in the middle. This leaves the possibility of three differently functionalised modifier chains exposed to the surface of the SAM (Figure 3.8(a)). As the microcapsule is drawn away from the surface of the SAM, bonds formed between each of the chains and the SAM break at different points giving the drawn out pull off force observed in these measurements.

The alkyl modifier molecule only has one NH_x group within its structure which can bind into the polymeric wall of the microcapsule. Therefore a 'cleaner' pull of force is expected as shown here as the modifier chains are of the same length and

composition. However, the lengths of the modifier molecules are extremely short compared to the dimples in the microcapsule surface meaning that the pull off force will be mainly affected by the surface of the capsule rather than the modifier molecule attached to the surface.

Figure 3.11 shows the adhesive force measured between an alkyl modified (•), sulfonate modified (•) and unmodified (•) microcapsule to an OH terminated SAM over a range of pH (2-11). Differences in the relative magnitude of the adhesion force were observed between the three types of microcapsule. The error bars shown represent the distribution of forces over the 300 force measurements made per pH step.

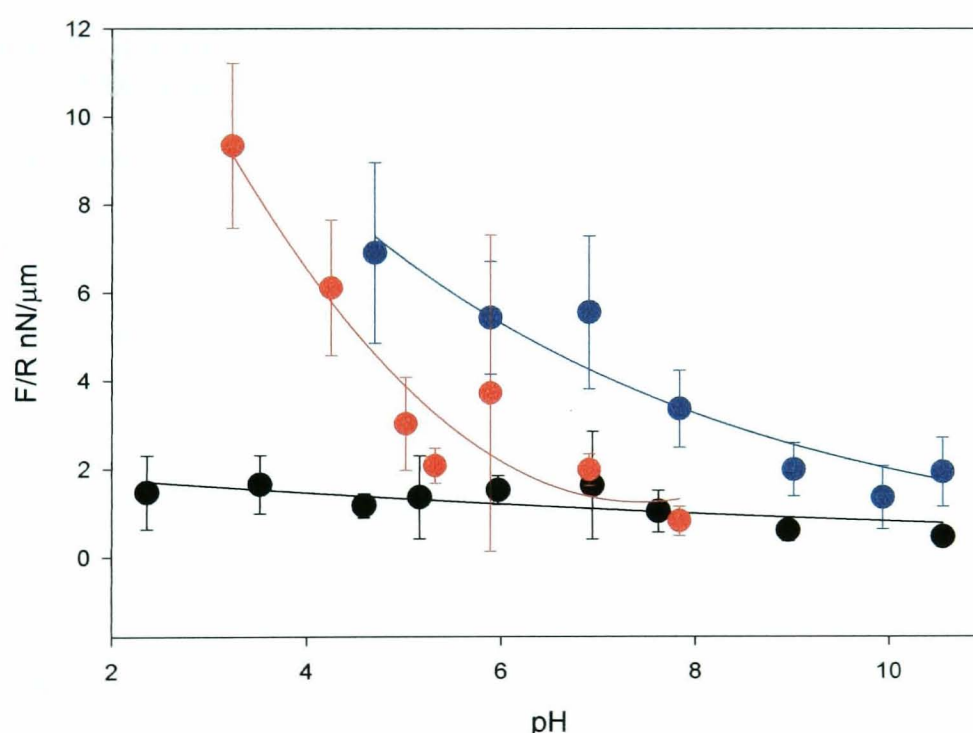


Figure 3.11 Force titration showing adhesion forces normalised with respect to the radius of microcapsule to an OH-terminated SAM for an alkyl (•), sulfonate (•) and an unmodified (•) microcapsule.

A significantly larger adhesive force is measured between the modified microcapsules and OH-SAM compared to the unmodified microcapsule at all the pH's especially in the lower range. The fact that an adhesive force is observed when looking at the adhesion of the unmodified microcapsule to the OH-terminated SAM suggests some interaction between the aromatic wall of the microcapsule and the OH-terminated SAM. The structures of the monomers which make up the wall of the capsules are shown in Figure 3.12 along with a representative sample of the structure of the wall.

The shape of the force titration curve is similar for all three types of capsules with larger adhesion observed between microcapsule and substrate at low pH compared to high pH.

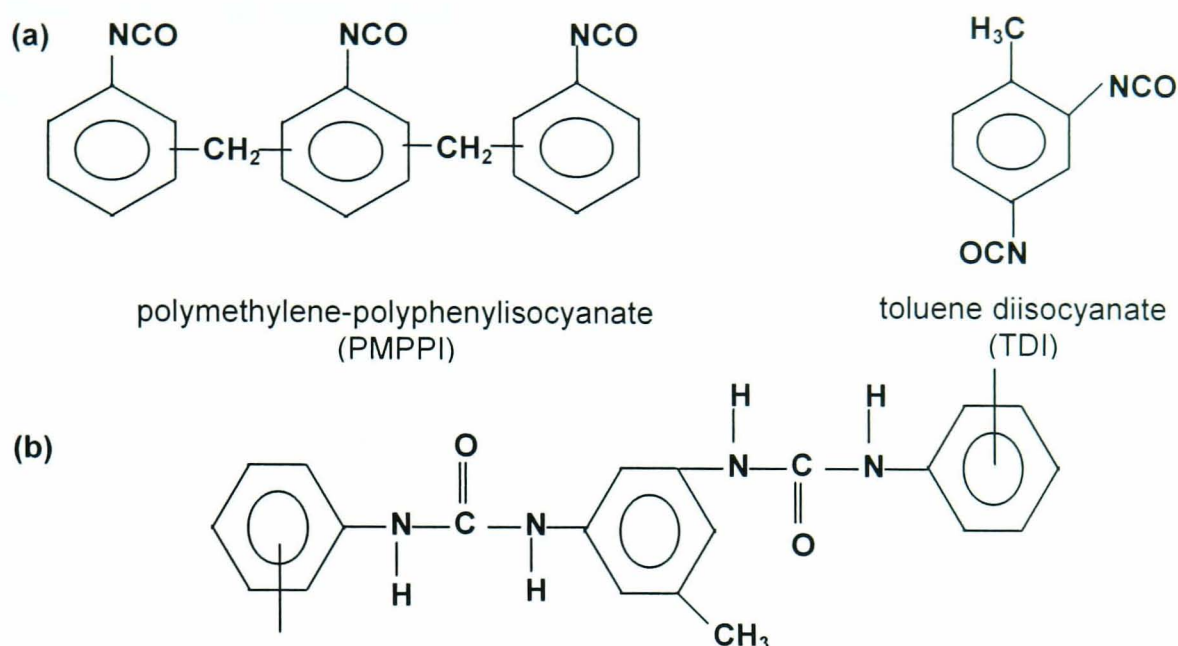


Figure 3.12 (a) Monomers used in the polyfunctional isocyanate microcapsule system **(b)** Representative portion of microcapsule wall structure.

The adhesion observed between the unmodified microcapsule wall and the OH-terminated SAM is due to the fact that there are hydrogen bonding groups exposed on the surface of the polymer wall which are capable of interacting with the OH functional groups which terminate the SAM. The fact that for each of the capsules, enhanced adhesion is observed at low pH suggests that at low pH the cross linking within the microcapsule starts to break up leading to an increased number of hydrogen bonding groups which are exposed to the SAM which would lead to greater adhesion.

The difference in the magnitude of the adhesive force between modified and non-modified microcapsules could be due to the presence of ethylene oxide and propylene oxide groups in the modifier molecules, hydrogen bonding with OH groups terminating the SAM. Multiple interactions cause the microcapsule to adhere to the surface past the initial point of contact; the adhesive force recorded and shown here represents the breaking of multiple interactions as the microcapsule is pulled off the SAM.

The gradient of the force titration curves obtained for the three systems studied varies as well. A much sharper increase in adhesive force measured is observed with the sulfonate modified microcapsule at approximately pH 5 whereas with the other two microcapsules, a gradual increase in adhesion is observed as the curve runs from high to low pH.

This sharp increase in adhesion at low pH could be due to partial protonation of the sulfonate group terminating the modifier molecule. The difference in the acid-base behaviour of functional groups incorporated on a surface compared to that of the same functional group on a molecule in solution is a key feature of the surface chemistry of hydrogen bonding. A factor which needs to be taken into account is the fact that the solution pH (measured here) and the surface pH are not the same as the surface pH is shifted relative to the bulk value by the presence of surface potential^{29,30}. Generally this shift is small less than 0.5 pH units. This does mean however, that the solution pH at which exactly half the surface groups are ionised, $pK_{1/2}$, does not represent the surface pK_a .

It should also be taken into account that the surface pK_a should be expected to shift relative to the solution phase. The limited ability of the solvent to shield charge species at the interface compared to solution and in-plane hydrogen bonding between molecules on the surface should both increase the difficulty in ionising surface bound species³¹. This would lead to an upward shift in the surface pK_a value relative to the solution phase for acidic groups and a downward shift for basic groups.

From this force titration data, a surface $pK_{1/2}$ of the microcapsule can be estimated (at the pH of the sharp increase in adhesion) as ~ 4 . This result is much higher than for a sulfonate group attached to a freely dissolving species. Here the pK_a is 1.5²⁹. However, it has been shown that the $pK_{1/2}$ of a sulfonate group attached to a surface is

higher than when free in solution³¹. In this study the chemical force titration method was used to determine the surface $pK_{1/2}$ of sulfonic acid modified poly(dimethylsiloxane). This study indicated a $pK_{1/2}$ value of 3.0 ± 0.5 . However, the result seen here is still higher than expected for a surface group. This could be due to the fact that the modifier molecule could bond to the wall of the microcapsule via either one of the two NH_x group in the structure (see Figure 3.8(a)). This would expose not just the sulfonate group to the SAM but an NH_2 group which may cause the surface pK_a to increase further than expected.

Figure 3.13 shows the variation in the size of the ‘jump to contact’ portion of the force-distance curves measured for the sulfonate and alkyl modified microcapsules to the OH-terminated SAM. A similar trend to the force titration curves recorded for the adhesive forces is observed here with a general increase in the size of the force observed from high to low pH. The shapes of these curves are also similar with the alkyl modified microcapsule system having a gentle slope over the pH range studied whereas the sulfonate modified microcapsule shows a sharp increase in the size of this force at approximately pH 5 once again suggesting that the sulfonate group on the microcapsule becomes partially protonated, interacting with the OH groups of the SAM.

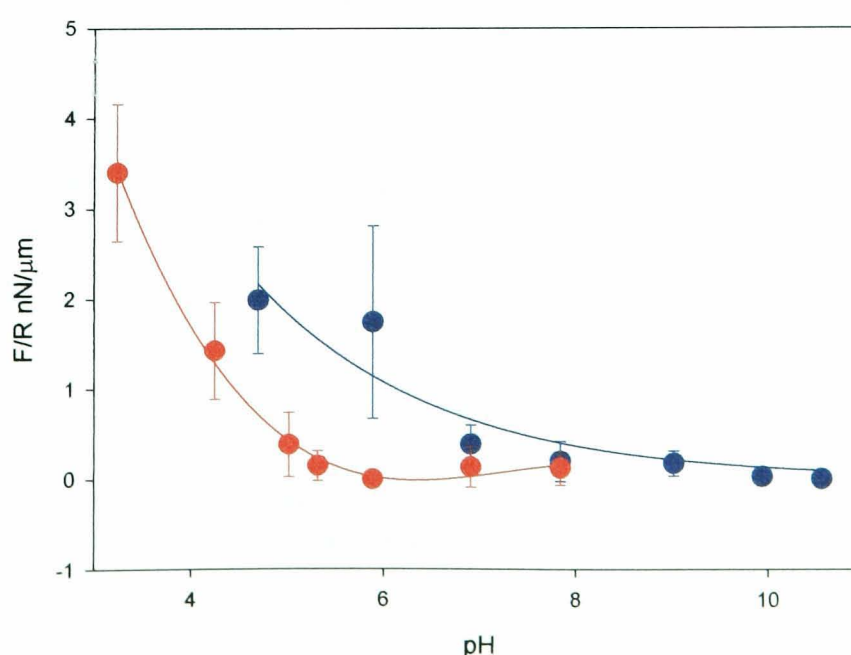


Figure 3.13 Force titration showing ‘jump to contact’ forces observed in adhesion measurements normalised with respect to the radius of microcapsule to an OH-terminated SAM for an alkyl (●) and a sulfonate (●).

The adhesion characteristics of the cationic modified microcapsule to an OH-terminated SAM, compared to an unmodified microcapsule (Figure 3.14), are similar (the functional groups exposed to one another in these measurements are shown in 3.8 (d)). The increase in adhesion from high to low pH is once again seen for these microcapsules providing further evidence for the disruption of the cross linking within the polymer wall at low pH. However, the anionic modified microcapsule exhibited virtually no adhesion over the entire pH range studied. This could be due to in-plane hydrogen bonding between the sulfonate groups of the modifier molecules effectively shielding the wall of the microcapsule from the SAM. The forces seen in all of these experiments are significantly smaller (0-3 nN) than those observed for the sulfonate and alkyl modified microcapsules to the OH-terminated SAM (1-10 nN) and this is due to the absence of ethylene and propylene oxide groups enhancing the hydrogen bonding capabilities of the microcapsule wall with the SAM.

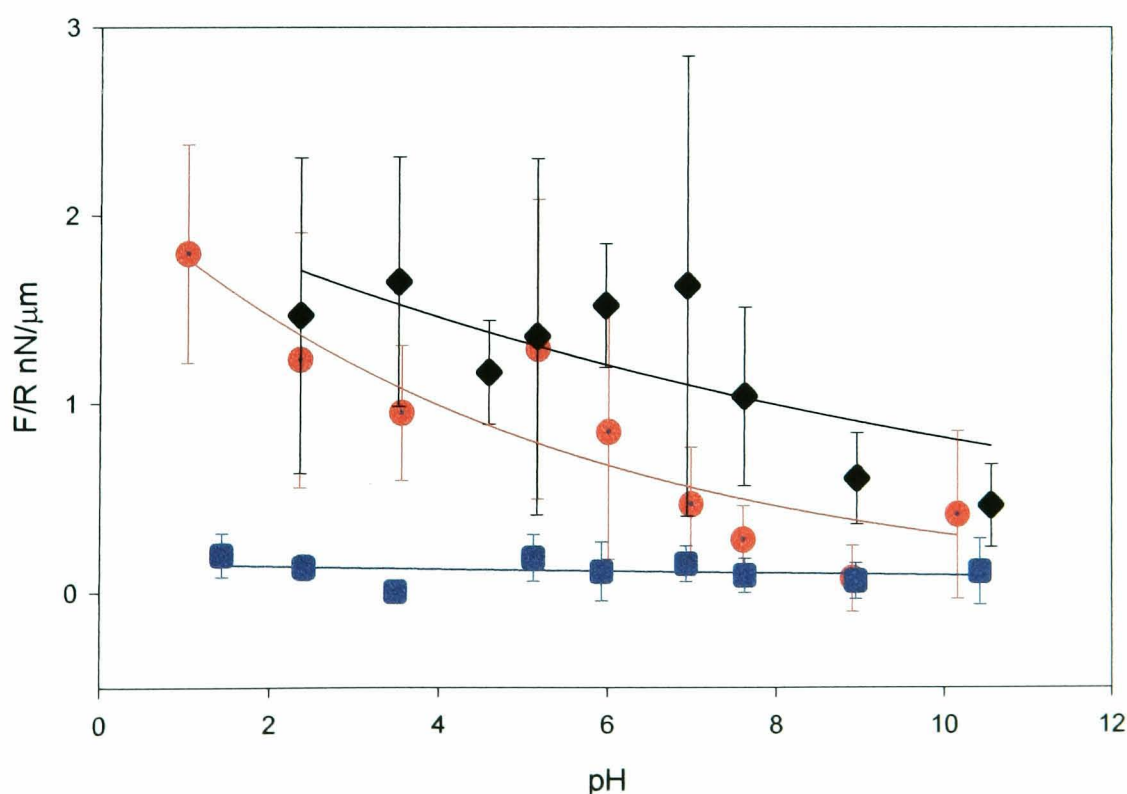


Figure 3.14 Force titration showing adhesion forces normalised with respect to the radius of microcapsule to an OH-terminated SAM for a cationic (●), anionic (■) and an unmodified (◆) microcapsule.

3.3.5 Force measurements between functionalised microcapsules and SAMs of differing functionality

Figure 3.15 shows a comparison of the adhesive forces observed between the sulfonate (a) and alkyl (b) modified microcapsules to an OH-terminated SAM (■) and a CH₃ terminated SAM (●) as a function of pH. For both the alkyl and sulfonate modified microcapsules, there is a large difference observed in the magnitude of the adhesive force measured between the two substrates with a much larger adhesive force recorded to the OH-terminated SAM than the CH₃-terminated SAM.

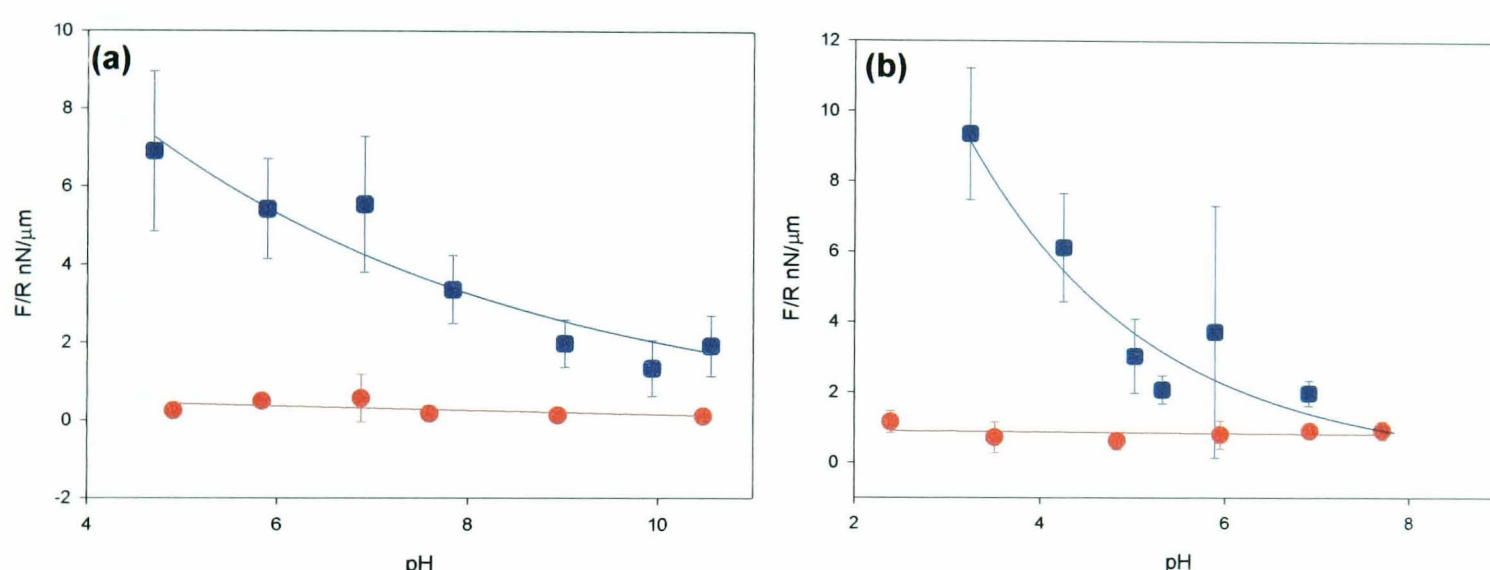


Figure 3.15 (a) Force titration showing adhesion forces normalised with respect to the radius of a sulfonate modified microcapsule to an OH-terminated SAM (■) and a CH₃ terminated SAM (●). **(b)** Force titration showing adhesion forces normalised with respect to the radius of an alkyl modified microcapsule to an OH-terminated SAM (■) and a CH₃ terminated SAM (●).

These results provide further evidence that the increased adhesion observed between these sulfonate and alkyl modified microcapsules to the OH-terminated SAM is due to the hydrogen bonding of the ethylene and propylene oxide groups in the modifier molecules. The CH₃ terminated SAM is hydrophobic so little, if any, interaction between the hydrophilic groups in the modifier molecules and the SAM is expected.

In order to simulate the surface of a leaf, a mixed monolayer was formed from a solution consisting of 70:30 CH₃: COOH-terminated alkyl thiols. According to XPS studies by Bain and Whitesides^{5,6} an ethanolic bathing solution containing this

proportion of alkyl thiols should give a surface coverage of approximately 15% COOH terminated alkyl thiol and 85% CH₃ terminated alkyl thiol. This mainly hydrophobic surface represents the actual proportion of hydrophilic/hydrophobic sites on the surface of a leaf cuticle³², the ultimate substrate of interest.

Comparing force titration data for the adhesion of, for example, the alkyl and sulfonate modified microcapsules to a mixed SAM and a CH₃ terminated SAM as shown in Figure 3.16, it is apparent that there is very little difference, within error, in the adhesive force measured between the two surfaces. For both types of capsule, if an enhanced adhesion was observed between the mixed SAM and the capsules, this may suggest a greater proportion of hydrophilic sites present on the monolayer capable of hydrogen bonding with the propylene and ethylene oxide groups present in the modifier molecules of the microcapsules. As it is, an enhanced adhesion was not observed suggesting that, as expected, the SAM is predominantly hydrophobic.

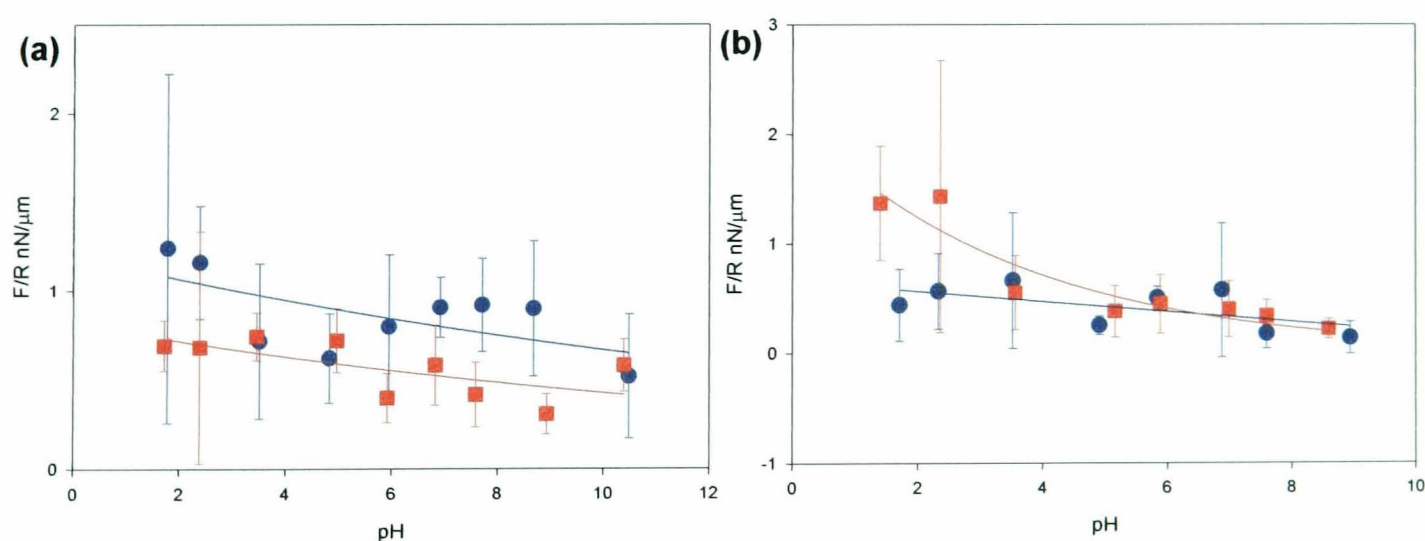


Figure 3.16 (a) Force titration showing adhesion forces for a sulfonate modified microcapsule to an CH₃-terminated SAM (●) and a mixed 70:30 CH₃:COOH terminated SAM (■). **(b)** Force titration showing adhesion forces for an alkyl modified microcapsule to an CH₃-terminated SAM (●) and a mixed 70:30 CH₃:COOH terminated SAM (■).

There is some debate in the literature over the existence of phase separation in mixed SAMs^{3,6,33-35}. It has been suggested that should phase separation occur, the

macroscopic, single component domains of the two components of the monolayer will occur as islands which are a few tens of angstroms across in size³. Due to the size of the microcapsule used in these measurements ($r \approx 8 \mu\text{m}$) the area of the capsule which is in contact with the surface during force measurements is much greater than a few tens of angstroms. This means that the capsule will not be able to detect specifically regions of homogeneous hydrophobicity or hydrophilicity.

Adhesion measurements were made to various sites on the surface of the SAM and at each pH studied; the adhesion observed remained constant within error. This indicates that there are no large areas of hydrophilic sites present on the surface of the SAM and for the purpose of these studies; the functionality of the surface is largely heterogeneous. Examples of force curves measured at different sites on the SAM are shown in Figure 3.17.

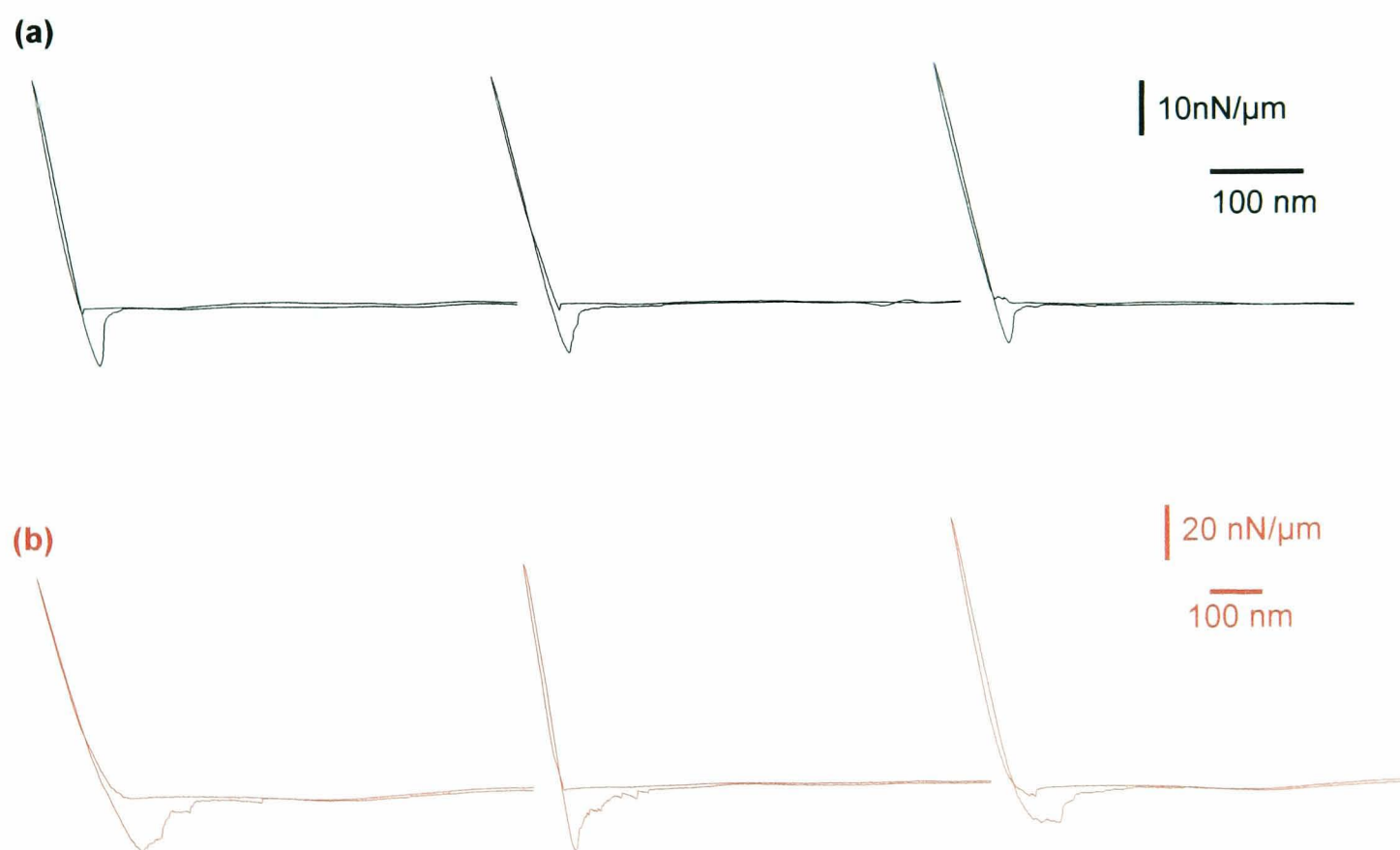


Figure 3.17 Examples of force distance curves for (a) a sulfonate modified microcapsule and (b) an alkyl modified microcapsule to a 70:30 CH_3 : COOH mixed SAM at 3 different sites on the surface of the SAM.

3.3.6 Force measurements between functionalised microcapsules and a leaf cuticle

Force measurements were made between the alkyl, sulfonate, cationic and unmodified microcapsules to a leaf cuticle which had been extracted from a leaf of the *Prunus laurocerasus* as detailed in section 2.2.2. Details of the force titration behaviour for each of these capsules are shown in Figure 3.18.

The most noticeable observation from these sets of data is that the forces observed in these measurements are extremely small ≤ 1 nN/ μ m. There is far more irregularity with the distribution of the magnitude of forces measured over the pH range studied for the cuticle compared to the measurements made to the SAMs which have more uniform surface topography and functionality. There is still enhanced adhesion observed for the alkyl and sulfonate modified microcapsules relative to the cationic and blank modified microcapsules but this enhanced adhesion is distributed over the entire pH range studied, perhaps increasing slightly at low pH in the case of the alkyl and sulfonate modified microcapsule.

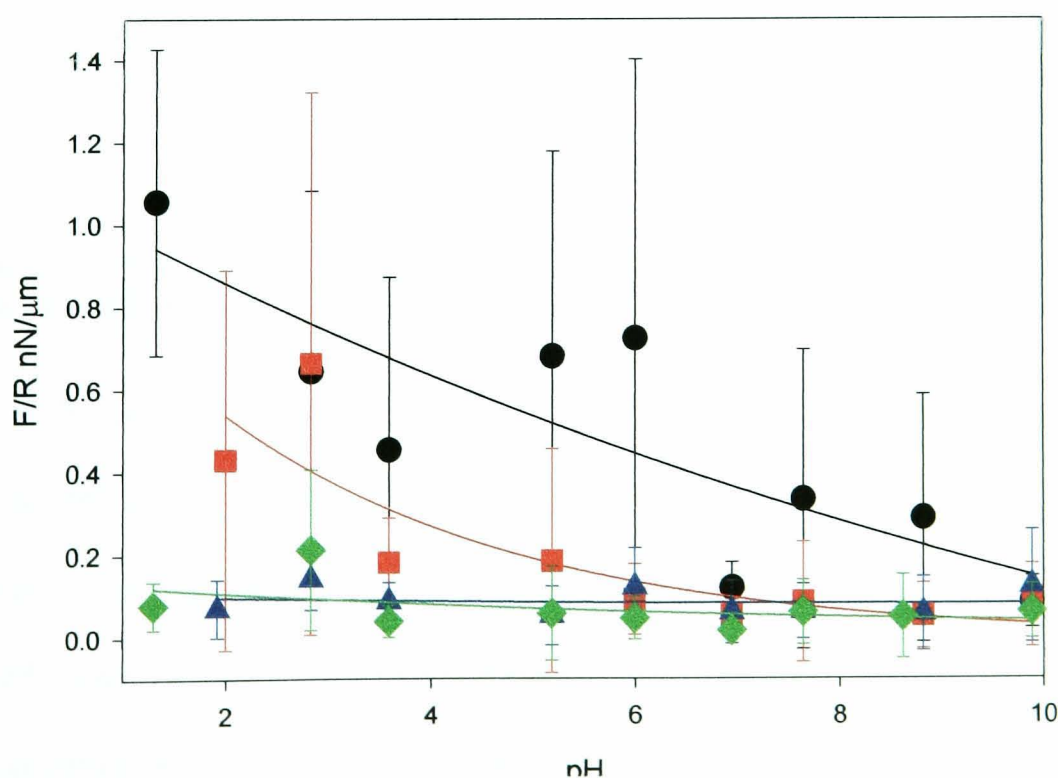


Figure 3.18 Force titration showing adhesion forces normalised with respect to the radius of microcapsule to a cuticle of the *Prunus laurocerasus* leaf for an alkyl (●), sulfonate (■) cationic(◆) and an unmodified (▲) microcapsule.

The reason for the irregularity in the force measurements between the microcapsules and the leaf cuticle is the inhomogeneity of the functionality of the surface of the leaf. It appears that there are areas of hydrophilic sites interspersed between the large hydrophobic domains. Figure 3.19 shows examples of force curves measured between an alkyl modified microcapsule and the leaf cuticle. All measurements were carried out at the same pH but at different areas on the surface of the leaf cuticle.

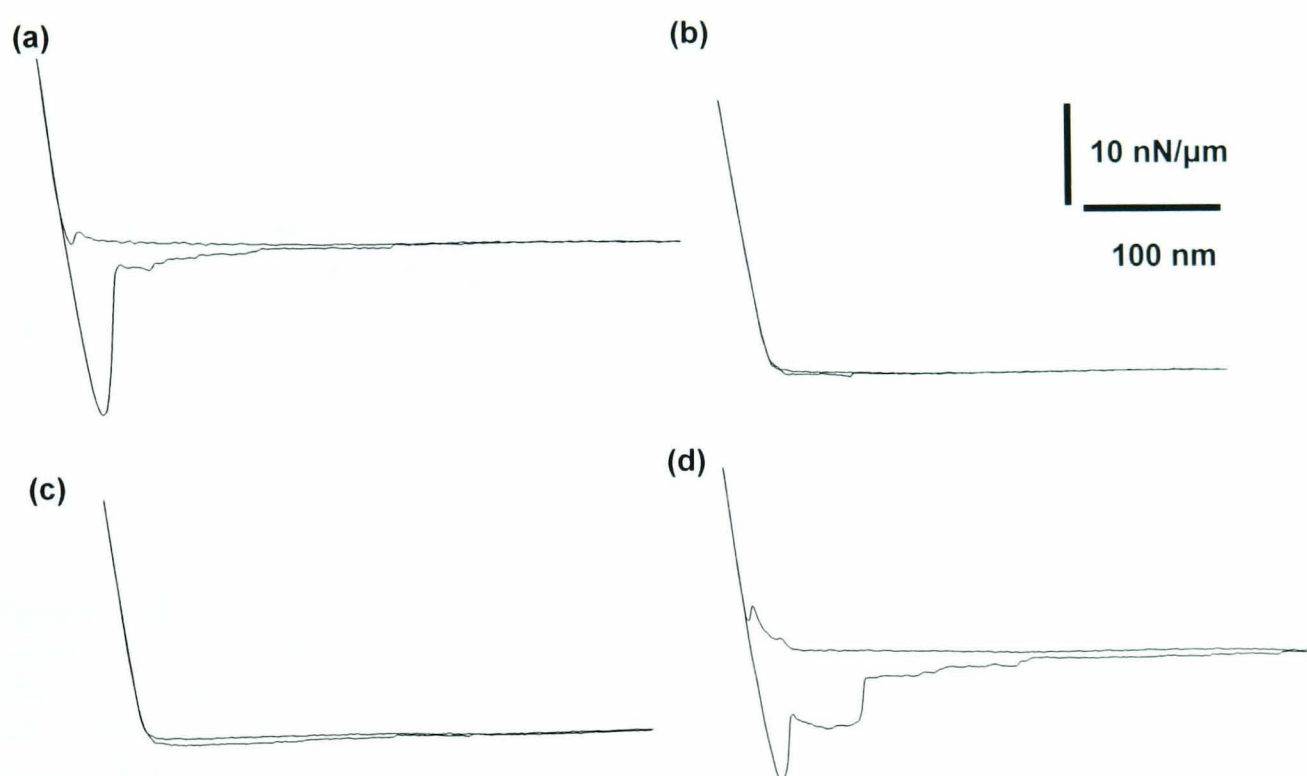


Figure 3.19 Examples of force distance curves of an alkyl modified microcapsule to a leaf cuticle all measured at the same pH at 4 different locations on the cuticle surface.

It is apparent from these measurements that there are areas of hydrophobicity and hydrophilicity on the leaf surface. The hydrophilic sites cause the ethylene and propylene oxide groups within the modifier molecules on the alkyl and sulfonate modified microcapsules to hydrogen bond with the leaf leading to the enhanced adhesion observed in Figure 3.19 (a) and (d). These areas of enhanced adhesion were

not observed for the cationic and blank microcapsules which do not have hydrogen bonding groups present on the surface of their polymeric walls. The adhesion forces measured between these capsules and the leaf cuticle were extremely small ≤ 0.4 nN/ μ m.

There is good agreement however between the magnitude of the average force measured between the microcapsule and the leaf and the mixed SAM. Figure 3.20 shows a comparison of force titrations measured for the alkyl and sulfonate capsules to the leaf and the mixed SAM.

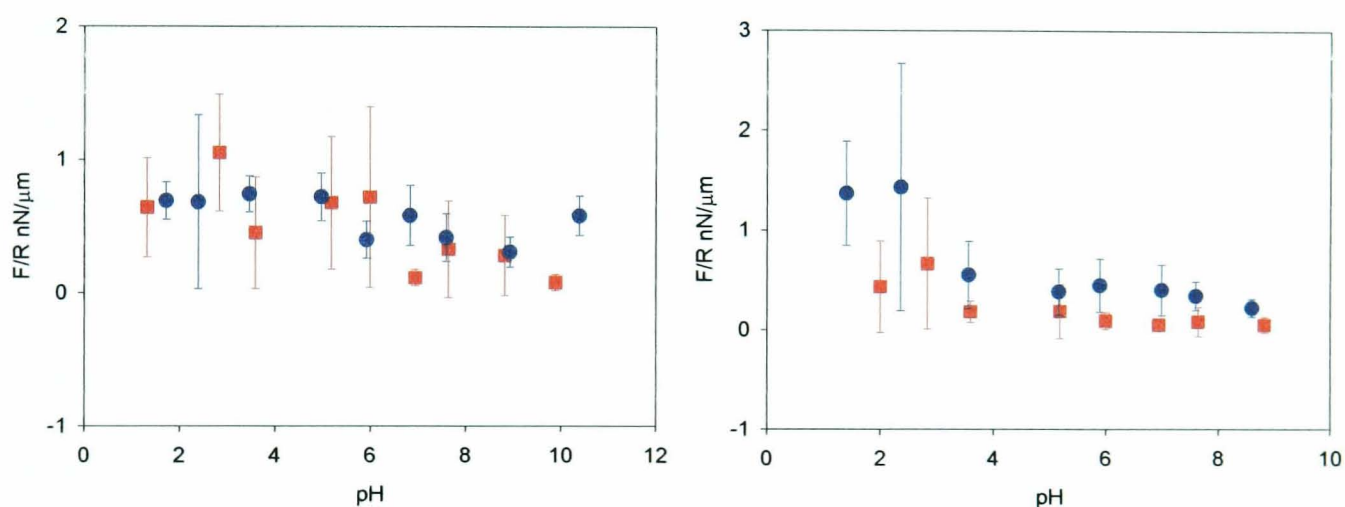


Figure 3.20 (a) Force titration showing adhesion forces normalised with respect to the radius of a sulfonate modified microcapsule to a leaf cuticle (■) and a mixed 70:30 $\text{CH}_3\text{:COOH}$ terminated SAM (●). **(b)** Force titration showing adhesion forces normalised with respect to the radius of an alkyl modified microcapsule to a leaf cuticle (■) and a mixed 70:30 $\text{CH}_3\text{:COOH}$ terminated SAM (●).

These graphs demonstrate the agreement between the magnitudes of forces measured. The forces measured to the SAM are much less irregular than to the cuticle and this is due to the dispersion of hydrophilic alkyl thiol groups over the whole surface of the SAM not separated into domains as appears to be apparent for the surface of the leaf cuticle.

3.4 Conclusions

AFM has been used for the first time to investigate the adhesion properties of functionalised polymeric microcapsules. It has been shown that microcapsules whose

surfaces have been modified with molecules containing ethylene and propylene oxide functional groups experience increased adhesion to an OH-terminated SAM. Factors affecting the shape of the pull-off force in the force-distance curves for all microcapsules studied include the surface topography of the capsule and its elasticity.

The surface $pK_{1/2}$ of the sulfonate modified microcapsule was estimated to be ca. 4. This value is higher than expected due to the variety of functional groups exposed to the surface in these adhesion measurements.

The microcapsules whose surfaces were modified with molecules not containing ethylene or propylene oxide groups exhibited similar adhesion to the OH-terminated SAM as the unmodified capsule. Further evidence was gained towards the theory that hydrogen bonding was occurring between the OH-terminated SAM and the ethylene and propylene oxide groups when adhesion measurements were made using the same capsules to a CH_3 -terminated SAM. In this case only a small adhesive force was observed over the pH range studied.

Measurements were made to a mixed monolayer composed from a solution of 70:30 CH_3 -terminated: $COOH$ -terminated thiols and it was found that similar adhesion was observed on this monolayer to that of a pure CH_3 terminated monolayer. No sites of enhanced adhesion due to interaction with hydrophilic groups were recorded.

The adhesion of microcapsules to a leaf surface was investigated and it was found that there were large sites of increased hydrophilicity on the leaf surface, capable of being detected by the large surface area of contact the microcapsule had with the substrate. Areas of minimal adhesion and enhanced adhesion were observed at the same pH but on different areas of the leaf. The average adhesion observed over the areas studied compared favourably with the adhesion measured to the mixed monolayer.

3.5 References

1. Sengupta, A.; Nielsen, K. E.; Barinshteyn, G.; Li, K.; Banovetz, J. P. Suspensions of microcapsules containing biologically active ingredients and adhesive microspheres US, 1997.
2. Gerold, T. Microcapsule system for the environmental release of agents. In *European Patent* EU, 2001.
3. Bain, C. D.; Evall, J.; Whitesides, G. M. *J. Am. Chem. Soc.* **1989**, *111*, 7155.
4. Bain, C. D.; Evans, S. D. *Chem. Br.* **1995**, *31*, 46.
5. Bain, C. D.; Troughton, E. B.; Tao, Y. T.; Evall, J.; Whitesides, G. M.; Nuzzo, R. G. *J. Am. Chem. Soc.* **1989**, *111*, 321.
6. Bain, C. D.; Whitesides, G. M. *J. Am. Chem. Soc.* **1989**, *111*, 7164.
7. Lulevich, V. V.; Radtchenko, I. L.; Sukhorukov, G. B.; Vinogradova, O. I. *J. Phys. Chem. B* **2003**, *107*, 2735.
8. Zimmermann, H.; Hillgartner, M.; Manz, B.; Feilen, P.; Brunnenmeier, F.; Leinfelder, U.; Weber, M.; Cramer, H.; Schneider, S.; Hendrich, C.; Volke, F.; Zimmermann, U. *Biomaterials* **2003**, *24*, 2083.
9. Ducker, W. A.; Senden, T. J.; Pashley, R. M. *Langmuir* **1992**, *8*, 1831.
10. Ducker, W. A.; Senden, T. J.; Pashley, R. M. *Nature* **1991**, *353*, 239.
11. Butt, H. J. *Biophys. J.* **1991**, *60*, 777.
12. Nolte, M.; Fery, A. *Langmuir* **2004**, *20*, 2995.
13. Nolte, M.; Fery, A. *IEEE Trans. Nanobiosci.* **2004**, *3*, 22.
14. Vezenov, D. V.; Noy, A.; Rozsnyai, L. F.; Lieber, C. M. *J. Am. Chem. Soc.* **1997**, *119*, 2006.
15. Wallwork, M. L.; Smith, D. A.; Zhang, J.; Kirkham, J.; Robinson, C. *Langmuir* **2001**, *17*, 1126.
16. He, H. X.; Li, C. Z.; Song, J. Q.; Mu, T.; Wang, L.; Zhang, H. L.; Liu, Z. F. *Mol. Cryst. Liq. Cryst. Sci. Technol. Sect. A-Mol. Cryst. Liq. Cryst.* **1997**, *294*, 99.
17. vanderVegte, E. W.; Hadziioannou, G. *J. Phys. Chem. B* **1997**, *101*, 9563.
18. Zhang, J.; Kirkham, J.; Robinson, C.; Wallwork, M. L.; Smith, D. A.; Marsh, A.; Wong, M. *Anal. Chem.* **2000**, *72*, 1973.
19. Schonherr, H.; Hruska, Z.; Vancso, G. J. *Macromolecules* **2000**, *33*, 4532.
20. He, H. X.; Huang, W.; Zhang, H.; Li, Q. G.; Li, S. F. Y.; Liu, Z. F. *Langmuir* **2000**, *16*, 517.

21. Smith, D. A.; Wallwork, M. L.; Zhang, J.; Kirkham, J.; Robinson, C.; Marsh, A.; Wong, M. *J. Phys. Chem. B* **2000**, *104*, 8862.
22. Jetter, R.; Schaffer, S. *Plant Physiol.* **2001**, *126*, 1725.
23. Jetter, R.; Schaffer, S.; Riederer, M. *Plant Cell Environ.* **2000**, *23*, 619.
24. Drelich, J.; Wilbur, J. L.; Miller, J. D.; Whitesides, G. M. *Langmuir* **1996**, *12*, 1913.
25. Cleveland, J. P.; Manne, S.; Bocek, D.; Hansma, P. K. *Rev. Sci. Instrum.* **1993**, *64*, 403.
26. Hutter, J. L.; Bechhoefer, J. *Rev. Sci. Instrum.* **1993**, *64*, 1868.
27. Burchiel, S. W.; Edwards, B. S.; Kuckuck, F. W.; Lauer, F. T.; Prossnitz, E. R.; Ransom, J. T.; Sklar, L. A. *Methods* **2000**, *21*, 221.
28. Walters, D. A.; Cleveland, J. P.; Thomson, N. H.; Hansma, P. K.; Wendman, M. A.; Gurley, G.; Elings, V. *Rev. Sci. Instrum.* **1996**, *67*, 3583.
29. Lide, D. R. *CRC Handbook of chemistry and physics*, 72nd ed.; Boca Raton: Florida, 1991.
30. Smith, C. P.; White, H. S. *Langmuir* **1993**, *9*, 1.
31. Wang, B.; Oleschuk, R. D.; Horton, J. H. *Langmuir* **2005**, *21*, 1290.
32. Shirley, I. *Private communication* **2002**.
33. Folkes, J. P.; Laibinis, P. E.; Whitesides, G. M. *Langmuir* **1992**, *8*, 1330.
34. Bain, C. D.; Whitesides, G. M. *Science* **1988**, *240*, 62.
35. Buck, M.; Fischer, J.; Grunze, M.; Trager, F. *Applied Physics* **1991**, *A53*, 552.

Chapter 4

Investigations into the release of pesticide from microcapsules under solution

This chapter investigates the release properties of polymeric microcapsules into solution using confocal laser scanning microscopy. It includes details of preliminary studies which were carried out to find the optimum species to use inside the microcapsule and the solution into which the species should be released. The release characteristics of six varieties of microcapsule differing in the wall thickness and cross linking density were investigated and from the release profiles, the product of the mass transfer and solubility coefficients of species across the wall were obtained.

4.1 Introduction

The main application of microcapsules is for the controlled delivery of species to a specific site. An important factor in controlled delivery is the release rate of the active ingredient from the centre of the microcapsule, across the polymeric wall to the site of interest. The predominant factor affecting the release rate of active ingredient is the permeability of the microcapsule wall. The permeability of the wall is controlled by the thickness and cross linking density of the wall, which influences the ability of the active ingredient to diffuse across it.

There has been considerable research into the release of active ingredient from microcapsules and a number of techniques have been used to measure release rates. Common techniques used to measure the release of active from capsules include UV spectroscopy¹⁻⁵, HPLC^{6,7} and gas chromatography⁸, which analyse the concentration of active species present in the elute over time. All of these techniques look at the bulk release from microcapsules, whereas the studies in this chapter are concerned with the release at the single capsule level.

Möhwald et al have recently used CLSM to investigate the permeation properties of the walls of polyelectrolyte microcapsules^{9,10}. CLSM has been used to examine the permeation of fluorescent macromolecules into polyelectrolyte microcapsules, by monitoring the percentage of microcapsules which were filled with the dye over time, for different electrolyte concentrations¹⁰. A further study, mentioned previously⁹, used FRAP technique, in which lasers on the confocal microscope were used to photo-bleach inside the capsule, and the fluorescence recovery within the capsule was subsequently monitored over time, to determine the permeability of the capsule wall.

The diffusion of species out of, and away from, a spherical object has been modelled on numerous occasions. A general solution for the diffusion from a hollow sphere with both inner and outer surface maintained at a constant concentration has been presented by Carslaw and Jaeger¹¹. Special cases have been considered by Barrer¹² who also suggested some practical systems to which the solutions could be applied. Crank presents well-known expressions for the diffusion in a sphere¹³.

A study by Dappert and Thies presented work on the rationale and theory of statistical models for controlled release microcapsules, taking into account the fact that microcapsules have walls of arbitrary geometry¹⁴. This study modelled the kinetics of release of material by a single microcapsule and the model has been incorporated into a statistical model for the kinetics of release from populations of microcapsules.

Zhou and Wu have applied the finite element method (FEM) to problems of diffusion-controlled drug release from complex matrix systems including spherical objects¹⁵⁻¹⁷. They have also used the method to investigate the effect of interparticulate interactions on release kinetics of microspheres¹⁸. More recent studies have probed the kinetics of dispersed drug release at a more complex level, using FEM once more¹⁹⁻²¹.

4.2 Theory

The theory behind the estimation of the release rate of an active ingredient from a microcapsule across a polymer wall uses parameters which are represented schematically in Figure 4.1.

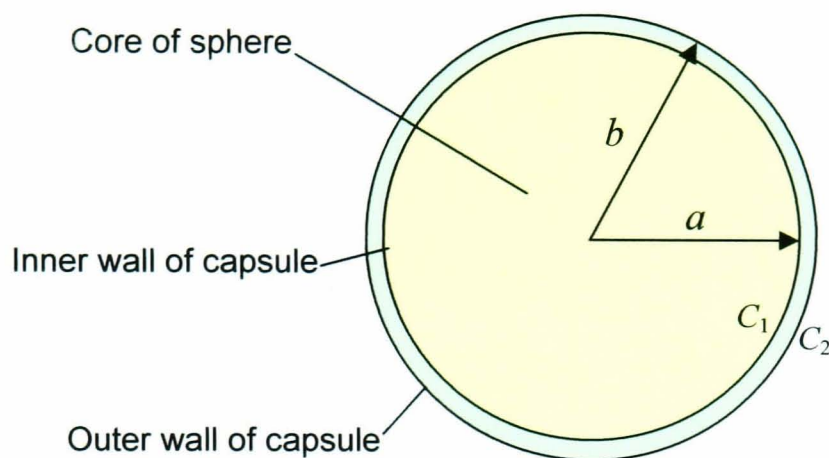


Figure 4.1 Schematic representation of the parameters described in equation 4.1.

Assuming that diffusion outside and inside the capsule is fast and that release is limited only by diffusion across the capsule wall and that a is approximately equal to b the release rate equation for the release of pesticide through molecular diffusion through the microcapsule wall is given in Equation 4.1²²,

$$\frac{dM}{dt} = \text{release rate} = \frac{(4\pi ab)P(C_1 - C_2)}{b - a} \quad 4.1$$

where M is the amount (mol) within the capsule, $4\pi ab$ is the surface area of the sphere, $C_1 - C_2$ is the concentration difference across the polymer wall, $b - a$ is the thickness of the microcapsule wall. P is the permeability of the microcapsule, which is the product DK , where D is the diffusion coefficient of species within the microcapsule wall and K is the solubility coefficient, referring to the solubility of the active species in the capsule wall with respect to the internal compartment. This equation shows that the

release rate of material from the microcapsule is directly proportional to the surface area, permeability and concentration difference across the wall and is inversely proportional to the wall thickness.

Assuming that the concentration outside of the capsule (C_2) is zero, integrating equation 4.1 gives equation 4.2:

$$M_0 - M_t = \frac{4\pi ab}{b-a} PC_1 t \quad 4.2$$

The concentration change within the capsule can be determined from this equation taking into account the volume of a sphere (Equation 4.3).

$$\frac{C_0 - C_t}{C_t} = \frac{3Pt}{(b-a)a} \quad 4.3$$

where C_0 is the initial concentration of species within the microcapsule and C_t is the concentration at time t .

For this particular problem the concentration of active present within the capsule at any time is assumed equal to, and is measured by the intensity of fluorescence exhibited within the capsule i.e. concentration is proportional to intensity. Therefore,

$$\frac{I_0 - I_t}{I_t} = \frac{3Pt}{(b-a)a} \quad 4.4$$

Release measurements in this chapter are presented in plot of $\frac{I_0 - I_t}{I_t}$ against time, t . A plot of this type will have a gradient of $\frac{3P}{(b-a)a}$.

The mass transfer coefficient of the active ingredient can be estimated according to equation 4.5:

$$k_t = \frac{D}{b-a} \quad 4.5$$

By substituting this term into equation 4.4, the mass transfer coefficient of species across the microcapsule membrane can be calculated from the gradient of these plots.

i.e. the gradient of a plot of $\frac{I_0 - I_t}{I_t}$ against time will be $\frac{3k_t K}{a}$.

4.3 Experimental

All polyurea microcapsules used in these experiments were prepared at Syngenta (Jealott's Hill, Bracknell) using interfacial condensation microencapsulation of the monomers polymethylene-polyphenylisocyanate (PMPPI) and toluene diisocyanate (TDI) (for details see section 1.1.2). Microcapsules studied contained either the dye Nile Red or the pesticide lambda cyhalothrin suspended in the organic solvent Solvesso® 100. Properties of microcapsules were observed using a confocal laser scanning microscope (LSM 510, Axioplan 2, Carl Zeiss, Jena, Germany).

To investigate microcapsules containing the dye Nile Red, a droplet of solution containing the capsules suspended in deionised water was placed on a glass slide and allowed to dry. CLSM images (512 x 512 pixels, 8 bit pixel depth) were acquired using an objective lens (Zeiss, Epiplan Neofluar 50x/ 0.80 NA W) with a 10x tube lens. To observe the Nile Red dye within the capsules, a helium/neon laser was used ($\lambda = 543$ nm) in conjunction with a long pass filter ($\lambda = 505$ nm).

The wall thickness and cross linking density of the polymeric wall of the lambda cyhalothrin filled capsules were varied. 6 sets of microcapsules were prepared whose properties are outlined in Table 4.1. Further details of microcapsule composition can be found in section 2.3.2.2.

Table 4.1 Details of properties of microcapsules used in release into solution experiments.

Microcapsule	% monomers in original organic phase	Ratio of monomers PMPPI:TDI
1	10%	1:1
2	10%	1:10
3	10%	1:20
4	15%	1:1
5	15%	1:10
6	15%	1:20

A droplet of solution containing microcapsules suspended in deionised water was left to dry overnight on a thin layer of araldite on the bottom of a petri dish. The petri dish was then placed on the stage of the confocal microscope and filled with 25 cm³ of an ethanol/water solution. All CLSM images (512 x 512, 8 bit pixel depth) were obtained with a water immersion objective lens (Zeiss Achroplan 20x/0.50 W) with a 10 x tube lens which was dipped into the ethanolic solution and focused on the microcapsules. See Figure 4.2 for experimental set-up for release measurements.

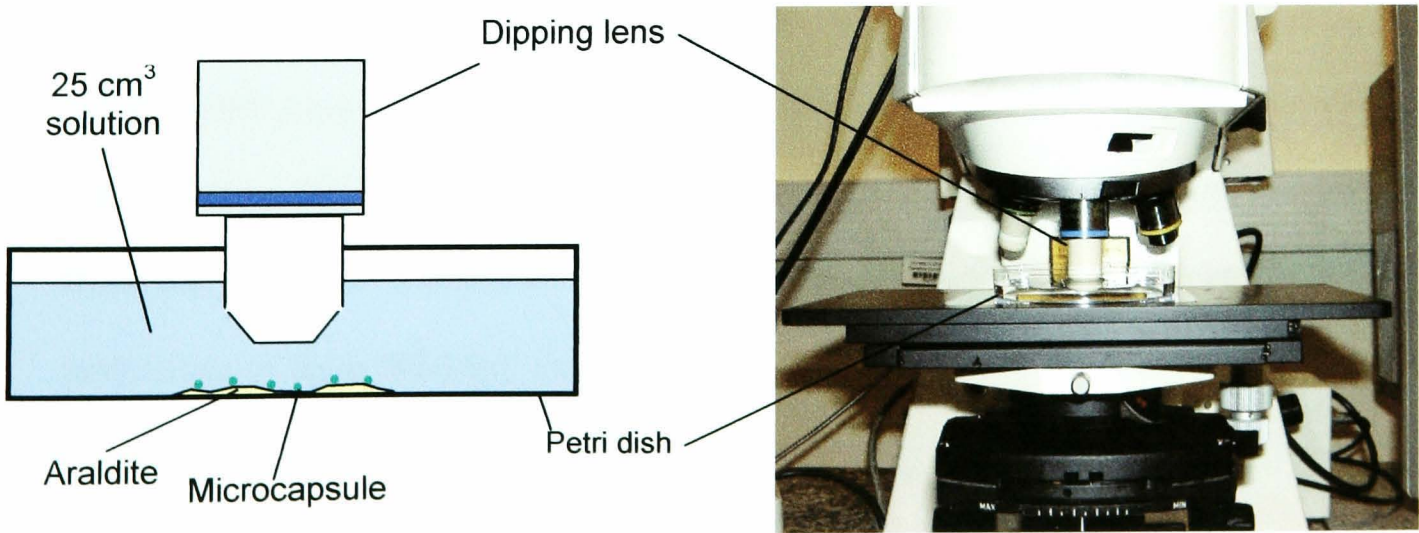


Figure 4.2 Experimental set up for studying the release of active ingredient from microcapsule into solution.

To observe the autofluorescence of the lambda cyhalothrin within the microcapsules a multi-track laser configuration was used. An argon laser ($\lambda = 488$ nm) was used in conjunction with a long pass filter ($\lambda = 560$ nm) and simultaneously, a helium/neon laser ($\lambda = 543$ nm) was used in conjunction with a band pass filter ($\lambda = 505$ - 530 nm) in order to achieve the maximum fluorescence signal possible.

Black level (background offset) was adjusted to eliminate autofluorescence from the background solution. To achieve the optimum compromise between resolution and image intensity, the confocal aperture was set to give an optical slice of $9.2\text{ }\mu\text{m}$. A scan in the x - y plane was taken through the centre of the microcapsule as soon as possible after the addition of solution and a scan was recorded every minute until the fluorescence within the capsule had completely diminished.

Images were processed using the LSM Image Browser software (Zeiss). Average pixel intensities were calculate over the area corresponding to single microcapsules (typically 60×60 pixels) using Paint Shop Pro software (Jasc Software).

4.4 Results and Discussion

4.4.1 Preliminary studies

The morphology of microcapsules was investigated using confocal microscopy to study microcapsules encapsulating the dye Nile Red. This dye was used as its spectroscopic properties have been fully characterised²³ and functional groups which may have reacted into the wall of the microcapsule were absent from the dye's molecular structure. This meant that the dye could be encapsulated successfully. 3D projections of these Nile Red microcapsules built up from x - y slices taken through the capsules every $1\text{ }\mu\text{m}$ are shown in Figure 4.3.

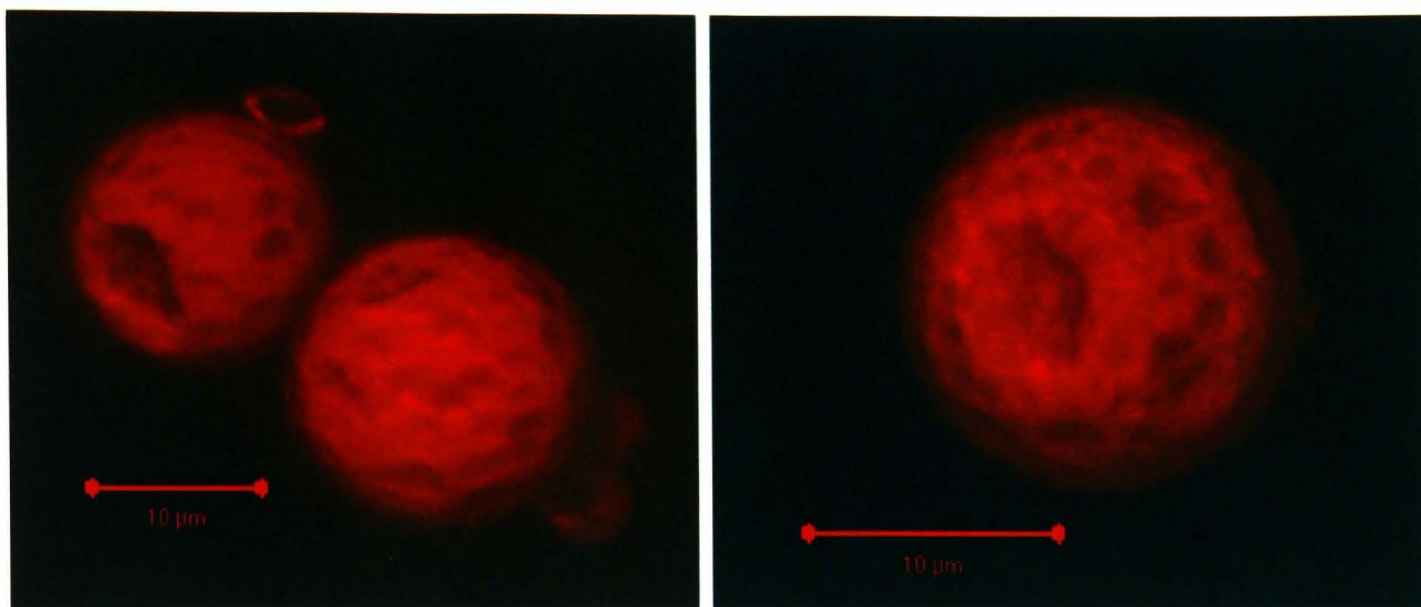


Figure 4.3 3D projection images of polyurea microcapsules filled with the dye Nile Red.

It is apparent from these images that the surface topography of the microcapsules encapsulating Nile Red is even more dimpled and pitted compared to the surface of the capsules containing the pesticide lambda cyhalothrin (see Figure 3.7). This irregularity in the surface topography is due to the non-ideal nature of the dye which has been encapsulated. This type of polyurea microcapsule has been designed and developed to contain a pyrethroid insecticide in its oily core. It is thus not unexpected that the use of other compounds would have an effect on the formation and morphology of the microcapsule wall.

Whilst imaging in a plane bisecting the centre of these microcapsules, it was apparent that the Nile Red within the capsules experienced photo bleaching, with the intensity of the fluorescent signal diminishing rapidly over time as shown in Figure 4.4. Images were recorded every half hour for two and a half hours. As there is a very small, finite amount of dye within the capsule, the fluorescent signal was unable to recover over time.

These two factors, the photobleaching effect and the irregularity of the surface topography of the capsules, led to the decision not to use Nile Red microcapsules to investigate the permeability properties of the microcapsule wall.

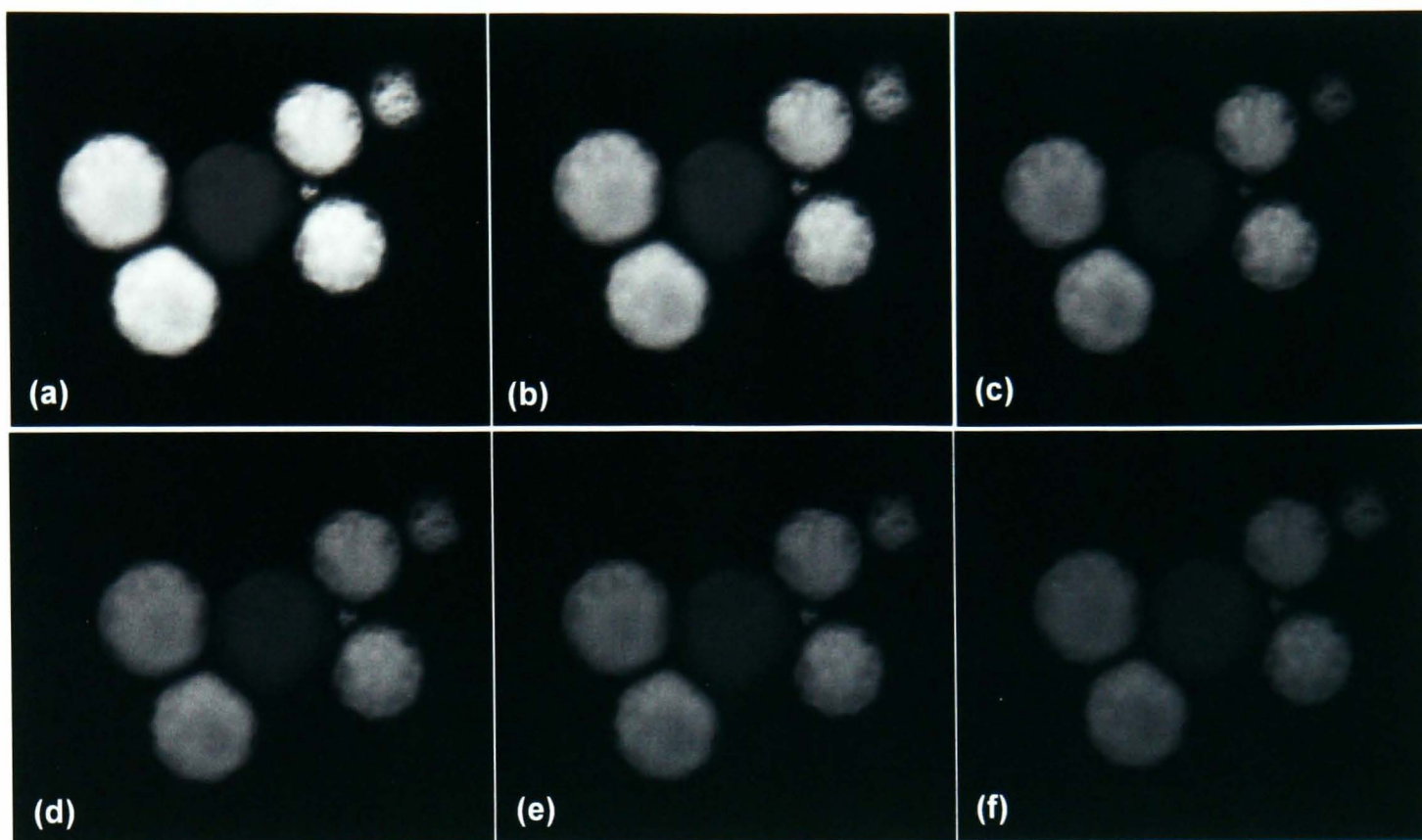


Figure 4.4 Slice through the centre of a group of microcapsules containing the dye Nile Red at (a) 0 min, (b) 30 min, (c) 60 min, (d) 90 min (e) 120 min (f) 180 min.

Preliminary CLSM studies of capsules containing the pesticide lambda cyhalothrin showed that a substance within the capsule could be excited within the wavelengths of the lasers available.

In order to investigate whether or not the solvent within the capsule was the origin of this fluorescence, capsules with identical wall composition containing just the solvent with no pesticide were imaged. It was found that removing the pesticide diminished the observed fluorescence within the capsule considerably. An example of this is shown in Figure 4.5 which shows an x - y slice taken through the centre of a capsule filled with lambda cyhalothrin dissolved in solvent and a capsule which contained just the solvent. The settings for the confocal microscope, the gains and pinholes used, were identical for the imaging of both capsules, as was the composition of the microcapsule wall.

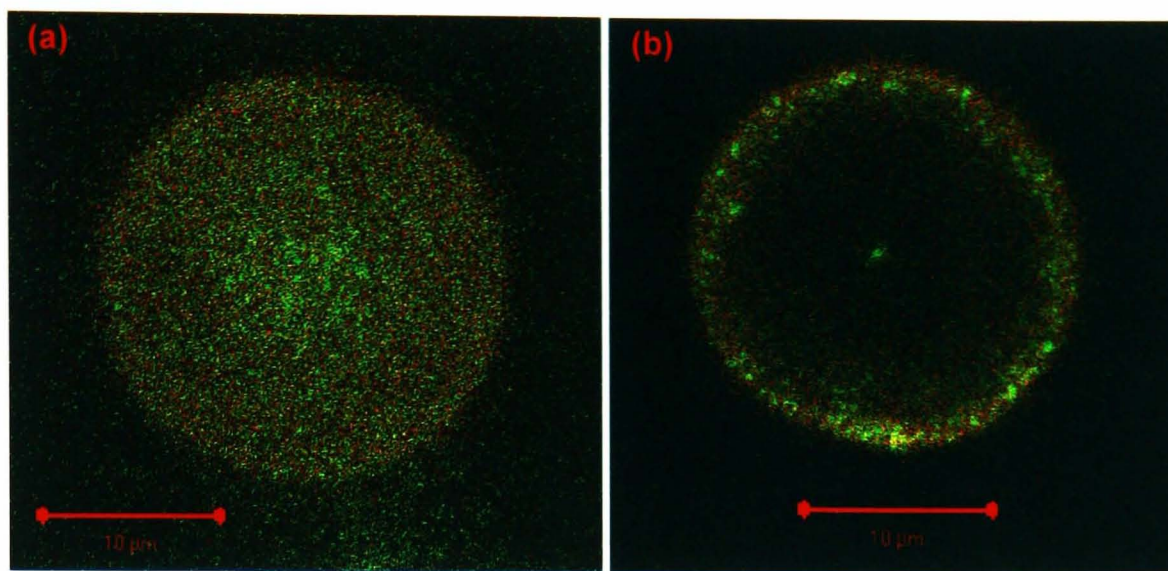


Figure 4.5 Slices through the centre of polyurea microcapsules containing **(a)** the pesticide lambda cyhalothrin and the solvent Solvesso and **(b)** the solvent Solvesso alone.

4.4.2 Release studies into ethanolic solution.

The capsules studied in this project are designed so as not to release their oily core into the aqueous solution in which they are stored. The mechanism of release is such that when the water from the spray droplet has evaporated after application, the capsules controlled release mechanism is triggered. The release of active ingredient can be encouraged if the capsule is in contact with a ‘sink’ site such as a waxy surface or an ethanolic solution. In order to study the release properties of microcapsules on a reasonable time scale, the release into ethanolic solutions of various ethanol: water mixes was investigated.

Figure 4.6 shows an example of how the release of pesticide was monitored as a function of light intensity within the capsule with time. This was done by taking an x - y frame through the centre of the microcapsule and recording the average light intensity within single capsules over time. Each x - y frame was taken in 1.94 seconds. This approach is reasonable because diffusion of the pesticide within the wall is expected to be rate limiting; the diffusion coefficient in the oily core and external solution is much higher.

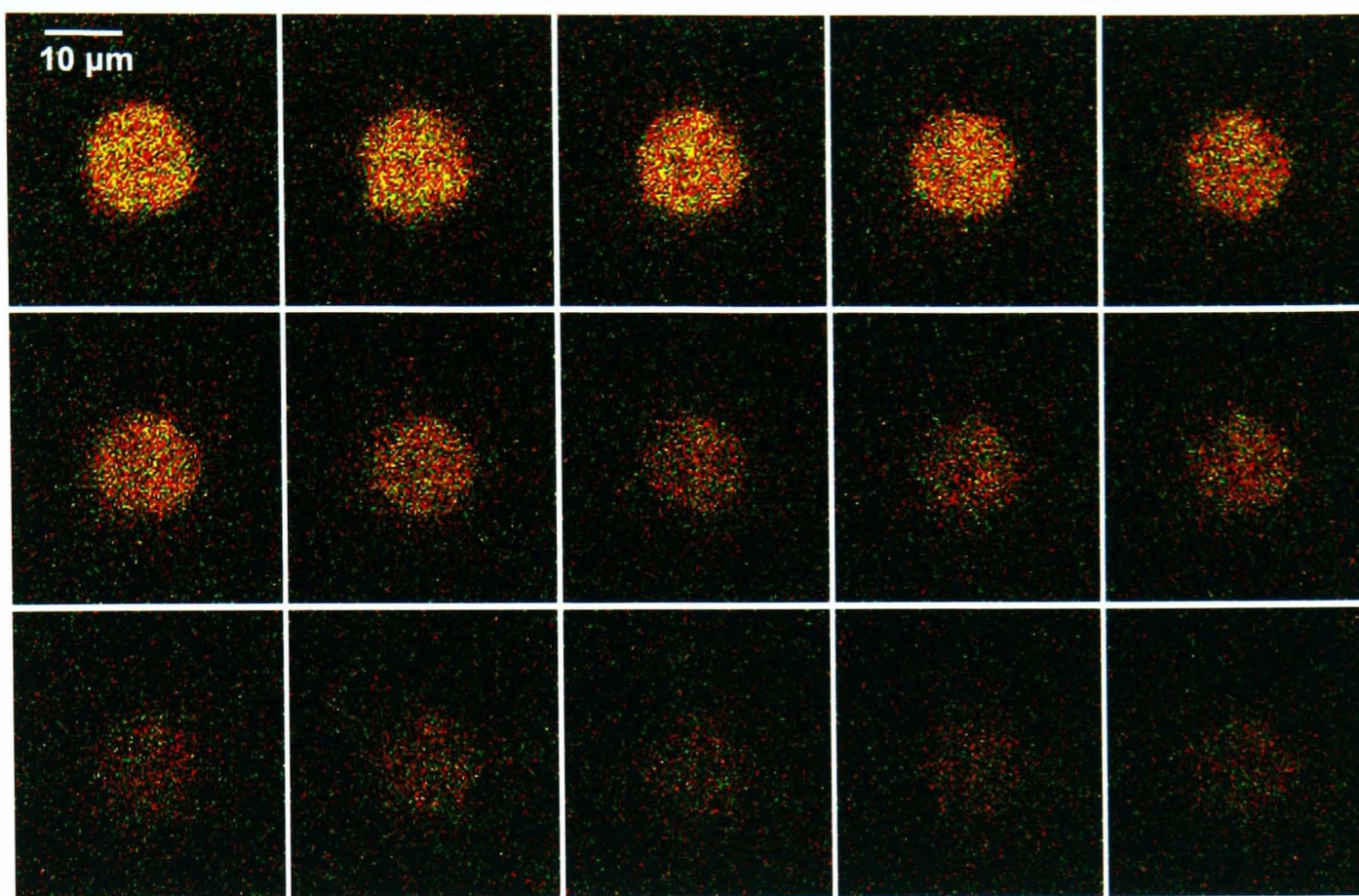


Figure 4.6 Series of images taken through the centre of a lambda cyhalothrin filled microcapsule showing the release of the pesticide over time. The time scale between each image was 2 minutes with the first being taken at 0 minutes.

Using this methodology, the release properties of individual microcapsules with a 10% wall and 1:10 cross linking density were measured into solutions with differing ethanol: water compositions. Figure 4.7 demonstrates the release curves of lambda cyhalothrin into 25:75, 75:25 ethanol: water solutions and into 100% water. The change in fluorescence within the capsule, $(I_0 - I)/I_t$, is plotted against time in order to obtain the product of the mass transfer and solubility coefficients of the pesticide as described in section 4.2.

4.4.2.1 Concentration of ethanolic solution used

The properties of the wall of the microcapsule used in this study to explore the most effective proportion of ethanol in the release solution were such that it was one of the weaker walls studied. These results demonstrated that a 75: 25 ethanol: water solution was optimal for these measurements, as the entire release profile of this weak

walled capsule could be recorded over ~ 10 minutes. The 75:25 ethanol: water solution provided the fastest release of active from the microcapsule as it was the most organic of the solutions studied and would therefore encourage the active ingredient, which is dissolved in an organic solvent, to cross the microcapsule wall into solution.

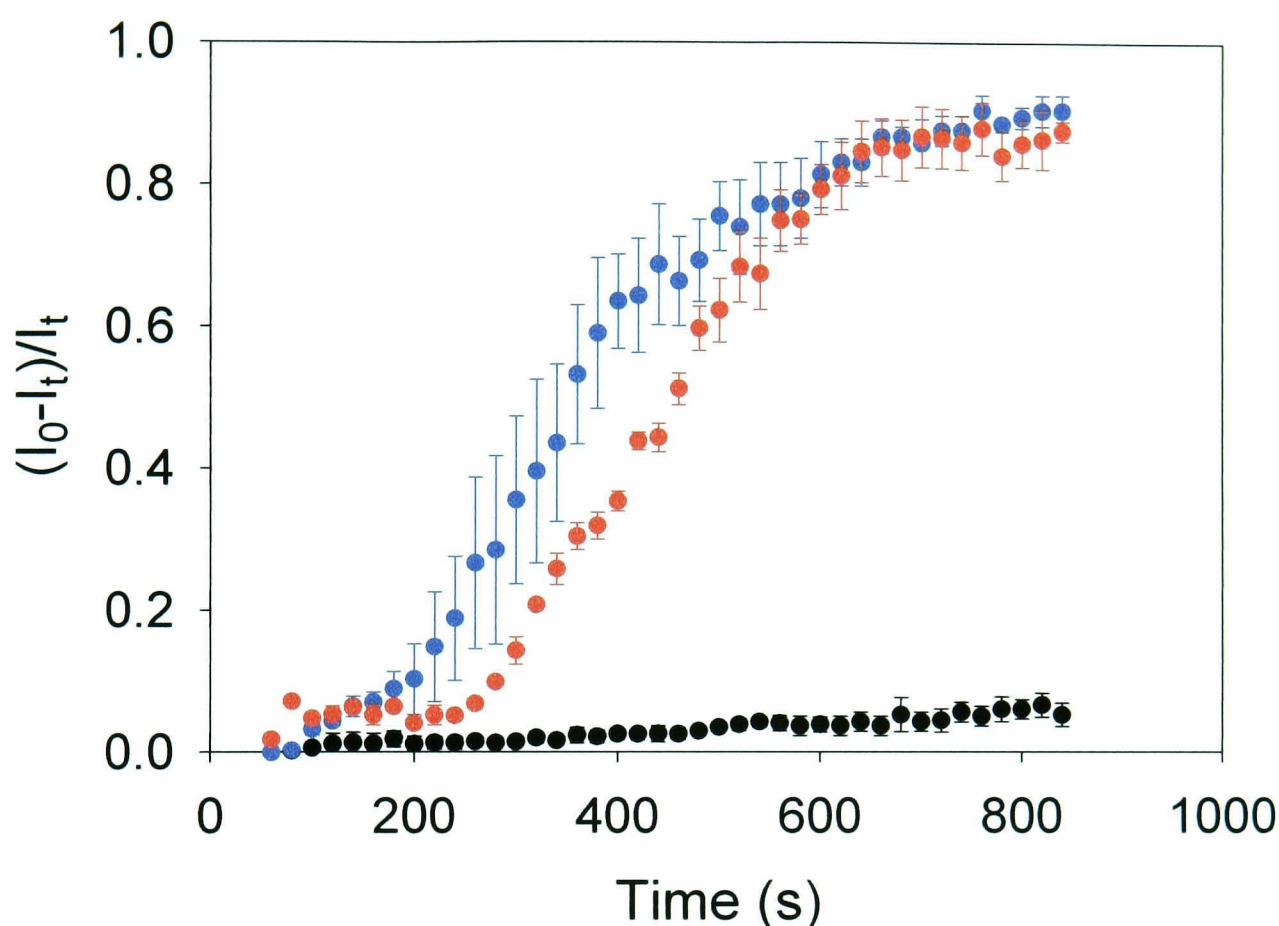


Figure 4.7 Plots of $(I_0 - I_t)/I_t$ vs time showing the release of lambda cyhalothrin from capsules with 10% wall, 1:10 crosslinking density. Measurements were taken in solutions of differing ethanol:water concentrations; • 100% water, • 25:75 EtOH:Water, • 75:25 EtOH:Water.

Capsules with a stronger wall were expected to take longer to release, so the solution which allowed the observation of the full release profile of the weaker walled capsule in the fastest time possible would be the best solution to use as this would be the solution which would encourage the capsules with the stronger walls to release.

These preliminary studies also demonstrated that very little photobleaching is occurring within the capsules studied. The release profile shown in Figure 4.6 for the release of active into a solution containing only water showed very little decrease in fluorescence over the time period studied. This result is as expected as the oily core of the capsule is not likely to release into a purely aqueous solution. The minimal decrease

in fluorescence observed in this result is a good indication that no photobleaching has occurred.

4.4.2.2 Investigation of the effect of wall thickness and cross linking density on the permeability of microcapsules

Within this study the effect of the thickness of the microcapsule wall on the release rate of active ingredient from the capsule was investigated. The thickness of the wall is controlled by the percentage of monomers present in the oil phase at the beginning of the synthesis of the capsules. The two systems investigated in these studies had either 10% or 15% of monomers making up the oil phase at the start of synthesis. The greater the percentage of monomers present, the thicker the microcapsule wall. Equation 4.1 shows the relationship between release rate and wall thickness, indicating that the release of active ingredient from the microcapsule is inversely proportional to the thickness of the wall.

The other factor investigated in this study was the effect of the cross linking density of the polyurea wall of the microcapsule on its release rate. In the case of the microcapsules studied, the polymeric wall is formed via the interfacial polymerisation of the isocyanate monomers PMPPI and TDI. The cross linking density of the microcapsule wall can be varied by changing the ratio of these two monomers in the oil phase of the original reaction mixture.

In this study the ratio of the monomers investigated were 1:1, 1:10 and 1:20 PMPPI: TDI. The higher the ratio, the more cross linking within the wall of the capsule. This might be expected to lower the diffusion coefficient of the species across the wall, i.e. to lower the permeability. According to equation 4.1 the release rate of active

ingredient out of the microcapsule and away is directly proportional to the permeability of the microcapsule.

Figures 4.8 and 4.9 show the typical experimental data for the release of lambda cyhalothrin from the 6 sets of microcapsules described in section 4.2 into a 75:25 ethanol: water solution. The plots show the average intensity of the fluorescence observed within the capsules normalised with respect to the initial intensity observed i.e. $(I_0 - I_t)/I_t$ recorded over time. A measurement was taken every minute and the intensity ratio recorded is that for four different capsules to obtain the mean intensity value and standard deviation.

The plots in Figure 4.8 and 4.9 demonstrate that the release profile changes as the properties of the microcapsule wall are altered. As the capsule wall becomes thicker and denser, a lag time appears at the start of the release profiles. This lag time, which increases as the capsule wall becomes thicker, is a culmination of two factors which are directly related: the time taken for the wall of the microcapsule to adjust to its ethanolic environment and the time required for the pesticide to establish a pathway from the oily core to the exterior of the microcapsule wall for eventual release.

As the wall of the capsule becomes thicker and denser, as a consequence of the increased cross linking between monomers, a more prominent lag time is observed. This is particularly evident in the release profiles for the stronger walled capsules, i.e. the 15% 1:1 and 15% 1:10 samples, shown in Figure 4.9 (c) and (b). In the weaker walled capsules, i.e. the 10% 1:20 and 10% 1:10 samples, this lag time is absent from the release profiles as the time taken for the wall to adjust to its new environment and for the pesticide to diffuse across the wall is so rapid that this period is missed in the time to make the initial measurement.

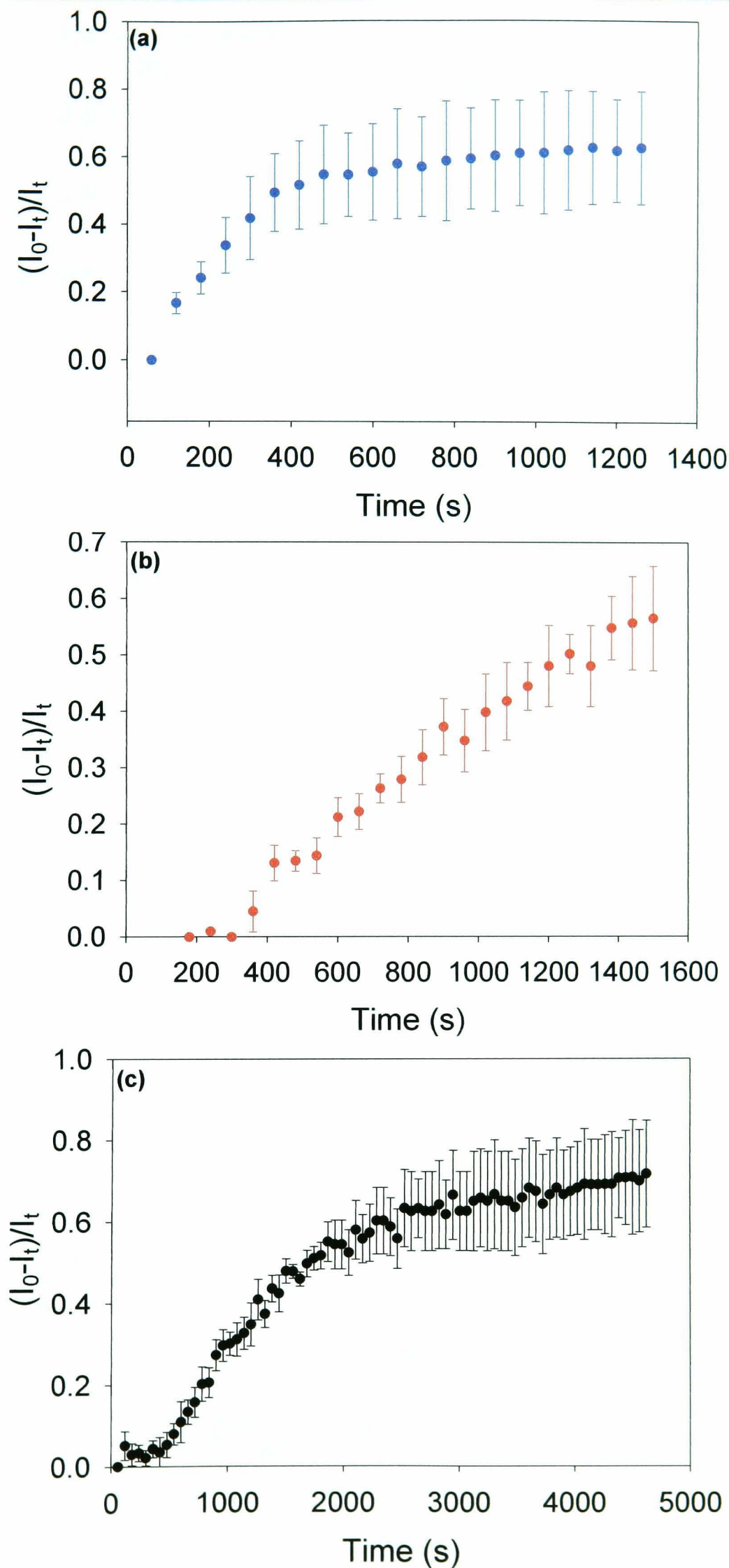


Figure 4.8 Graphs detailing the release of lambda cyhalothrin from capsules measured as the average light intensity within the capsules normalised with respect to the initial intensity against time. Measurements were taken in 75:25 EtOH:Water and the capsules used were 10% wall with (a) • 1:20 crosslinking, (b) • 1:10 crosslinking, (c) • 1:1 crosslinking.

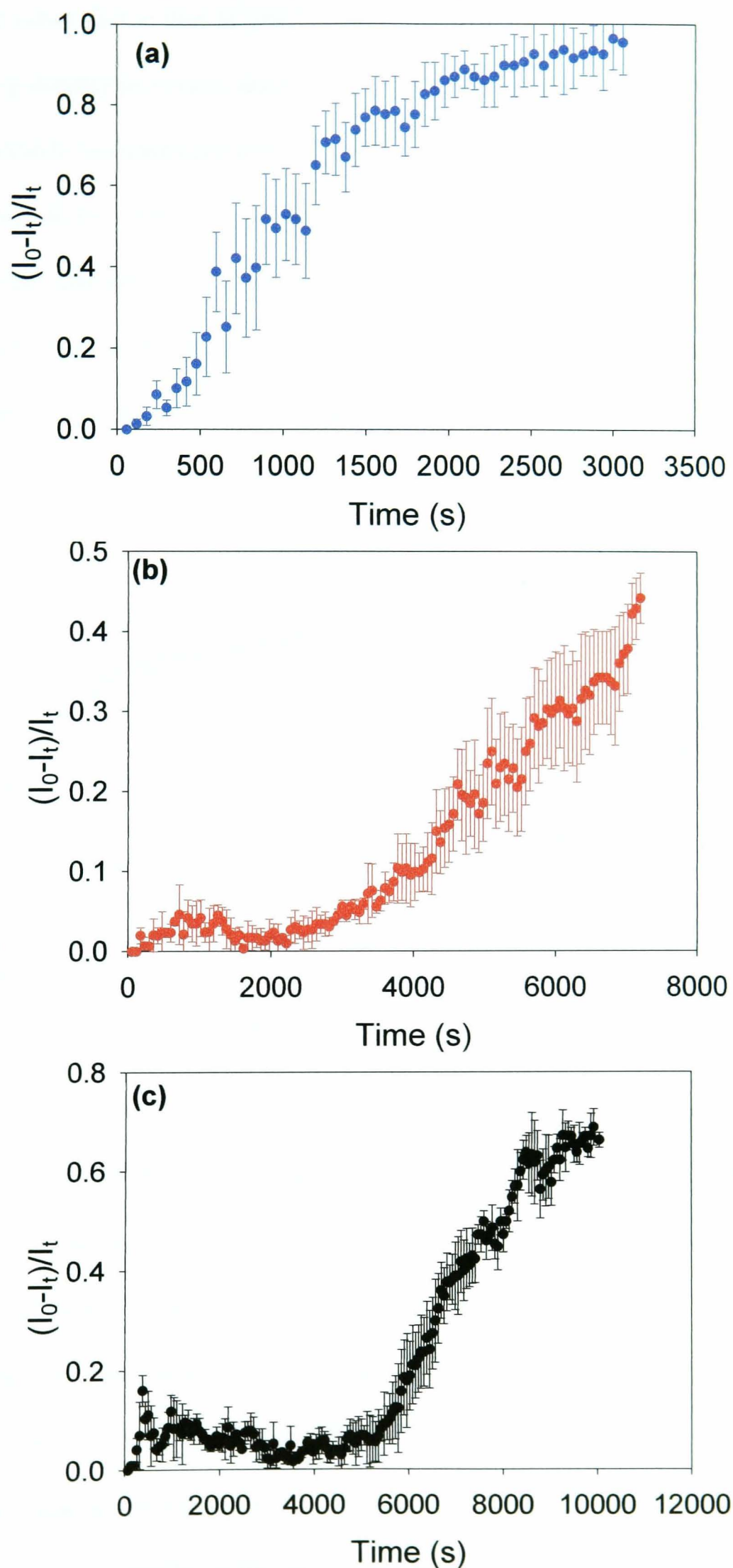


Figure 4.9 Graphs detailing the release of lambda cyhalothrin from capsules measured as the average light intensity within the capsules normalised with respect to the initial intensity against time. Measurements were taken in 75:25 EtOH:Water and the capsules used were 15% wall with (a) • 1:20 crosslinking, (b) • 1:10 crosslinking, (c) • 1:1 crosslinking;

The other factor that is obvious from these plots is that as the wall thickness/cross linking density increases, the time taken for the complete release of pesticide from the microcapsule increases considerably. The ‘weakest’ walled capsule releases its total pesticide content in 1,300 seconds. In contrast, the period of release for the capsule with supposedly the strongest wall is an order of magnitude longer, $\sim 10,000$ seconds.

Figure 4.10 demonstrates the effect that varying the cross linking density of the microcapsule wall has on the release profile of active ingredient out of the microcapsule.

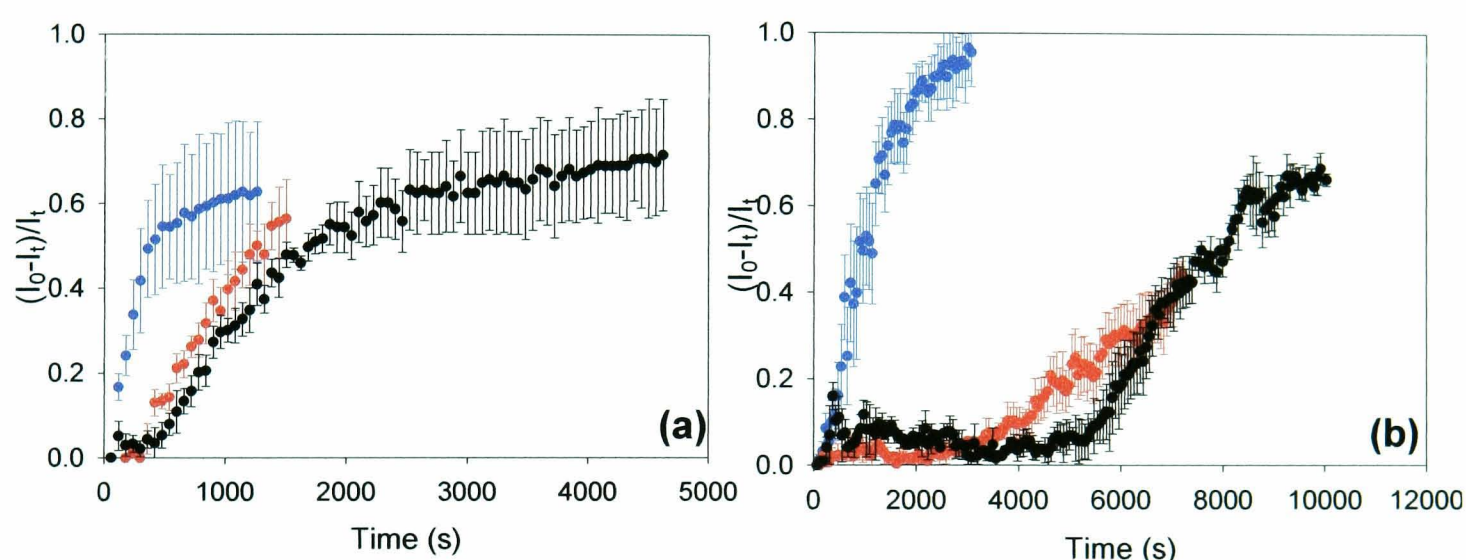


Figure 4.10 Graphs detailing the release of lambda cyhalothrin from capsules measured as the average light intensity within the capsules normalised with respect to the initial intensity against time. **(a)** 10% wall with ● 1:20 cross linking, ● 1:10 cross linking, ● 1:1 cross linking; **(b)** 15% wall with ● 1:20 cross linking, ● 1:10 cross linking, ● 1:1 cross linking.

These plots illustrate that changing the cross linking density of the microcapsule wall has a significant effect on the release profile of the capsule. The greatest effect is seen when comparing the 1:20 and 1:10 cross linking density ratios. For both wall thicknesses, 10% and 15%, the time lag does not appear in the 1:20 cross linking wall profile but at 1:10 cross linking ratio, a time lag is clearly visible especially for the 15% wall where it is seen to be ~ 3000 seconds.

The shape and position of the 1:10 and 1:1 release profiles for each of the wall thicknesses are more similar, with the 1:1 having a slightly longer lag time as expected and an increase in the time taken for full release to occur.

Figure 4.11 shows the same data sets presented to show the effects of changing the thickness of the microcapsule wall on the release profiles of the pesticide from the microcapsules. A more pronounced effect is observed for changing the wall thickness than for changing the cross linking density of the wall with a much longer release time observed for the 15% wall then the 10% wall at all cross linking density ratios studied.

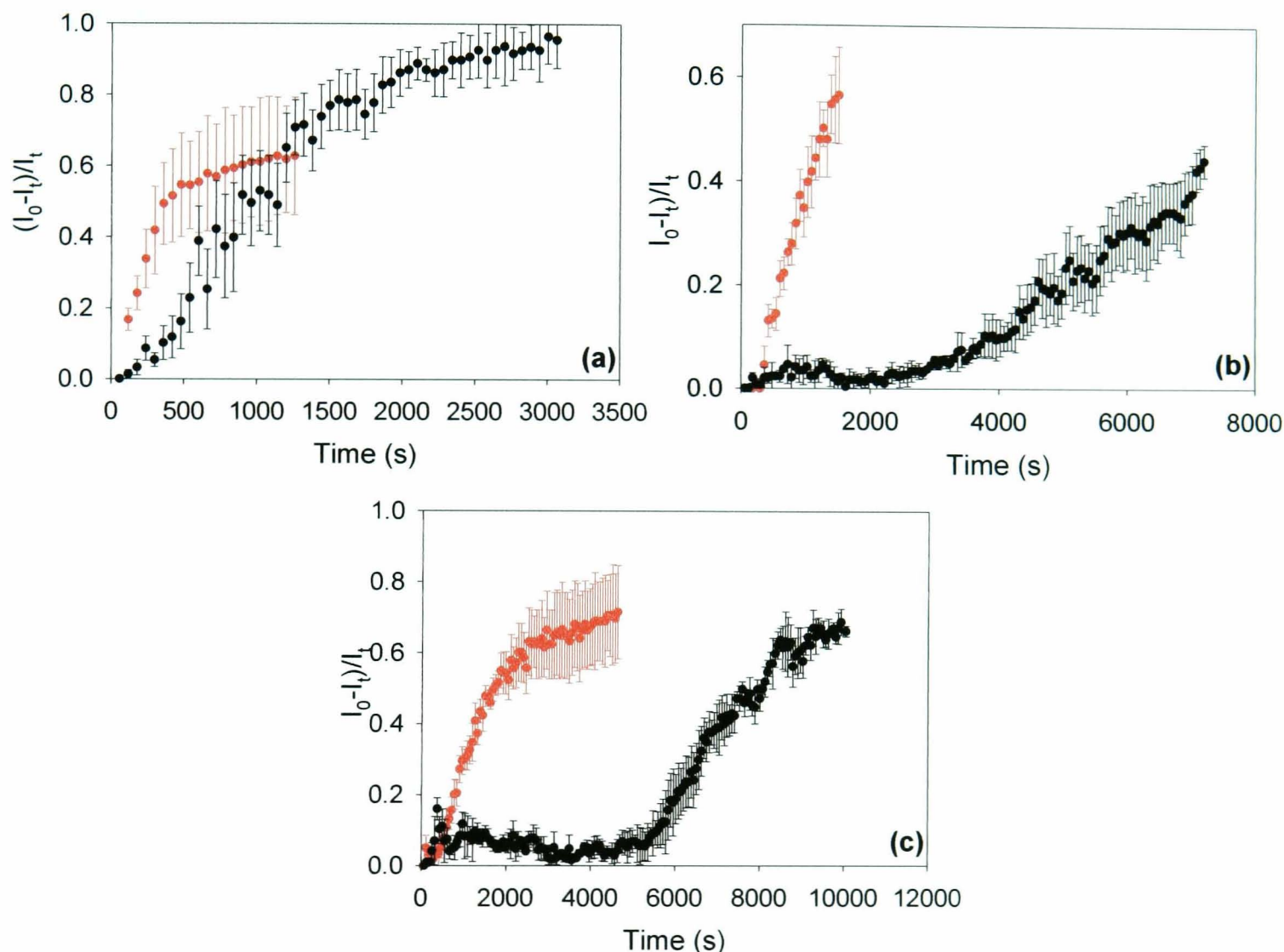


Figure 4.11 Graphs detailing the release of lambda cyhalothrin from capsules investigating the effect of changing the wall thickness on the release profile. **(a)** 1:20 cross linking with ● 10% wall, ● 15% wall; **(b)** 1:10 cross linking with ● 10% wall, ● 15% wall and **(c)** 1:1 cross linking with ● 10% wall, ● 15% wall.

4.4.2.3 Calculation of the product of the mass transfer coefficient of lambda cyhalothrin across the microcapsule wall and the solubility coefficients of the pesticide in the polymer wall.

The product of the mass transfer and solubility coefficients of lambda cyhalothrin across the wall of the microcapsule can be determined from these release profiles for all 6 sets of microcapsule studied. Section 4.2 describes the theory behind

the fact that a plot of normalised intensity, $\frac{I_0 - I_t}{I_t}$ against time, t , will have a gradient of $\frac{3k_t K}{a}$ where k_t is the mass transfer coefficient of lambda cyhalothrin across the microcapsule wall, K is the solubility coefficient referring to the solubility of the active species in the microcapsule wall and a is the average external radius of the microcapsule which is determined experimentally by confocal imaging.

From the release profiles obtained in section 4.4.2.2, $k_t K$ can be estimated from the steep part of the release curve. An example of this is shown in Figure 4.12 which shows the steep part of the release curve for the capsule with 10% wall thickness and 1:1 cross linking ratio of monomers.

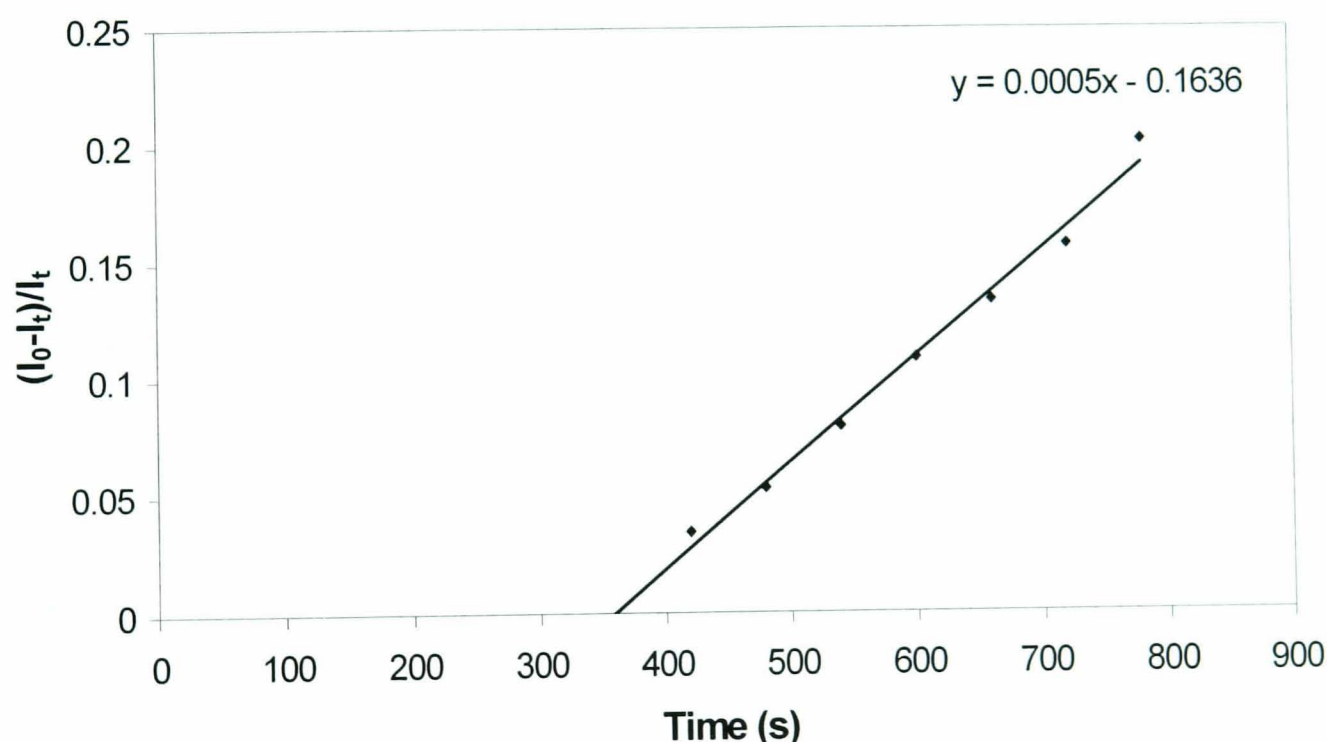


Figure 4.12 Cropped release profile for microcapsule with 10% wall and 1:1 crosslinking density ratio.

The gradients of the release curves for all of the microcapsules in the study were determined in this manner and the average radius of microcapsule studied for each set of capsules was measured from the confocal images. From this data, the $k_t K$ could be calculated. A summary of these findings are shown in Table 4.2.

Table 4.2 Product of mass transfer and solubility coefficients of microcapsules with differing wall properties.

Microcapsule	Wall thickness	Ratio of monomers PMPPI:TDI	$k_t K$
1	10%	1:1	$9.1 \times 10^{-8} \pm 5 \times 10^{-10}$
2	10%	1:10	$1.1 \times 10^{-7} \pm 5 \times 10^{-9}$
3	10%	1:20	$3.7 \times 10^{-7} \pm 5 \times 10^{-9}$
4	15%	1:1	$3.7 \times 10^{-8} \pm 5 \times 10^{-10}$
5	15%	1:10	$3.0 \times 10^{-8} \pm 5 \times 10^{-10}$
6	15%	1:20	$1.9 \times 10^{-7} \pm 5 \times 10^{-9}$

The value obtained here is the product of the mass transfer coefficient and the solubility coefficient of species into and across the microcapsule wall. A trend is observed showing that the product of these coefficients decreases as the thickness and cross linking density of the microcapsule wall increases. This is as expected due to the fact that it is harder for the pesticide to move through the microcapsule wall and away from the microcapsule.

The main observation from this data is that there is very little difference between the coefficients recorded for the 1:1 and 1:10 cross linking density ratios for both the 10% and 15% wall but there is a huge difference observed between the capsules with the 1:20 ratio and the other two sets of capsules with the same wall thickness. This could be due to the fact that lambda cyhalothrin may have increased solubility in the 1:20 wall leading to an increase in the value observed here. The 1:10 and 1:1 walls may not have such an affinity for the pesticide which would cause the rate of release to decrease.

It appears that overall the wall thickness of the microcapsule has the more significant effect on the product of the mass transfer and solubility coefficients of

species across the wall, rather than the cross linking density of the wall. A larger difference is observed between values measured for capsules with the same cross linking density but differing wall thickness than values measured for capsules with the same wall thickness but differing cross linking density. This fact is true over all of the different ratios of monomers studied.

4.5 Conclusions

The studies outlined in this chapter have shown the development of confocal microscopy as a technique for the study of the controlled release of polymeric microcapsules into an aqueous-ethanolic solution. It has been shown that the technique can be used to record the release profiles of the pesticide from the capsule. The products of the mass transfer coefficients of the pesticide through the polymeric wall and the solubility coefficient of the pesticide in the polymer wall, $k_p K$, have been estimated from these profiles.

The technique has been able to identify the release characteristics of microcapsules with differing thickness and cross linking density of their polymeric walls. The release profiles demonstrated that the thicker, denser-walled microcapsules took longer to release the pesticide lambda cyhalothrin encapsulated inside the polymer wall. The values for $k_p K$ obtained were further evidence for this phenomenon, the thicker, denser walled capsules having much small coefficients associated with their release profiles.

4.5 References

1. Berkland, C.; Kim, K.; Pack, D. W. *Pharm. Res.* **2003**, *20*, 1055.
2. Chu, L. Y.; Yamaguchi, T.; Nakao, S. *Adv. Mater.* **2002**, *14*, 386.
3. Hong, K.; Park, S. *J. Mater. Sci.* **1999**, *34*, 3161.
4. Jabbari, E.; Khakpour, M. *Biomaterials* **2000**, *21*, 2073.

5. Sato, T.; Yamamoto, T.; Shibako, S.; Ichikawa, K.; Dobashi, T. *J. Membr. Sci.* **2003**, *213*, 25.
6. Mu, L.; Feng, S. S. *J. Control. Release* **2003**, *86*, 33.
7. Yang, Y. Y.; Chung, T. S.; Ng, N. P. *Biomaterials* **2001**, *22*, 231.
8. Yadav, S. K.; Khilar, K. C.; Suresh, A. K. *J. Membr. Sci.* **1997**, *125*, 213.
9. Ge, L. Q.; Mohwald, H.; Li, J. B. *ChemPhysChem* **2003**, *4*, 1351.
10. Georgieva, R.; Moya, S.; Hin, M.; Mitlohner, R.; Donath, E.; Kiesewetter, H.; Mohwald, H.; Baumler, H. *Biomacromolecules* **2002**, *3*, 517.
11. Carslaw, H. S.; Jaegar, J. C. *Conduction of heat in solids*, 2nd ed.; Oxford University Press, 1959.
12. Barrer, R. M. *Phil. Mag.* **1944**, *35*, 802.
13. Crank, J. *The mathematics of diffusion*, 2nd ed.; Oxford University Press, 1975.
14. Dappert, T.; Thies, C. *J. Membr. Sci.* **1978**, *4*, 99.
15. Wu, X. Y.; Zhou, Y. *J. Control. Release* **1998**, *51*, 57.
16. Zhou, Y.; Wu, X. Y. *J. Control. Release* **1997**, *49*, 277.
17. Wu, X. Y.; Zhou, Y. *J. Pharm. Sci.* **1999**, *88*, 1050.
18. Wu, X. Y.; Eshun, G.; Zhou, Y. *J. Pharm. Sci.* **1998**, *87*, 586.
19. Zhou, Y.; Chu, J. S.; Wu, X. Y. *Eur. J. Pharm. Sci.* **2004**, *22*, 251.
20. Zhou, Y.; Wu, X. Y. *J. Control. Release* **2002**, *84*, 1.
21. Zhou, Y.; Wu, X. Y. *J. Control. Release* **2003**, *90*, 23.
22. Baker, R. W.; Lonsdale, H. K. *Chemical Technology* **1975**, *5*, 668.
23. www.molecularprobes.com.

The release of pesticide from microcapsules to surfaces in the dry state

The studies in this chapter demonstrate the high resolution imaging capabilities of the confocal microscope to provide detail on the structure of the leaf of the *Prunus laurocerasus* plant and the caterpillars *Heliothis virescens* and *Plutella xylostella*. The release to leaf surfaces from two types of polyurea microcapsules, which have different release mechanisms, were investigated. It was found that one type of capsule released upon drying out of solution onto a surface and the other did not. Detailed release studies were carried out onto model surfaces to provide further evidence for this claim. A release rate was determined for the capsule that did release in the dry state.

5.1 Introduction

The application of a pesticide treatment to a crop introduces chemicals to the leaf surface of plants, the cuticle. The cuticle is a hydrophobic lipid structure, typically 0.1-10 μm thick^{2,3}. It can be divided into five generalised compartments – the epicuticular wax, the cuticle proper, the cuticle layer, the pectinous layer and the cell wall. Diffusive movement through these layers is controlled by the properties of the compound and the plant, environmental conditions and time.

Confocal laser scanning microscopy has been used previously to image both leaves and insects⁴⁻⁷, which are the substrates of interest in these studies. Three dimensional images of insect morphology have been constructed using the z-stacking ability of the confocal microscope along with 3D reconstruction techniques^{4,5}. In these instances, the autofluorescence of the insect cuticle was used to visualise small complex structures in insects. These studies demonstrated the fine scale of resolution that this instrument can achieve.

Plant cuticles have also been visualised using confocal microscopy^{6,7}. In one case⁶, selected isolated fruit and leaf cuticles were studied using the autofluorescence of phenolics and flavanoids present in the leaf cuticle to build up three-dimensional images of cuticular membranes. The wax layer of apple has been investigated in order to demonstrate how CLSM can be used as a technique for non-destructive analysis of biological specimens⁷. CLSM was used in this study to monitor the changes in the structure and thickness of the waxy cuticle during storage of apples.

The permeability properties of the cuticular membrane have been investigated using techniques other than CLSM⁸⁻¹⁰. The rates of penetration of alkali metal cations through isolated pear fruit cuticular membranes were studied as a function of pH using atomic absorption spectroscopy⁸. Liquid scintillation spectrometry was used to measure the penetration of radioactive 2-(1-naphthyl)-[1- ¹⁴C]acetic acid (NAA) from simulated spray droplets through isolated tomato fruit cuticle⁹ and the same approach was also used to investigate the co-permeability of ³H-labelled water and ¹⁴C-labelled organic acids across isolated cuticular membranes of various plant species¹⁰.

Confocal microscopy has been introduced as a technique which could be used to study the uptake of pesticides into plant foliage¹¹⁻¹³. In one study, three fluorescent dyes of contrasting polarities and low molecular weight were selected to represent foliage-applied pesticides¹¹. The transcuticular diffusion behaviour, the compartmentation into epidermal cells and the influence of surfactant on the uptake of these fluorescent compounds were visualised using CLSM. Differences were found in the rates of diffusion of the dyes across the cuticle and also in the distribution of the different dyes into the cell compartments within the leaves.

The release of active ingredient from microcapsules into solution has been studied extensively as described in Chapter 4. The main use of these microcapsules is

for the controlled delivery of pesticides to crops and hence insects. In reality the microcapsules release their active ingredient when in the dry state i.e. once they have dried down out of solution onto the crop or insect of interest. It would therefore be beneficial to study the release rates of these microcapsules in the dry state.

The investigations by Liu et al described above¹¹⁻¹³ have demonstrated that it is viable to use CLSM as a technique to investigate the uptake of pesticide into plant foliage. However, in these studies, the pesticide was applied directly to the plant surface. This chapter details how CLSM has been used to investigate the release of pesticides from microcapsules onto the leaves of *Prunus laurocerasus*.

The properties of the cuticle of the *Prunus laurocerasus* have been studied extensively^{10,14-16}. The leaf has an extremely thick waxy cuticle which should encourage pesticide to release from the microcapsule within a reasonable time span. The permeation properties of the leaf cuticle have been well documented.^{10,16}

5.2 Experimental

5.2.1 Leaf, caterpillar and microcapsule selection

The leaves used in these investigations were from the *Prunus laurocerasus* plant, also known as the Cherry Laurel, which was cultivated in a garden centre near Coventry and potted and kept outside. A single leaf was removed from the plant on the day of the experiment. The end of the cut leaf was kept moist during experiments using a small quantity of cotton wool soaked in water.

The caterpillars used were supplied by Syngenta (Jealott's Hill Bracknell). They were stored in the freezer and defrosted prior to use. Two species of caterpillar were investigated; the *Heliothis virescens* (tobacco budworm) and the *Plutella xylostella* (Diamond Back Moth).

Three types of microcapsule were used in these investigations. Two of them, the Nile red and the lambda cyhalothrin capsules have been mentioned previously in Chapter 4. Both of these capsules were made by the interfacial condensation polymerisation process using the isocyanate monomers P MPPI and TDI described in section 1.1.2. The third microcapsule studied was formed by the cross-linking of a butylated urea-formaldehyde prepolymer with a tetrafunctional thiol (see section 1.1.2). These capsules contained the pesticide emamectin benzoate, the structure of which is shown in Figure 2.6.

5.2.2 Confocal microscopy measurements

For the detailed study of the structure of the leaf of the *Prunus laurocerasus*, a cork borer was used to cut a circle of diameter 1 cm out of the leaf avoiding the veins in the leaf. The underside of the leaf was attached to a glass slice using a sticky tab and a cover slip placed on top of the leaf. A drop of immersion oil (Zeiss ImmersolTM 518F) was placed on the cover slip and the objective was immersed in the oil and focused on the surface of the leaf.

An oil-immersion objective was used (Zeiss, Plan-neofluar 40x / 1.3 W) to record high resolution (1024 x 1024 pixels, 12 bit pixel, averaging 4 times) frames through the leaf every 1 μm in order to build up a detailed z-stack of images through the leaf. In order to observe the autofluorescence of the leaf, both the helium/neon (543 nm) and the argon (488 nm) lasers were used in conjunction with long pass 560 nm and band pass 505-530 nm filters, respectively. A 3D projection of the leaf was built up using the image manipulation software of the microscope (Zeiss).

To study the characteristics of the caterpillar cuticle, a single caterpillar was defrosted and placed on a glass slide under the microscope. An objective lens (Zeiss,

epiplan-neofluar 50x/0.80 W) was used in air to take a z-stack through the cuticle of the caterpillar. The slices taken in the z-stack were 1 μm apart (1024 x 1024 pixels, 8 bit pixel, averaging 4 times). A 3D projection of the caterpillar was built up as for the leaf using the image manipulation software. The laser used to image the autofluorescence of the caterpillar cuticle was the argon (488 nm) laser with a long pass filter (505 nm).

To image the Nile red microcapsules on the surface of the *Heliothis virescens* caterpillar, a droplet of solution containing the microcapsules suspended in water was placed on the surface of the caterpillar and allowed to dry. A z-stack was then taken of the capsules on the surface of the caterpillar using the same objective and slice properties as previously used to study the caterpillar. The lasers used were the helium/neon (543 nm) and the argon (488 nm) lasers in conjunction with long pass 560 nm and band pass 505-530 nm filters, respectively.

Release was studied from the emamectin benzoate capsules and the lambda cyhalothrin capsules onto the leaf of the *Prunus laurocerasus*. For these time series studies, an intact leaf was used with its cut end wrapped in cotton wool soaked in water. Release studies were also carried out on the emamectin benzoate containing capsules onto borosilicate glass slides and Parafilm (American national, Chicago, IL).

A droplet of solution containing the microcapsules suspended in water was placed upon the surface of interest and allowed to dry. A slice was taken through the centre of three capsules every hour using an objective lens (Zeiss, epiplan-neofluar 50x/0.80 W). Prior to and at the end of the experiment, a z-stack was taken through the capsules of interest and also capsules which were not investigated in this time sequence. The slices were taken every 1 μm through the specimen. The lasers and filters used were as described for the imaging of the leaf surface.

In each case the confocal aperture and background offset were adjusted to achieve the optimum compromise between resolution and image intensity.

5.3 Results and Discussion

5.3.1 High resolution imaging of *Prunus laurocerasus*

CLSM was used to determine the autofluorescent features of the leaf of the *Prunus laurocerasus*. Figure 5.1 shows a schematic representation of the structure of a leaf which can be used to aid in the identification of the structures observed with confocal microscopy imaging.

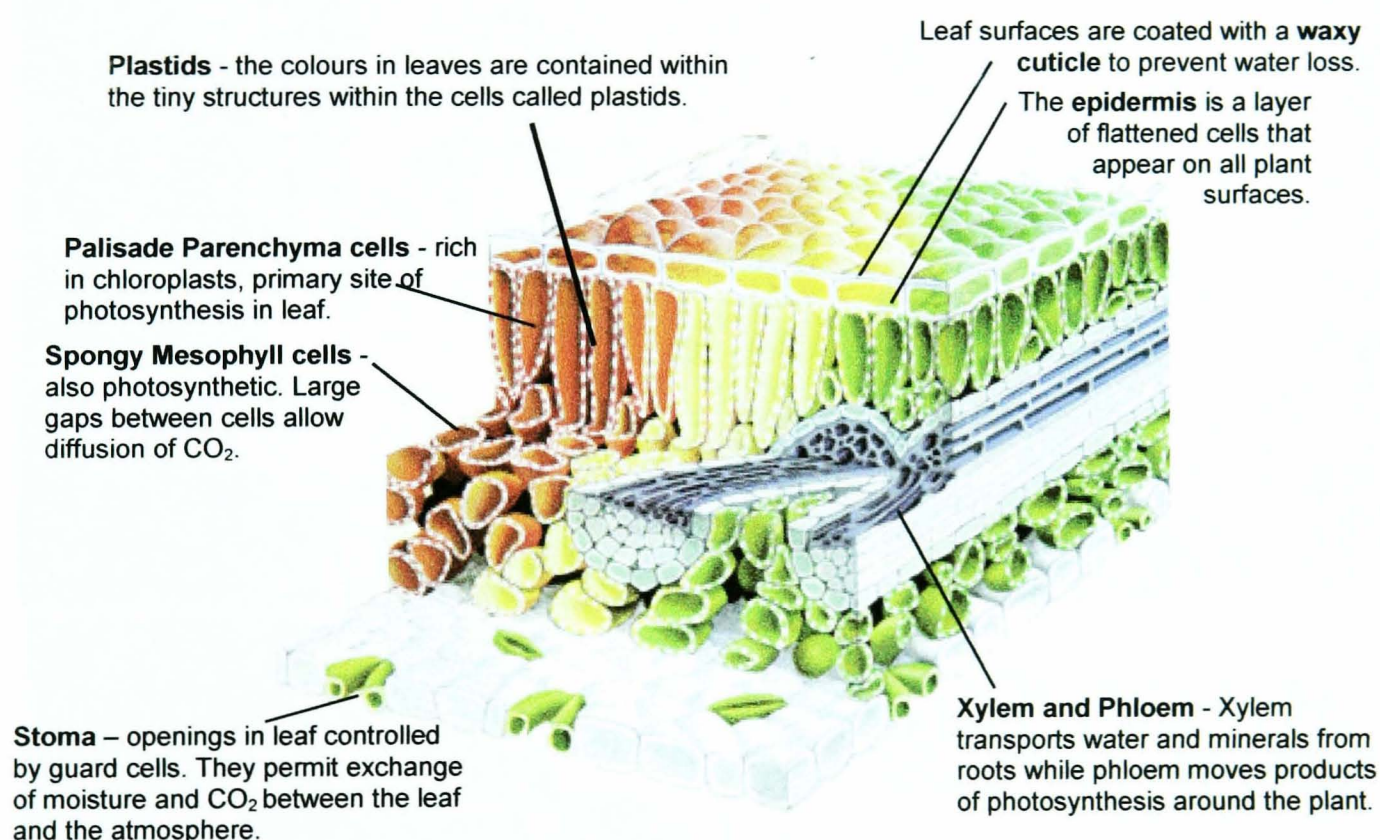


Figure 5.1 Schematic representation of the structure of a leaf showing the different components present within the leaf. Reproduced from reference¹

High resolution slices were taken at 1 μm intervals through the leaf starting above the leaf and passing through it. Signal averaging (as described above) was used to optimise the image resolution. Figure 5.2 shows a representative sample of slices taken through the leaf surface (Figure 5.2(a)), a 3D reconstruction of the total slices taken (Figure 5.2(b)) and finally an orthogonal cross section of the x-z and y-z planes through the leaf of the *Prunus laurocerasus* (Figure 5.2 (c)).

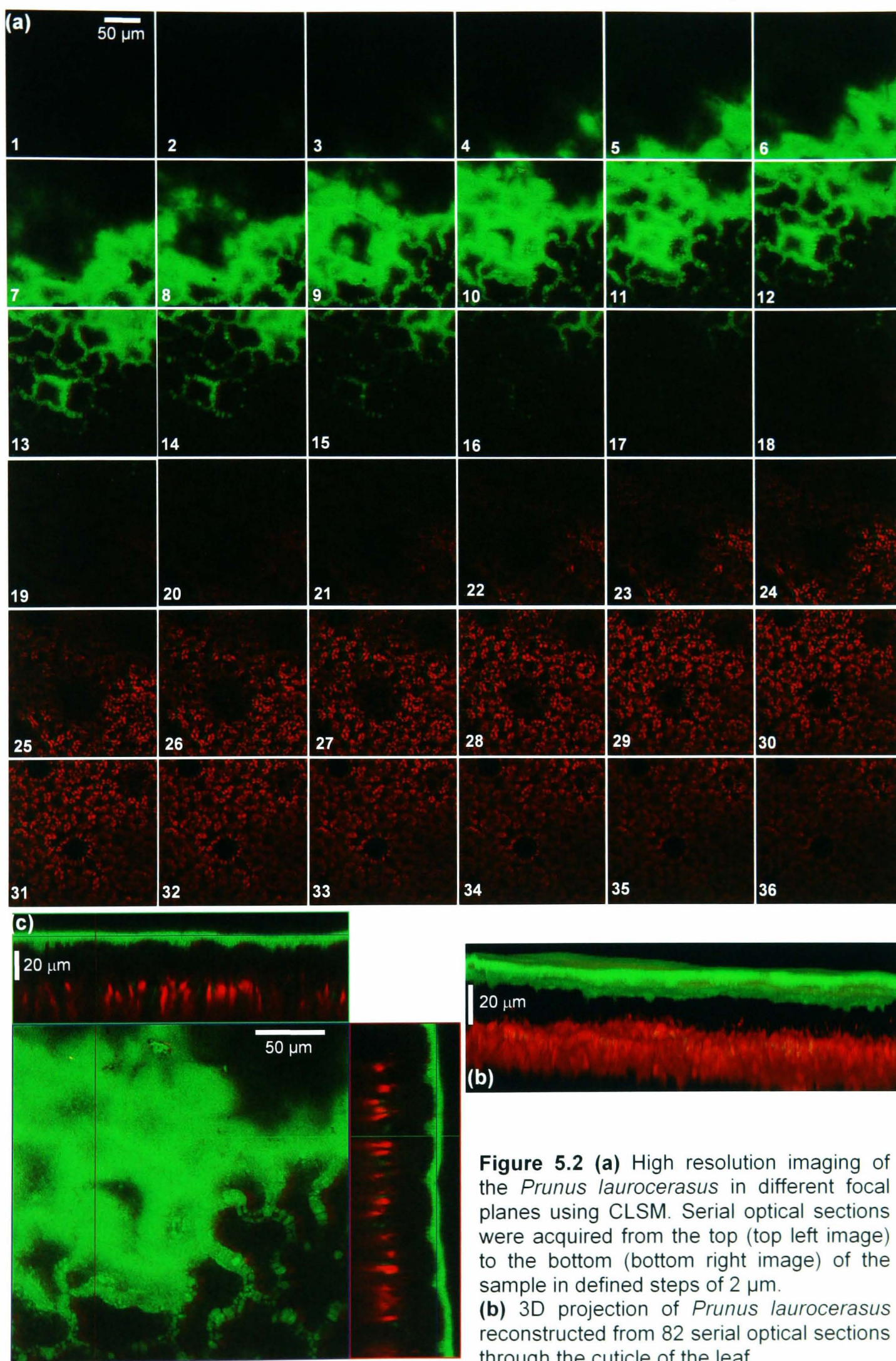


Figure 5.2 (a) High resolution imaging of the *Prunus laurocerasus* in different focal planes using CLSM. Serial optical sections were acquired from the top (top left image) to the bottom (bottom right image) of the sample in defined steps of 2 μm . (b) 3D projection of *Prunus laurocerasus* reconstructed from 82 serial optical sections through the cuticle of the leaf.

(c) Single optical slice on surface of *Prunus laurocerasus* and reconstructions of 82 serial optical sections (step size 1 μm) to produce orthogonal cross-sections in the x-z and y-z planes, along directions defined by the green and red line. The position of the single slice image in the z-stack is shown by the blue line in the x-z and y-z orthogonal projections.

In all of the images shown in Figure 5.2 the solid green area observed is the waxy cuticle of the leaf. From Figure 5.2 (a) it is apparent that the cuticle wraps around the upper epidermal cells of the leaf. The outline of the top of these cells can be observed as irregular spherical objects shown in slices 8-16 within the z-stack. Figure 5.2 (b) and (c) also show this effect on the underside of the waxy cuticle.

The most impressive part of these images is the autofluorescence observed of the chloroplasts present in the palisade and spongy mesophyll cells within the structure of the leaf. These can be seen extremely clearly as red objects in the confocal images. The chloroplasts appear to be distributed in circular structures and this is because they are present in the plastids in the cell wall of the palisade cells, so in effect they are outlining these cellular structures.

This is an excellent example of how the confocal microscope can be used for direct non-invasive imaging. In this case the leaves of the plants studied were discs that had been cut out of the leaf but it is possible that the leaf could be examined whilst still attached to the plant ensuring that the plant was still alive.

In order to ascertain how best to prepare the leaf sample of the *Prunus laurocerasus* in the release experiments, the leaf was monitored over time to see how its conformation changed for various preparations. A z-stack through the leaf was taken every half hour on two samples which had been prepared in a different manner. For the first sample, a cork borer was used to remove a disc of diameter 1 cm from the leaf, which was then stuck down onto a glass slide using a sticky pad. It was thought that this may give the best, flat surface to work with. The second sample used an intact leaf connected to water soaked cotton wool, stuck down to the microscope stage with a sticky tab. Figure 5.3 demonstrates how the innards of the leaf changed with time (a) on a disc of a leaf and (b) on an intact leaf attached to water soaked cotton wool.

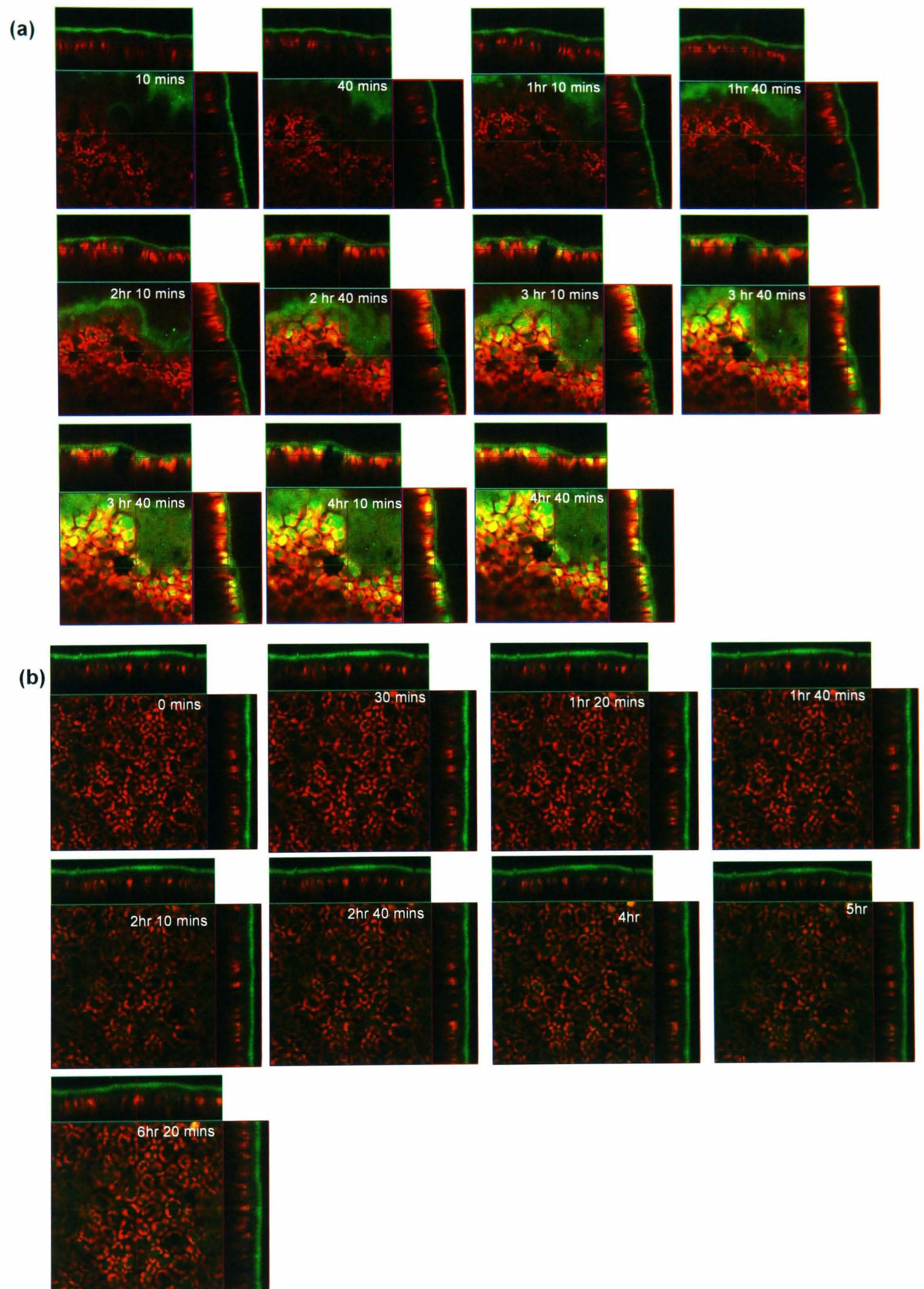


Figure 5.3 Series of single optical slices taken just below cuticle of *Prunus laurocerasus* and reconstructions of 82 serial optical sections (step size 1 μm) to produce orthogonal cross-sections in the x-z and y-z planes, along directions defined by the green and red line. The position of the single slice image in the z-stack is shown by the blue line in the x-z and y-z orthogonal projections. Each slice in the series was taken in the same position of the leaf at half hour time intervals. Samples used were (a) a 1 cm diameter disc cut out of a leaf and (b) an intact leaf attached to water soaked cotton wool.

From the images shown in Figure 5.3 it is obvious that when a disc cutting from the leaf is used, the conformation of the leaf changes dramatically over a very short period of time. When an intact leaf is used, the internal structure of the leaf appears to be much more stable and its internal structure is barely altered over the time period studied.

It can be observed in Figure 5.3(a) that the epidermal cells situated below the waxy cuticle of the leaf appear to collapse so that there is little or no layer of cells between the chloroplast containing palisade and spongy mesophyll cells and the waxy cuticle. The x - z orthogonal cross section shows that the surface topography of the leaf changes as the leaf dries out with a ridge developing within the cuticle of the leaf.

These studies showed that in order to carry out release studies of microcapsules on the surface of a leaf of the *Prunus laurocerasus*, an intact leaf should be used as the drying out effect observed for the leaf not kept hydrated may have a dramatic effect on the release properties of the microcapsule.

5.3.2 Release studies of emamectin benzoate and lambda cyhalothrin capsules

The studies in this thesis are largely concerned with the release from lambda cyhalothrin containing capsules. These capsules work by releasing their oily core once they have either dried down from aqueous solution onto the surface of sink materials, such as a leaf or caterpillar cuticles or, as shown in Chapter 4, the microcapsules are in the presence of an organic solvent.

The main objective of the studies in this chapter is to examine the microcapsule system in the most relevant situation, i.e. release onto a leaf. Figure 5.4 shows images of microcapsules with the 15% wall thickness and 1:1 ratio of cross linking monomers, during release of the contents onto the leaf of *Prunus laurocerasus*.

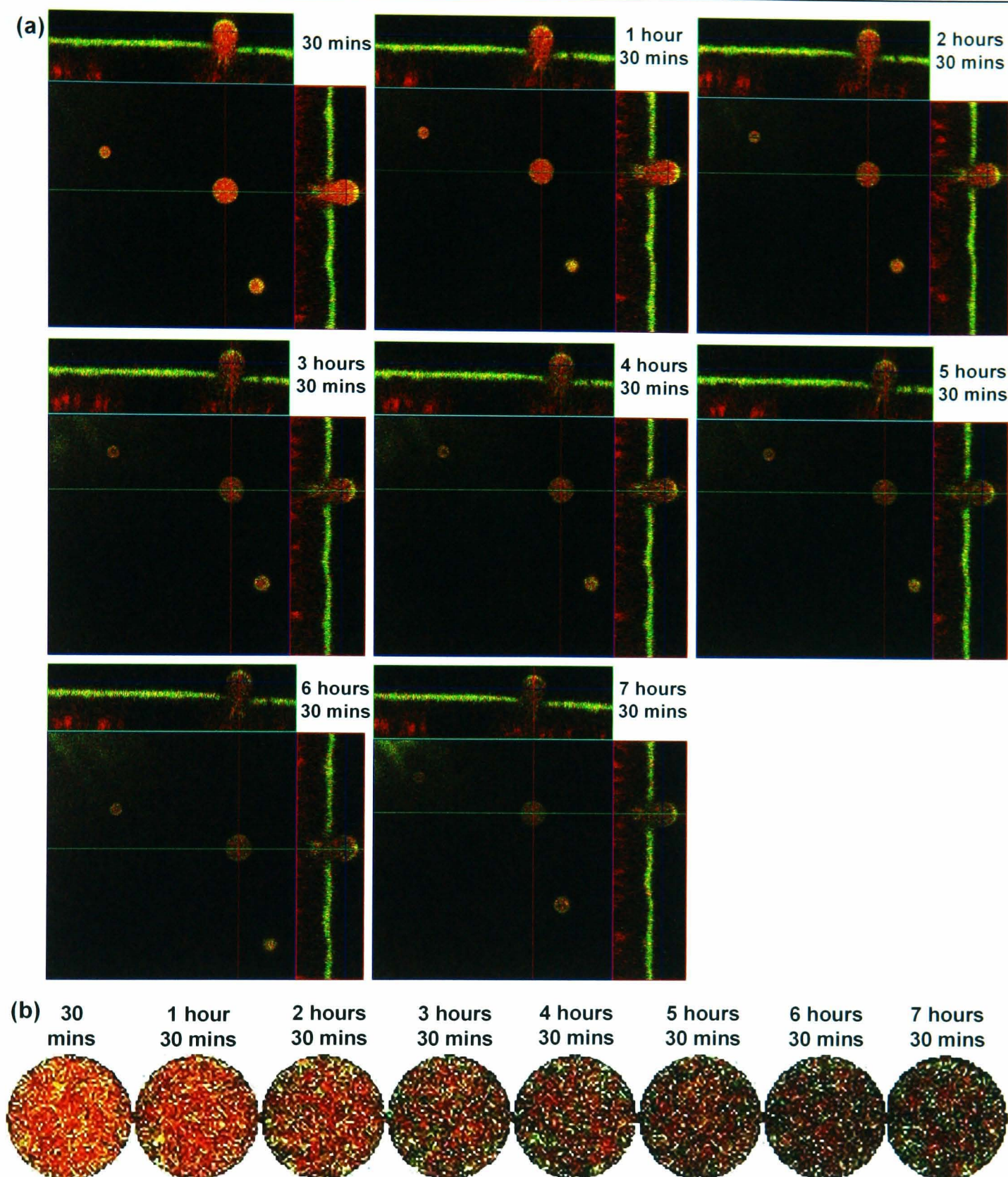


Figure 5.4 (a) Series of single optical slices taken in the centre of a single microcapsule on the surface of a leaf of the *Prunus laurocerasus* and reconstructions of 55 serial optical sections (step size 1 μm) to produce orthogonal cross-sections in the x-z and y-z planes, along directions defined by the green and red lines. The position of the single slice image in the z-stack is shown by the blue line in the x-z and y-z orthogonal projections. Each slice in the series was taken in the same position of the leaf at hour time intervals. **(b)** Slices taken through the centre of a single capsule, showing the decrease in fluorescence relating to the release of pesticide with time.

The images shown in Figure 5.4, above, show clearly that fluorescence from the capsule decreases with time. Fluorescence from the microcapsule can be attributed to the presence of the pesticide lambda cyhalothrin within the microcapsule. Thus it can be

seen quite clearly in both Figures 5.4(a) and (b) that the microcapsule releases pesticide over the time period studied. The release profile is represented graphically in Figure 5.5., in terms of normalised intensity, I_t/I_0 , as a function of time, t , where I_0 is the initial fluorescence intensity within the capsule and I_t is the fluorescence intensity within the capsule at time, t .

From the orthogonal cross sections in the x - z and y - z planes, it appears that the microcapsule releases its contents into the leaf. Unfortunately, the location to which release occurs cannot be observed unequivocally using this specific pesticide and leaf combination, as the cuticle of the leaf exhibits strong autofluorescence at wavelengths used to excite the pesticide.

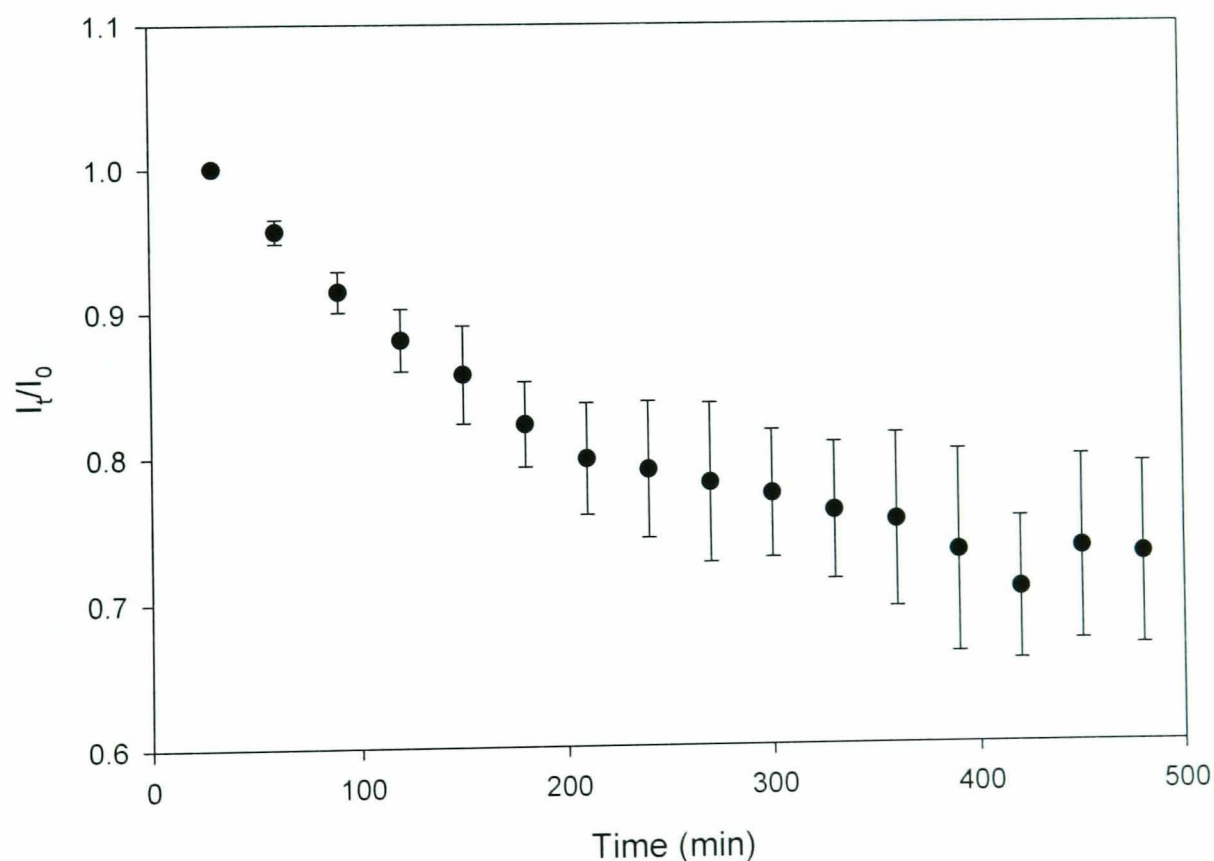


Figure 5.5 Plot of the release of the pesticide lambda cyhalothrin from microcapsules onto a leaf of *Prunus laurocerasus* as a function of time.

A simple model for the release from the lambda microcapsules can be proposed that allows the rate constant for release to be estimated. Consider the schematic shown in Figure 5.6:

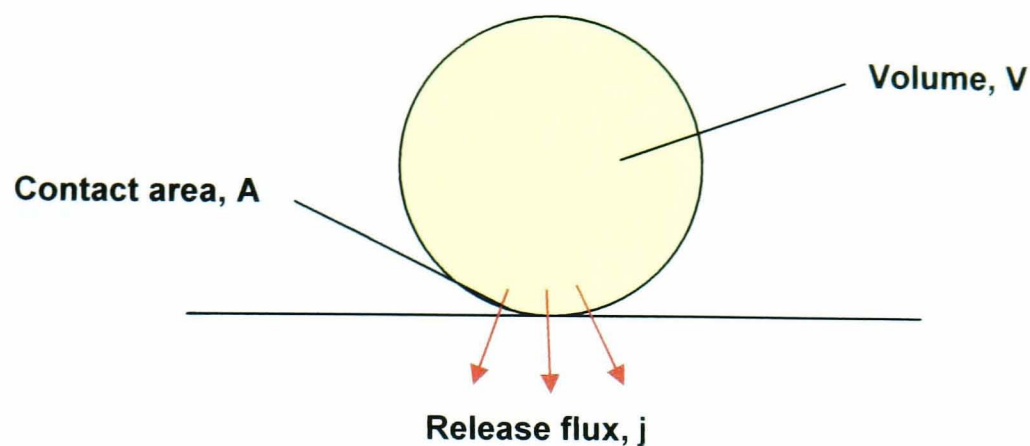


Figure 5.6 Schematic representation of parameters involved in the release of lambda cyhalothrin from a polymeric microcapsule onto a surface.

The equation relating to the release of a species from a sphere onto a surface is given by:

$$V \frac{dc}{dt} = -Aj \quad 5.1$$

where V is the volume of the microcapsule, c is the concentration inside the capsule at any time, t , A is the contact area of the capsule with the surface upon which it is placed and j is the release flux of species out of the microcapsule. The equation assumes that diffusion inside the capsule is fast compared to that outside and the timescale of the experiment (which is long) and that there are no limitations from the ‘sink’ onto which the material is released.

The rate constant for release, k' , is related to the release flux and concentration of species inside a capsule by equation 5.2

$$j = k'c \quad 5.2$$

It follows that:

$$V \int_{t=0}^t \frac{dc}{c} = -Ak' \int dt \quad 5.3$$

$$V \ln c = -Ak't \quad 5.4$$

$$V \ln \frac{c_t}{c_0} = -Ak't \quad 5.5$$

Since concentration is proportional to intensity,

$$\ln \frac{I_t}{I_0} = \frac{-Ak't}{V} \quad 5.6$$

A plot of $\ln \frac{I_t}{I_0}$ against time will give a straight line, the gradient of which will be $-\frac{Ak'}{V}$. The contact area, A , of the capsule with the surface can be estimated from the confocal images which means the rate constant for the release can also be estimated. Figure 5.7 shows this plot for the lambda cyhalothrin release onto *Prunus laurocerasus*.

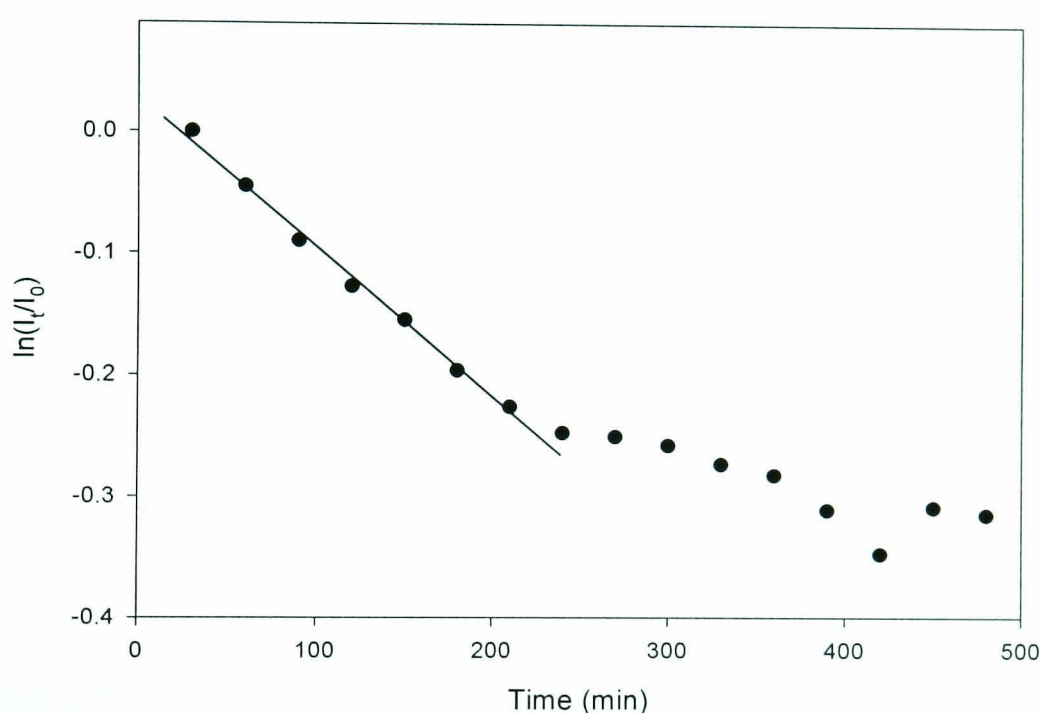


Figure 5.7 Plot of $\ln(I_t/I_0)$ against time for lambda cyhalothrin release onto *Prunus laurocerasus*.

The initial rate of release from the microcapsule can be measured from the gradient of the early part of the release profile. The mean contact area of microcapsule with the leaf is $6.81 \times 10^{-11} \text{ cm}^2$ and V is $6.48 \times 10^{-15} \text{ cm}^3$. Therefore the rate constant for the release of lambda cyhalothrin from a polymeric capsule onto a leaf of *Prunus laurocerasus* is $1.12 \times 10^{-7} \pm 0.05 \text{ cm s}^{-1}$.

It was considered beneficial to compare the release properties of these polyurea lambda cyhalothrin containing capsules with a capsule which had a different mechanism

of release. The capsules containing the pesticide emamectin benzoate (for structure see Figure 2.6) are formed by the cross linking of a butylated urea-formaldehyde prepolymer with a tetrafunctional thiol (see section 1.1.2). These microcapsules have a different mechanism of release to that of the lambda capsules.

These capsules have been designed so that they release once inside the pest. They have a base-trigger release system in which the capsule wall, when exposed to the basic conditions that occur inside the caterpillar, changes its conformation to become permeable to the pesticide. They are designed so as not to release when applied directly to the crop. It has been shown, however, by research carried out internally at Syngenta, that there may be some loss from the capsules upon application¹⁷.

Using CLSM, it may be possible to visualise any processes that occur when these capsules are applied to a leaf. Figure 5.8 shows a series of 3D projections of a single emamectin benzoate capsule on the leaf of the *Prunus laurocerasus* taken at differing time intervals. A time series of slices through the centre of a single microcapsule is also shown.

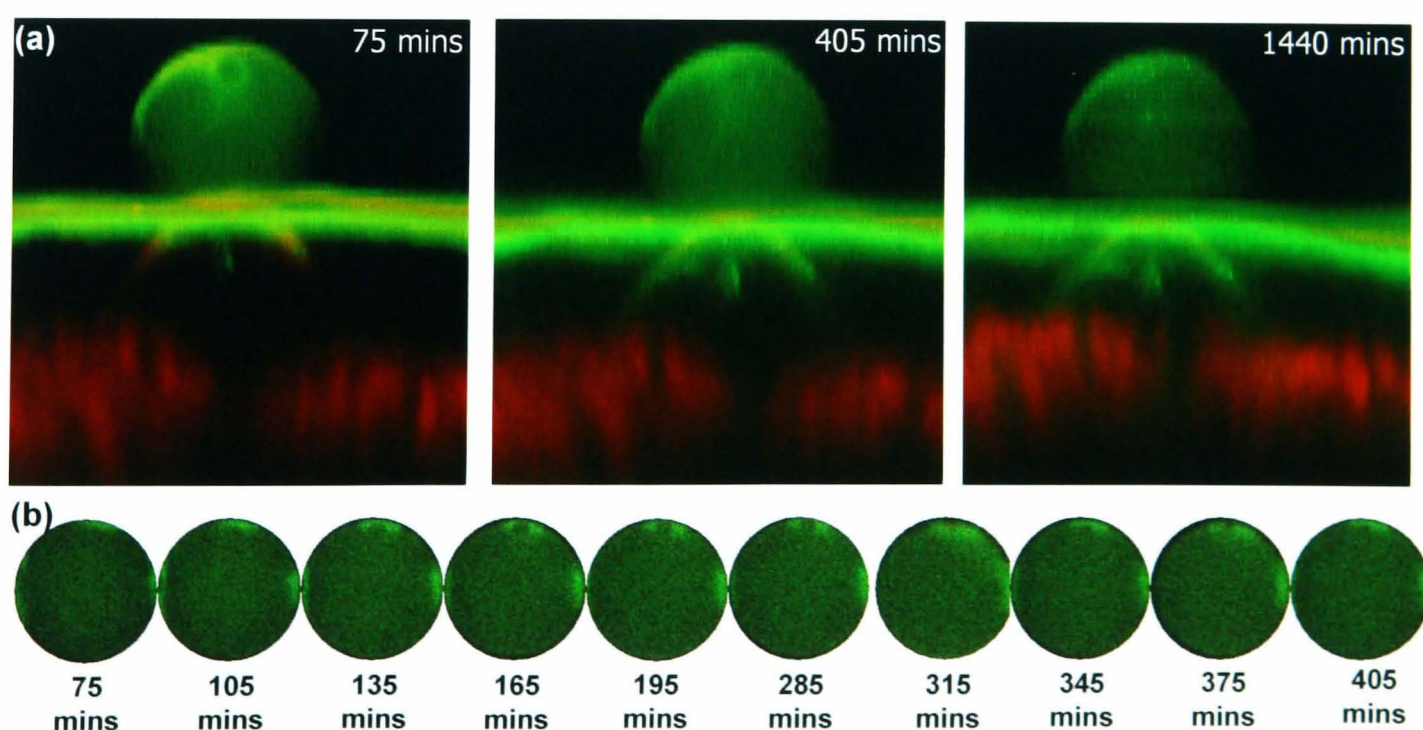


Figure 5.8 (a) 3D projections of an emamectin benzoate capsule on the surface of a leaf of *Prunus laurocerasus* reconstructed from a z-stack consisting of 125 slices taken 1 μm apart. The images were taken at different times after application of microcapsule to the leaf. (b) Slice through the centre of the emamectin benzoate capsule taken at half hour time intervals.

The images shown in Figure 5.8(a) provide an interesting insight into the processes that occur within the capsule upon application to the surface of a leaf. It appears that the fluorescence intensity within the capsule is stable over the time period studied for the lambda release (0 to 405 mins) suggesting that little or no release occurs. The small changes in fluorescence observed are likely to be associated with the change in conformation of the capsule upon drying down from solution onto the leaf.

Comparing the release of this capsule with the release from a lambda cyhalothrin containing capsule for the same period of time, it is clear that the two capsules are very different in their behaviour on surfaces. The plot shown in Figure 5.9 shows the different intensity profiles measured from a slice through the centre of these two types of capsules.

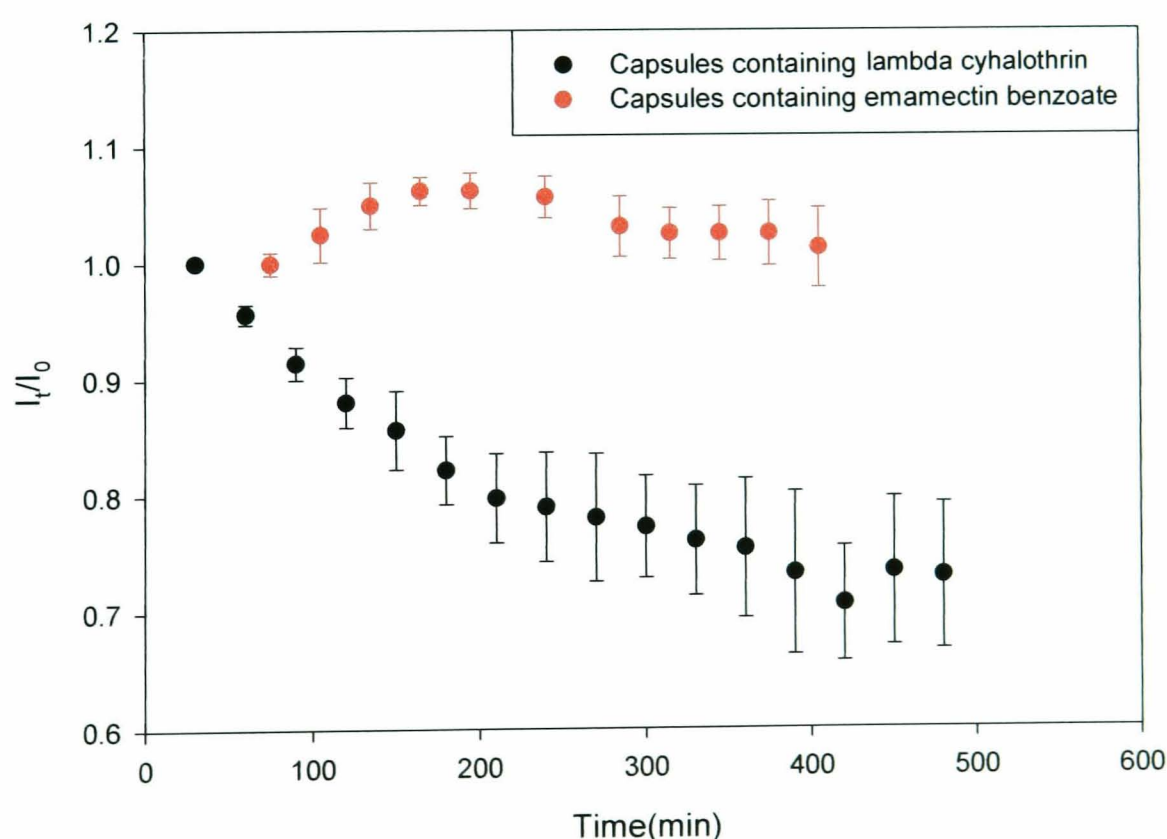


Figure 5.9 Graph detailing the release of the pesticides • lambda cyhalothrin and • emamectin benzoate from microcapsules onto a leaf of the *Prunus laurocerasus*.

Figure 5.9 shows clearly that the lambda cyhalothrin capsules release at an increased rate over the time period studied. The emamectin benzoate capsules in fact

appear to have an extremely small change in fluorescence intensity compared to that of the lambda cyhalothrin capsules indicating that little release occurs.

However, when the capsule was left overnight on the leaf it is apparent from the 3D projection at 1440 mins, shown in Figure 5.8 (a), that a small decrease in fluorescence intensity is observed. In order to investigate this further, detailed investigations were carried out on the release of the pesticide from the microcapsule onto the surface of Parafilm and glass. These two surfaces were chosen for this study as they exhibited distinctly different surface characteristics; the hydrophilic borosilicate glass slide and the extremely hydrophobic Parafilm. It was expected that if capsules did release in the dry state, with no trigger, then it would release far more quickly onto Parafilm than onto glass, as the waxy surface would act as a sink site for the pesticide which is dispersed in an oily solvent.

Figure 5.10 shows a comparison between the average release profiles of emamectin benzoate capsules when on a hydrophilic glass surface and when on the hydrophobic Parafilm coated glass slide.

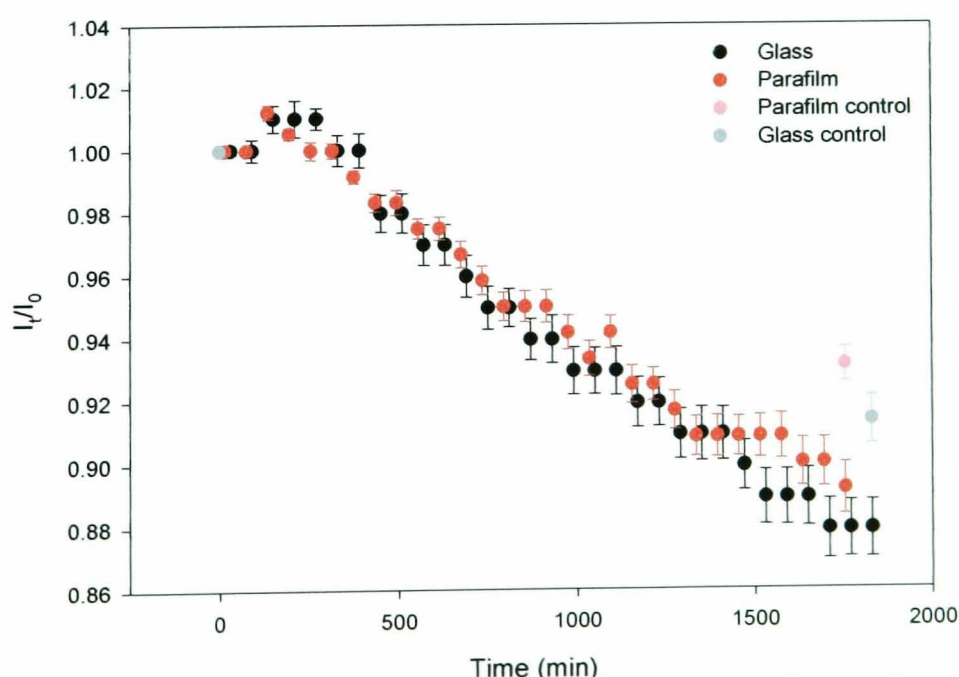


Figure 5.10 Graph detailing the average release from microcapsules containing the pesticide emamectin benzoate when applied to • a glass slide and • a glass slide covered in Parafilm.

It is apparent from the graph shown in Figure 5.10 that the surface upon which the capsule is located does not have a significant effect on the fluorescence-time profile.

In fact the average release profiles measured are similar within error. Control experiments were carried out along with these release profiles in order to ascertain if the decrease in fluorescence observed in these measurements was real or due to photobleaching of the pesticide within the capsule. It was found that there was minimal photobleaching of the pesticide during the measurement. The results of the control experiments are also shown in Figure 5.10.

The decrease in intensity shown here is extremely small compared to what is observed for the lambda cyhalothrin capsules in half the time. However, a small decrease in fluorescence is observed over the time period studied. The fact that the surface upon which the capsule was placed has little effect upon the fluorescence-time profile, suggests that the change in fluorescence is unlikely to be due to release out of the microcapsule. Rather, the small change in fluorescence which is observed could be due to small changes in the volume of the capsule over time after it has dried out of solution onto the surface of interest. For example, the 10% change in fluorescence observed would only require a change in the radius of the microcapsule of a few percent which would not even be seen by the confocal microscope.

Another explanation for the decrease in fluorescence intensity over time, without a trigger, is that upon drying down, the pesticide may partition into the capsule wall. The results from these studies are further evidence that the two types of capsules studied have different stabilities on surfaces.

5.3.3 High resolution imaging of caterpillars

Microcapsules are applied in a spray over crops or leaves. As well as sticking to crops, these microcapsules are designed to stick to the pests, enabling the pesticide to pass into the pest through its cuticle. It would therefore be beneficial to study the release

of active from microcapsules onto the surface of caterpillars. CLSM was used to build up 3D topographical images of two types of caterpillar, with typical results shown in Figure 5.11 and 5.12.

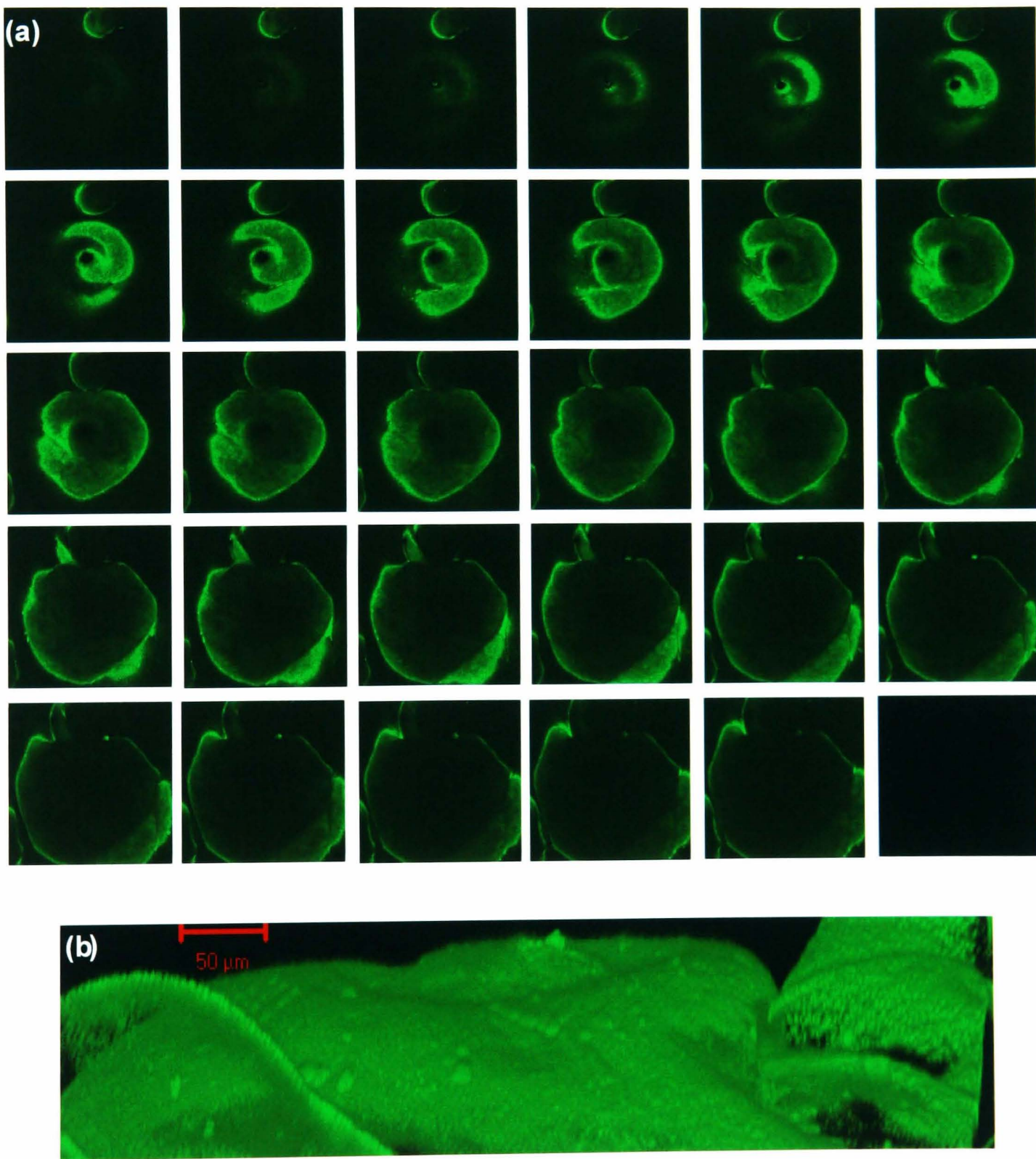


Figure 5.11 (a) High resolution image series z-stacking through the cuticle of *Plutella xylostella*. Images shown are taken at 5 μm intervals from above to below the cuticle. **(b)** 3D projection reconstructed from 150 serial optical sections through the cuticle of the caterpillar.

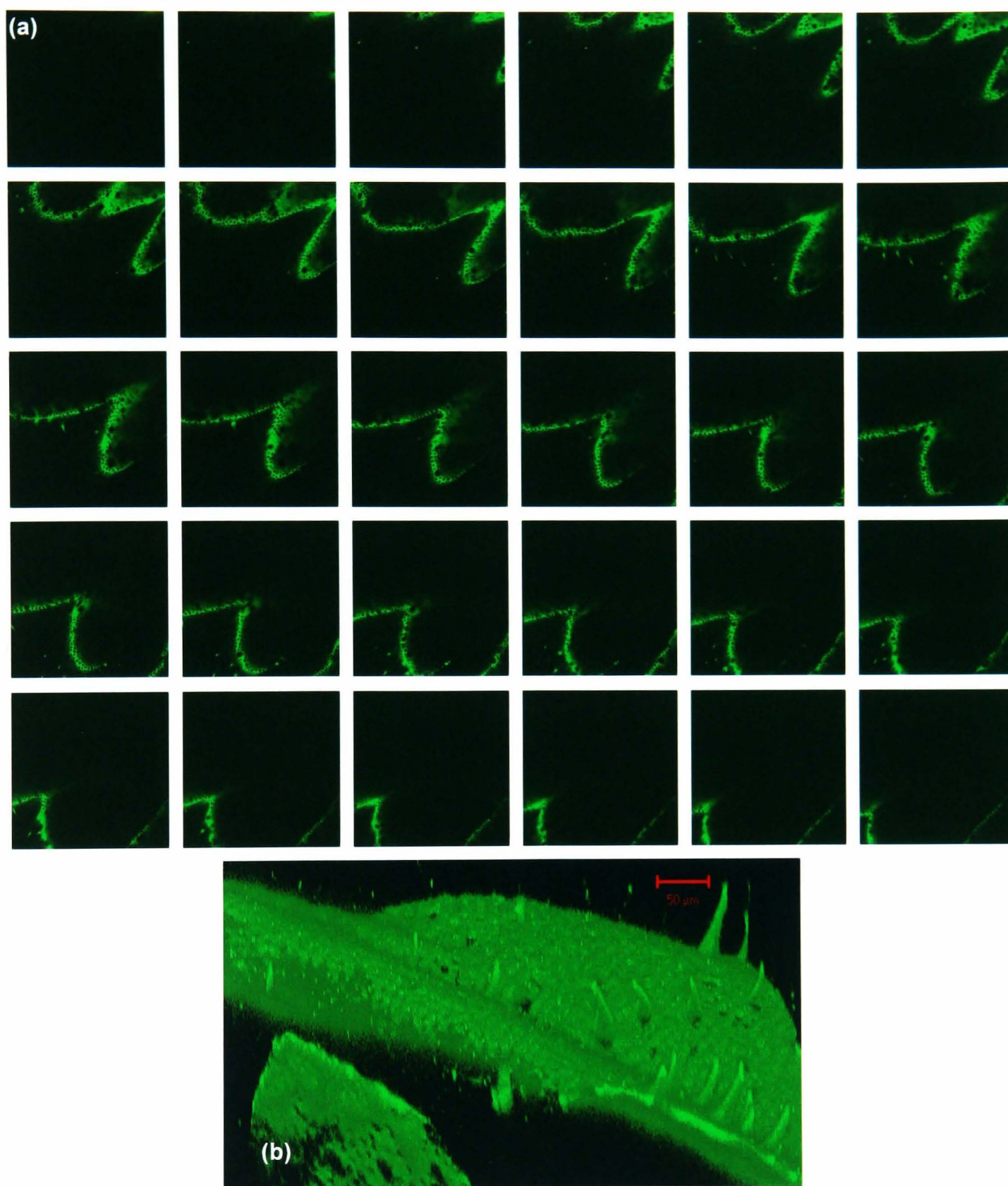


Figure 5.12 (a) High resolution image series z-stacking through the cuticle of *Heliothis virescens*. Images shown are taken at 5 μm intervals from above to below the cuticle. (b) 3D projection reconstructed from 150 serial optical sections through the cuticle of the caterpillar.

From these studies it became apparent that the cuticle of both of these caterpillars is very strongly autofluorescent at the wavelengths used to excite both of the pesticides, lambda cyhalothrin and emamectin benzoate. The surface topography of the caterpillars differs dramatically with one having far more hair than the other. Both types, however, have extremely irregular surfaces. The unevenness of the cuticle and its

strong autofluorescence meant that it was extremely difficult to locate any of the capsules containing the two pesticides used in these studies. It was possible however to image the Nile red capsules on the surface of the caterpillar (Figure 5.13).

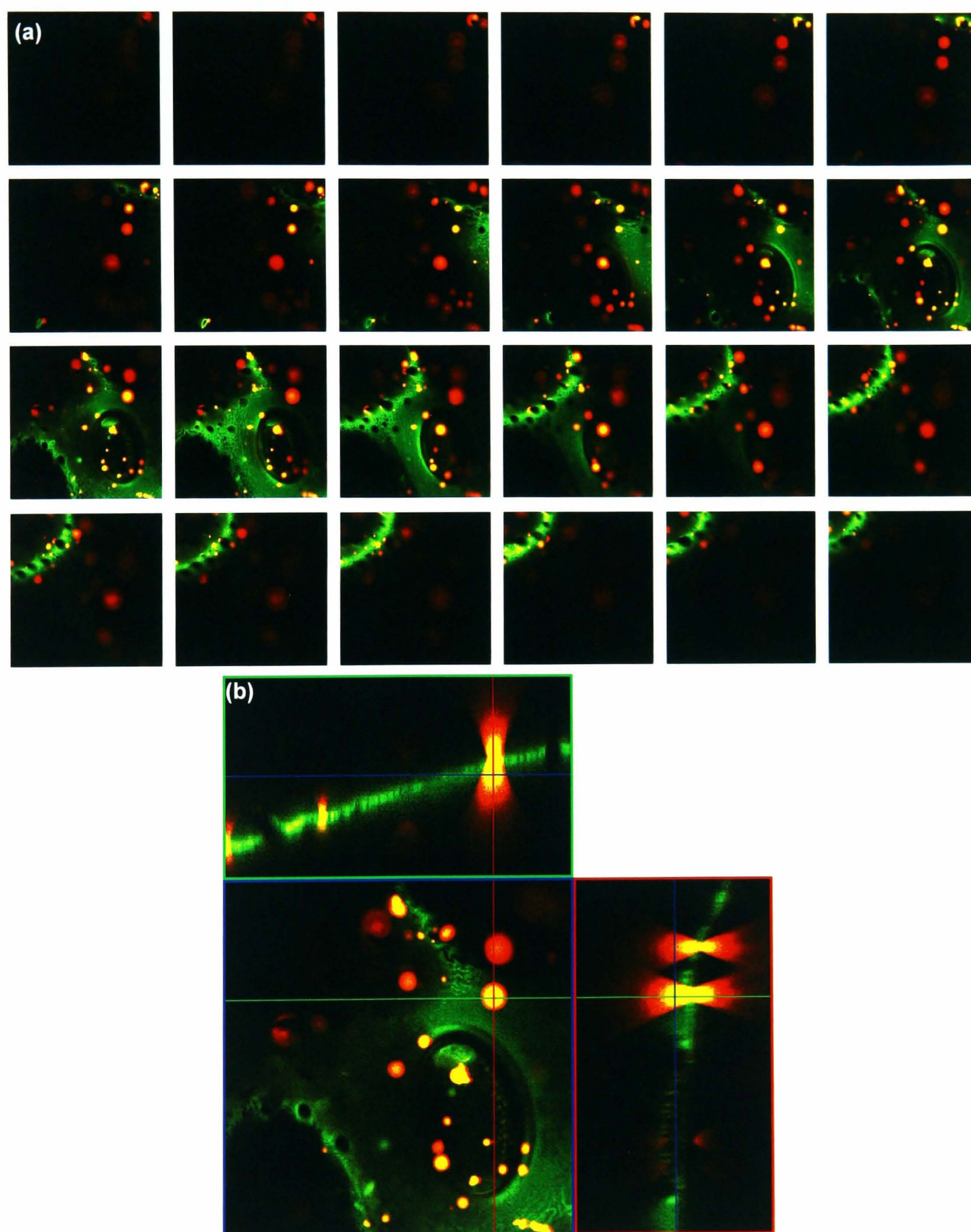


Figure 5.13 (a) z-stack through Nile red microcapsules on the surface of the *Heliothis virescens*. Images were taken every 5 μm . (b) Single optical slice on surface of *Heliothis virescens* and reconstructions of 150 serial optical sections (step size 1 μm) to produce orthogonal cross-sections in the x-z and y-z planes, along directions defined by the green and red line. The position of the single slice image in the z-stack is shown by the blue line in the x-z and y-z orthogonal projections.

Although it is possible to visualise the Nile Red capsules on the surface of the caterpillar, the high gains used to visualise the caterpillar cuticle mean that the images of the capsules were not clear and have a reflected image which is not a true image. It has also been shown in experiments detailed in Chapter 4 that over time the Nile Red dye inside the capsules photobleaches and so the measurement of release rates would be difficult for this dye.

5.4 Conclusions

The high resolution imaging capabilities of CLSM have been used in this chapter to investigate the structure of leaf and caterpillar cuticles. This approach was also used the direct non-invasive properties of the technique to investigate the internal structure of the leaf of the *Prunus laurocerasus*. It has been shown how this technique can be used to investigate the effect of the preparation of leaf sample on the internal structure of the leaf.

The release properties of the lambda cyhalothrin containing capsules and the capsules encapsulating the emamectin benzoate pesticide were investigated onto the leaf of the *Prunus laurocerasus*. It was found that the lambda cyhalothrin capsules showed a significant release over time whereas the emamectin benzoate capsules showed a decrease in fluorescence over time but it was not significant enough to be attributed to release of pesticide. A simple model was used to obtain a rate constant for release from the lambda cyhalothrin capsule.

The emamectin benzoate capsules were not designed to release in the dry state and so more detailed studies were carried out with the capsules deposited onto hydrophilic and hydrophobic surfaces to investigate whether or not the decrease in fluorescence observed on the leaf surface was due to release of pesticide from the

capsule. These studies revealed that the surface upon which the microcapsule was placed had no significant effect on the release, the same small decrease in fluorescence was observed. If this decrease was to be attributed to release then a large decrease should have been observed onto the hydrophobic surface. As this was not the case, the decrease in fluorescence could be due to changes in the microcapsule wall over time after drying down from solution, such as small volume changes. Alternatively, pesticide entering the microcapsule wall may also be a factor that causes a slight decrease in fluorescence observed.

5.5 References

1. <http://www.conservation.state.mo.us/nathis/seasons/fall/lefstruc/lefstruc.htm>.
2. Kirkwood, R. C. *Pestic. Sci.* **1999**, *55*, 69.
3. Kerstiens, G. *The Plant Cuticle: An integrated functional approach*; Bios Scientific Publishers: Oxford, 1996.
4. Klaus, A. V.; Kulasekera, V. L.; Schawaroch, V. J. *Microsc.-Oxf.* **2003**, *212*, 107.
5. Zill, S.; Frazier, S. F.; Neff, D.; Quimby, L.; Carney, M.; Dicaprio, R.; Thuma, J.; Norton, M. *Microsc. Res. Tech.* **2000**, *48*, 367.
6. Fernandez, S.; Osorio, S.; Heredia, A. *Plant Physiol. Biochem.* **1999**, *37*, 789.
7. Veraverbeke, E. A.; Bruaene, N. V.; Oostveldt, P. V.; Nicolai, B. M. *Planta* **2001**, *213*, 525.
8. Ersoz, M.; Duncan, H. J. *J. Colloid Interface Sci.* **1995**, *169*, 143.
9. Knoche, M.; Petrcek, P. D.; Bukovac, M. J. *Pest Manag. Sci.* **2000**, *56*, 1005.
10. Niederl, S.; Kirsch, T.; Riederer, M.; Schreiber, L. *Plant Physiology* **1998**, *116*, 117.
11. Liu, Z. *J. Microsc.-Oxf.* **2004**, *213*, 87.
12. Liu, Z. Q.; Gaskin, R. E. *Pest Manag. Sci.* **2004**, *60*, 434.
13. Liu, Z. Q.; Gaskin, R. E.; Zabkiwicz, J. A. *Weed Res.* **2004**, *44*, 237.
14. Jetter, R.; Schaffer, S. *Plant Physiology* **2001**, *126*, 1725.
15. Jetter, R.; Schaffer, S.; Riederer, M. *Plant Cell Environ.* **2000**, *23*, 619.

16. Kirsch, T.; Kaffarnik, F.; Riederer, M.; Schreiber, L. *J. Exp. Bot.* **1997**, *48*, 1035.
17. Shirley, I. *Private communication* **2004**.

Chapter 6

Preliminary studies on the combined use of CLSM and electrochemistry for the trace detection of heavy metal ions

In the previous two chapters, the release characteristics of microcapsules were investigated using confocal microscopy to monitor the change in fluorescence within a single capsule, which related directly to the amount of pesticide, which could be followed in time. It would be beneficial to extend the use of CLSM to monitor the diffusion characteristics of species away from surfaces into solution.

This chapter details preliminary studies of the development of a technique which is capable of visualising the release and diffusion of a species (Cd^{2+}) from a hemisphere in solution. Anodic stripping voltammetry has been used in conjunction with CLSM to monitor quantitatively and visually the preconcentration and release of Cd^{2+} into and away from a mercury hemisphere UME.

6.1 Introduction

6.1.1 Stripping Voltammetry

The hanging mercury drop electrode (HMDE) and the mercury film electrode (MFE) have been widely used for the detection of heavy metal ions³⁻¹¹. Heavy metals are reduced to the corresponding metal at reasonably negative potentials, and a large background current is recorded for a lot of electrode materials at these potentials. However, mercury has a large cathodic window in which measurements can be made because of the large hydrogen overpotential, making it the ideal material for these measurements.

To increase sensitivity and enhance detection limits, the mercury electrodes are often used in pre-concentration or stripping techniques. In these techniques a pre-concentration step accumulates the electroactive species into the small volume of a mercury electrode or onto the surface of an electrode. The material is then stripped from the electrode using a voltammetric technique such as linear sweep voltammetry (LSV). These techniques have been used for cations, anions and complexing neutral species, the detection limit being of the order of $10^{-10} \text{ M}^{9,10,12}$.

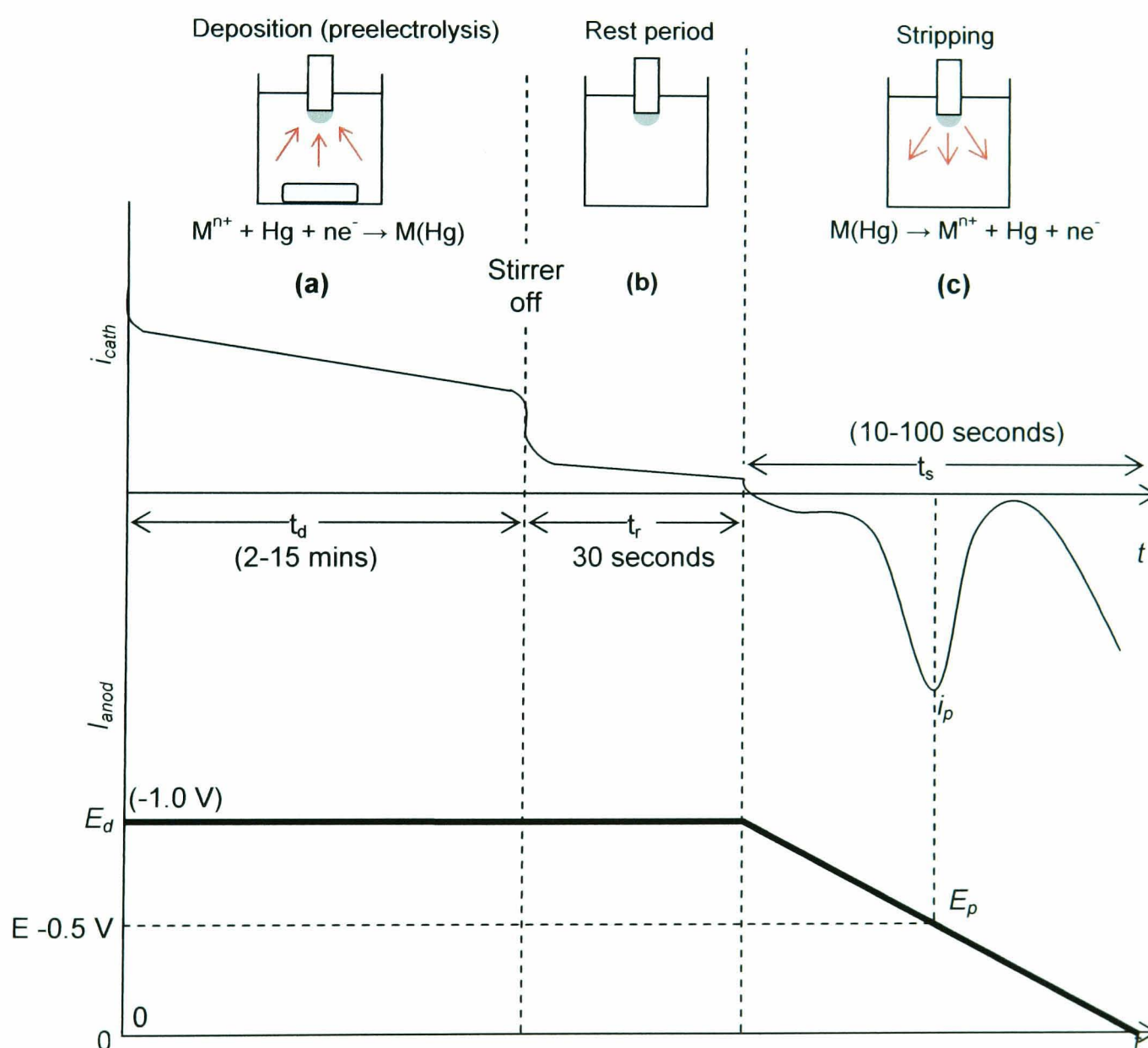


Figure 6.1 Principles of anodic stripping. Values shown are typical ones used; potentials and E_p are typical of Cu^{2+} analysis. **(a)** Preelectrolysis at E_d ; stirred solution. **(b)** Rest period; stirrer off. **(c)** Anodic scan ($v = 10\text{-}100 \text{ mV/s}$). Adapted from reference 2.

The stripping technique utilised in these studies is known as anodic stripping voltammetry, the principles of which are represented in Figure 6.1. The cathodic deposition step is carried out in a stirred solution with the electrode held at a potential

(E_d) which is several tenths of a volt more negative than the potential at which the metal is oxidised back to metal ions (E). After electrodeposition, a rest period is applied when the stirrer is turned off and the solution becomes quiescent allowing the concentration of metal within the mercury to become more uniform. The potential is finally scanned linearly towards more positive values in a stripping step.

The introduction of ultramicroelectrodes (UMEs) to the field of stripping analysis has brought with it a number of improvements to the technique^{3-8,13-18}. Studies have demonstrated that the use of UMEs resulted in the elimination of sample deoxygenation and stirring in the preconcentration step¹³. This is because the enhanced mass transport associated with small electrodes leads to a decrease in the preconcentration time negating the need for stirring and therefore removing one source of error in the experiment.

The utilisation of UMEs also led to miniaturisation and simplification of the instrumentation^{3,13-18}. Compared to stripping analysis conducted at conventional-sized mercury drops and thin mercury film electrodes⁹⁻¹¹, other important aspects of stripping analysis have been improved such as precision⁶, signal to noise ratio^{6,19}, sample consumption^{3,13,15} and throughput¹⁶.

There are a number of possible choices for the solid substrate on which to deposit mercury UMEs. The ideal substrate would be one which is easily wetted by mercury yet has a low solubility in mercury. Substrates that have been used in the past include glassy carbon which has the added advantage that the glassy carbon can also be used as an electrode for anion determinations²⁰. However, the substrate surface shows poor wetting leading to the formation of inhomogeneous scattered mercury droplets²¹.

Metals such as platinum, silver and gold lead to the formation of intermetallic compounds at the base metal, so restricting the cathodic potential window²². The use of

Pt-based Hg UMEs for routine stripping analysis was first demonstrated by Wehmeyer and Wightman⁶. It was shown that spherical drops could easily be made and that the dissolution of platinum was hindered by the presence of surface oxides and could often be neglected following deposition of a thick mercury layer. It has also been shown that mercury UMEs formed at platinum substrates are more stable hydrodynamically^{15,16,23}.

The use of Hg UMEs for stripping analysis instead of conventional-sized HMDEs has the added advantage that one of the important properties of UMEs is the low ohmic drop which characterises their relevant voltammetric responses²⁴. This feature allows measurements to be taken in highly resistive solutions, for example aqueous solutions which contain little or no supporting electrolyte²⁵⁻³². In cases where the addition of supporting electrolyte could lead to interference such as low solubility or interaction with the electroactive analyte, such experimental conditions may be beneficial.

6.1.2 Fluorescence detection of metal ions

Fluorescent probes that show a spectral response upon binding Ca^{2+} have enabled researchers to investigate changes in intracellular free Ca^{2+} concentrations using fluorescence microscopy, flow cytometry and fluorescence spectroscopy³³⁻³⁸. It has been found that many of the fluorescent probes developed specifically for the purpose of detecting calcium ions, also have high affinity for other metal ions such as zinc, cadmium, and lead. Upon binding to the metal or calcium ion, these indicators exhibit an increase in fluorescence emission intensity with little shift in wavelength. Figure 6.2 shows the visual screening of Ca^{2+} selective fluorescence indicator responses to different metal ions.

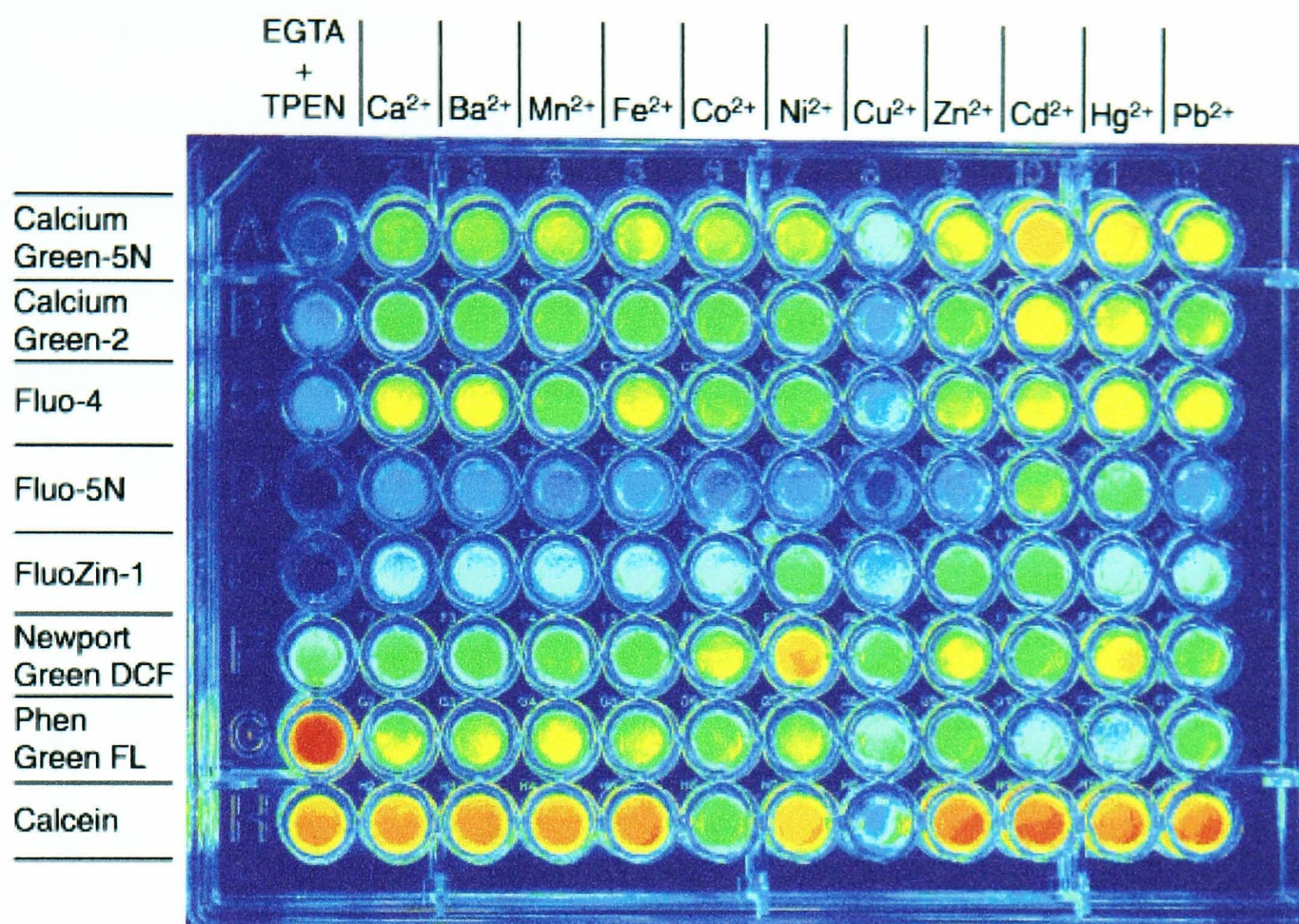


Figure 6.2 Visual screening of fluorescent indicator responses to metal ions. The image shows a 96-well microplate containing various combinations of ions and indicators in 50 mM MOPS pH 7.0. Each row of wells represents a different indicator; each column of wells represents a different ion. The indicators (top to bottom) are: Calcium Green-5N (0.5 μ M), Calcium Green-2 (0.2 μ M), fluo-4 (2 μ M), fluo-5N (2 μ M), FluoZin-1 (2 μ M), Newport Green DCF (2 μ M), Phen Green FL (2 μ M) and calcein (0.5 μ M). The left-hand column of wells contains 10 mM EGTA + 10 μ M TPEN (ion-free reference solution). Subsequent columns (left to right) represent 1 μ M concentrations of Ca²⁺, Ba²⁺, Mn²⁺, Fe²⁺, Co²⁺, Ni²⁺, Cu²⁺, Zn²⁺, Cd²⁺, Hg²⁺, and Pb²⁺, respectively. The microplate was scanned using a FLA3000G laser scanner (Fuji Photo Film Co.) with excitation at 473 nm and fluorescence emission detected at 520 nm. The image is pseudocolored according to fluorescence intensity (high = red > orange > yellow > green > blue = low). Image reproduced from reference 1.

The results from this microplate clearly show that the best indicators for the detection of cadmium ions are Calcium Green-5N and Calcein. Calcein, however, is easily contaminated by other metal ions present which may lead to quenching of the fluorescence induced by the presence of cadmium ions. Calcium Green-5N is also far more selective for cadmium ions over other metal ions. Traditional heavy metal indicator fluorophores could not, unfortunately, be used in the experiments as their excitation wavelengths were low, outside the region of the spectrum available on the confocal microscope.

Figure 6.3a shows the fluorescence response of Calcium Green-5N to different metal ions relative to an ion free reference solution. The fluorescence response is shown for 1 μM (blue) and 100 μM (red) solutions of the metal ion. A strong response is observed for the detection of Cd^{2+} at both high and low concentrations. The molecular structure of the indicator is shown in Figure 6.3(b).

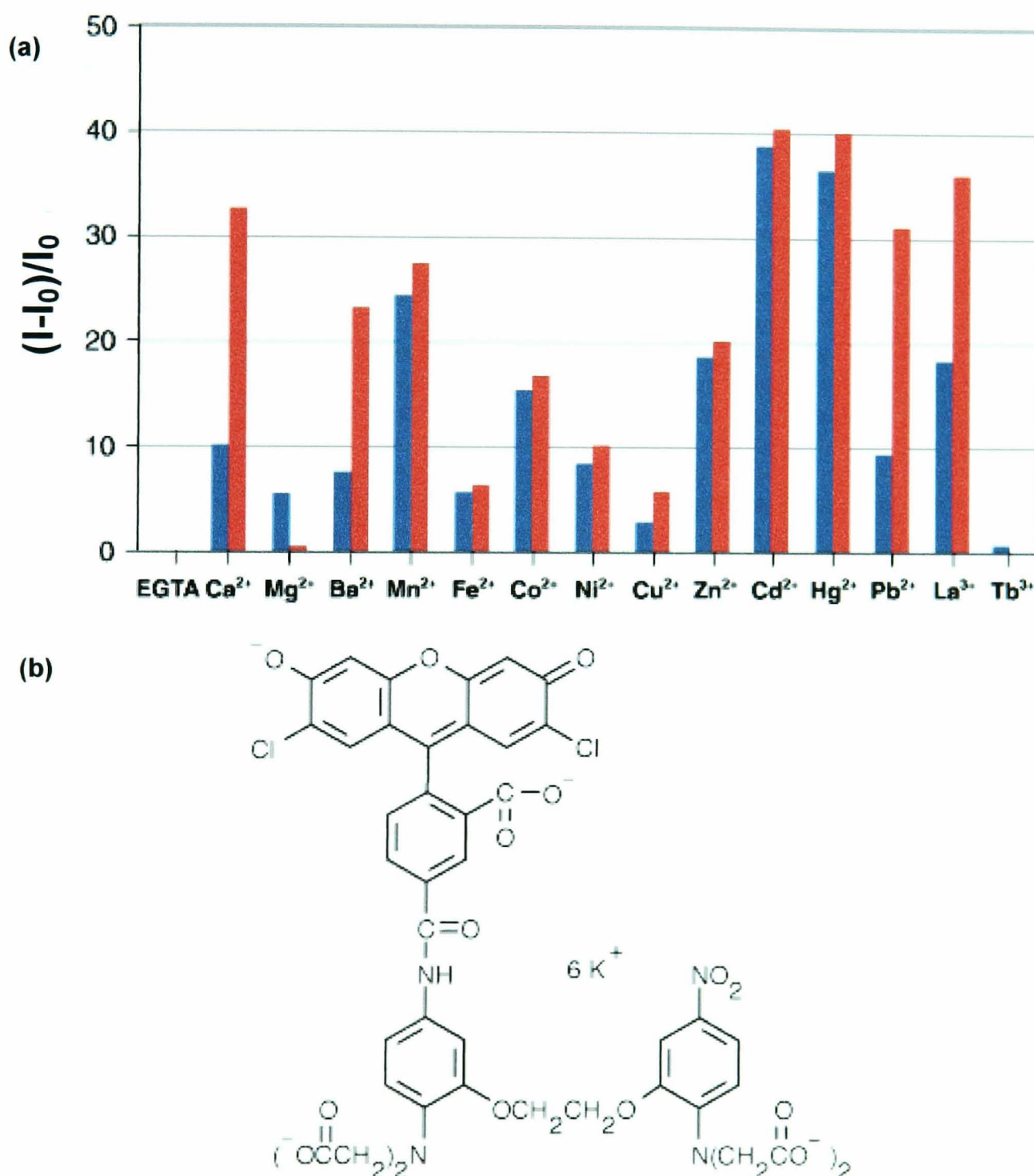


Figure 6.3 (a) Metal-ion response screening for Calcium Green-5N. The maximum relative fluorescence intensity was measured for indicator concentrations in solutions containing 10 mM EGTA + 10 μM TPEN, 1 μM ion (100 μM for Mg^{2+}) and 100 μM ion (10 mM for Mg^{2+}). Results are plotted as fluorescence changes relative to the ion-free (10 mM EGTA + 10 μM TPEN) reference solution expressed as $(I-I_0)/I_0$, where I is the fluorescence intensity of ion-containing solutions and I_0 is the fluorescence intensity of the reference solution. Blue bars indicate the response to 1 μM ion (100 μM for Mg^{2+}), and red bars indicate the response to 100 μM ion (10 mM for Mg^{2+}). (Reproduced from reference 1) **(b)** Molecular structure of the fluorescence indicator Calcium Green-5N.

6.2 Experimental

The deposition of mercury onto a 25 μm diameter Pt-disc UME was achieved by sealing the UME into a purpose built Teflon trough, through a hole in the base, and filling the trough with a mercurous nitrate solution (Section 2.5.2). The UME was polished with alumina and vigorously rinsed prior to deposition. Mercury deposition on the Pt UME was carried out via the application of a constant potential of -0.225 V vs. an Ag/AgCl reference electrode typically for a period of ~ 300 seconds. After deposition, the mercury UME was thoroughly rinsed whilst still in the trough to remove any traces of the deposition solution.

Simple ASV experiments were carried out to characterise the Hg UME electrochemical response to cadmium ion detection. The trough was filled with a solution containing $5 \times 10^{-4} \text{ mol dm}^{-3} \text{ CdNO}_3$ and $2 \times 10^{-3} \text{ mol dm}^{-3} \text{ KNO}_3$ and 3 different experiments were performed

- To characterise the stripping peak observed, the Hg UME was held at -1.1V for a preconcentration time of 240 seconds with respect to an Ag/AgCl electrode, before being scanned from -1 to -0.45 V at a potential sweep rate of 50 mV/sec.
- Transient analyses on the oxidation of cadmium-mercury amalgamate to cadmium ions were carried out, to examine the current response with respect to time upon application of potential after preconcentration. After a preconcentration time of 120 seconds at -1.1 V, the potential was pulsed to -0.95 V, -0.875 V, -0.85 V, -0.80 V, -0.75 V and -0.70 V for 10 seconds. The current-time response was recorded for each potential.
- Further transient analysis was carried out to investigate the effect of varying the preconcentration time. The preconcentration time at -1.1V was varied (120 seconds,

240 seconds and 480 seconds) and the current-time response recorded once more when the electrode was pulsed to -0.8 V for 10 seconds.

The fluorescent properties of Calcium Green-5N were characterised for solutions of different cadmium ion concentrations. Solutions containing $5 \times 10^{-6} \text{ mol dm}^{-3}$ Calcium Green-5N and Cd^{2+} concentrations between 1×10^{-4} and $1 \times 10^{-9} \text{ mol dm}^{-3}$ were made up. A frame of $650 \mu\text{m} \times 650 \mu\text{m}$ was imaged (512×512 pixels). An argon laser of wavelength 488 nm was used as the excitation source and a 505 nm long pass filter was employed when recording the fluorescence. To achieve the optimum compromise between resolution and image intensity, the confocal aperture was set to give an optical slice of $1.1 \mu\text{m}$.

For the combined CLSM/electrochemical measurements, the solution contained $0.5 \mu\text{mol dm}^{-3}$ Calcium Green-5N (Molecular Probes Inc.) and $1 \times 10^{-5} \text{ mol dm}^{-3}$ cadmium nitrate. Cadmium ions were deposited into the mercury droplet for deposition times between 10-80 seconds with the Hg UME held at -1.1V with respect to a Ag/AgCl reference electrode. The cadmium ions were then released by oxidising Cd in the Hg electrode during a scan from -1.1 V to -0.4 V at a potential sweep rate of 10 mV s^{-1} . The experimental set up is shown in Figure 6.4.

A water immersion lens (Zeiss, Achroplan 20x/0.50 W) was dipped into solution and focused on the electrode surface and a line, ca. $100 \mu\text{m}$ across was selected across the centre of the electrode surface as illustrated schematically in Figure 6.4(b). Line scans were recorded concurrently with the stripping voltammetry for the different deposition times using the confocal microscope. 512 pixel line scans were taken every 100 msec with 16 x signal averaging for each line scanned. The laser configuration, gains and pinhole used were the same as in the calibration measurements for Calcium Green-5N.

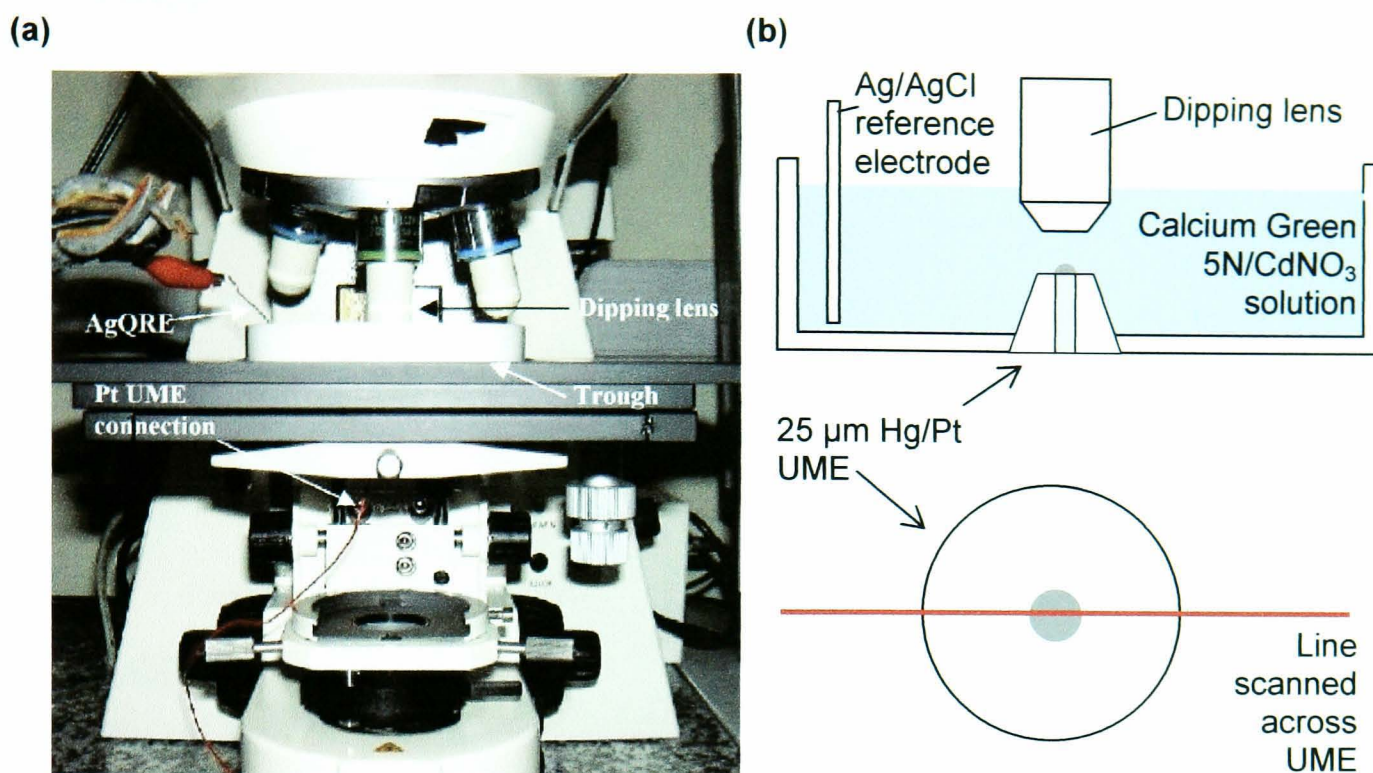


Figure 6.4 (a) Photograph of the experimental set-up showing the trough and electrode on the stage of the confocal microscope. (b) Schematic of experimental arrangements for studies of Cd²⁺ stripping experiments.

6.3 Results and Discussion

6.3.1 Mercury hemisphere ultramicroelectrode growth.

A typical growth transient for mercury deposition on the Pt UME, when the electrode was held at -0.225 V versus an Ag/AgCl reference electrode is shown in Figure 6.5. The diffusion limited current, i_{lim} , which flows at a disc UME is

$$i_{lim} = 4nFDac^* \quad 6.1$$

where n is the number of electrons transferred per redox event, F is Faraday's constant, D is the diffusion coefficient of the electroactive species, a is the electrode radius and c^* is the bulk concentration of the electroactive species. The diffusion limited current at a hemispherical mercury UME however, is given by equation 6.2.

$$i_{lim} = 2\pi maFDc^* \quad 6.2$$

Therefore, in the growth of a mercury hemisphere on a disc UME, the hemisphere is fully grown once the current has been increased by $2\pi/4$.

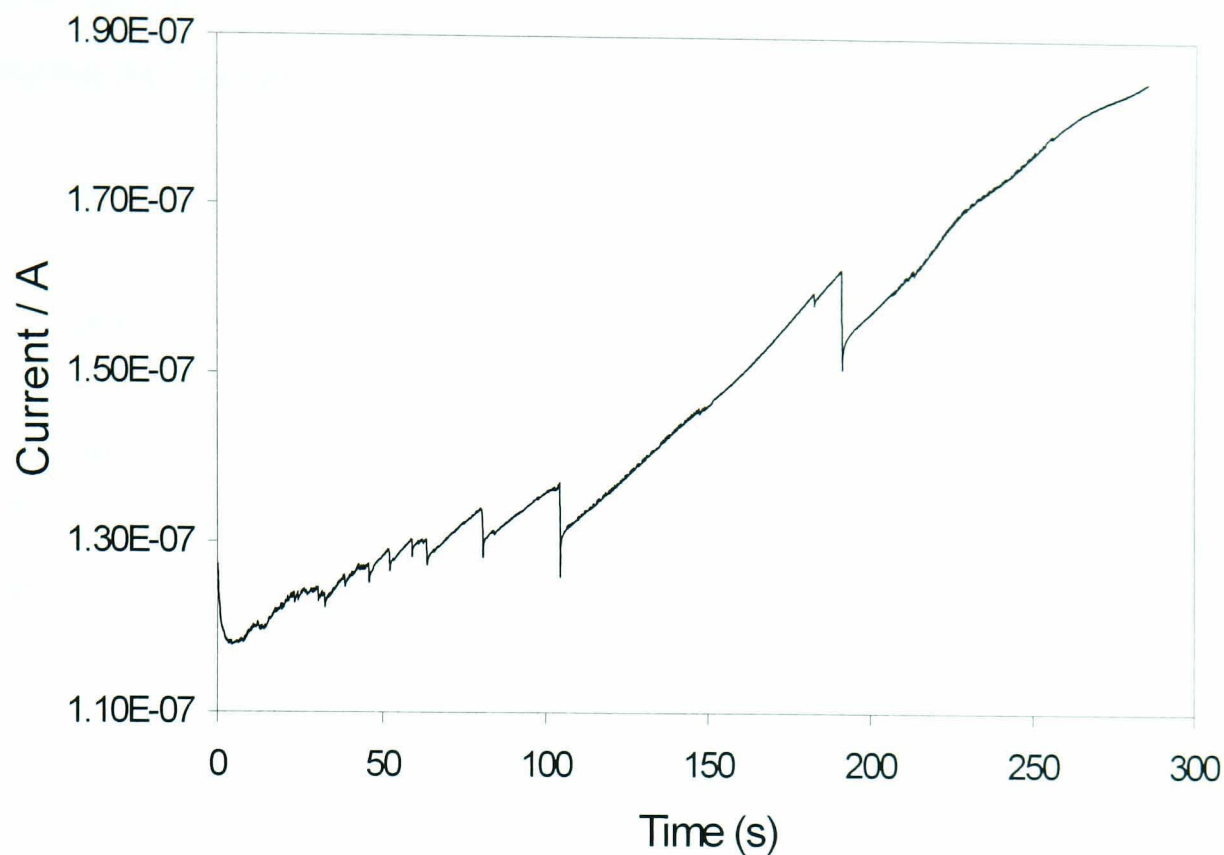


Figure 6.5 A typical current-time growth transient for the electrodeposition of mercury onto a 25 μm diameter Pt UME, from a solution containing 10 mM mercurous nitrate, 0.1 M HNO_3 and 0.5 M KNO_3 with the electrode held at -0.225 V.

Mercury electrodeposition at Pt occurs via the formation of a few isolated drops which do not cover the entire surface. The wetting process is slow and this results in a higher reduction current than would be expected for a surface spread evenly with mercury. When the mercury drops coalesce, a sudden drop in current is observed due to the decrease in surface area of the active electrode. The disappearance of these steps and the transition into a smooth linear growth is an indicator that a coherent mercury surface has been obtained.

6.3.2 Hg UME Stripping Voltammetry of Cd(II)

Cd(II) undergoes reduction at a potential which negates the use of Pt electrodes. The current for water reduction at these potentials masks the observation of Cd(II) reduction in this case. Mercury electrodes however, have a larger negative potential

range than Pt due to the high overpotential required for the evolution of hydrogen, thus making Hg a suitable electrode material for the trace detection of Cd(II).

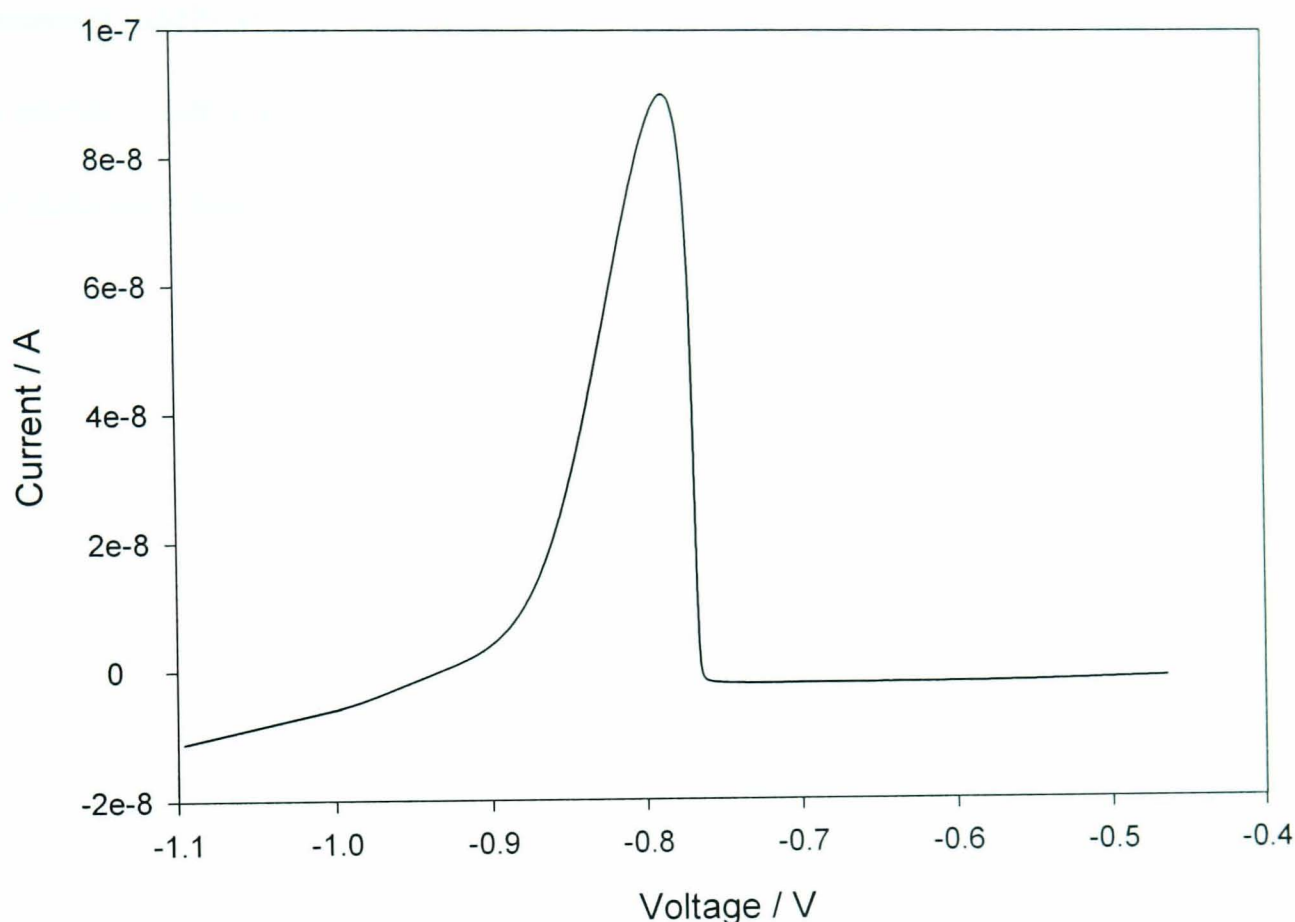


Figure 6.6 Typical stripping voltammogram of cadmium from a Hg/Pt UME. Preconcentration time 240 seconds.

Figure 6.6 shows a typical stripping voltammogram for the detection of a 5×10^{-4} mol dm⁻³ Cd²⁺ in 2×10^{-3} mol dm⁻³ KNO₃ solution at a mercury UME, fabricated as outlined in the previous section. Prior to stripping, the UME was held at a potential of -1.1 V for 240 seconds, to reduce cadmium ions to Cd to preconcentrate the mercury drop. The potential was then swept from -1.1 V to -0.4 V at a potential scan rate of 50 mV s⁻¹. A clear, well defined stripping peak is observed which is due to the oxidation of cadmium, deposited into the mercury hemisphere in the preconcentration step, to Cd²⁺ which diffuses into the solution.

6.3.3 Current-time studies of Cd^{2+} release from Hg

The characteristics of the stripping process can be confirmed by carrying out transient analysis on the oxidation of cadmium ions. Figure 6.7 shows the current response with respect to time upon application of several different potentials after preconcentration.

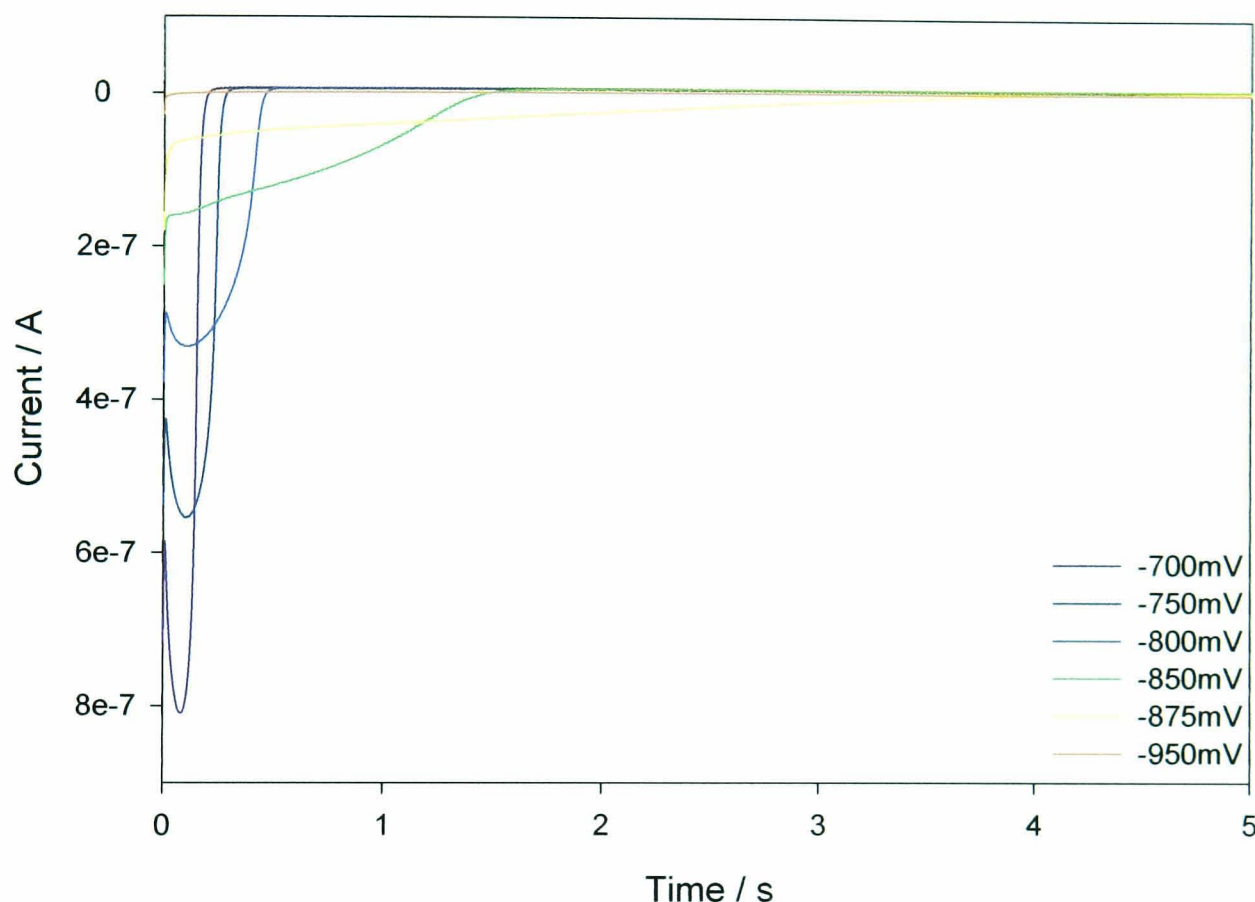


Figure 6.7 Current-time plots for the stripping of cadmium from a mercury UME. The electrode was preconcentrated for 120 seconds then held at the potentials shown in the legend.

The Hg/Pt UME was preconcentrated with cadmium ions at -1.1 V with respect to an Ag/AgCl electrode in a $5 \times 10^{-4}\text{ mol dm}^{-3}\text{ Cd}^{2+}$ and $2 \times 10^{-3}\text{ mol dm}^{-3}\text{ KNO}_3$ solution for 10 seconds. The potential was then stepped to a more positive value and the current-time response recorded. The results show that a faster release of cadmium ions (higher current) is observed when the preconcentrated electrode is pulsed to more positive potentials. The area under each of the transient peaks is equal to the electrical charge, Q , and this value is approximately the same for each of the potentials studied. A plot of charge against potential is shown in Figure 6.8 demonstrating this fact. This

means that the same amount of material is released in each transient, even though the rate of release from the hemisphere depends on the potential applied.

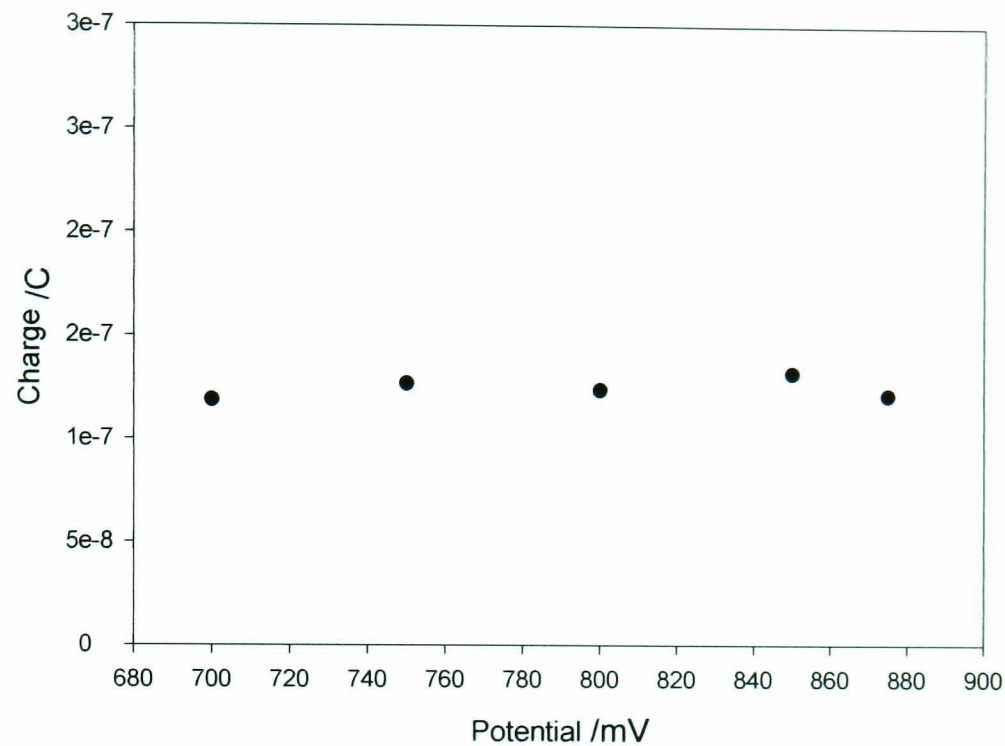


Figure 6.8 Plot showing the dependence of charge passed during stripping with the potential applied.

Figure 6.9 shows the current-time response when the preconcentrated electrode was jumped from -1.1V to -0.8 V. In this case the preconcentration time of the Hg/Pt UME was varied.

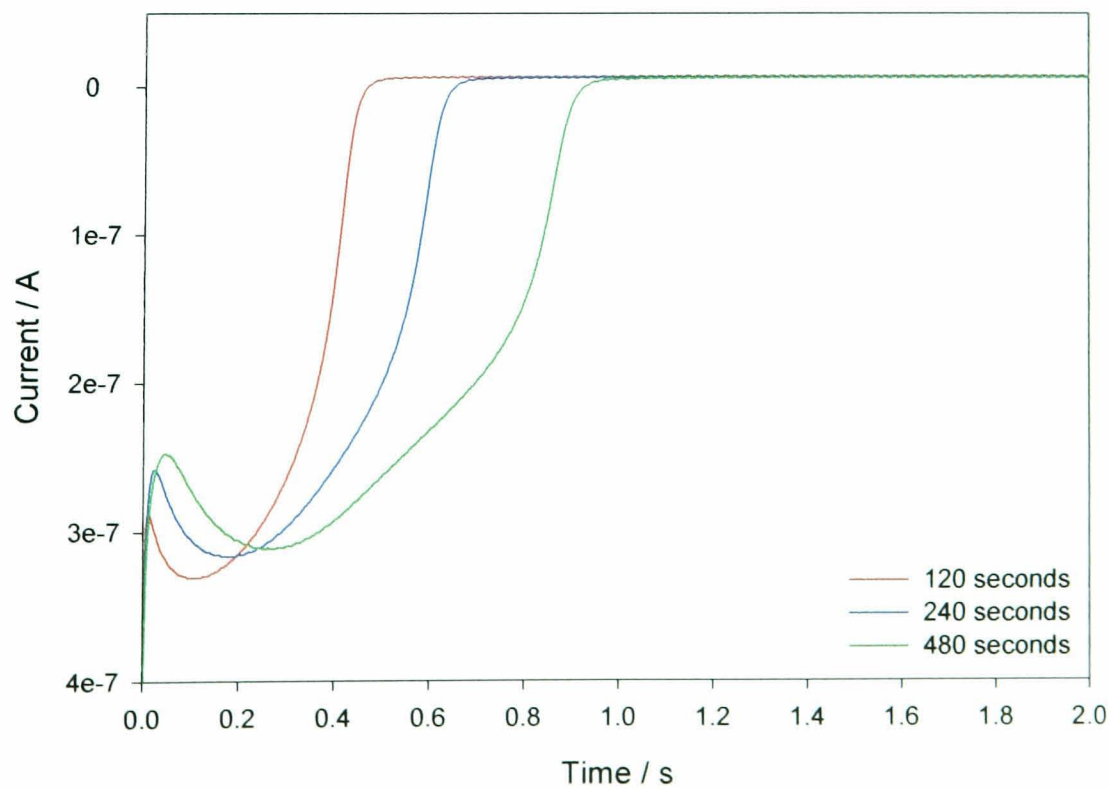


Figure 6.9 Current time plots for the stripping of cadmium from a mercury UME. The electrode was stepped from -1.1V to -0.8 V and was preconcentrated with cadmium for the times shown in the legend.

It is clear from these results that as the time taken to preconcentrate the mercury hemisphere UME with Cd^{2+} at -1.1 V is increased, the time taken for the electrode to release Cd^{2+} once the potential has been switched to -0.8 V also increases due to the greater amount of cadmium in the hemisphere electrode. As before, the area under the transient is equivalent to the electric charge passed during stripping and therefore the amount of Cd^{2+} released with, in this case, the log of charge shows an exponential dependence on the log of the preconcentration time, t , as shown in Figure 6.10.

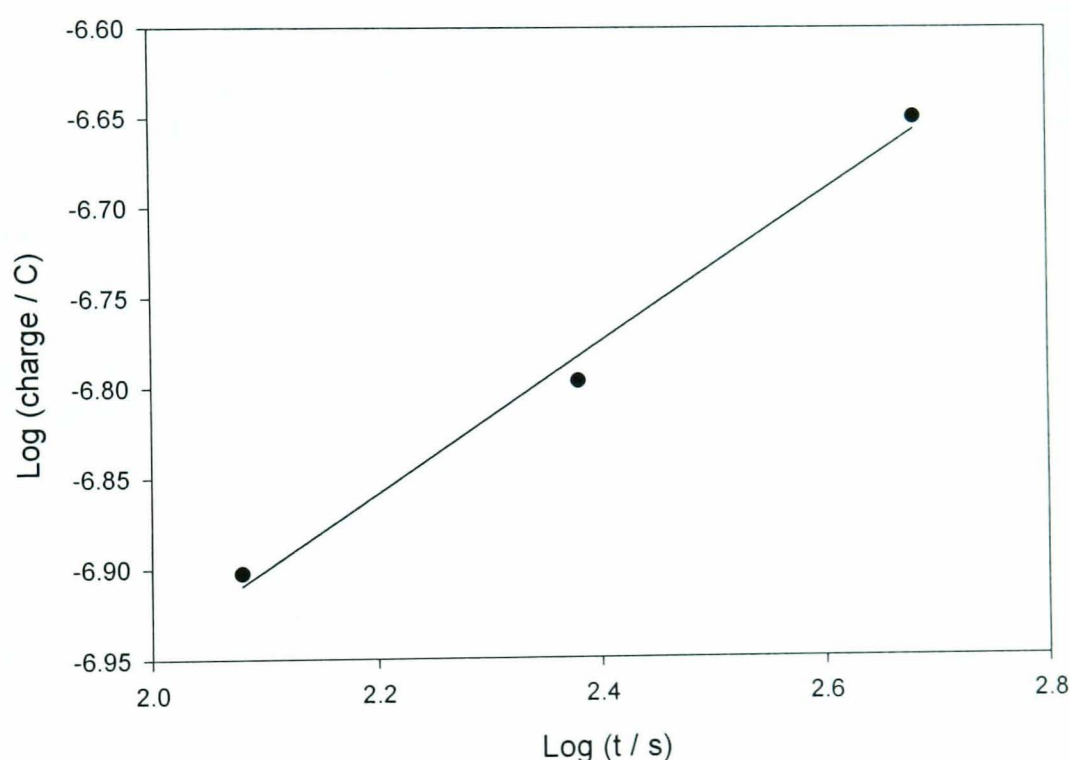


Figure 6.10 Plot showing the dependence of charge passed during stripping with deposition time.

6.3.4 Combined ASV and CLSM studies for the detection of Cd^{2+}

The dependence of the fluorescence of the indicator Calcium Green-5N on the amount of Cd^{2+} present in solution was established by averaging the light intensity, captured over a constant area, of solutions containing various cadmium concentrations. The appearance of all the solutions was uniform across a $650\text{ }\mu\text{m} \times 650\text{ }\mu\text{m}$ frame. Figure 6.11 shows the resulting plot with CLSM images collected at the marked concentration values.

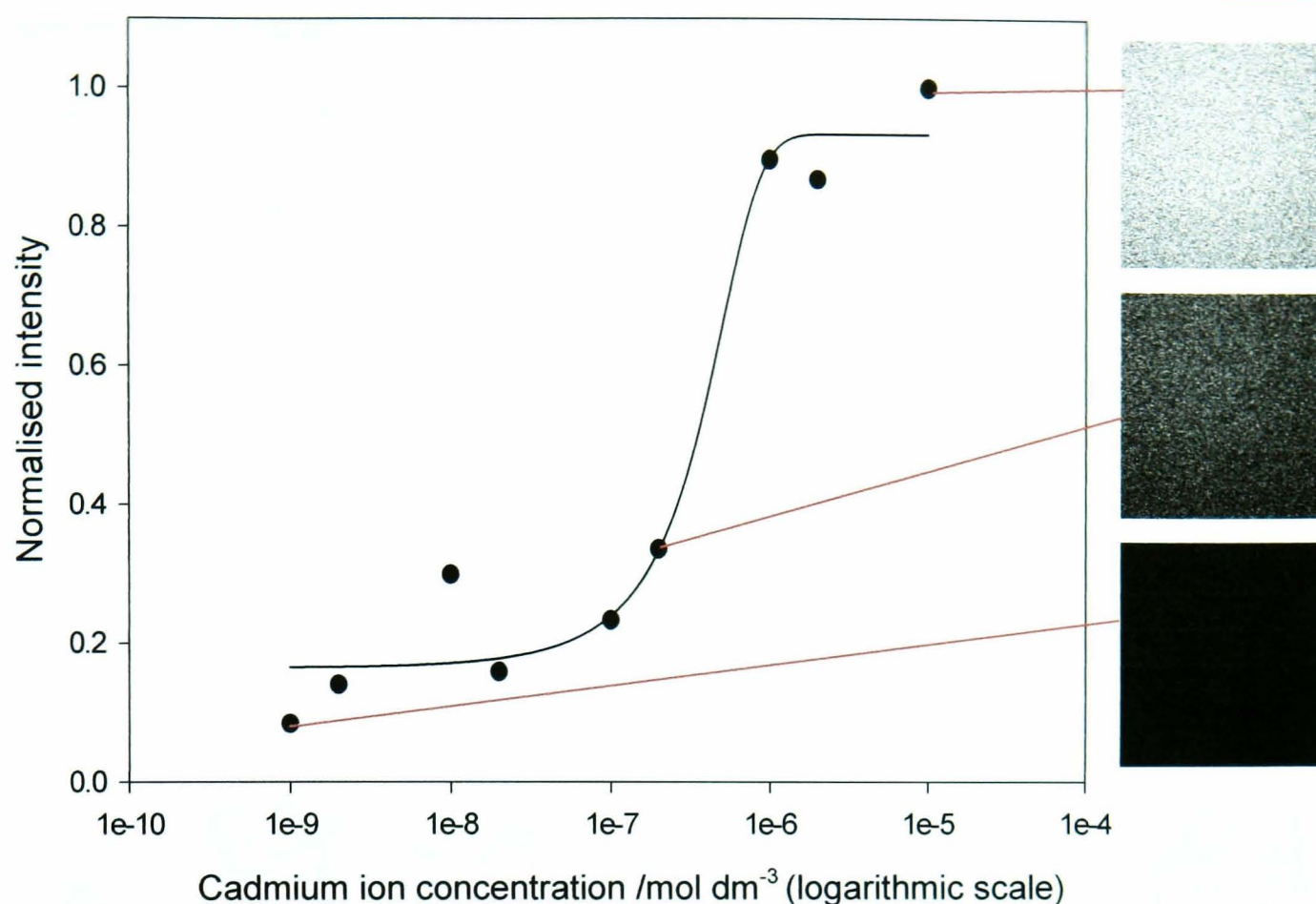


Figure 6.11 Normalised light intensity as a function of Cd^{2+} concentration for a solution of Calcium green 5N (5×10^{-7} M) and cadmium nitrate with CLSM images at marked concentration values.

The molecular structure of the fluorescent indicator Calcium Green-5N is shown in Figure 6.3. The calcium green indicator self quenches in the absence of divalent metal ions. Once the calcium binds it changes the net charge of the molecule and the resulting structural-conformational change relieves the quenching, which yields fluorescence. This mechanism also applies to Cd^{2+} . In the plot in Figure 6.11, the fluorescence begins to increase when the concentration of Cd^{2+} rises above 10^{-7} mol dm⁻³ and maximum fluorescence is achieved at about 10^{-6} mol dm⁻³.

Calcium Green-5N in its water soluble form exists as a hexa-potassium salt (Figure 6.3). Therefore, when attempting the trace detection of Cd^{2+} using ASV with potassium nitrate as a background electrolyte, no fluorescence was observed due to the preferential binding of the large amount of K^+ present in solution over the small amount of Cd^{2+} . All combined electrochemical-fluorescence measurements were therefore

carried out in solutions without background electrolyte which is possible due to the properties of Hg UMEs (see section 6.1).

To illustrate the capabilities of CLSM in this application, a fairly high concentration of cadmium nitrate solution was used ($1 \times 10^{-5} \text{ mol dm}^{-3}$), so that the solution would initially fluoresce. A decrease in fluorescence could then be observed around the mercury hemisphere during preconcentration time (due to depletion of Cd^{2+}) and a huge increase in fluorescence should be observed when the Cd^{2+} ions were stripped out the hemisphere. Figure 6.12 shows a typical fluorescence response of the Calcium Green 5N solution during anodic stripping voltammetry.

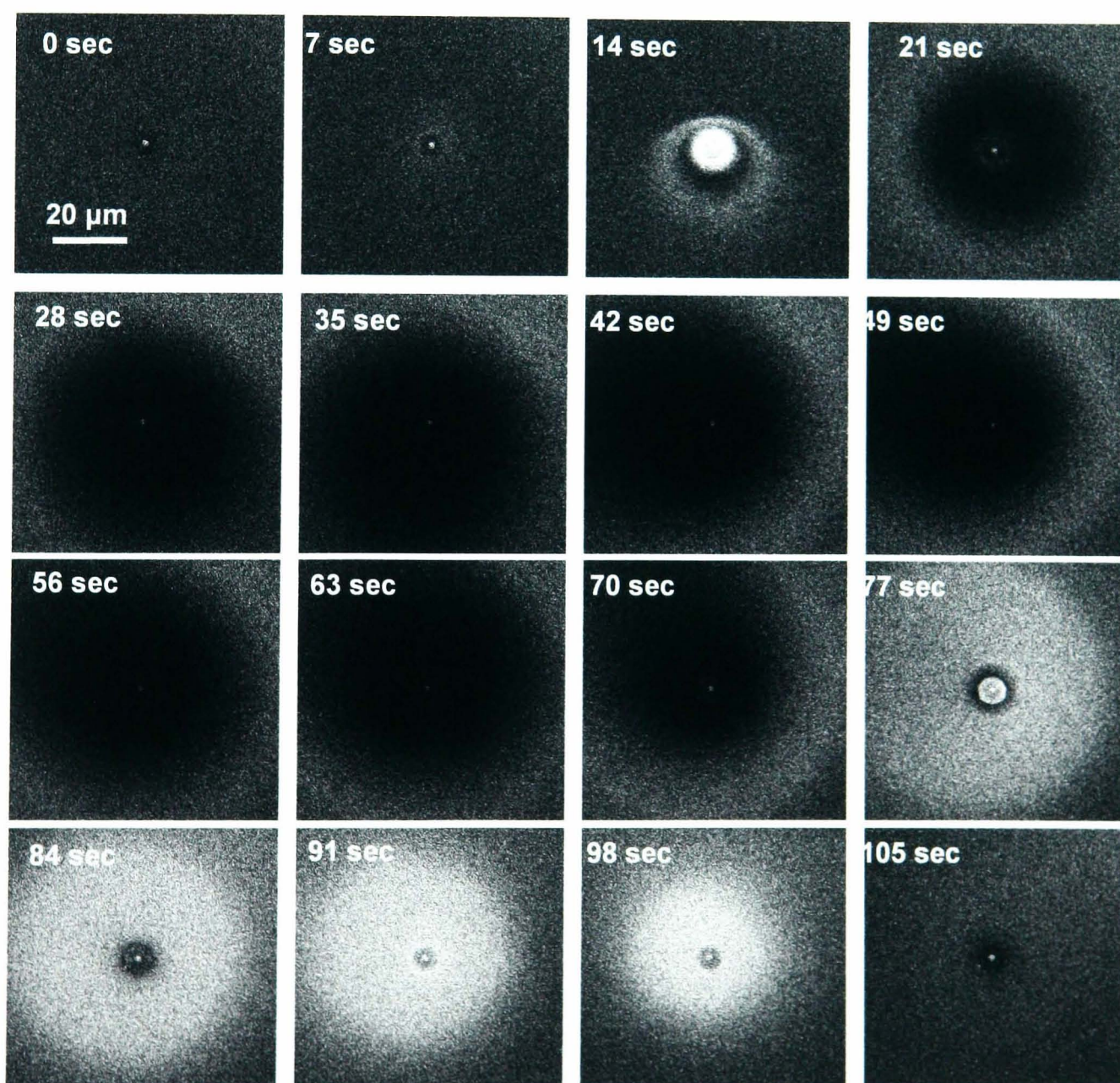


Figure 6.12 Time series of frames taken over the surface of an electrode in $1 \times 10^{-5} \text{ mol dm}^{-3} \text{ CdNO}_3$ and $0.5 \mu\text{mol dm}^{-3}$ Calcium Green 5N. Frames were taken every 7 seconds. Series recorded concurrently with ASV with preconcentration time of 60 seconds. Preconcentration time started at 14 seconds. Preconcentration was followed by a potential sweep from -1.1 to -0.5 V .

In this experiment, the preconcentration time was 60 seconds. The time at which the potential was stepped to -1.1 V can be clearly seen in these images as a bright spot after 14 seconds. This can be attributed to the Cd^{2+} moving through solution to surround the hemisphere prior to preconcentration. During the preconcentration time, from 14 to 74 seconds, a dark region forms around the electrode in solution. This is because Cd^{2+} ions are removed from solution into the mercury hemisphere. As the Calcium Green 5N indicator only fluoresces in the presence of Cd^{2+} once the ions are depleted the intensity decreases considerably as shown in these images.

At 77 seconds a bright ring of fluorescence around the electrode is established after the potential which scans at 50 mV s^{-1} (from -1.1 to 0.5 V), from $t = 74$ seconds onwards, reaches a potential where Cd^{2+} is released from the mercury hemisphere into solution. The electrochemical response, recorded at the same time as the CLSM imaging, established that the release was recorded electrochemically in a stripping peak, a few seconds before the bright ring of fluorescence was observed in the confocal images. This would suggest that there may be a delay in the binding of Cd^{2+} to the fluorescent indicator upon release. Additionally, there is an inherent diffusion time involved in Cd^{2+} diffusing from the electrode and establishing the diffusion profile. The time taken to establish the diffusion profile can be estimated from³⁹:

$$t = \frac{d^2}{2D} \quad 6.3$$

where t is the time taken for diffusion profile to be established, d is the diameter of the diffusion profile and D is the diffusion coefficient of the species in solution ($4 \times 10^{-6} \text{ cm}^2 \text{ s}^{-1}$ for Cd^{2+}). The approximate diameter of the diffusion profile is $55 \text{ }\mu\text{m}$ which means that the time taken to establish the diffusion profile is approximately 2.5 s.

In order to obtain CLSM data at an increased rate to compare more accurately with the electrochemical data, line scans over the centre of the electrode were recorded

every 100 msec during preconcentration and release of Cd^{2+} . Figure 6.13 represents how the data recorded relates to the system studied.

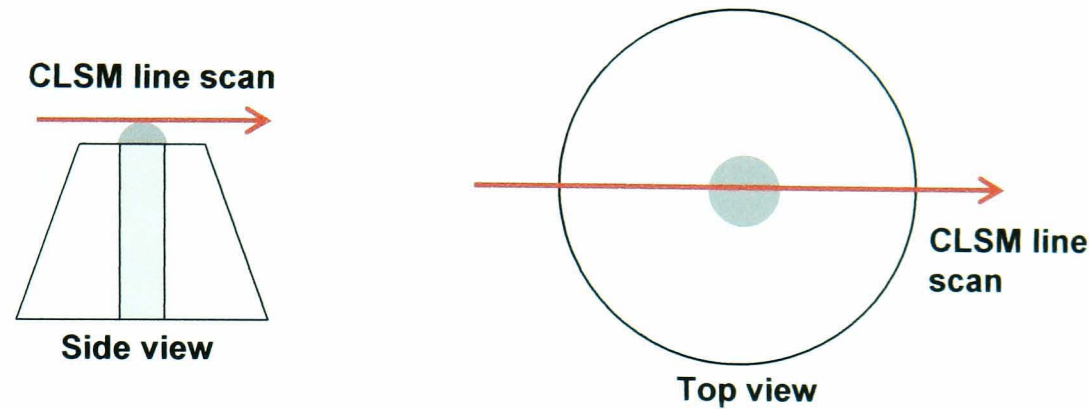


Figure 6.13 Schematic representation showing how spatiotemporal data collected relates to the system studied.

Spatiotemporal images were built up from this data (see later). Figure 6.14 shows the stripping peaks which were recorded simultaneously with the images. The preconcentration time was varied to examine the effect of increasing the amount of Cd^{2+} that would subsequently be released.

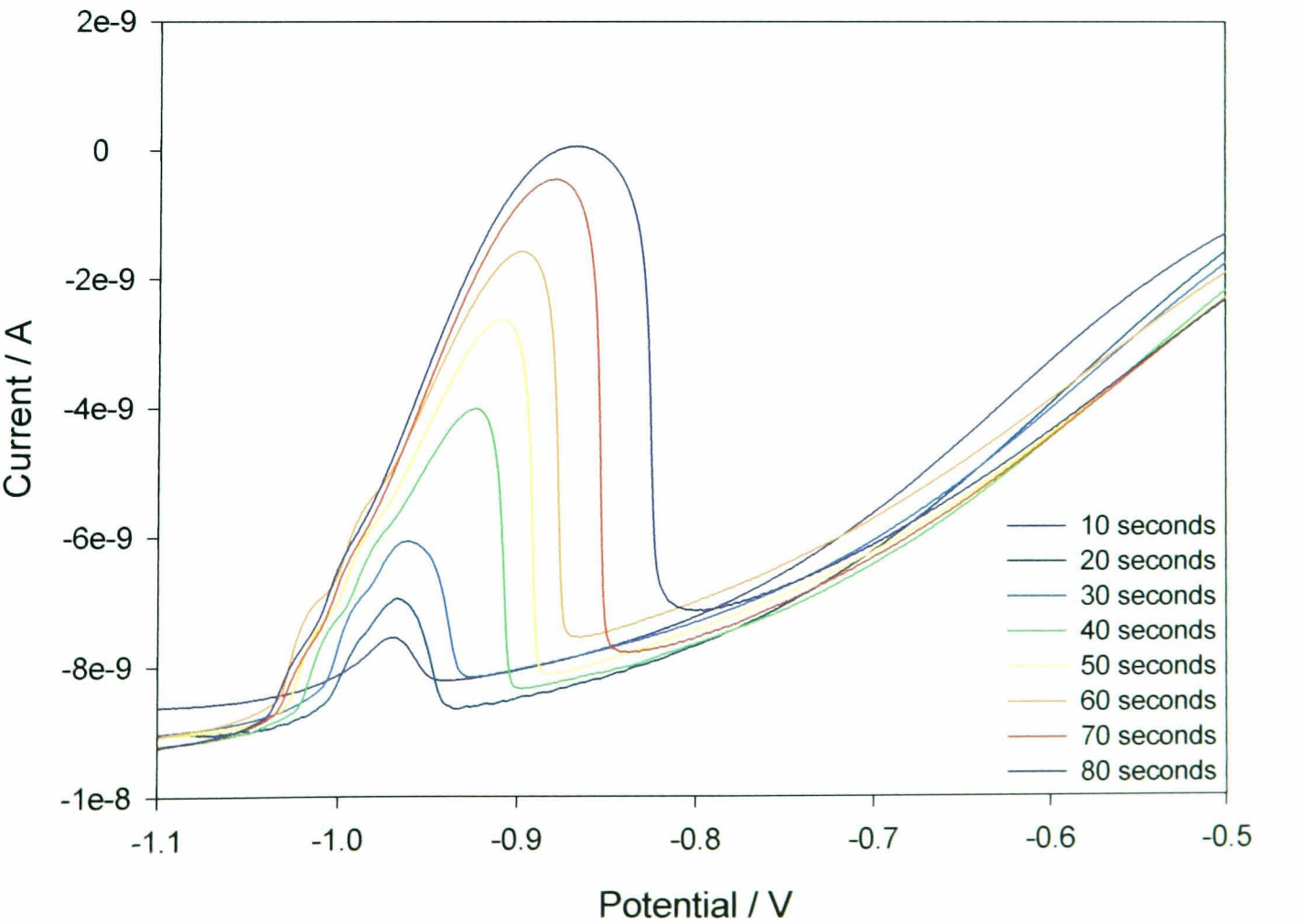


Figure 6.14 Stripping voltammograms of Cd^{2+} from a Hg UME recorded after specified preconcentration times. Associated spatiotemporal images are shown in Figure 6.12.

Figure 6.14 shows electrochemically that as the preconcentration time of cadmium ions into the mercury hemisphere increases, the current response from the stripping peak is amplified significantly. The shapes of the stripping peaks are not ideal; they are broad compared to measurements made when background electrolyte is present (Figure 6.6). The potential shifts anodically and there is a linear non-zero baseline. These are all the effects of having no supporting electrolyte present, which leads to significant ohmic effect. Nonetheless, electrochemical measurements can be made.

Figure 6.15 presents this data in an alternative way showing that the charge passed as Cd^{2+} ions are stripped out of the mercury hemisphere into solution is largely dependent on the time taken to deposit cadmium. A linear relationship is observed in a plot of log charge against log t with a much larger charge observed at longer deposition times corresponding to a larger amount of Cd^{2+} being released from the hemisphere.

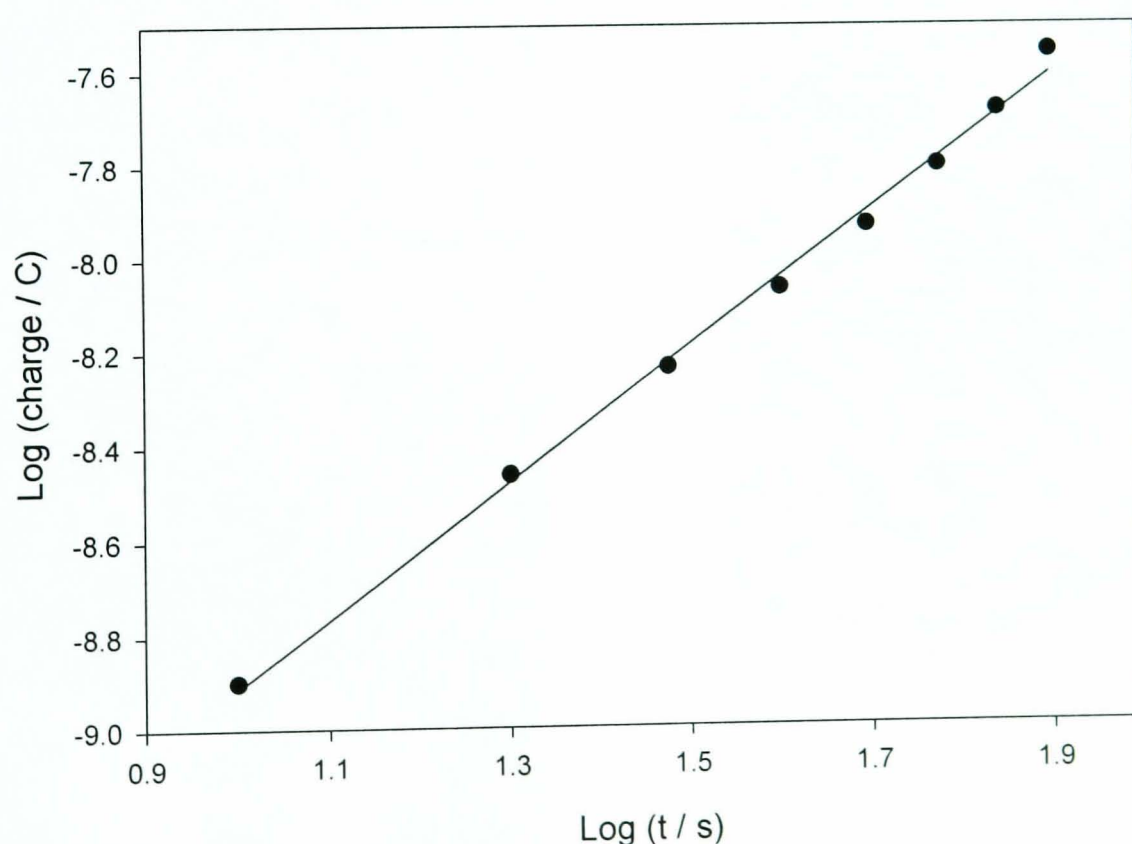


Figure 6.15 Plot showing the dependence of charge passed during stripping on the deposition time of cadmium into the mercury hemisphere UME.

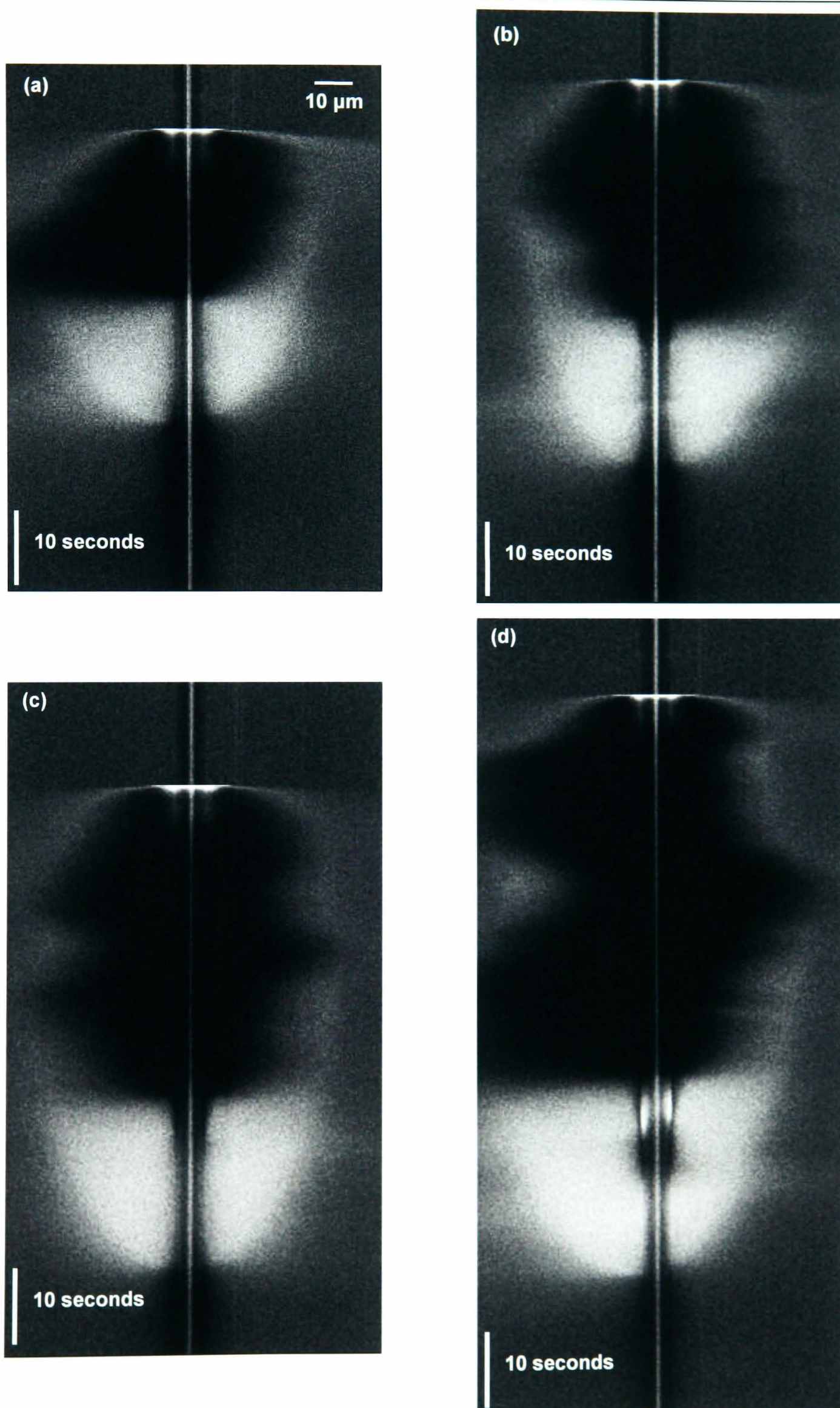


Figure 6.16 Line scans taken across the centre of the electrode over time for deposition times of (a) 10 seconds, (b) 20 seconds, (c) 30 seconds, (d) 40 seconds. Top of image represents start of experiment.

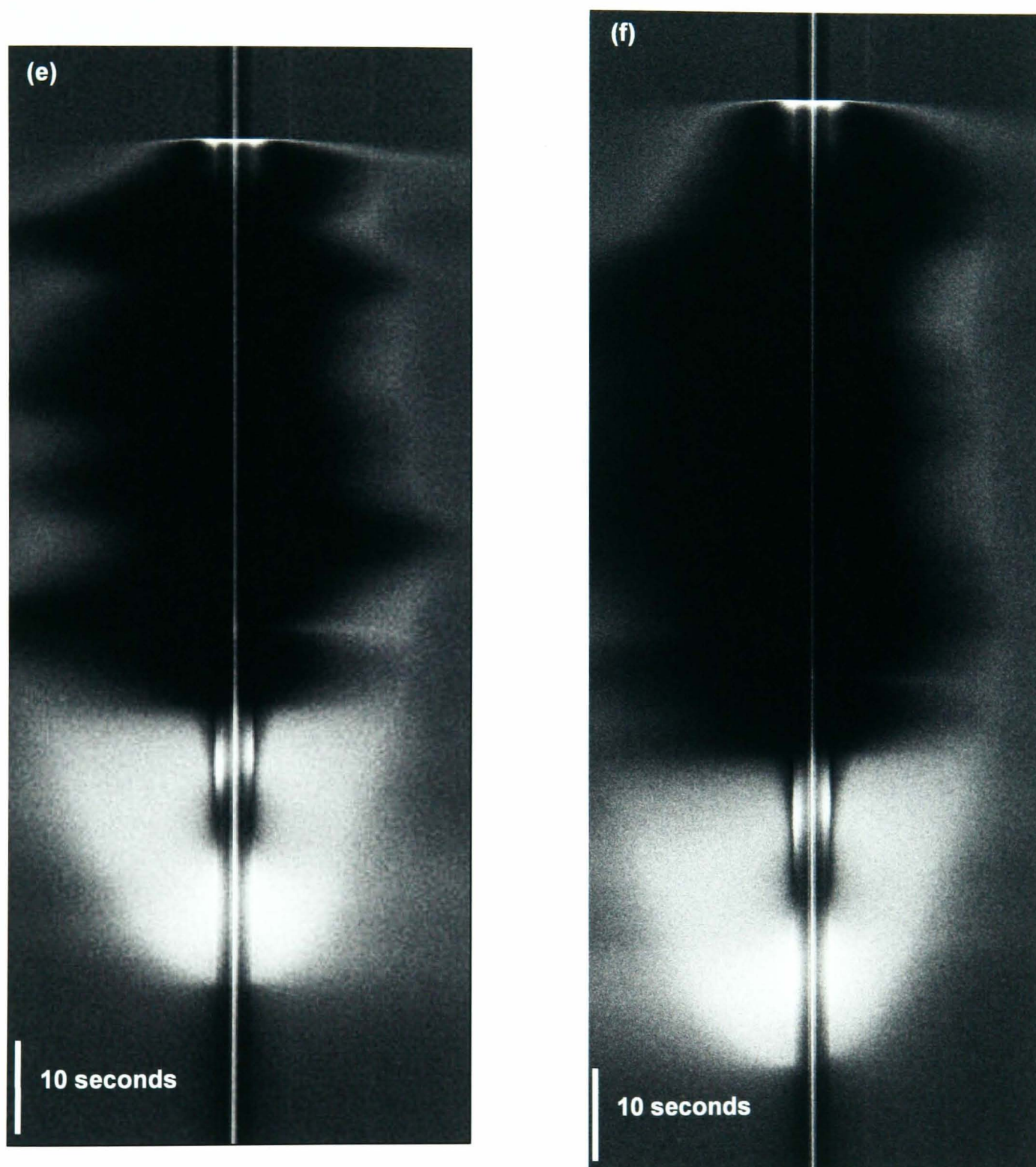


Figure 6.16 Line scans taken across the centre of the electrode over time for deposition times of (e) 50 seconds, (f) 60 seconds. Top of image represents start of experiment.

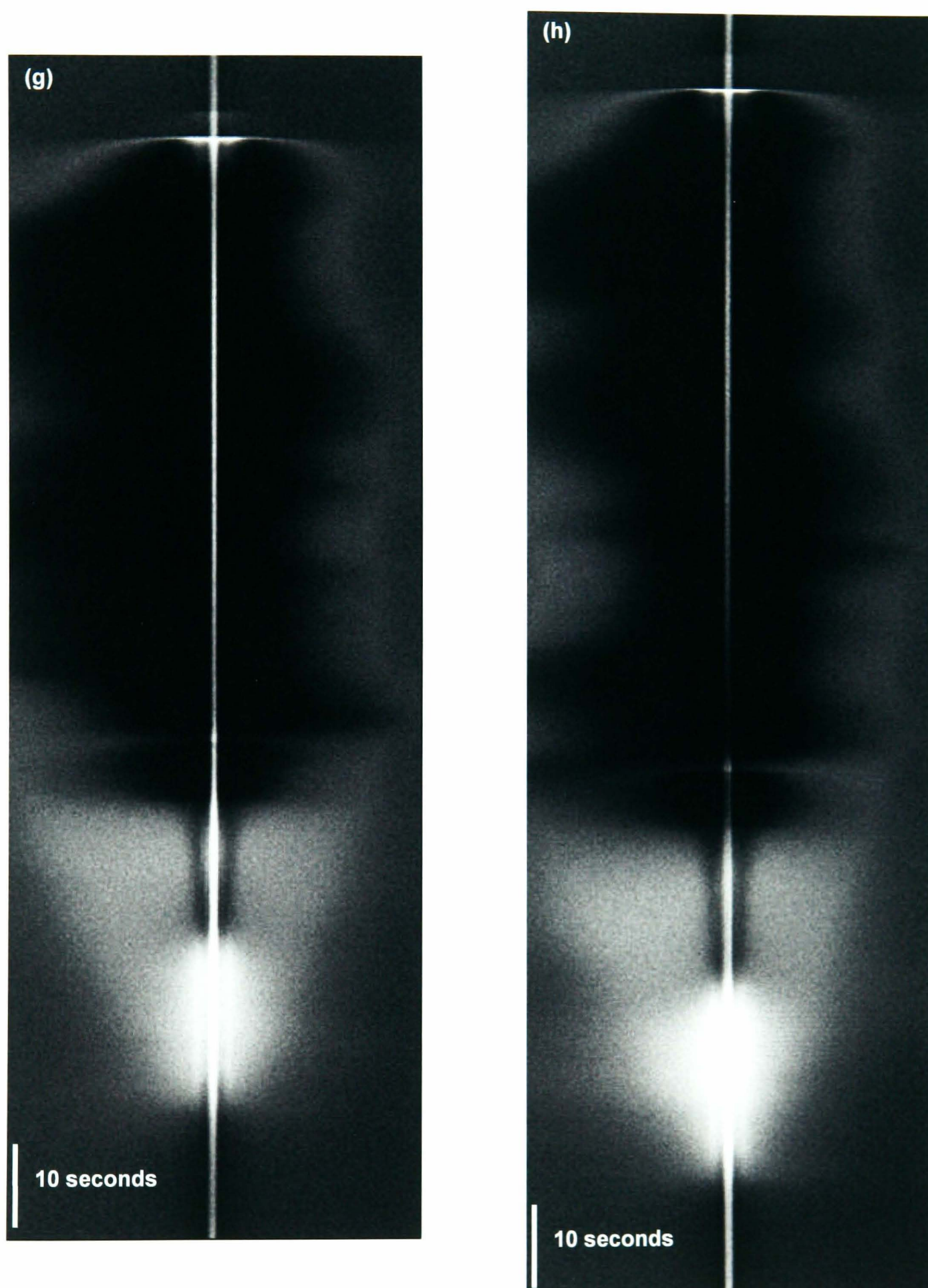


Figure 6.16 Line scans taken across the centre of the electrode over time for deposition times of (g) 70 seconds (h) 80 seconds. Top of image represents start of experiment.

The spatiotemporal images shown in Figure 6.16 are potentially very rich in information. Starting from the top of each of the images, at $t = 0$ sec, it is clear that during the preconcentration stage, i.e. when a potential of -1.1V has been applied to the Hg UME, a dark circular profile is rapidly established around the electrode. In all the deposition times the diameter of the dark ring observed is ca. 55 μm and corresponds to the diffusion field around the UME.

Since the Pt UME used to form the liquid Hg hemisphere was relatively large in UME terms, there is some movement in the diffusion field around the electrode during preconcentration time, due to movement of the liquid electrode. To overcome this problem, and to develop this technique further, a much smaller UME should be used in subsequent studies.

Another feature which is apparent in each of these images is that the depletion zone prevails for 10 seconds longer than the deposition time. This is evident from the dark circular zone giving way abruptly to an increase in fluorescence intensity. It would be expected that this would be seen at the same time as the stripping peak recorded in the voltammetry, but this is not the case. The time lag observed maybe associated with the diffusion time or the binding kinetics of the cadmium ions to the indicator Calcium Green-5N. However, binding kinetic studies on this indicator have only been carried out for Ca^{2+} ions⁴⁰. These studies showed that rate constant for the binding of calcium ions to Calcium Green-5N is relatively fast $4.0 \times 10^8 \text{ M}^{-1} \text{ s}^{-1}$.

A feature of these images which becomes more apparent as the preconcentration time increases is the dual nature of the release of Cd^{2+} . By examining the spatiotemporal images for 70 seconds preconcentration (Figure 6.16(g)) and 80 seconds preconcentration (Figure 6.16(h)), it can be seen that there is an initial release of cadmium ions, evident from the increase in fluorescence after the dark region, followed

by a far more intense release where the fluorescence corresponding to the concentration of cadmium ions present increases considerably. This pattern could correspond to an initial release of Cd^{2+} ions which are very near to or on the surface of the mercury hemisphere, followed by the bulk release of ions from the centre of the droplet.

In all of the images, the bright ring of fluorescence which is observed upon release of the cadmium ions is of approximately the same diameter as the dark ring observed during preconcentration time (ca. 55 μm) and this is associated with the diffusion field. A sharp return to background fluorescence after the Cd^{2+} release is also observed in all of the images suggesting that the fluorescence observed can be attributed to voltammetric experiments.

6.4 Conclusions

A technique has been developed which is capable of visualising the release and diffusion of a species (Cd^{2+}) from a hemisphere. Electrochemistry has been used in conjunction with CLSM to monitor quantitatively and visually the preconcentration and release of Cd^{2+} into and away from a mercury hemisphere UME. Using the fluorescent indicator Calcium Green-5N there is a delay between the release of Cd^{2+} from the hemisphere (determined voltammetrically) and binding to the molecules of the fluorophore. Further studies may involve using a much smaller Hg/Pt UME to eliminate movement of the liquid electrode during measurement so that a 3D diffusion profile of Cd^{2+} diffusing to and from the mercury hemisphere can be determined.

6.5 References

1. www.molecularprobes.com.
2. Barendrecht, E. *Electroanalytical Chemistry* 1967, 2, 53.
3. Baranski, A. S. *Analytical Chemistry* 1987, 59, 662.

4. Daniele, S.; Baldo, M. A.; Corbetta, M.; Mazzocchin, G. A. *Journal of electroanalytical chemistry* **1994**, 379, 261.
5. Macpherson, J. V.; Unwin, P. R. *Analytical Chemistry* **1997**, 69, 5045.
6. Wehmeyer, K. R.; Wightman, R. M. *Analytical Chemistry* **1985**, 57, 1989.
7. Wu, H. P. *Analytical Chemistry* **1996**, 68, 1639.
8. Zhou, F.; Aronson, J. T.; Ruegnitz, M. W. *Analytical Chemistry* **1997**, 69, 728.
9. Wang, J. *Stripping analysis - Principles, Instrumentation and Applications*; VCH: Deerfield Beach, Florida, 1985.
10. Vydra, F.; Stullk, K.; Julakova, E. *Electrochemical stripping analysis* Chichester, Sussex U.K., 1976.
11. Wiederin, D. R.; Smith, F. G.; Howk, R. S. *Analytical Chemistry* **1991**, 225.
12. Wang, J. *Electroanalytical chemistry*; Dekker: New York, 1989; Vol. 16.
13. Baranski, A. S.; Quon, H. *Analytical Chemistry* **1986**, 58, 407.
14. Harman, A. R.; Baranski, A. S. *Anal. Chim. Acta* **1990**, 239, 35.
15. Matysik, F. M.; Werner, G. *Analyst* **1993**, 118, 1523.
16. Tay, E. B. T.; Khoo, S. B.; Loh, S. W. *Analyst* **1989**, 114, 1039.
17. Wojciechowski, M.; Balcerzak, J. *Anal. Chim. Acta* **1990**, 237, 127.
18. Wojciechowski, M.; Balcerzak, J. *Anal. Chim. Acta* **1991**, 249, 433.
19. Cushman, M. R.; Bennett, N. G.; Anderson, C. W. *Anal. Chim. Acta* **1981**, 130, 323.
20. Golub, D.; Soffer, A.; Oren, Y. *Journal of electroanalytical chemistry and interfacial electrochemistry* **1989**, 260, 383.
21. Wu, H. P. *Analytical Chemistry* **1994**, 66, 3151.
22. Yoshmina, Z. *Chem. Soc. Jpn.* **1981**, 54, 556.
23. Matysik, F. M.; Glaser, P.; Werner, G. *Analyst* **1994**, 349, 646.
24. Montenegro, I.; Queiros, M. A.; Daschbach, J. L. *Microelectrodes: Theory and Applications*; Kluwer: Dordrecht, 1991.
25. Pena, M. J.; Fleischmann, M.; Garrard, N. *Journal of electroanalytical chemistry* **1987**, 213, 189.
26. Ciszowska, M.; Stojek, Z. *Journal of electroanalytical chemistry* **1986**, 213, 189.
27. Amatore, C.; Deakin, M. R.; Wightman, R. M. *Journal of electroanalytical chemistry* **1987**, 1987, 49.
28. Stojek, Z.; Osteryoung, J. *Analytical Chemistry* **1988**, 60, 131.

29. Ciszowska, M.; Stojek, Z.; Osteryoung, J. *Analytical Chemistry* **1990**, 62, 349.
30. Drew, S. M.; Wightman, R. M.; Amatore, C. *Journal of electroanalytical chemistry* **1991**, 317, 117.
31. Cooper, J. B.; Bond, A. M. *Journal of electroanalytical chemistry* **1991**, 315, 143.
32. Daniele, S.; Mazzocchin, G. A. *Anal. Chim. Acta* **1993**, 273, 3.
33. Burchiel, S. W.; Edwards, B. S.; Kuckuck, F. W.; Lauer, F. T.; Prossnitz, E. R.; Ransom, J. T.; Sklar, L. A. *Methods* **2000**, 21, 221.
34. Haugland, R. P.; Johnson, I. D. *Fluorescent and luminiscent probes for biological activity*, 2nd ed., 1999.
35. Kao, J. P. *Methods of Cell Biology* **1994**, 40, 155.
36. Lipp, P.; Bootman, M. D.; Collins, T. *Cellular calcium practical approach*, 2nd ed., 2001.
37. Silver, R. B. *Methods of Cell Biology* **1998**, 56, 237.
38. Takahashi, A.; Camacho, P.; Lechleiter, J. D.; Herman, B. *Physiology Review* **1999**, 79, 1089.
39. Bard, A. J.; Faulkner, L. R. *Electrochemical methods: Fundamentals and applications*, Second ed.; John Wiley and Sons: America.
40. Naraghi, M. *Cell Calcium* **1997**, 22, 255.

Chapter 7

Conclusions

For the first time, the structural, adhesion and release properties of polyurea microcapsules have been characterised at the single capsule level. These microcapsules are designed for use in agriculture, for the controlled delivery of pesticides to crops. Little is known about how or why the microcapsules work and the studies in this thesis present new methodologies for investigating specific properties of the microcapsules which had either not previously been studied or had only been examined at the bulk level.

The adhesion characteristics of functionalised microcapsules have never before been investigated for this polyurea microcapsule system and these studies show how by using an adaptation of AFM, specifically CFM, the adhesion properties are able to be fully characterised. Previously, the release characteristics of these microcapsules have been investigated in bulk. The studies presented in this thesis provide more detailed information regarding the mechanism of release for different pesticides both in solution and in the dry state at the single capsule level.

The adhesion characteristics of polymeric microcapsules is of particular importance in agriculture as the amount of pesticide which is delivered to the pest is directly proportional to the number of microcapsules which adhere to the surface of crops/leaves and therefore the effectiveness of the treatment. In Chapter 3, the use of AFM has been described as a technique for investigating the adhesion characteristics of single functionalised microcapsules, attached to the tip of an AFM cantilever, to model surfaces over a range of pHs. SAMs of OH-terminated alkyl thiols on gold have been characterised and used as the model surface in adhesion measurements.

Adhesion was observed between all microcapsules and the OH-terminated SAM. This adhesion can be attributed to the presence of hydrogen bonding groups

within the wall of the microcapsule. Enhanced adhesion was observed between microcapsules whose surfaces had been modified with molecules containing ethylene and propylene oxide functional groups. This is thought to be due to further hydrogen bonding between these groups and the SAM. Supplementary evidence for this was provided from studies into the adhesion of the same microcapsules to CH₃-terminated SAM, where enhanced adhesion was not observed.

The surface topography and elasticity of the microcapsules will have had a huge effect on the contact area and surface groups exposed and hence the number of bonds formed during contact of the microcapsule with the surface of interest. It was found that the microcapsules deformed upon compression and SEM images showed that the surface topography of the microcapsules varied considerably for each microcapsule.

For all microcapsules enhanced adhesion to the OH-terminated SAM was observed at low pH. This could be attributed to the fact that at low pH the cross-linking between the polymer chains may start to weaken, leading to an increase in the amount of hydrogen bonding groups within the wall of the capsule which are exposed to the hydrophilic SAM. The microcapsules whose surfaces had been modified with molecules not containing the ethylene and propylene oxide groups exhibited similar adhesion to the unmodified microcapsule with slightly enhanced adhesion at low pH.

The surface $pK_{1/2}$ for the sulfonate-modified microcapsule was estimated to be ca. 4. This value is much higher than that of a sulfonate group free in solution, but the value is expected to increase due to the fact that the limited ability of the solvent (and ions) to shield charged species at the interface, compared to solution. Furthermore, in-plane hydrogen bonding between molecules on the surface should increase the difficulty in ionising surface bound species. The variety of functional groups on the microcapsule

surface which are exposed to the substrate in these measurements may also be a contributing factor.

The ultimate aim of these studies was to investigate the adhesion of the functionalised microcapsules to the surface of a leaf. A solution of 70:30 CH₃: COOH-terminated thiol was used to form a mixed monolayer mimicking the proportions of hydrophobic/hydrophilic sites on a leaf cuticle. Similar adhesion was observed on this monolayer to that of a pure CH₃-terminated monolayer. No sites of enhanced adhesion were observed.

Adhesion measurements of microcapsules to the cuticle of a leaf of the *Prunus laurocerasus* showed that sites of enhanced adhesion were present. This could be attributed either to large areas of hydrophilicity on the leaf cuticle, or more likely, the enhanced adhesion was due to the fact the leaf surface was not flat. The cuticle surfaces are extremely irregular and if the capsule was brought into contact with a ridge then a small contact area would result leading to decreased adhesion.

Overall, these studies have provided a vast amount of detail about the adhesion characteristics of polymeric microcapsules. The 'bare' wall of the capsule was shown to exhibit adhesive properties to hydrophilic surfaces and this adhesion could be enhanced considerably by the addition of modifier molecules containing hydrogen-bonding groups such as ethylene and propylene oxide. It has been shown that the surface topography of the leaf/crop has a large effect on the adhesion characteristics of the microcapsules to the surface.

The release properties of microcapsules have been investigated in bulk, into solution, using a variety of techniques. In Chapter 4 CLSM is presented, for the first time, as a technique which can be used in the study of the release of active ingredient from microcapsules at the single capsule level. CLSM has been used to track the levels

of active ingredient inside the microcapsule following release into an aqueous-ethanolic solution. Release profile of pesticide from a capsule was recorded using this technique. From the data, the products of the mass transfer coefficient and the solubility coefficient of the pesticide in the polymeric wall have been estimated.

In order to investigate how changing the polymeric wall affects the controlled release properties of microcapsules, the thickness and the cross-linking density of the polymer wall were varied. Using CLSM, it was found that, as expected, the microcapsules with the thicker, denser walls took longer to release the pesticide (lambda cyhalothrin) encapsulated inside the polymer wall. The product of the mass transfer coefficient and solubility coefficient of the pesticide in the polymeric wall provided further evidence for this phenomenon, with the thicker, denser walled microcapsules having much smaller coefficients associated with their release profiles. This indicates that the mass transfer coefficient and/or the solubility coefficient decrease with increasing wall density.

These studies provide a detailed insight at the single capsule level into how the microcapsules release species into solution. The results could be used to determine the optimum wall thickness/cross linking density that should be employed to obtain the most effective crop protection.

In order to study the most life-like system, release measurements were made in the dry state, i.e. with the capsules dried down from their aqueous storage solution. Chapter 5 provides details of CLSM investigations into the release properties of both lambda cyhalothrin and emamectin benzoate containing capsules. It was shown that the two types of capsule exhibited different release properties when dried down onto the leaf of the *Prunus laurocerasus*.

Investigations found that the lambda cyhalothrin containing capsules showed a significant decrease in fluorescence, indicating significant release over time, whereas the emamectin benzoate capsules showed a very small decrease in fluorescence over time. A simple model was used to obtain a rate constant for release from the lambda cyhalothrin capsule which compared well with literature.

The emamectin benzoate capsules were not designed to release in the dry state and so the small decrease in fluorescence observed in these measurements was cause for concern. To investigate this further, more detailed studies were carried out with the microcapsules deposited onto hydrophilic and hydrophobic surfaces to determine whether the decrease in fluorescence observed on the leaf was due to release of pesticide from the microcapsule. If pesticide was released from the microcapsule then an increased rate of release should have been observed onto the hydrophobic surface. However, this was not observed; the surface upon which the microcapsule was placed had no significant effect on the release, with the same small decrease in fluorescence observed in each case. The observed decrease in fluorescence was thus attributed to a redistribution of pesticide within the microcapsule which could be, for example, a slight increase in the radius of the microcapsule upon drying down onto the leaf surface.

The high resolution imaging capabilities of CLSM have been used to investigate the structure of leaf and caterpillar cuticles. This approach also used the direct non-invasive properties of the technique to investigate the internal structure of the leaf of the *Prunus laurocerasus*. It was shown how this technique can be used to determine the effect of the preparation of leaf sample on the internal structure of the leaf.

The results presented in Chapters 4 and 5 demonstrate the viability of CLSM as a technique which can be used for the study of the release of species from single microcapsules in both the dry state and under solution. Data obtained from these

experiments can be directly compared to theoretical values calculated for release from single microcapsules.

Imaging the release of pesticide from microcapsules into solution has been demonstrated using CLSM. It would be beneficial to develop the methodology further to monitor the diffusion of species away from surfaces into solution. Chapter 6 detailed the development of a technique which is capable of visualising the release and diffusion of a species (Cd^{2+}) from a hemisphere in solution. Voltammetry was used in conjunction with CLSM to monitor quantitatively and visually the preconcentration and release of Cd^{2+} into and away from a mercury hemisphere UME.

Using the fluorescent indicator Calcium Green-5N a delay was observed between the release of Cd^{2+} from the hemisphere (determined voltammetrically) and binding to the molecules of the fluorophore. The time lag observed may be associated with the diffusion time or the binding kinetics of the cadmium ions to the indicator molecule. These studies have shown that it is possible to use CLSM to monitor the diffusion of species into and away from surfaces in solution. Further studies could involve the use of a much smaller Hg/Pt UME to eliminate movement of the liquid electrode during measurement so that a 3D diffusion profile of Cd^{2+} diffusing to and from the mercury hemisphere could be determined. This technique could be developed to study the release of species from a microcapsule. For example, a change in the environment surrounding the capsule brought about by electrochemistry may cause the capsule to release which could be monitored using CLSM.

Overall, the aims of this thesis have been achieved. For the first time the adhesive properties of functionalised polyurea microcapsules have been characterised and new methodologies have been developed with the use of CLSM to investigate the release characteristics of single polymeric microcapsules both in the dry state and in

solution. Preliminary studies on the combined use of CLSM and electrochemistry have proved promising in the development of the technique for the visualisation of the release and diffusion characteristics of species from a mercury hemisphere.